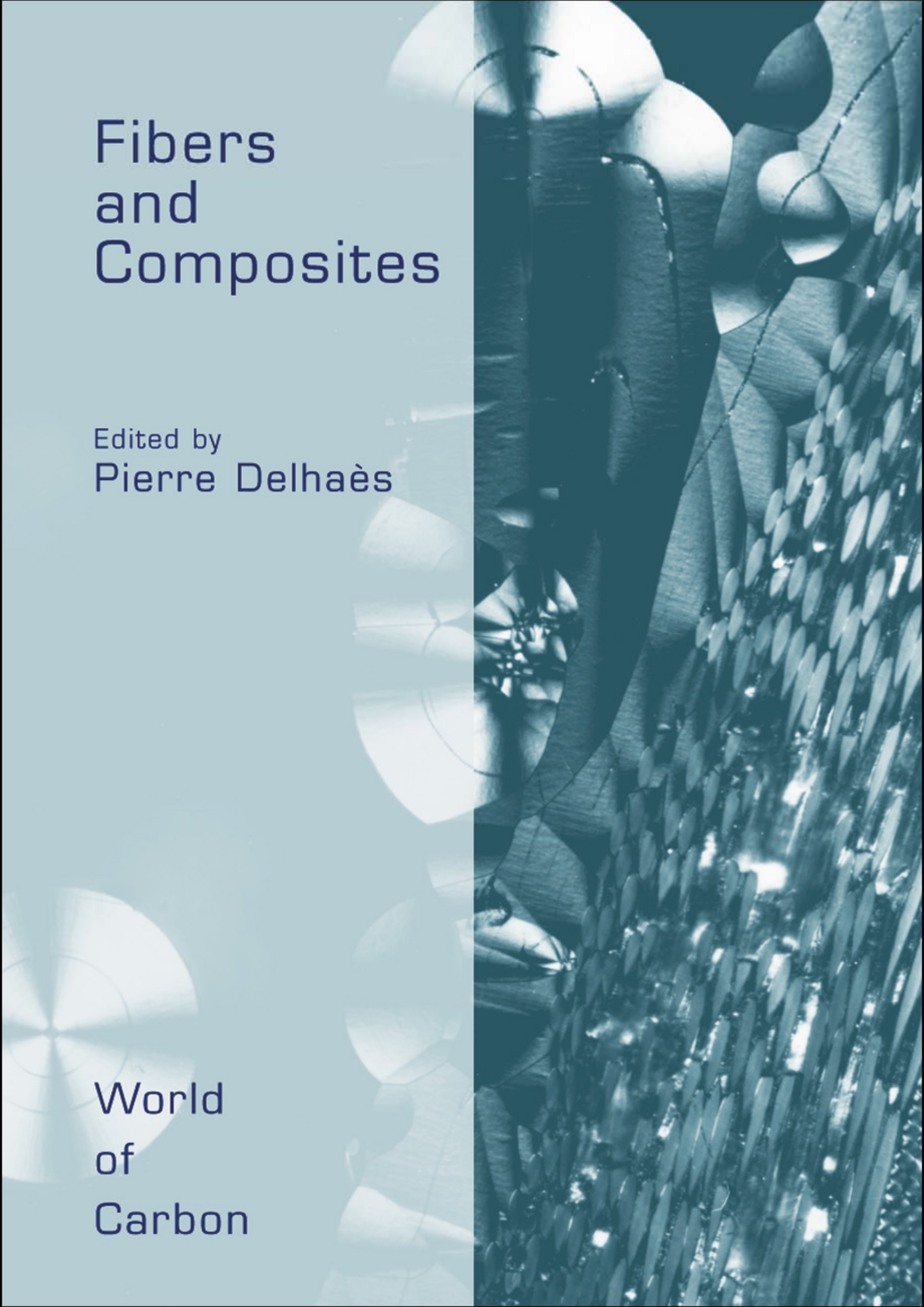

Fibers and Composites

Edited by
Pierre Delhaès

World
of
Carbon

FIBERS AND COMPOSITES

This book considers advanced composite materials based on carbon fibers and several kinds of matrices and is divided into three main parts. The first presents an alternative way to process and prepare carbon fibers issued from either natural or artificial precursors. Recent achievements in carbon fiber technologies have been introduced, including their main physical characteristics such as high modulus or high strength type.

In the second part, both classical and novel ways to prepare carbon matrices are presented. The chemical vapor deposition (CVD) technique as well as chemical vapor infiltration (CVI) inside a porous preform are analyzed.

In addition, the liquid impregnation of a preform by a pitch or some other precursor is described. The associated C–C composites exhibit high thermal and mechanical properties, useful, for example, in aeroplane brakes and space rockets. Finally, other carbon based composites, with polymers or cement as matrices, are explained including the role of interfacial characteristics such as wetting or adhesions for their final application. This book will be of interest to engineers, graduate students, and researchers in the field of solid state physics, chemistry, and materials science.

Pierre Delhaès is a CNRS Research Director at the Centre de Recherche Paul Pascal, University of Bordeaux, France. He was President of the French Carbon Group (1994–2000) and a spokesman for the European Carbon Association. His research interests involve carbon materials, organic conductors and superconductors and electrical and magnetic thin organized films.

WORLD OF CARBON
Series Editor: Dr Pierre Delhaès
Centre de Recherche
Paul Pascal – CNRS, Pessac, France

Volume 1
GRAPHITE AND PRECURSORS
Edited by Pierre Delhaès

Volume 2
FIBERS AND COMPOSITES
Edited by Pierre Delhaès

FIBERS AND COMPOSITES

Edited by
Pierre Delhaès

Taylor & Francis
Taylor & Francis Group
LONDON AND NEW YORK

First published 2003
by Taylor & Francis
11 New Fetter Lane, London EC4P 4EE

Simultaneously published in the USA and Canada
by Taylor & Francis Inc,
29 West 35th Street, New York, NY 10001

Taylor & Francis is an imprint of the Taylor & Francis Group

This edition published in the Taylor & Francis e-Library, 2004.

British Library Cataloguing in Publication Data
A catalogue record for this book is available from the British Library

Library of Congress Cataloging in Publication Data
A catalog record for this book has been requested

ISBN 0-203-16678-7 Master e-book ISBN

ISBN 0-203-34162-7 (Adobe eReader Format)
ISBN 0–415–30826–7 (Print Edition)

CONTENTS

PART II
CVD/CVI processes 73

PART III
Properties of matrices and composites 157

INTRODUCTION TO THE SERIES

The *World of Carbon* book series aims to propose different approaches to carbon materials which summarize the essential information regarding advances and results accumulated in basic and applied research during the last century. Indeed, carbon associated with other atoms is a key element in nature and life. The focus of these books is, however, elemental carbon in a condensed phase, that is, mainly related to materials science.

Besides the natural forms of carbon found in earth and in extraterrestrial media, the artificial ones have led to manifold technical applications. They cover areas such as industrial chemistry and metallurgy, terrestrial transports as well as aircraft and aeronautics or environmental protection. These examples are related to the numerous old and new forms of carbon that we have partly presented in the first book of the series.

The field of research of carbon materials is a beautiful example of the strong interactions between science and technology, where back and forth activity has worked together for a long time. As with other scientific events, a historical approach shows that advances are step-by-step rather than linear with strong breakthroughs; different strata of knowledge are accumulated but sometimes with a loss of memory of the previous one. It is crucial for scientific knowledge, as a part of human activity, that a basic synthesis is realized, which summarized the numerous annual publications. The aim of this series is thus to provide short tutorial articles containing a comprehensive summary of the different topics related to the science of carbon materials. They will be addressed to engineers, scientists and students who are seeking fundamental points whithout "reinventing the wheel".

World of Carbon series will be devoted to specific subjects, which cover all forms of carbons: the old ones like graphites or diamonds, but also the applied ones as fibers and composites. Each volume will cover fundamental research in chemistry and physics, as well as current applications and future developments. Such is the case of the second volume, which is devoted to the different forms of fibers, their precursors and their uses. This is one part of the most important industrial applications of graphitic carbons as also carbon blacks, foams and aerogels, insertion and reactivity products. Other polymorphic forms will not be neglected in the future, as carbynes or the new molecular curved forms, fullerenes and nanotubes, which are opening new avenues in nanotechnology.

Finally, we expect to present a collection of articles at a level and a style accessible to a large audience that will cover almost all aspects of carbon materials.

Pierre Delhaès
January 2003

CONTRIBUTORS

X. Bourrat
Université de Bordeaux1
Laboratoire des Composites
Thermo-Structuraux
LCTS, 3 Allée La Boëéie
F-33 600 Pessac, France
e-mail: bourrat@lets.u-bordeaux.fr

E. Casal
Instituto Nacional del Carbón, CSIC
Apartado 73, 33080 Oviedo, Spain
e-mail: ecasal@incar.csic.cs

D. D. L. Chung
Composite Materials Research Laboratory
University at Buffalo
The State University of New York
Buffalo, NY 14260-4400, USA
e-mail: ddlchung@aesu.buffals.edu

P. Delhaès
Centre de recherche Paul Pascal
(CNRS and Université de Bordeaux1)
33600 Pessac, France
e-mail: delhaes@crpp.u-bordeaux.fr

D. D. Edie
Department of Chemical Engineering and
Center for Advanced Engineering Fibers
and Films
Clemson University, Clemson
South Carolina 29634–0909, USA
e-mail: dan.edie@ccs.clemson.edu

P. Ehrburger
Université de Haute-Alsace, Laboratoire
Gestion des Risques et Environnement
25 rue de Chemnitz – 68200 Mulhouse
France
e-mail: P.Ehrburger@uha.fr

B. Fathollahi
Chemical Engineering Program
Jacobs School of Engineering
University of California, San Diego
La Jolla, CA 92093-0411, USA
e-mail: bfatholl@ucsd.edu

I. Golecki
Corporate R&D Materials Laboratory
Honeywell International, Inc.
Mail Stop CTC-1, 101 Columbia Road
Morristown, NJ 07962, USA
e-mail: ilan.golecki@honeywell.com

M. Granda
Instituto Nacional del Carbón, CSIC
Apartado 73, 33080 Oviedo, Spain
e-mail: mgranda@incar.csic.cs

K. J. Hüttinger
Institut für Chemische Technik
Kaiserstrasse 12.76128 karlsruhe
Universität Karlsruhe, Germany
e-mail: Huettinger@ict.uni-karlsruhe.de

J.-P. Issi
Unité de Physico-Chimie et de Physique
des Matériaux
Université Catholique de Louvain
1, Place Croix du Sud, B-1348
Louvain-la-Neuve
Belgique
e-mail: issi@pcpm.ucl.ac.bc

R. Menéndez
Instituto Nacional del Carbón, CSIC
Apartado 73, 33080 Oviedo, Spain
e-mail: rosmenen@incar.csic.cs

C. Vix-Guterl
Institut de Chimie des Surfaces et Interfaces
15 rue Jean Starcky
68057 Mulhouse Cedex, France
e-mail: C.Vix@uha.fr

J. L. White[†]
Chemical Engineering Program
Jacobs School of Engineering
University of California, San Diego
La Jolla, CA 92093-0411
USA

Part I

CARBON FIBERS

1

FORMATION OF MICROSTRUCTURE IN MESOPHASE CARBON FIBERS

J. L. White[†]*, B. Fathollahi, and X. Bourrat*

1 Introduction

Mesophase carbon fiber was invented in the 1970s, independently and simultaneously, from our viewpoint today, by Leonard Singer in the US (Singer, 1978) and by Sugio Otani in Japan (Otani, 1981). Both based their concepts on the role of the liquid-crystalline carbonaceous mesophase described by Brooks and Taylor in 1965. Both recognized two key steps: flow of the anisotropic liquid in the shear-stress field of the spinneret to align the disk-like molecules, and oxidation thermosetting to stabilize the shape and microstructure of the fiber prior to carbonization.

These inventions led to high expectations in the carbon materials community for the rapid attainment of fiber with superior properties at the low costs anticipated for a pitch product. Vigorous research activities ensued, many under conditions of proprietary secrecy. An important advance, with potential for many carbon materials besides fiber, was the development of more satisfactory mesophase pitches, fully transformed to the liquid-crystalline state and of low viscosity (Lewis and Nazem, 1987; Mochida *et al*., 1988; Sakanishi *et al*., 1992).

However for mesophase carbon fiber, the results fell short of expectations. The mechanical properties were not competitive with PAN-based fiber, except for some high-modulus grades. Low costs were never achieved, apparently due to the lengthy process of stabilization and the early 1990's saw downsizing and abandonment of research programs, with only a few products commercialized.

Nevertheless the prospects for a carbon fiber spun in the liquid-crystalline state continued to fascinate carbon scientists. Comprehensive microstructural studies initiated by Hamada *et al*. in 1987 demonstrated the remarkable flow memory of viscous mesophase in a simple spinneret. Then Bourrat *et al*. (1990a–c) showed that the nanostructure of as-spun filaments can be described in terms of the basic microstructural features of liquid crystals: bend, fold, splay, and disclinations.

Some practical results of manipulating the flow of mesophase in the spinneret became apparent. In a 1990 patent, Hara *et al*. showed that a fine-weave screen placed across the mesophase stream flowing to the spinneret can profoundly alter the microstructure of as-spun fiber. In 1993, Taylor and Cross reported their study of screened flow prior to spinning; their observations were rationalized in terms of an array of fine mesophase cylinders, leading directly to the concept of a filament comprised of a linear composite of near-nanotubes. Then rheologists entered the scene to study the flow instabilities of a discotic liquid crystal under the flow conditions in a spinneret (Singh and Rey, 1995, 1998; Didwania *et al*., 1998), thus providing basic guidance for spinning experiments.

[†] In memorial of Jack White deceased in 2002.

Thus the stage is being set for a new class of mesophase carbon fibers, with designed microstructures produced by manipulating flow of the anisotropic liquid in the spinneret.

2 Microstructural approach

Consider first the microstructure of manufactured mesophase carbon fiber, keeping in mind that such fiber has been processed through stabilization, carbonization, and graphitization after spinning of the viscous mesophase. “Nanostructure” may seem more suitable to describe the architecture of graphitic layers in a filament whose diameter is near ten microns. The scanning electron micrograph (SEM) of Fig. 1.1 offers an example of fibers

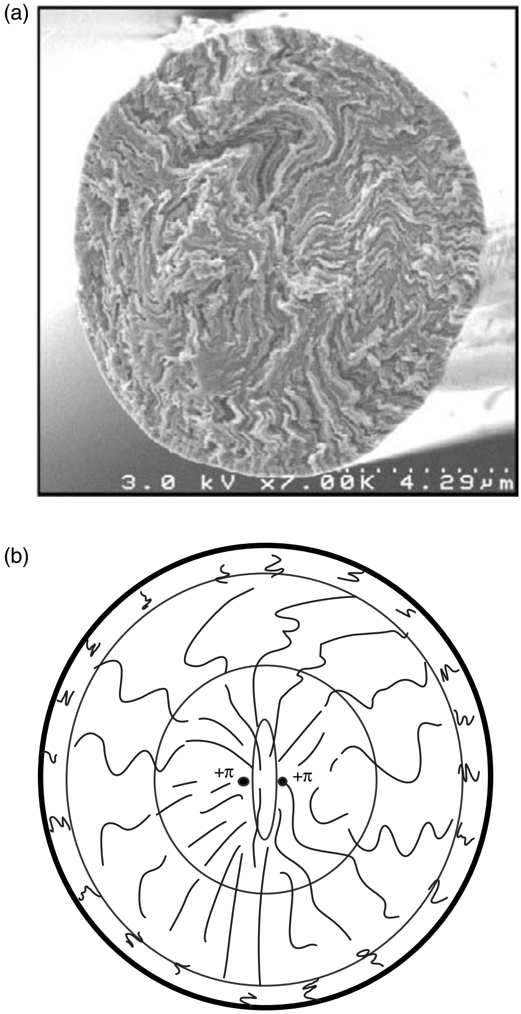

Figure 1.1 Fracture surface of a mesophase carbon filament (a) manufactured by DuPont (E35). The schematic diagram (b) outlines an oriented core bounded on each side by a $+\pi$ super-disclination and with wavy and rippled layers leading from the core to zigzag bands at the rim. From Bourrat (2000).

available in the 1980s. Such fibers, manufactured by Union Carbide and by DuPont, were studied extensively by Fitzgerald, Pennock, and Taylor (1991, 1993). Although there is some variability in structural detail, even in filaments from the same tow, the sketch outlines transverse features that are generic to most mesophase carbon fibers. This filament exhibits an oriented core with the surrounding layers in radial orientation. As a function of increasing radius, three zones may be seen in which the radial layers waver, ripple, and corrugate increasingly to form zigzag bands near the rim. Finally there is a thin skin, finely structured and highly corrugated.

Figure 1.2 includes a transmission electron micrograph (TEM) of the same type of fiber. The diffraction contrast defines the oriented core as well as the $+\pi$ super-disclination that accommodates the parallel layers of the oriented core to the radial layers in the surrounding zone. The term "super-disclination" is used to distinguish a new disclination imposed on an oriented mesophase body or stream that already may carry many disclinations from its previous history of coalescence and flow. An example is the formation of $+2\pi$ super-disclinations by passage of mesophase pitch through a screen, described later in some detail.

The higher-magnification TEM micrographs of Fig. 1.3 define layer orientations within the bands located near the rim of a DuPont fiber, here again in the as-spun condition.

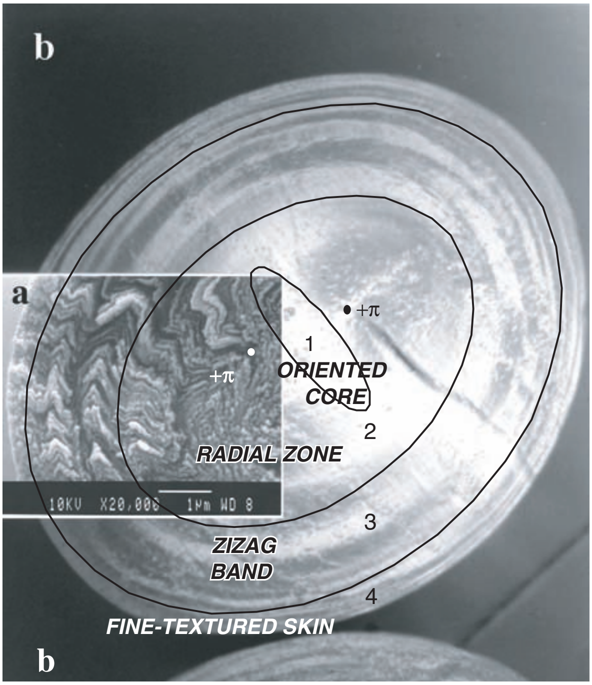

Figure 1.2 An SEM of a carbonized DuPont E35 filament superposed on a TEM dark-field image of the same type of fiber at the as-spun stage (a). The four zones observed in the carbonized filament are evident in the as-spun state (b). The elliptic shape is due to the angle of cutting of a circular filament. From Bourrat (2000).

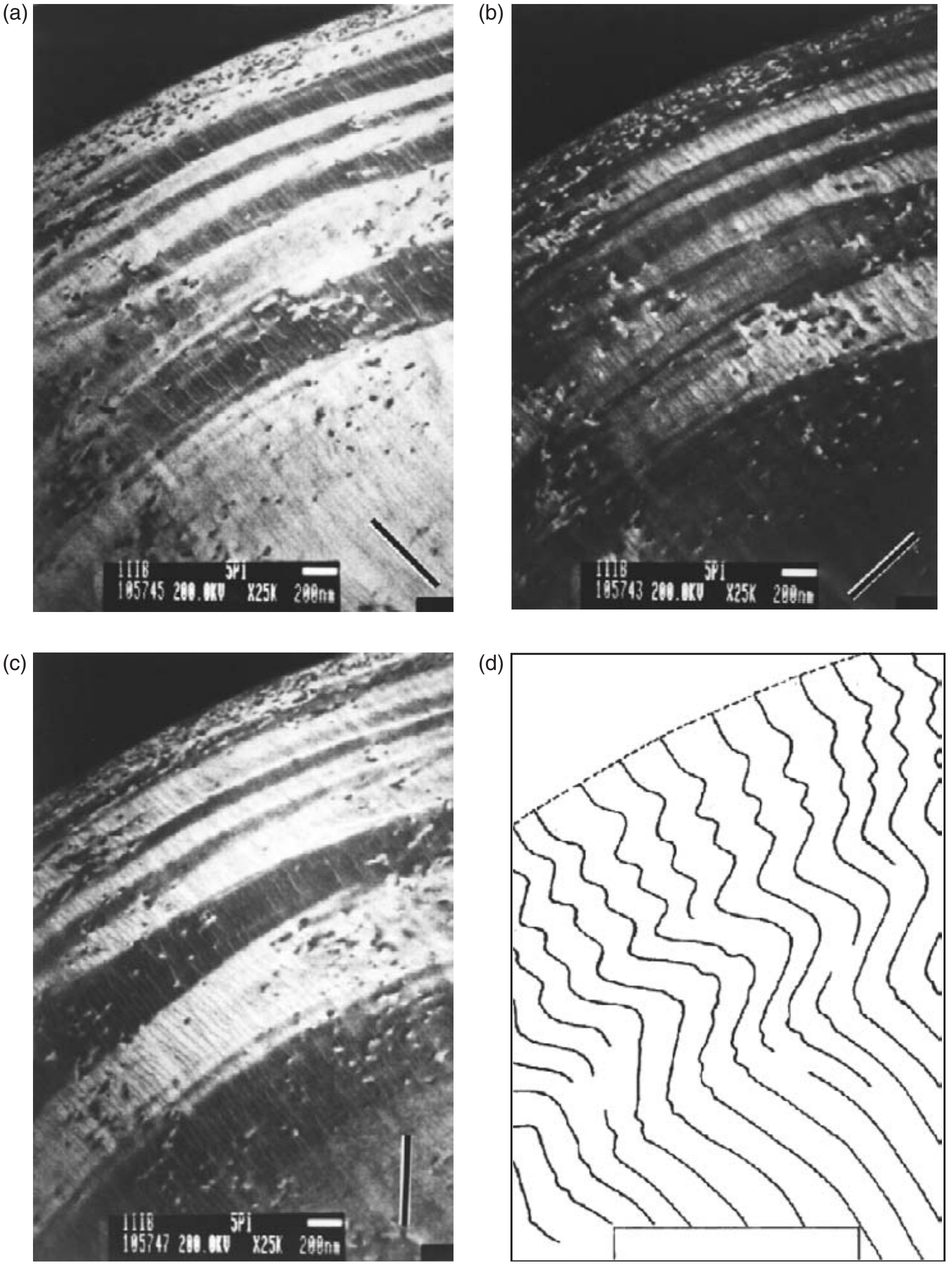

Figure 1.3 (a,b,c) Three TEM dark-field image at 45º rotation of diffraction vector show the zigzag bands in the rim of the Dupont filament in the as-spun condition. The bar in each micrograph defines the orientation of mesophase layers that appear bright. (d) Structural sketch illustrating the corrugated layer orientation.

The zigzag bands, only a fraction of a micron in width, consist of well-aligned layers within each band, and the boundaries are sharply defined. The zigzag angle, referred to later as the ripple angle, appears not to be fixed, but tends to 90° in the outer bands. Note the presence of many dots and short dashes appearing in reverse contrast to the bands in which they occur. These appear to be $+\pi/-\pi$ disclination loops (Zimmer and White, 1982) inherited from the mesophase pitch as it enters the spinneret; the contrast is due to the local rotation of mesophase molecules in the disclination loop. The density of dots is much higher in the skin, which may reflect the shear experienced briefly at the capillary wall as the stream exits the spinneret.

In 1990, Bourrat *et al.* (1990a) published observations by high-resolution electron microscopy (HREM) to identify $+\pi$ and $-\pi$ wedge disclinations on transverse sections of mesophase fiber heat-treated to 1600 °C. Later these authors (Bourrat *et al.*, 1990b,c) demonstrated the presence of $+2\pi$ and -2π as well as $+\pi$ and $-\pi$ disclinations, along with bend, splay, and folding, in mesophase filaments in the as-spun condition. The presence of these liquid-crystalline structural features in finished fiber was confirmed by Pennock *et al.* (1993). Figure 1.4 is a lattice-fringe image of an Amoco P25 mesophase carbon filament (Bourrat *et al.*, 1990c); the structural diagram locates the $+\pi$, $-\pi$, and -2π disclinations in the micrograph. From these observations, mesophase carbon fibers may be viewed as carbonized fossils of highly oriented mesophase streams with non-equilibrium microstructures frozen in place as each stream is swiftly drawn to a filament.

Although an extensive patent literature has come to exist for mesophase carbon fiber, little information was published on the formation of microstructure within the spinneret until Hamada and co-workers at Nippon Steel undertook their comprehensive micrographic

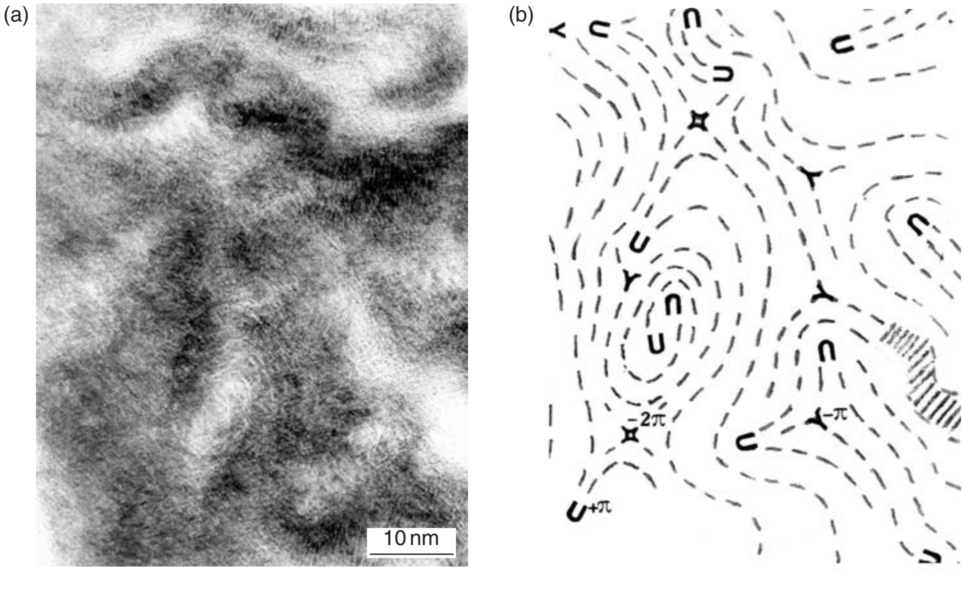

Figure 1.4 (a) A high resolution lattice-fringe of an Amoco P25 mesophase carbon filament. (b) The structure diagram locates $+\pi$ disclinations by U and $-\pi$ disclinations by Y. From Bourrat *et al.* (1990c).

studies, commencing with publication in 1987. The investigations included optical and electron micrography, as well as x-ray and electron diffraction, applied to monofilaments spun from a spinneret as outlined in Fig. 1.5a. The transverse microstructure, as-received from the pitch reservoir, or as modified by stirring before entrance to the capillary, was maintained with little loss of detail through extrusion and draw-down. The microstructural scale, as measured by the spacing of extinction contours, was found to be proportional to the diameter of the rod or filament, thus establishing the strong quantitative memory of viscous mesophase. When the stirrer was not in place, transverse sections of both extruded rods and spun filaments exhibited radial preferred orientation (PO), which was ascribed to convergent flow in the precapillary cone. Then the rapid extension and quench experienced in the draw-down cone were seen as critical factors in determining the final degree of radial orientation in the spun filaments (Hamada *et al*., 1990).

Figure 1.5 illustrates schematically three types of monofilament spinnerets that have been used in exploring the formation of microstructure in mesophase fiber. Although some designs might be difficult to incorporate in an industrial multi-filament spinneret, their principal use at this point has been to demonstrate the wide range of microstructures that are accessible in spinning mesophase.

Figure 1.6 illustrates four such microstructures (Fathollahi, 1996) extruded from a low-viscosity mesophase pitch produced by alkylbenzene polymerization and pyrolysis (Sakanishi *et al*., 1992). Figure 1.6a is a polarized-light micrograph of an extruded mesophase rod, at a stage just prior to draw-down to filament; in this case no special manipulation was applied to flow in the spinneret. The microstructure is that expected of a nematic liquid crystal, but the scale is very fine, e.g., disclinations can just be resolved. Sensitive-tint observations indicate a radial PO that strengthens with increasing radius. There are concentric markings in the rim (not shown here) that correspond in location to the zigzag bands of finished fiber.

In recent years rheologists have turned their attention to modeling the flow of a discotic nematic liquid crystal through a spinneret. The flow of an anisotropic liquid comprised of disk-like aromatic molecules was found to be inherently unstable, and rippled and zigzag structures are to be expected when the liquid enters a shear field (Didwania *et al*., 1998; Singh and Rey, 1998). In 1D extension, the molecules will align with their largest dimension parallel to the extension, and 2D extension (as in the wall of an expanding bubble) will effect stronger alignment than 1D extension (Singh and Rey, 1995). The formation of $+2\pi$

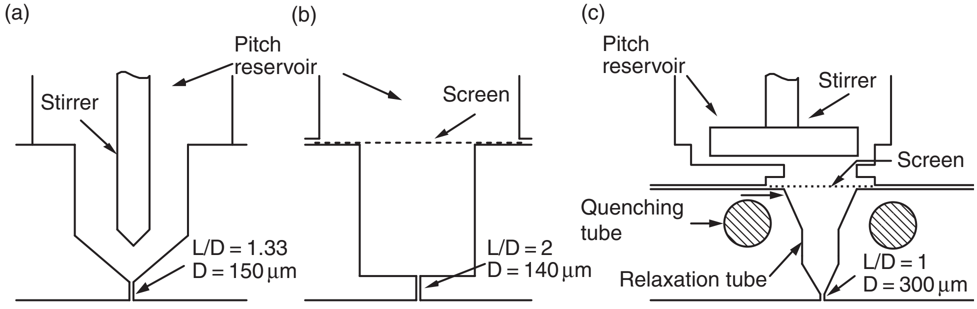

Figure 1.5 Schematic designs of three monofilament spinnerets used in laboratory-scale spinning: (a) stirring within the spinneret, from Hamada *et al*. (1988); (b) screened flow, from Matsumoto *et al*. (1993); (c) stirring with screened flow and quenching capability, from Fathollahi *et al*. (1999a).

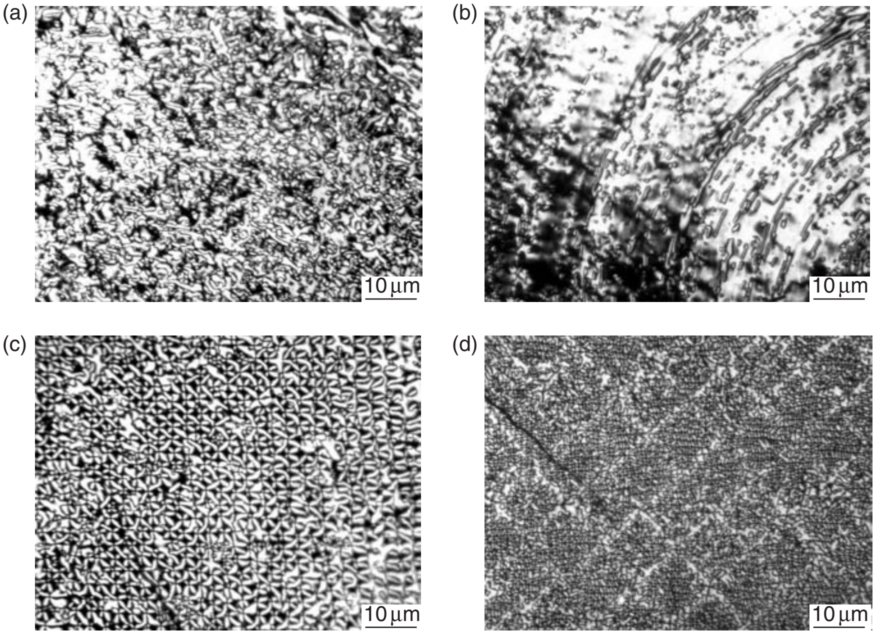

Figure 1.6 Some effects of manipulating mesophase flow within the spinneret, as observed on transverse sections of extruded rods: (a) direct flow from pitch reservoir without manipulation, some radial PO is present; (b) flow with strong stirring, concentric PO can be produced; (c) flow through a single 200-mesh screen, with some relaxation after passing the screen; (d) flow through two screens of 400- and 50-mesh, oriented at 45° each other. Crossed polarizers.

disclination arrays in screened flow (described later) has been modeled using Ericksen-Leslie continuum equations (Didwania *et al.*, 1999a). The analysis reveals a class of spatially periodic solutions to these equations for specific values of Leslie viscosities. An array of $+2\pi$ disclinations, oriented along the flow direction is observed in the regions of negligible shear in the transverse plane.

3 Manipulation of mesophase flow in a spinneret

Hamada's observations (1988) of the proportional reduction of microstructure by spinning lead directly to a concept of microstructural miniaturization, in which flow is manipulated to produce a desired microstructure at a workable scale in the upper part of the spinneret, then this is reduced by a thousand-fold to a nearly identical nanostructure by convergent flow in the capillary and draw-down to the filament.

Flow manipulation must be limited by the need for simple design because industrial spin-packs use multiple spinnerets to spin fiber tow with as many filaments as practical. Even simple stirring may be difficult if the stirrer must extend into each spinneret as in Fig. 1.5a. Spinneret design should also avoid 180º entry geometry, as in Fig. 1.5b, where the corners can create a vortex or weak secondary flow which can produce pyrolysis bubbles into the mainstream (Fathollahi, 1996). Some practical flow manipulations include the use of screens, perforated plates, or even just a single transverse bar or slot (Ross and Jennings, 1992). A relaxation zone below the region of flow disruption may be useful to allow the decay of short-lived structures generated by flow instabilities (Didwania *et al.*, 1999b).

Stirring in the pitch reservoir may be desirable to maintain thermal and chemical homogeneity, but this can induce concentric PO in the feed to the spinneret. Stirring also refines the scale of fibrous or lamellar microstructures entering the spinneret (Hamada *et al.*, 1988). Strong concentric stirring at the spinneret entrance can introduce a concentric PO sufficient to outweigh the radial PO induced by convergent flow later in the spinneret, thus producing a concentric microstructure in the extruded rod (see Fig. 1.6b).

Wire screens are readily incorporated in a spinneret and, if the mesh is sufficiently fine, can profoundly alter the microstructure to the grid pattern seen in Fig. 1.6c. Fine screens may need support by a coarse screen to withstand the stress involved in spinning at high levels of viscosity; this can produce the grid-within-a-grid microstructure seen in Fig. 1.6d. Hara *et al.* (1990) appear to have been first to publish the use of screens to benefit the microstructure and properties of mesophase carbon fiber; their patent emphasizes the need for timely passage from screen to capillary in order to produce a clear reduced grid in the spun filament. The studies of screened flow by Matsumoto *et al.* (1993) confirm Hamada's rule that the scale of microstructure remains proportional to the diameter of the stream.

Taylor and Cross (1993) used optical and electron microscopy to examine screened-flow microstructures and found the orthogonal arrays outlined in Fig. 1.7, where the lighter lines represent traces of mesophase layers on the transverse section. Even in extruded rods, the extinction contours lie near the limit of optical resolution, but the √2-effect sketched into the diagram is helpful in recognizing, on a microscope with rotating stage, the orthogonal array of mesophase cylinders, each of which comprises a concentric $+2\pi$ disclination. Thus the microstructures in Figs. 1.6c–d indicate potential precursors for filaments consisting of a composite of nanotubes.

Non-circular spinnerets have been used to produce particular shapes, such as ribbons, where the goal is not a particular transverse microstructure but highly oriented mesophase in convenient form for good thermal conductivity (Robinson and Edie, 1996; Edie, 1998; Lu *et al.*, 2000). Matsumoto *et al.* (1993) have shown how a square or rectangular spinneret can be used to modify screened flow to give elegant Moire-like patterns of extinction contours.

The regular array of $+2\pi$ and $-\pi$ disclinations shown in Fig. 1.8 was observed in the initial screened flow experiments (Fathollahi, 1996). The balanced array of disclinations was produced by gentle flow through a 200-mesh screen. The potential feasibility of such detailed control of microstructure in the spinneret motivated the studies described next.

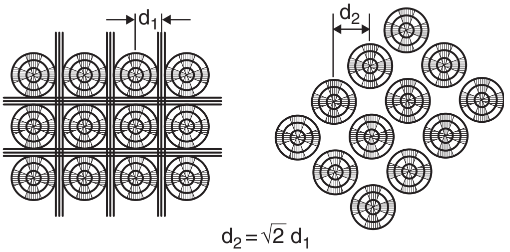

Figure 1.7 The orthogonal grid sketched by Taylor and Cross (1993) to represent the microstructure of a mesophase filament spun from a spinneret with a fine screen and observed on transverse section by crossed polarizers. On rotating the microscope stage by 45°, the spacing of extinction contours changes by √2 (Fathollahi, 1996).

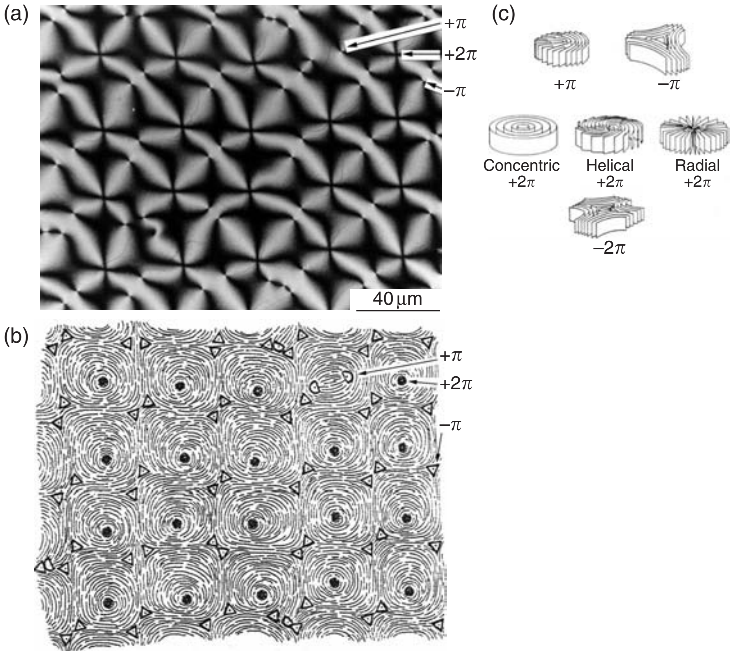

Figure 1.8 A regular array of wedge disclinations formed by mesophase after flow through a 200-mesh screen: (a) transverse section observed by crossed polarizers; (b) map of wedge disclinations defined by $\Delta = -\pi$, D $= +\pi$, $\bullet = +2\pi$; (c) wedge disclinations in a discotic liquid crystal (Zimmer and White, 1982). For a material in which the layers are parallel everywhere except at disclination cores, the total disclination strength over any appreciable field tends to zero.

3.1 Screened flow within the spinneret

Here we summarize studies at University of California at San Diego to understand how microstructure forms within a spinneret, utilizing stirring, screening, and relaxation to manipulate flow. Spinnerets of various designs were used; that shown in Fig. 1.5c is typical. All were machined from aluminum, for good thermal properties, and all incorporated quenching tubes to freeze structures in place when a desired spinning condition had been attained. Many spinnerets included one or two screens to establish cellular microstructures, and most included a relaxation tube to allow some decay of transient structures. The work described here used an alkylbenzene-based pitch (Sakanishi *et al*., 1992), fully transformed to mesophase, and supplied by the Mitsubishi Oil Co. The softening point is 285 °C, and flow temperatures ranged from 290 to 315 °C, corresponding to a viscosity range of 325 to 20 Pa.s.

Upon passing through a plain square screen, a mesophase stream splits into a set of ministreams that rejoin below the screen to form an array of square cells (Fathollahi and White, 1994). Below each screen wire, a weld-zone forms, as seen in Fig. 1.9. The weld zone is narrow relative to the wire diameter, and initially the new and strongly oriented microstructure is finer than can be resolved by polarized light. The strong planar orientation in the weld zone result from 2D extension in passing the aperture (Singh and Rey, 1995). Mesophase more centrally located in each cell develops "ripples" in the shear fields of

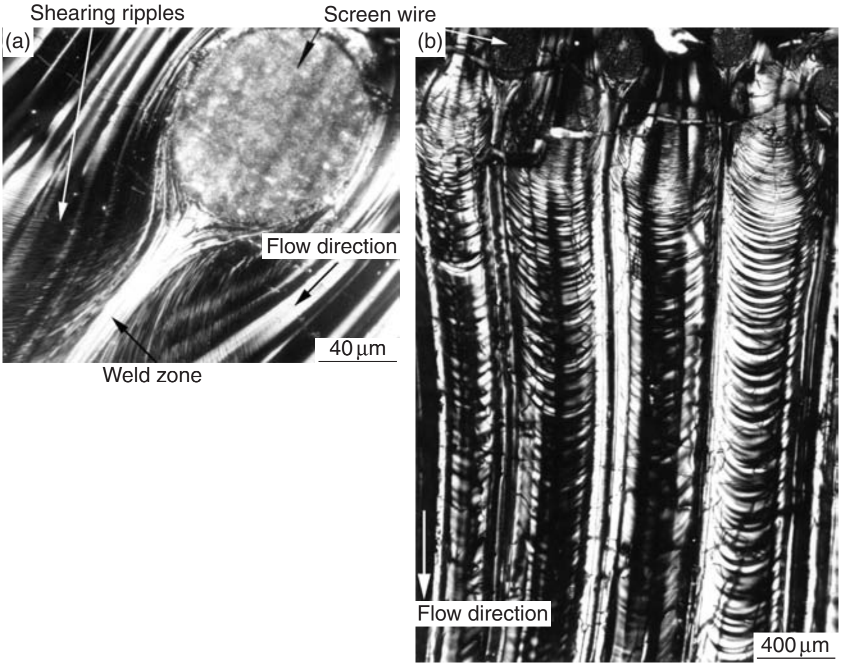

Figure 1.9 The passage of mesophase through a plain-weave screen. From Fathollahi (1996). (a) A highly oriented weld zone forms under the screen wire, and ripples appear in the shear field of the screen wire and (b) at lower magnification, the ripples are seen to decay soon after passage through the screen.

the wires. Although the ripples are extensive, they decay soon after the ministreams resume tubular flow, but substantial amounts of mesophase are left misoriented relative to the flow direction.

A transverse view at high-magnification of a mesophase stream immediately after penetrating a 100-mesh screen is given in Fig. 1.10a. The strong planar PO of the cell wall also appears on this transverse section, and the interior of the cell is intensely rippled in a concentric pattern everywhere but in the center. The same cell 330 microns below, or the equivalent of four seconds later, is illustrated in Fig. 1.10b. The cell walls have relaxed to lamellar microstructures that resemble the bubble walls found in needle coke (Zimmer and White, 1982). Within each cell, the ripples have coarsened and many have vanished, leaving a microstructure near that existing before passage through the screen.

If the foregoing experiment is conducted with a finer screen, e.g. 325 mesh, the cell walls tend to dominate the formation of new microstructure, as in Fig. 1.11. On this transverse section, relaxation has been sufficient for ripples to disappear, and most cells are dominated by a single $+2\pi$ super-disclination with a continuous core, indicated by the breadth of extinction at the core of each co-rotating cross. The cell walls have lost their strong lamellar PO, and their original locations are now defined by near-linear arrays of disclinations; in fact, the microstructure approaches that of the regular disclination array in Fig. 1.8.

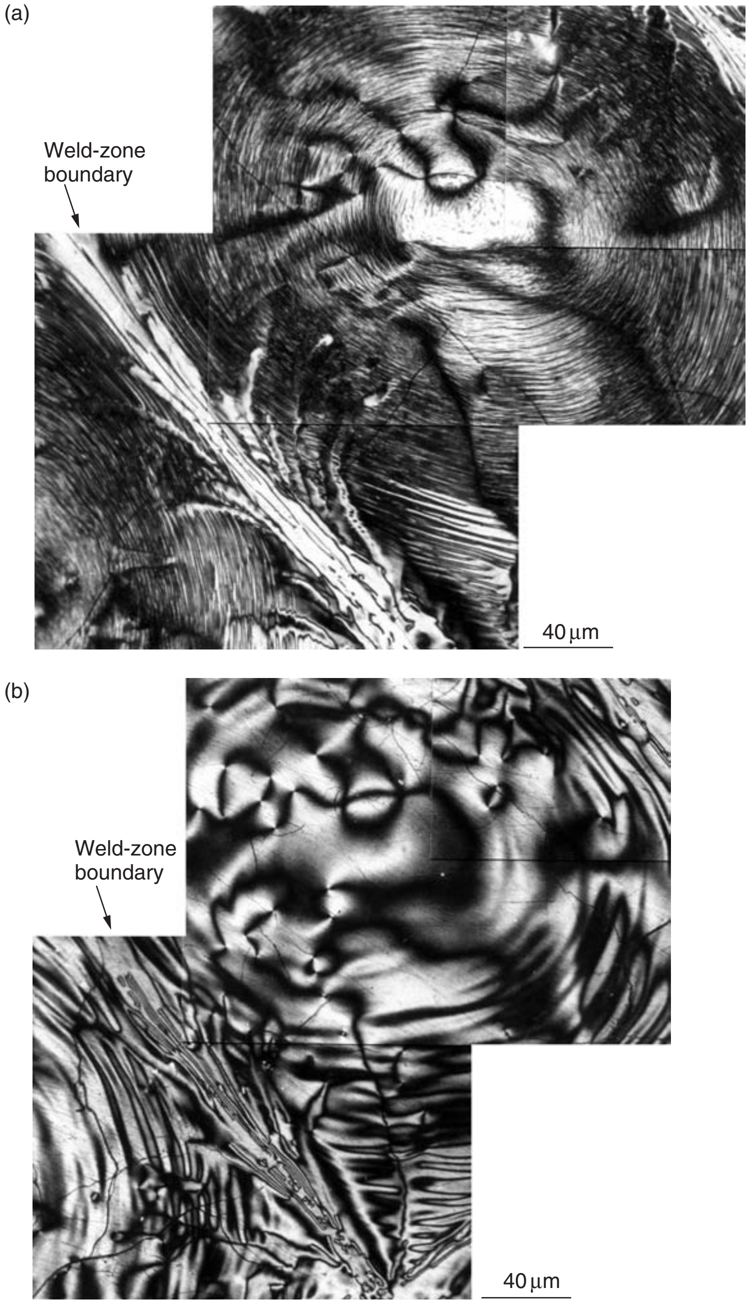

Figure 1.10 Transverse views of a mesophase ministream after passage through a 100-mesh screen: (a) immediately below screen and (b) 330 mm below section A. From Fathollahi (1996).

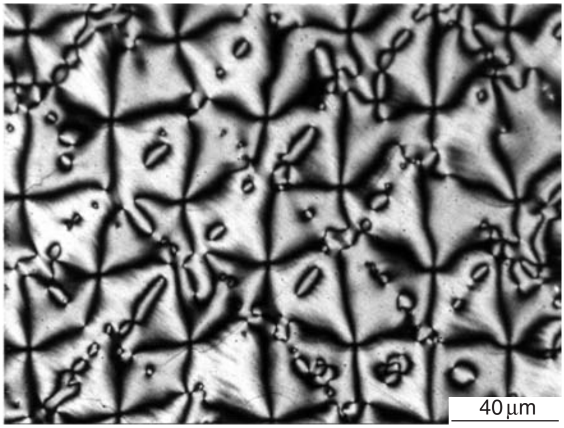

Figure 1.11 An array of $+2\pi$ disclinations formed after flow through a 325-mesh screen.

The observations of screen penetration confirm and add detail to the flow mechanism suggested by Taylor and Cross (1993), i.e. that flow over the wire of a square screen orients mesophase layers parallel to the wire. Thereafter two relaxation mechanisms operate with differing scales of relaxation time. The preferred orientations in cell walls and shear ripples decay rapidly. Disclination motions and reactions also occur, but much more slowly. Thus the weld zones, initially evident by strong lamellar PO, tend to be anchored by disclinations and are later located by the characteristic linear alignment of disclinations.

Passage through a screen directs flow along the spinneret axis (Fathollahi *et al.*, 1999a), but within each cell the mesophase can be seriously misoriented, as seen in Fig. 1.12a. Relaxation during tubular flow has little or no effect in reorienting layers within a cell, but when the stream enters a cone, convergent flow is strikingly effective, as seen in Figs. 1.12b and 1.12c. However some bright streaks do not disappear, and sensitive-tint observations find that most such streaks are blue on the right-hand side and orange on the left, indicating that the plane of section has intersected a cup-shaped structure similar to that sketched in Fig. 1.12e. Thus each bright streak corresponds to a $+2\pi$ disclination with the continuous core pointed downstream (Fathollahi *et al.*, 1996).

The transverse sections of Fig. 1.13 illustrate the effect of convergent flow in inducing radial PO in a mesophase stream. In this experiment, stirring in the reservoir produced some concentric PO that survived passage through the screen, as described for Fig. 1.13a. Sensitive-tint observations on extruded rod after convergent flow to the short capillary (Fig. 1.13b) indicate radial PO that increases in intensity with radius. This micrograph also displays fine concentric markings that cross the cell walls from the coarse screen; only the central core of the extruded rod is free of such markings. Figure 1.13c shows that the markings in some coarse cell walls fade or disappear upon rotation of the microscope stage.

The fine concentric markings were traced to their origin in the relaxation tube and were seen to be similar to ripples formed when mesophase penetrates a screen aperture (White *et al.*, 2001). Here the concentric geometry of the markings implies that they occur preferentially in radially oriented mesophase, i.e. when shear can act to wrinkle mesophase layers. Two observations at high magnification are offered in Fig. 1.14 to show that the

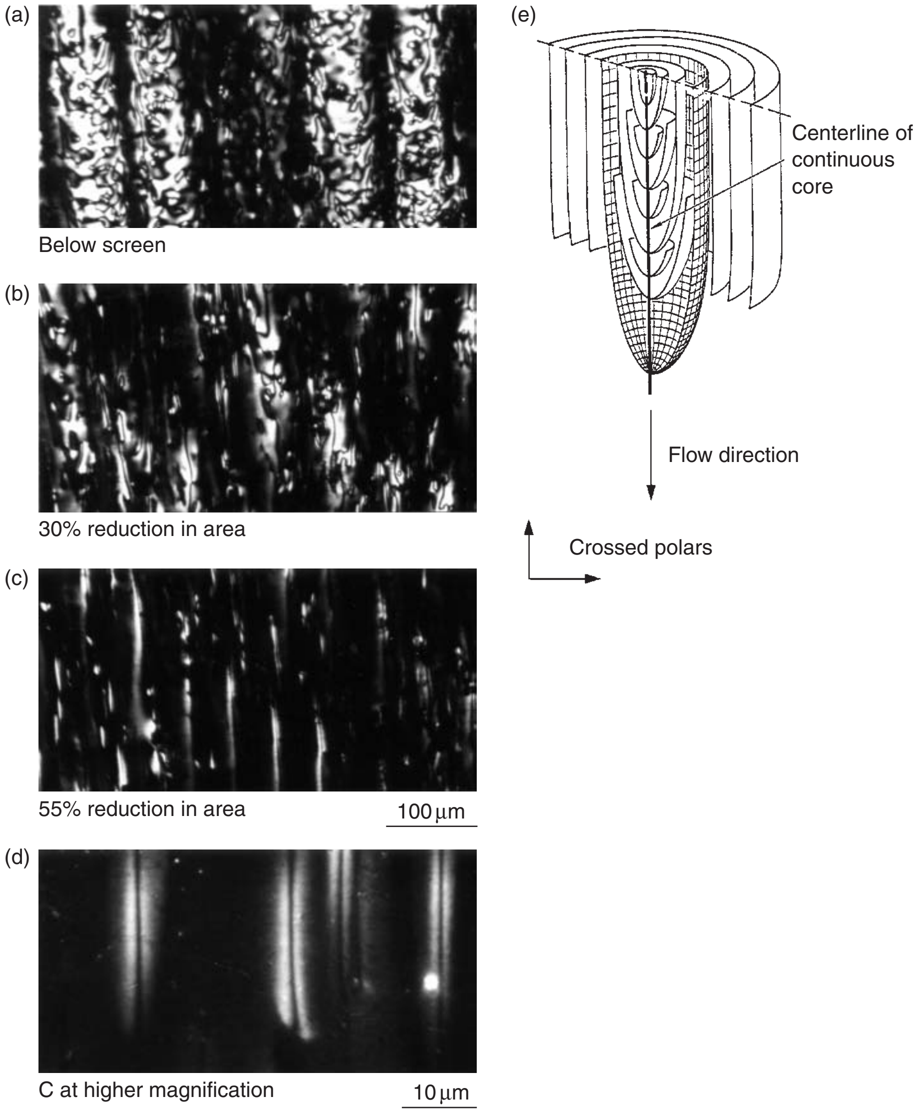

Figure 1.12 Longitudinal alignment of a screened stream by convergent flow in the entrance cone of a spinneret. From Fathollahi (1996). Polarizers oriented so that mesophase layers parallel to flow direction are dark. The bright streaks in (c) and (d) that are not eliminated by convergent flow correspond to cups of $+2\pi$ disclinations pointed in the flow direction, as sketched in (e).

markings vary in detail over the radius of the rod. Figure 1.14a illustrates blurred ripples that disappear upon stage rotation, while Fig. 1.14b shows more crisply defined bands that are common at high radius; the latter do not vanish upon stage rotation.

Measurements of the ripple angle **R** suggest the corrugated models of Fig. 1.15; the ripple angle is not fixed, but tends to increase with radius. Near the rim, the ripple angle

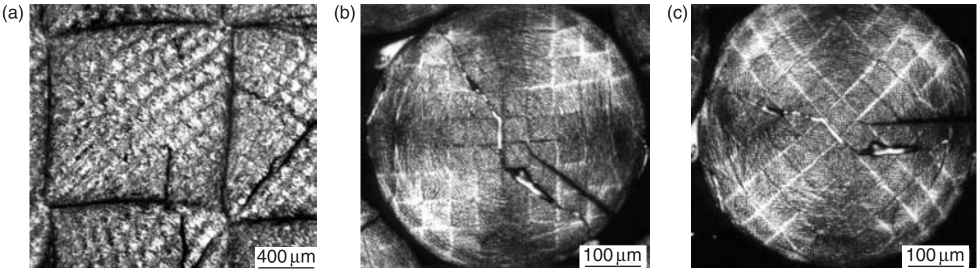

Figure 1.13 Convergent flow induces radial PO, as observed on transverse section below a screen: (a) in north-east quadrant of a stream just below screen, the sensitive-tint response is largely orange, indicating concentric PO; (b) for the same stream after convergent flow extruded rod, sensitive-tint response indicates radial PO that increases with radius; (c) same rod rotated by 45°, note that some concentric markings vanish upon rotation.

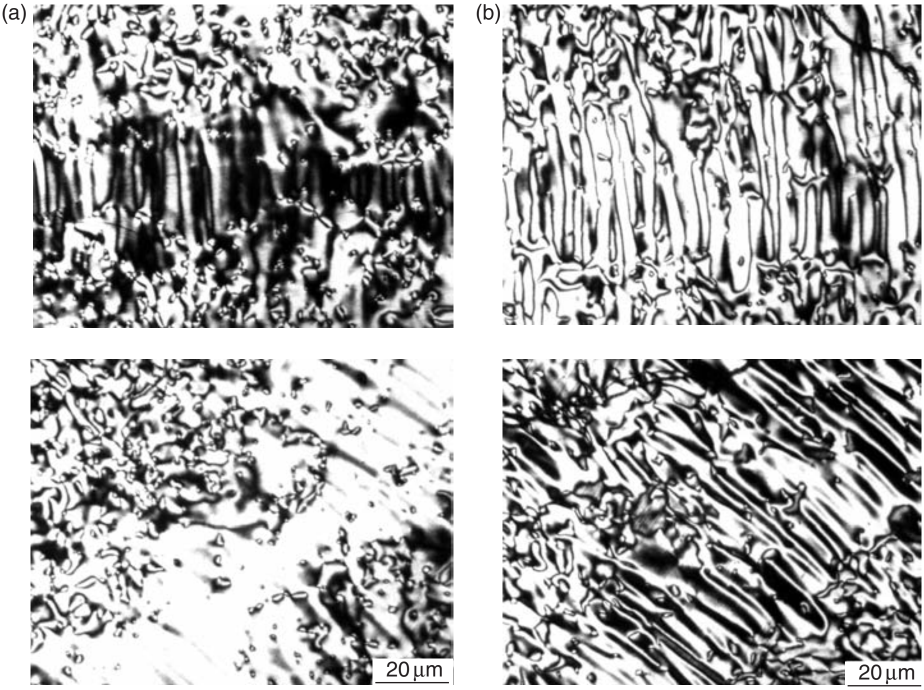

Figure 1.14 Two types of concentric ripples formed by shear of radially oriented mesophase in thick weld zone; the specimen was rotated 45° for the lower micrograph: (a) blurred ripples that disappear upon stage rotation and (b) crisply defined ripples that do not vanish upon stage rotation.

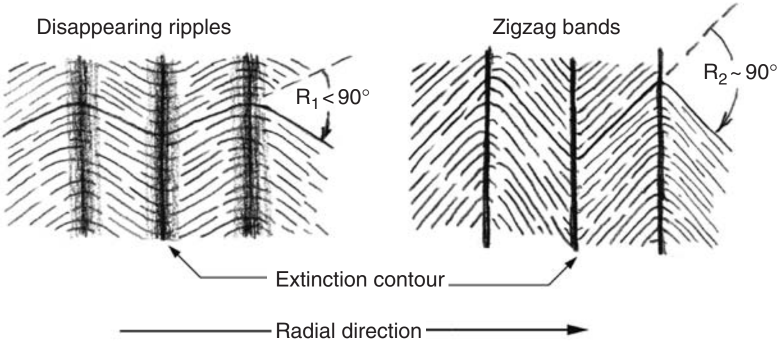

Figure 1.15 Schematic models, on transverse section, of ripples in radially oriented mesophase layers. If the ripples angle **R** is well under 90°, the ripples disappear upon rotation of the microscope stage.

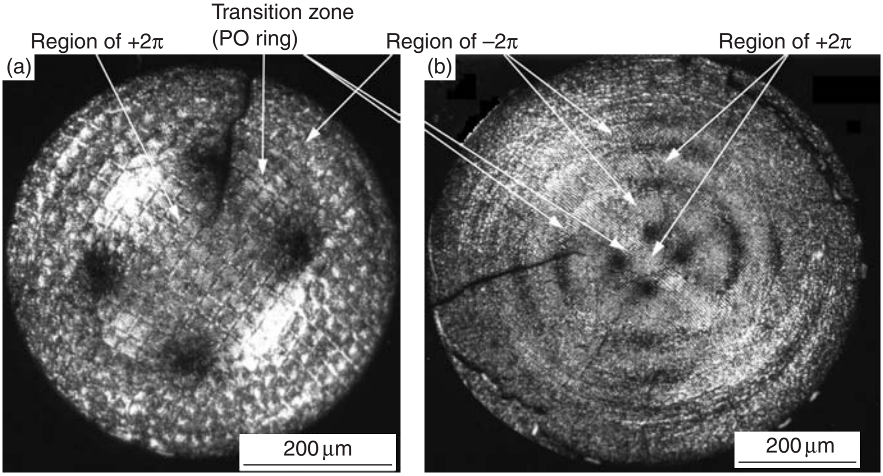

Figure 1.16 Preferred-orientation rings superposed on a screened grid by flow through a capillary: (a) rod extruded from a 457 μm-diameter capillary with L/D = 4 and (b) rod extruded from a 710 mm – diameter capillary with L/D = 20.

reaches 90° or higher, accounting for bands that do not fade upon stage rotation. Thus the ripples produced by shear acting on radially oriented mesophase appear to be precursors of both the wavy and zigzag microconstituents that are found in finished fiber.

3.2 Mesophase flow in capillary and draw-down cone

The linear flow rates in the capillary can limit further microstructural effects, since the residence time, even in a long capillary, is only a fraction of a second. McHugh and Edie (1995) have shown that the tendency to radial PO continues in the capillary. Two transverse effects of flow in a long capillary are illustrated in Fig. 1.16 for streams that were screened and received some relaxation in the upper, slower-moving part of the spinneret. The radial PO appears in the form of rings that decrease in diameter and increase in number as the capillary is traversed (Fathollahi *et al.*, 1996). A thin banded layer, too fine in texture for optical resolution, appears at the rim and gradually grows in depth along the length of the capillary. Upon reaching the transition from shear to elongational flow at the capillary exit, this rim must accelerate more than the interior of the filament, leaving a thin, fine-textured outermost skin.

Mapping of the PO rings in the capillary finds each ring to consist of radially oriented mesophase sandwiched between regions of alternating arrays of $+2\pi$ and -2π disclinations, beginning with $+2\pi$ disclinations at the center (Fathollahi, 1996). Between the radially oriented rings, the disclination arrays retain their regularity of spacing, so the transition regions appear to be the scene of short-range reversible reactions between neighboring sets of disclinations; formally the reactions may be written as

$$(+2\pi) + 2(-\pi) = (-2\pi) + 2(+\pi)$$

Mesophase in the draw-down cone experiences rapid acceleration to spinning speed and sharp increases in viscosity as the filament cools. Despite the severe conditions, Fig. 1.16

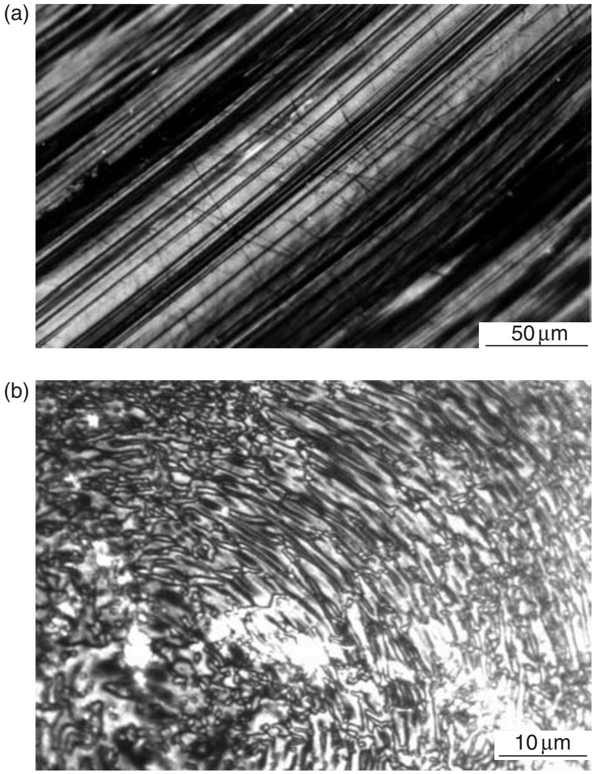

Figure 1.17 Draw-down cone quenched during spinning without a screen. (a) Longitudinal section, flow direction NE/SW and (b) transverse section. From Fathollahi (1996).

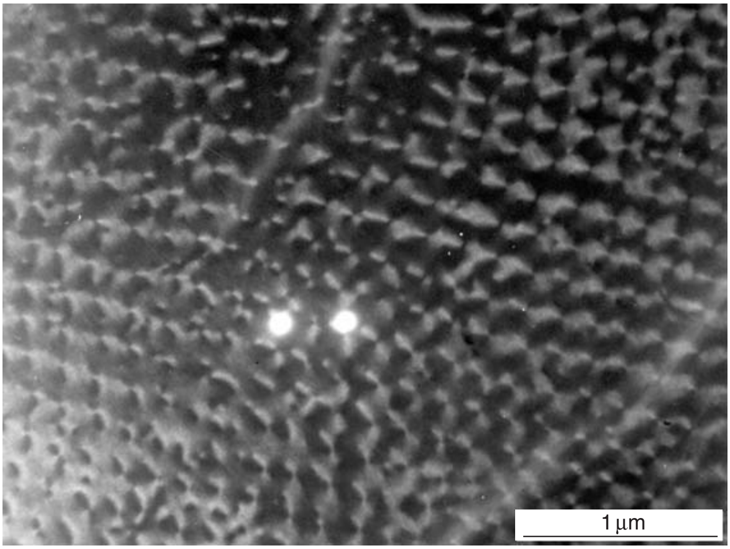

Figure 1.18 Dark-field electron micrograph at the core of an as-oxidized 30 µm filament. From Subramoney *et al.* (1996). The $+2\pi$ disclination are spaced at about 187 nm.

suggests that the processes of mesophase alignment and microstructural miniaturization run smoothly.

Figure 1.18, a dark-field electron micrograph of a filament spun with screened flow, shows that well-defined disclination arrays can be retained through spinning and stabilization with disclination spacings proportional to the filament diameter. This point has also been demonstrated for a grid-within-a-grid (Fathollahi *et al.*, 1997), for the $+2\pi$ and -2π disclination rings developed by flow through a capillary (Subramoney *et al.*, 1996; Fathollahi *et al.*, 1997), and for $+2\pi$ disclinations spaced as closely as 65 nm (Fathollahi *et al.*, 1999b).

3.3 Stabilization and heat treatment

To stabilize as-spun fiber against softening and loss of structure during carbonization, oxidation is practised at temperatures as high as 300 °C. However oxidation at such high temperatures appears to induce substantial carbon loss (Miura *et al.*, 1995) and reduced strength in the finished fiber (Yoon *et al.*, 1994). The potential for damage by carbon burnoff is most serious at the filament surface, since steeper oxygen gradients are required at higher oxidation temperatures to ensure stabilization to the center of the filament (Mochida *et al.*, 1989; Kasmer and Diefendorf, 1991).

Recent work indicates that oxidation can be conducted at temperatures as low as 130 °C, with substantial improvements to carbon yield and the depth of stabilization (Cornec *et al.*, 1992; Fathollahi *et al.*, 2000; Jones *et al.*, 2001). These benefits are thought to result from a reduced variety of active reaction sites on mesophase molecules at lower temperatures and thus less interference with oxygen diffusion. Although exposure times may be lengthy, the oxygen pressure can be increased to speed the process. Thus pressurized oxidation at low

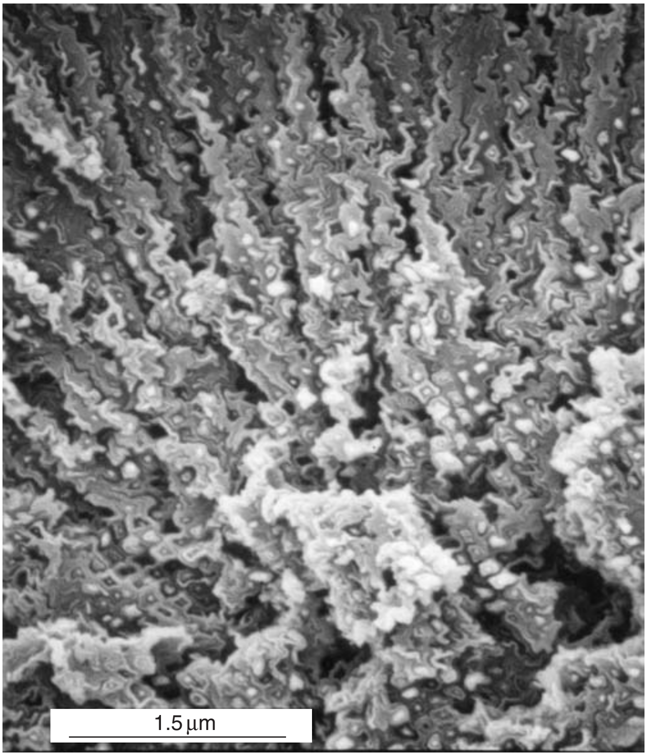

Figure 1.19 Shrinkage-cracking and $+2\pi$ disclination arrays in a screened filament that has been stabilized and heat-treated to 2,400 °C. SEM of a filament fractured in tension. From Fathollahi *et al*. (1997).

temperature appears to offer stabilization with better oxygen distribution and less potential for damage by carbon burnoff near the fiber surface.

Figure 1.19 is a scanning electron micrograph of the fracture surface of a screened mesophase filament after stabilization and carbonization to 2,400 °C (Fathollahi *et al*., 1997). The most obvious effects of carbonization are the wavering shrinkage cracks in the more radially oriented regions away from the core of the filament. Ordered arrays of white puffs, sometimes in small distorted boxes, appear most frequently near the core; these are believed to be $+2\pi$ disclination arrays because their spacing is proportionate to the filament diameter. Other types of disclinations are not readily identified in the highly serrated fracture surface, perhaps because $+\pi$ and $-\pi$ disclinations do not possess a structure like the cup-shaped core of the $+2\pi$ disclination shown in Fig. 1.12.

4 Discussion

The transverse microstructure sketched in Fig. 1.1 offers a useful framework to discuss mechanisms active in the spinning of mesophase fiber at viscosity levels where the structural memory is effective. The ripples, zigzag bands, and fine structure in the rim of the filament appear to be rheological consequences of the tendency for carbonaceous mesophase to align radially during convergent and tubular flow in the spinneret (Didwania *et al.*, 1998; Singh and Rey, 1998).

To some extent, the thickness of outermost skin is open to control by spinneret design, such as the lengths of the relaxation and capillary tubes. Thus a major fraction of the filament within the skin will reflect a miniaturized microstructure of the mesophase entering the spinneret unless the filament designer elects to manipulate flow by such means as stirring, screens, and relaxation.

Plain-weave screens, at suitably fine mesh, can establish a completely new tubular microstructure, and the concept by Taylor and Cross (1993) of a composite filament consisting of a parallel array of graphene tubes, at a scale approaching that of a thick-walled buckytube, seems well worth pursuing. Their measurements of the mechanical properties on fibers only partially converted to nanotubular microstructures are promising, and the fiber user should be interested in such further developments as more fully nanotubular fibers, and in the mechanical toughness that might be contributed by adjusting capillary length to produce PO rings dominated alternately by $+2\pi$ and -2π disclinations.

The concept of producing nanotubular structures by screened spinning of mesophase pitch is intriguing. How far such a process can be driven to produce structures approximating thick-walled buckytubes seems to depend on the precision with which the layer-by-layer polymerization of mesophase molecules in a spun filament can be conducted through stabilization and carbonization to form graphene tubes or scrolls.

The process of low-temperature stabilization (Cornec *et al.*, 1992; Jones *et al.*, 2001) may play a role in improving fiber properties by offering better oxygen distribution at depth in the filament as well as less carbon burnoff at the surface. The practical objections of process length and increased cost may be relieved, at least in part, by using oxygen at pressures of the order of 1 MPa, but the immediate goal should be to learn if pressurized stabilization at low temperature offers a path to the high strengths that Bacon (1960) observed in carbon whiskers recovered from carbon deposits formed in high-pressure graphite arcs.

In closing, we are reminded that the present studies of what can be done to design and control the microstructure in spinning mesophase filaments was enabled by the development of low-viscosity, fully transformed mesophase pitches that are relatively stable at spinning temperatures. It is perhaps now reasonable to ask further help from aromatic organic chemists, to produce more ribbon-like than disk-like mesophase molecules with the length-to-width ratio of the molecules defined by rheological considerations, and to design only enough oxygen-reactive sites on the molecules to ensure stabilization with minimal carbon burn-off.

Acknowledgments

The authors are much indebted to Drs S. Subramoney and J. G. Lavin of the DuPont Experimental Station for their extensive electron microscopy; to B. D. Jones and Professor P. C. Chau for recent results on low-temperature stabilization; and to Dr A. K. Didwania for rheological insight. We also thank Professor G. H. Taylor (Australian National University) and Dr L. S. Singer (retired from Union Carbide) for valuable discussions. Mitsubishi Oil, Mitsubishi Gas Chemical, and Amoco Performance Products have been generous in providing mesophase pitches. This review, as well as the experimental work at UCSD, were supported by the US National Science Foundation under Grant No. 9700177.

References

Bacon, R. (1960) “Growth, Structure, and Properties of Graphite Whiskers,” *J. Applied Phys.,* **31**, 283–90.

Bourrat, X. (2000) “Structure in Carbon and Carbon Artefacts,” in *The Science of Carbon Materials*, H. Marsh and F. Rodriguez-Reinoso, Eds, Universidad de Alicante, Spain.

Bourrat, X., E. J. Roche, and J. G. Lavin (1990a) “Lattice Imaging of Disclinations in Carbon Fiber,” *Carbon*, **28**, 236–8.

Bourrat, X., E. J. Roche, and J. G. Lavin (1990b) “Structure of Mesophase Pitch Fibers,” *Carbon*, **28**, 435–46.

Bourrat, X., E. J. Roche, and J. G Lavin (1990c) “The Role of Disclinations in the Structure of Mesophase-Pitch-Based Carbon Fiber,” Proc. International Symposium on Carbon, Tsukuba, Japan, 4–8 Nov. 1990, *Tanso publisher*, 790–3 and 320–2.

Brooks, J. D. and G. H. Taylor (1965) “The Formation of Graphitizing Carbons from the Liquid Phase,” *Carbon*, **3**, 185–93.

Cornec, L. P., D. K. Rogers, C. C. Fain, and D. D. Edie (1992) “A Novel Stabilization Technique and its Influence upon Carbonization Yield,” *Extended Abstracts, Carbon’92*, 710–12.

Didwania, A. K., B. Fathollahi, and J. L. White (1998) “Formation of Banded Microstructure during Capillary Flow of Mesophase Pitch,” *Extended Abstracts, Eurocarbon’98*, **2**, 531–2.

Didwania, A. K., B. Fathollahi, and J. L. White (1999a) “Periodic Disclination Arrays in Carbonaceous Mesophase Pitch,” *Extended Abstracts, Carbon’99*, 112–13.

Didwania, A. K., B. Fathollahi, and J. L. White (1999b) “Capillary Flow of Carbonaceous Mesophase and its Stability,” *Extended Abstracts, Carbon’99*, 482–3.

Edie, D. D. (1998) “The Effect of Processing on the Structure and Properties of Carbon Fibers”, *Carbon*, **36**, 345–62.

Fathollahi, B. (1996) “Flow-Induced Microstructures in the Spinning of Carbonaceous Mesophase, a Discotic Nematic Liquid Crystal,” PhD Thesis, University of California, San Diego.

Fathollahi, B. and J. L. White (1994) “Polarized-Light Observations of Flow-Induced Microstructures in Mesophase Pitch,” *J. Rheology*, **38**, 1591–607.

Fathollahi, B., J. L. White, S. Subramoney, and J. G. Lavin (1996) “Designed Microstructures in Spinning Mesophase Pitch Fibers: Part I – Optical Microscopy,” *Extended Abstracts, Carbon’96*, 200–1.

Fathollahi, B., J. L. White, S. Subramoney, and J. G. Lavin (1997) “Designed Nanotubular Microstructures in Mesophase Carbon Fiber,” in *Recent Advances in the Chemistry and Physics of Fullerenes and Related Materials*, **5**, K. M. Kadish and R. S. Ruoff, Eds, The Electrochemical Soc., Pennington, NJ, 538–48.

Fathollahi, B., A. K. Didwania, and J. L. White (1999a) “The Formation of $+2\pi$ Disclination Arrays during Flow of Mesophase Pitch through a Screen Mesh,” *Extended Abstracts, Carbon’99*, 362–3.

Fathollahi, B., J. L. White, S. Subramoney, and J. G. Lavin (1999b) “Nanotubular Microstructures in As-Spun and Heat-Treated Mesophase Filaments,” *Extended Abstracts, Carbon’99*, 486–7.

Fathollahi, B., B. Jones, P. C. Chao, and J. L. White (2000) “Mesophase Stabilization at Low Temperatures,” *Extended abstracts, Carbon’00* (Berlin, Germany), 259–60.

Fitzgerald, J. D., G. M. Pennock, and G. H. Taylor (1991) “Domain Structure in Mesophase Pitch-Based Fibres,” *Carbon*, **29**, 139–64.

Hamada, T., T. Nishida, Y. Sajiki, and M. Matsumoto (1987) “Structure and Physical Properties of Carbon Fibers from Coal Tar Mesophase Pitch,” *J. Mat. Res.*, **2**, 850–7.

Hamada, T., T. Nishida, M. Furukama, and T. Tomioka (1988) “Transverse Structure of Pitch Fiber from Coal Tar Mesophase Pitch,” *Carbon*, **26**, 837–41.

Hamada, T., M. Furukama, Y. Sajiki, T. Tomioka, and M. Endo (1990) “Preferred Orientation of Pitch Precursor Fibers, *J. Mat. Res.*, **5**, 1271–80.

Hara, R., M. Kagizaki, T. Takekura, and S. Tomono (1990) “Process for the Production of Pitch-Type Carbon Fibers,” US Patent 4,923,648.

Jones, B., B. Fathollahi, J. L. White, A. K. Didwania, and P. C. Chau (2001) “Mesophase Stabilization at Low Temperatures and Elevated Oxidation Pressures,” *Extended Abstracts, Carbon’01*.

Kazmer, A. J. and R. J. Diefendorf (1991) “Oxidative Stabilization of Bulk Carbonaceous Materials,” *Extended Abstracts, 20th Conf. on Carbon*, 178–9.

Lewis, I. C. and F. F. Nazem (1987) “Rheology of Mesophase Pitch – Effects of Chemical Constitution,” *Extended Abstracts, 18th Conf. on Carbon*, 290–1.

Lu, S., S. P. Appleyard, and B. Rand (2000) “Novel Highly Oriented Mesophase-Based Graphite (HOMG) for Thermal Management Applications,” *Extended Abstracts*, Eurocarbon 2000, 236–7.

Matsumoto, M., T. Iwashita, Y. Arai, and T. Tomioka (1993) “Effect of Spinning Conditions On Structures of Pitch-Based Carbon Fiber,” *Carbon*, **31**, 715–20.

Miura, K., H. Nakagawa, and K. Hashimoto (1995) “Examination of the Oxidative Stabilization Reaction of the Pitch-Based Carbon Fiber through Continuous Measurement of Oxygen Chemisorption and Gas Formation Rate,” *Carbon*, **33**, 275–82.

McHugh, J. J. and D. D. Edie (1995) “Orientation of Mesophase Pitch in Capillary and Channel Flows,” *Liquid Crystasl*, **18**, 327–35.

Mochida, I., K. Shimizu, Y. Korai, H. Otsuka, and S. Fujiyama (1988) “Structure and Carbonization Properties of Pitches Produced Catalytically from Aromatic Hydrocarbons with HF/BF3,” *Carbon*, **26**, 843–52.

Mochida, I., H. Toshima, Y. Korai, and T. Hino (1989) “Oxygen Distribution in Mesophase Pitch Fiber after Oxidation Stabilization,” *J. Mat. Sci.*, **24**, 389–94.

Otani, S. (1981) “Carbonaceous Mesophase and Carbon Fibers,” *Mol. Cryst. Liq. Cryst.*, **63**, 249–64.

Pennock, G. M., G. H. Taylor, and J. D. Fitzgerald (1993) “Microstructure in a Series of Mesophase Pitch-Based Fibers from DuPont: Zones, Folds, and Disclinations,” *Carbon*, **31**, 591–609.

Robinson, K. E. and D. D. Edie (1996) “Microstructure and Texture of Pitch-Based Ribbon Fibers for Thermal Management,” *Carbon*, **34**, 13–36.

Ross, R. A. and U. D. Jennings (1992) “Method of Making Small Diameter High Strength Carbon Fibers,” US Patent 5,169,584 (December 8, 1992).

Sakanishi, A., Y. Korai, I. Mochida, K. Yanagida, M. Noda, I. Thunori, and K. Tate (1992) “Comparative Study of Isotropic and Mesophase Pitches Derived from C9 Alkylbenzenes,” *Carbon*, **30**, 459–66.

Singer, L. S. (1978) “The Mesophase and High-Modulus Carbon Fibers from Pitch,” *Carbon*, **16**, 408–15.

Singh, A. P. and A. D. Rey (1995) “Computer Simulation of Dynamics and Morphology of Discotic Mesophases in Extensional Flows,” *Liq. Crystals*, **18**, 219–30.

Singh, A. P. and A. D. Rey (1998) “Consistency of Predicted Shear-Induced Orientation Modes with Oberved Mesophase Pich-Based Carbon Fiber Textures,” *Carbon*, **36**, 1855–9.

Subramoney, S., J. G. Lavin, B. Fathollahi, J. L. White, and X. M. A. Bourrat (1996) “Designed Microstructures in Spinning Mesophase Pitch Fibers: Part II – Dark-Field Transmission Electron Microscopy,” *Extended Abstracts, Carbon’96*, 202–3.

Taylor, G. H. and L. F. Cross (1993) “Orthogonal Structure in Mesophase Pitch-Based Carbon Fibres,” *J. Materials Sci.*, **28**, 6503–9.

White, J. L., B., Fathollahi, and A. K. Didwania (2001) “Formation of Rippled and Zigzag Microconstituents in the Spinning of Mesophase Filaments,” *Extended Abstracts, Carbon’01*.

Yoon, S.-H., Y. Korai, and I. Mochida (1994) “Assessment and Optimization of the Stabilization Process of Mesophase Pitch Fibers by Thermal Analysis,” *Carbon*, **32**, 281–7.

Zimmer, J. E. and J. L. White (1982) “Disclination Structures in the Carbonaceous Mesophase,” *Adv. in Liq. Crystals*, **5**, 157–213.

2

THE EFFECT OF PROCESSING ON THE STRUCTURE AND PROPERTIES

D. D. Edie

1 Introduction

Carbon fibers are, perhaps, the most successful new carbon product to be commercialized in the past 35 years. Their high strength and stiffness, combined with their light weight, make these fibers attractive for high-volume applications ranging from sporting goods to aircraft structures. Today, carbon fibers are also being developed for a new class of applications, thermal management. Like other products, commercial carbon fibers must exhibit consistent mechanical and transport properties, and the optimum properties may differ for each application. Because of this, the control of structure and the interaction between the structure and properties has been extensively studied since high performance fibers were first commercialized by Union Carbide in the 1960s.

Nearly all commercial carbon fibers are produced by first converting a carbonaceous precursor into fiber form. The precursor fiber then is crosslinked in order to render it infusible. Finally, the crosslinked precursor fiber is heated at temperatures from 1,200 to about 3,000 °C in an inert atmosphere to drive off nearly all of the noncarbon elements, converting the precursor to a carbon fiber. Like other commercial fiber processes, the final properties are, to a great extent, determined by the material, the process, and the conditions used to form the precursor fiber. Post-treatment steps (in this case crosslinking and carbonization) merely refine and perfect the as-spun structure. This is not to say that fiber properties can not be dramatically altered during post-treatment. However, the fundamental fiber structure needed to develop high strength or high thermal conductivity must be created during the initial fiber formation step. With this in mind, we will begin by detailing the processes used to form the two dominant classes of carbon fibers, polyacrylonitrile-based (PAN-based) and mesophase pitch-based (pitch-based). Then, we will discuss the relationship between structure and properties for both classes of carbon fibers. Finally, we will review recent breakthroughs in the control of structure for pitch-based fibers and discuss the possible implications for PAN-based fiber producers.

Although considerable progress has been made over the past 35 years, the origin and development of structure as well as the relationship between structure and properties are still not *completely* understood for carbon fibers. Therefore, throughout this chapter, I will indicate areas where researchers are in general agreement and point out phenomena that are still subject to debate.

Unlike people, all carbon fibers are not created equal. The fundamental structural characteristics of PAN precursor fibers differ from those of mesophase pitch precursor fibers. Because of this, certain properties are easier to develop in PAN-based carbon fibers, while other properties are easier to develop in pitch-based carbon fibers. Therefore, if we are to understand structure and properties of these two classes of carbon fibers, we must begin by detailing the materials and processes used to form the precursor fibers.

2 PAN-based carbon fibers

Nearly all commercial fibers are produced using one of three techniques: melt spinning, wet spinning, or dry spinning. In melt spinning the precursor is merely melted and extruded through a spinneret containing numerous small capillaries. As the precursor emerges from these capillaries, it cools and solidifies into fiber form. In wet spinning a concentrated solution of the precursor is extruded through a spinneret into a coagulation bath. The solvent is more soluble in the coagulation fluid than it is in the precursor. Therefore, as the solution emerges from the spinneret capillaries, the precursor precipitates into fiber form. Dry spinning also involves spinning a concentrated solution through a spinneret. However, in dry spinning the solution is extruded into a drying chamber. Here, the solvent evaporates and the precursor precipitates into fiber form. Because melt spinning converts a pure precursor directly into fiber form and does not involve the added expense of solvent recycling and recovery, it is the preferred fiber formation process. However, either wet or dry spinning must be employed if the precursor degrades at or near its melting temperature.

2.1 Production of PAN precursor

PAN is an atactic, linear polymer containing highly polar nitrile pendant groups. Because of its highly polar nature, pure PAN has a glass transition temperature of approximately 120 °C and tends to decompose before it melts. Therefore, PAN precursor fibers must be produced by either wet- or dry-spinning processes using highly polar solvents. Actually, PAN homopolymer is rarely, if ever, used as a carbon fiber precursor. Commercial PAN precursor fibers normally contain from 6 to 9% of other monomers, such as itaconic acid, acrylic acid, methacrylic acid, methyl acrylate, vinyl bromide, etc. (Edie and Diefendorf, 1993; Capone, 1995). These additions lower the glass transition temperature and affect the reactivity of the polymer structure. Both of these changes can dramatically influence subsequent process steps.

2.2 Production of PAN precursor fibers

Although PAN fibers can be produced by either wet or dry spinning processes, wet spinning is used to produce nearly all precursor fibers used in commercial PAN-based carbon fiber processes. The solution used in a wet spinning process normally consists of from 10% to 30% by weight of PAN or (PAN copolymer) dissolved in a polar solvent, such as sodium thiocyanate, nitric acid or dimethylacetamide. As Fig 2.1 shows, this solution is first filtered and then extruded through a spinnerette into a coagulation bath (Ram and Riggs, 1972; Ziabicki, 1976). The coagulation bath can contain various solutions, ranging from water and sodium thiocyanate or dimethylacetamide to ethylene glycol and dimethylacetamide or dimethylformamide. The rate of fiber formation is controlled by adjusting parameters such as the solution concentration, the concentration of the coagulation bath, the bath temperature, the drawdown rate, and the rate of extrusion (Knudsen, 1963).

Mass transfer at the fiber/liquid interface is relatively slow in the wet-spinning process. The reason is that the solvent concentration of the coagulation bath is relatively high. Because of this the solvent can diffuse radially through the solidifying fiber faster than it

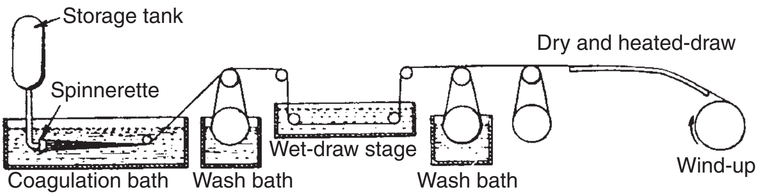

Figure 2.1 Schematic of wet-spinning process used to produce PAN precursor fibers (adapted from Ram and Riggs, 1972).

can diffuse away from the fiber surface. As a result, the solvent concentration is relatively uniform across the fiber's cross section during solidification. Therefore, the fiber shrinks uniformly in the radial direction, giving the circular cross section that is characteristic of wet-spun PAN. However, if the polymer concentration in the spinning solution is low, a relatively rigid fiber skin can also form in this process before the center of the fiber has solidified, yielding a dogbone-shape fiber.

As the PAN solution is forced through the spinneret capillaries, the shear field tends to orient the solidifying polymeric structure parallel to the direction of flow. In fact, various studies have found that a solvent can decrease the entanglement of polymers during extrusion and enhance orientation. Like many other polymers, PAN tends to precipitate into fibril form. Various processing parameters, such as coagulation bath temperature, solvent concentration and stretch, can influence the fibrillar structure and its orientation within the as-spun PAN fiber (Knudsen, 1963). In other words, wet-spinning yields a precursor fiber in which the PAN molecules are organized into fibrils which, in turn, are generally oriented parallel to the fiber axis. Electron micrographs of as-spun fibers show that these fibrils are joined together in a three-dimensional network (Riggs *et al.*, 1982).

After being spun into fibers, the orientation within the PAN is enhanced by stretching. Although the maximum degree of crystallinity within the PAN fiber is only 50%, this step is essential for producing a final carbon fiber with adequate strength and modulus. Like most polymeric fiber processes, stretching does not greatly increase the crystallinity or the molecular order within the PAN; rather, it enhances the axial orientation of the PAN fibrils. This fibrillar network appears to be the precursor of the graphene network that develops during final heat treatment.

2.3 Stabilization of PAN precursor fibers

The primary function of the stabilization step is to crosslink this as-spun structure, insuring that both the molecular and the fibrillar orientation will not be lost during final heat treatment. To accomplish this, either the inherent stiffness of the PAN molecules must be increased or the molecules must be "tied" together in order to eliminate, or at least limit, relaxation, and chain scission during the final carbonization step (Ehrburger and Donnet, 1983; Thorne, 1985). In most commercial processes, the PAN precursor fiber is stabilized by exposing it to air at temperatures ranging from 230 to 280 °C. Tension must be applied during this step to limit relaxation of the polymer structure (see Fig. 2.2). Most would agree that both cyclization and dehydrogenation can occur during the stabilization step. Cyclization, in particular, is highly exothermic, but the exotherm is reduced when PAN

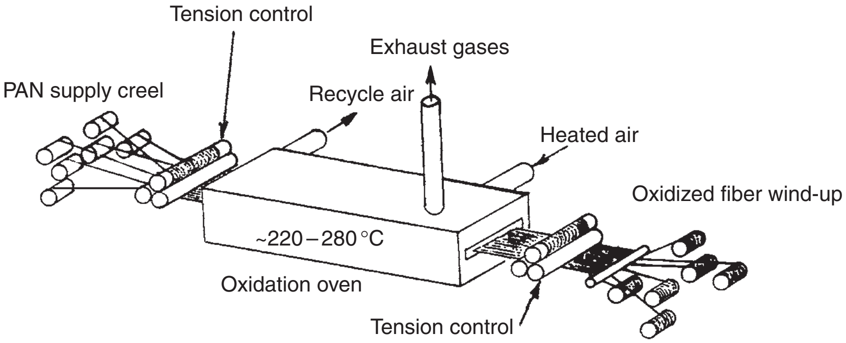

Figure 2.2 Schematic of commercial PAN stabilization oven (Edie and Diefendorf, 1993).

copolymer precursors are employed. Evidently, the comonomer acts as an initiator for the stabilization reaction (Fitzer, 1989a). Numerous studies (Grassie and Hay, 1962; Fitzer and Müller, 1972) have shown that the rate of oxidative stabilization is affected by the copolymer composition of the PAN precursor fiber, the temperature, and even the applied tension. Although most researchers agree that a ladder polymer forms during this process, its exact structure is still in doubt. In a recent review article, Bashir (1991) pointed out that the cyclization reaction may be stereospecific. In fact, a study by Colman *et al.* (1983) suggests that cyclization would occur preferentially in isotactic sequences. However, Chen *et al.* (1981) found that syndiotactic sequences were equally capable of cyclization. The problem may be that the polymer chains within the fibril form an irregular rod-like helix due to the intramolecular repulsion of the nitrile groups. These fibrils, in turn, contain both crystalline and amorphous regions. Gupta and Harrison (1996) found that intramolecular reactions within the rod-like helix dominate at lower temperatures (below about 290 °C), whereas intermolecular reactions between adjacent helices occur between 300 and 380 °C. Perhaps both Colman *et al.* and Chen *et al.* are correct – intramolecular reactions are stereospecific, but intermolecular reactions are not.

Thus, one might expect a stereoregular precursor polymer to offer advantages. However, to date, no research in this area has been reported.

2.4 Carbonization of stabilized PAN fibers

Once stabilized, the PAN fiber is carbonized at 1,000–1,500 °C in an inert atmosphere (Thorne, 1985; Edie and Diefendorf, 1993). During this step most of the non-carbon elements within the fiber are volatilized in the form of methane, hydrogen, hydrogen cyanide, water, carbon monoxide, carbon dioxide, ammonia, and various other gases (Riggs *et al.*, 1982; Fitzer *et al.*, 1986). The evolution of these compounds decreases the mass of the fiber by from 55 to 60 weight percent. As a result the fiber shrinks in diameter. Therefore, in a typical PAN process, the precursor fiber might begin with an as-spun diameter of 35 microns and then be stretched to a diameter of 10.5 microns. Finally, shrinkage during carbonization yields a carbon fiber with a diameter of seven microns. In other words, small carbon fiber diameters are a characteristic of the high weight loss of PAN during processing. Even though the diameter of most PAN-based carbon fibers is smaller than that of

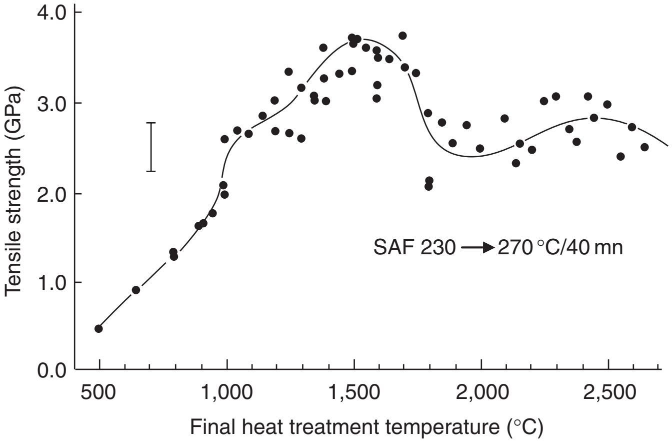

Figure 2.3 Influence of final heat treatment temperature on the tensile strength of PAN-based carbon fiber (Fitzer and Frohs, 1988).

most pitch-based carbon fibers, the as-spun diameter of the precursor fiber is actually significantly greater.

Initially, increasing the final heat treatment temperature increases tensile strength. However, as Fig. 2.3 shows, the tensile strength suddenly drops when heat treatment temperatures exceed 1,600 °C (Fitzer and Frohs, 1988). Fitzer claims that this decrease is associated with the release of nitrogen and that the reduction in strength can be minimized by applying tension during heat treatment (Fitzer, 1989b). By contrast, the degree of preferred orientation within the fiber and, thus, the modulus of the PAN-based carbon fibers increase continuously as heat treatment temperature is increased (Fitzer and Frohs, 1988). Because of this, the various grades of PAN-based carbon fiber available from a particular manufacturer are, normally, the result of changes in heat treatment temperature.

2.5 Structure of PAN-based carbon fibers

Pioneering studies by Diefendorf and Tokarsky (1975) Johnson (1987) and others showed that the structure of PAN-based carbon fiber is fibrillar in nature, mimicking the fundamental structure of the polymeric precursor fiber. Diefendorf and Tokarsky also showed that the amplitude of the undulation in the fibrillar structure was highest in the center and lowest near the surface of PAN-based carbon fibers. This indicated that the modulus of a PAN-based carbon fiber varies throughout its cross section. In a recent study Huang and Young (1995) confirmed this skin-core structural difference in PAN-based carbon fibers using Raman spectroscopy. Both Johnson (1987) and Endo (1988) employed wide-angle x-ray diffraction to show that the layer planes of PAN-based carbon fibers have no regular three-dimensional order. Also, by subjecting longitudinal and transverse sections to small-angle x-ray diffraction and transmission electron microscope (TEM) analysis, Johnson (1987) showed that needle-shaped voids exist between crystallites in the outer skin of the fiber and that, in this region, the layer planes are essentially parallel to the surface. However, in the core region, Johnson found that the layer planes were folded extensively, often through

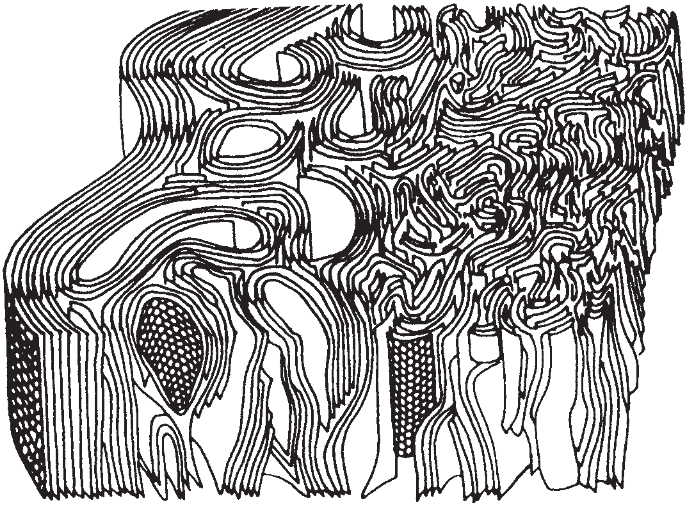

Figure 2.4 Microstructure of PAN-based carbon fiber (Johnson, 1987).

angles of 180°. Based on these results, Johnson developed the three-dimensional schematic representation of the microstructure of PAN-based carbon fiber shown in Fig. 2.4. Guigon *et al*. (1984) have proposed that the microtexture of PAN-based carbon fibers is even more complicated – "crumpled sheets" form these fibrils.

Each of these studies show that PAN-based carbon fibers contain extensively folded and interlinked turbostratic layers of carbon with interlayer spacings considerably larger than that of graphite. As a result, PAN-based carbon fibers have a low degree of graphitization. The turbostratic layers within PAN-based carbon fibers appear to follow the original fibril structure of the PAN precursor fiber. Although the turbostratic layers within these fibrils tend to be oriented parallel to the fiber axis, they are not highly aligned. As first proposed by Johnson (1987), it is this fibrillar structure that makes PAN-based fibers less prone to flaw-induced failure. He based his argument on the brittle-failure mechanism proposed by Reynolds and Sharp. As discussed above, the crystallites within PAN-based carbon fibers are not perfectly aligned, and misoriented crystallites are relatively common (see Fig. 2.5a). When a stress is applied parallel to the fiber axis, the crystallites align until their movement is restricted by a disclination in the structure (Fig. 2.5b). If the stress is sufficient, the misoriented crystallite will rupture and relieve the stress within the fiber (Fig. 2.5c). When the size of the ruptured crystallite (perpendicular to the fiber axis) is larger than the critical flaw size, a catastrophic failure occurs, and the fiber breaks. Even if the ruptured crystallite is smaller than the critical flaw size, catastrophic failure can occur if the crystallites surrounding the disclination are continuous enough to allow a crack to propagate into neighboring crystallites. According to Johnson, this failure mode explains the difference between the flaw sensitivity (and, therefore, the tensile strength) of the non-graphitic, fibrillar PAN-based carbon fiber and graphitic, mesophase pitch-based fiber. Recent work (Dobb *et al*., 1995) indicates that inter-crystalline and intra-crystalline disorder, most likely caused by the fibrillar structure of the PAN-based carbon fiber, is responsible for the superior compressive strength of this class of carbon fiber.

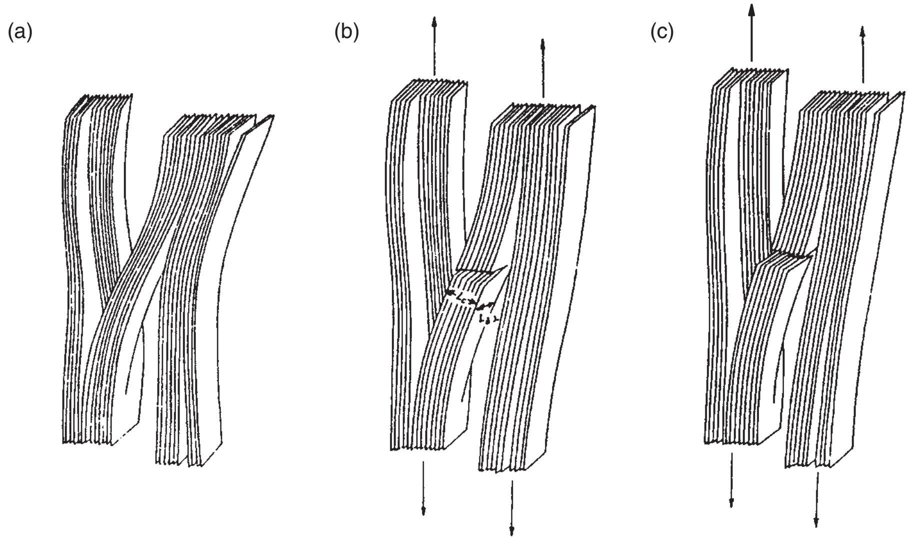

Misoriented crystallite linking two crystallites parallel to fiber axis

Tensile stress causes basal plane rupture in L_a direction

Catastrophic failure occurs if crystallite size > critical flaw size

Figure 2.5 Reynolds and Sharp mechanism for tensile failure of carbon fibers (Johnson, 1987).

Obviously, the fundamental fibrillar structure of PAN-based carbon fibers is created during initial fiber formation. However, little if any research into this fiber formation process has been done since PAN's adoption as a carbon fiber precursor. Instead, as the above review indicates, nearly all recent PAN-based carbon fiber research has concentrated on stabilization and carbonization. By contrast, research in pitch-based carbon fibers has concentrated on perfecting precursor chemistry and the development of structure during fiber formation. As we will see, pitch researchers appear to have chosen the more critical area for control and optimization of fiber properties.

3 Pitch-based carbon fibers

Its highly condensed aromatic structure gives mesophase pitch (the precursor for pitch-based carbon fibers) relatively good thermal stability. Because of this, mesophase pitch precursor fibers are melt spun. As previously mentioned, melt spinning is the preferred fiber formation process because it avoids solvent-related issues. Initially, it was felt that this less complicated spinning process, combined with the potential low cost of the precursor, would make pitch-based fibers a low-cost alternative to PAN-based carbon fibers. While this may come to pass eventually, the economics of pitch fiber processing are not quite this simple. Also, as researchers have discovered, the fundamental structure of pitch-based carbon fibers is very different than that of PAN-based carbon fibers, and each structure offers certain advantages. Like PAN-based fibers, the structure of pitch-based fibers is largely developed during fiber formation. Therefore, we will begin by discussing the peculiarities of mesophase and detailing how it is converted into carbon fibers. Hopefully, by the end of this discussion you will understand the tremendous potential as well as the inherent limitations of this class of carbon fibers.

3.1 Production of mesophase pitch

Like PAN-based carbon fibers, the peculiarities of pitch-based fibers are the direct result of the precursor and the process used to convert it to fiber form. In this case, the precursor is mesophase pitch, a liquid crystalline material consisting of large polynuclear aromatic hydrocarbons. The properties of mesophase, its formation, and mode of growth have been the subject of numerous articles (Brooks and Taylor, 1968; Marsh and Cornfield, 1976; White and Zimmer, 1976; Zimmer and White, 1982).

The first commercial mesophase precursors were produced by Union Carbide using a thermal polymerization process. Evidently, the original process produced a mixture of isotropic and mesophase pitch (Lewis, 1977; Singer, 1977). These early patents claim that small amounts of isotropic pitch are needed to reduce the viscosity of the polymerized mesophase and, therefore, the spinning temperature. These mixed precursors were prepared by thermally polymerizing a highly aromatic isotropic pitch feed (originating from either petroleum or coal tar) at temperatures of 400–410 °C for as long as 40 hours (Lewis, 1977; Singer, 1977). Coal tar pitch produces a mesophase product with higher aromaticity, whereas petroleum pitch yields a mesophase product with a more open structure and a higher content of aliphatic side chains (see Fig. 2.6) (Fitzer, 1989a; Azami *et al*., 1991). As revealed by Lewis (1977), agitation during heat treatment produces a lower molecular weight mesophase and creates an emulsion of the mesophase and isotropic pitch, making the material easier to spin. Later Chwastiak (1980) found that if an inert gas sparge was used to agitate the pitch during thermal polymerization, a spinnable 100% mesophase product could be produced. A single-phase precursor is preferable for melt-spinning processes because it avoids the stability problems associated with two-phase extrusion. Nevertheless, based on a recent TEM study (Fitzgerald *et al*., 1991) it would appear that some commercial pitch-based fibers are still produced from a mixed mesophase/isotropic pitch precursor.

Diefendorf and Riggs (1980) developed an alternative technique, solvent extraction, that produced a spinnable 100% mesophase precursor from an isotropic feed. In their process a portion of highly aromatic pitch was extracted using a solvent mixture such as benzene and toluene. The extraction step removes the smaller disordering molecules and concentrates the higher molecular weight material. The higher molecular fraction can be converted to a 100% mesophase by heating it to between 230 and 400 °C for only 10 minutes. In either the thermal polymerization or the solvent extraction process, a free-radical mechanism is

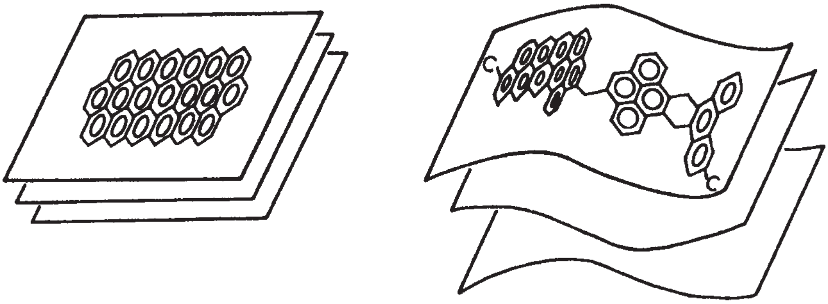

Figure 2.6 Typical polynuclear aromatic hydrocarbons in mesophases produced from coal-tar and petroleum (Azami *et al*., 1991).

believed to be responsible for polymerization of the carbonaceous material. Although solvent extraction does reduce the molecular weight distribution somewhat prior to heat treatment, this reaction mechanism still tends to create a product with a relatively broad molecular weight distribution.

Recently, Thies and coworkers developed a variation of this solvent-extraction process that uses a supercritical fluid instead of a conventional liquid solvent (Hutchenson *et al.*, 1991). In this process, an aromatic isotropic feed pitch is initially dissolved in an aromatic solvent, such as toluene, at supercritical conditions. The resulting homogeneous solution is then fractionated in a conventional manner, using changes in either temperature or pressure, to produce pitch fractions of relatively narrow molecular weight distribution. Tests have demonstrated that the process can be used to produce 100% mesophase fractions of a desired molecular weight and softening point (Bolaños and Thies, 1996).

Mochida also developed a process that produces a spinnable 100% mesophase precursor with a relatively narrow molecular weight distribution (Mochida *et al.*, 1992). This process, recently commercialized by Mitsubishi Gas Chemical Company, uses a strong Lewis acid catalyst (HF-BF$_3$) to catalyze a pure chemical feed, such as naphthalene or methyl-naphthalene, to a 100% mesophase product. As Mochida has shown, the use of HF-BF$_3$ greatly reduces the molecular weight distribution of the mesophase product compared to that produced by thermal polymerization.

Each of these processes are being explored, and, to varying degrees, used on a commercial scale. While each process and its mesophase product offer certain advantages, they also suffer from some disadvantages. Thermal polymerization avoids the use of solvents, but it produces a product with a broad molecular weight distribution (and perhaps even a two-phase mixture). Solvent extraction produces a product with a narrower molecular weight distribution, but it uses large amounts of solvents. Supercritical extraction and catalytic polymerization produce relatively uniform products with narrow molecular weight distributions. However, supercritical extraction has yet to be proven on a commercial scale, and processes using HF-BF$_3$ catalysis are being subjected to increasing environmental regulations.

The mesophase products produced by these four processes differ considerably, but they also exhibit many similarities. For instance, each process yields a product with a different molecular weight distribution and a different concentration of aliphatic side chains on the individual mesophase molecules. Consequently their viscous characteristics differ and, as will be explained later, their rate of stabilization differs as well. However, all of these mesophase products contain a range of molecular weights, with an average of from 800 to 1,200. Because of this these mesophases reach a viscosity of 200 Pa-s or lower well below their degradation temperature. Also, although somewhat irregular, the individual mesophase molecules are, in general, disc-like in shape. Recent work indicates that mesophase molecules can form a substructure and that the chemical nature of the molecule influences the size of this substructure (Korai and Mochida, 1992).

While coalesced mesophase can exhibit complicated extinction patterns caused by disclinations, no grain boundaries appear to be present (Zimmer and White, 1977). In other words, one might expect bulk mesophase to behave as an ideal liquid crystalline fluid – a single-domain liquid crystal. As we will see, this appears to be both true and false.

3.2 Production of mesophase pitch precursor fibers

As previously mentioned, the mesophase pitches used to form carbon fibers soften and flow well below their degradation temperature. Therefore, they can be melt spun into fiber form.

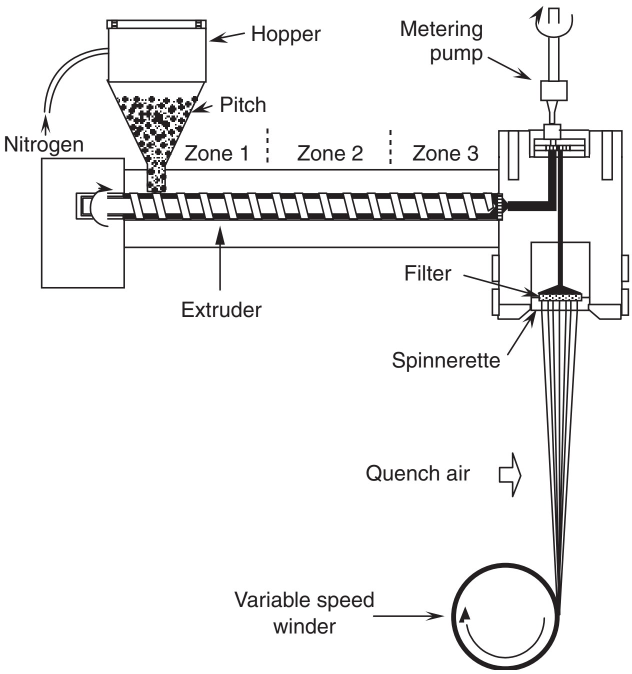

Figure 2.7 Schematic of melt-spinning process used to produce mesophase pitch precursor fibers (Edie *et al*., 1994).

The schematic for a typical melt-spinning process that might be used to produce mesophase pitch precursor fibers (Edie *et al*., 1994) is shown in Fig. 2.7. The precursor (in this case, mesophase pitch) is loaded into the feed hopper of the extruder as solid chips. The extruder's rotating screw conveys the chips into the melting section of the extruder where the chips are heated, forming a viscous melt. Then the molten precursor is conveyed into the pumping section of the extruder. In this section of the extruder the channel narrows, increasing the fluid pressure. The molten precursor, now at a relatively high pressure, exits the extruder and flows through the transfer manifold. As the precursor exits the manifold it enters a metering pump. The purpose of this positive-displacement pump is to minimize any pressure fluctuations created by the rotating extruder screw. The metering pump forces the molten precursor into the spin pack. Normally, the spin pack houses a filter, which is capable of removing any small solid particles from the molten precursor. As the precursor exits the pack, it is forced through a plate containing numerous small holes (i.e. the spinneret). Finally, as the molten precursor exits these holes, it is simultaneously quenched by the surrounding atmosphere and drawn down by the windup device, forming solid fibers. At first glance, this would appear to be a relatively simple process. In fact, the melt spinning is simple. However, melt-spinning mesophase is far from simple.

By applying heat, mass and momentum balances, Edie and Dunham (1989) showed that the mesophase melt-spinning process is extremely sensitive to small changes in process conditions. Although their model did not account for the liquid crystalline behavior of the mesophase precursor, it nevertheless demonstrated that, at typical process conditions, the

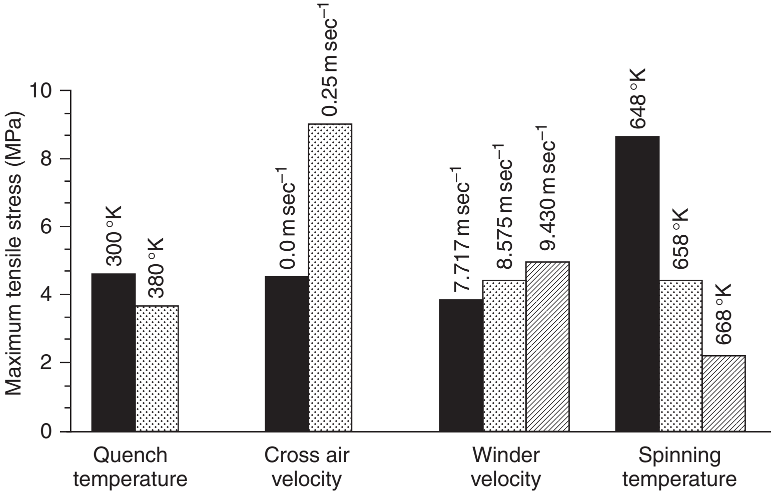

Figure 2.8 Predicted influence of major process variables during mesophase melt spinning (Edie and Dunham, 1989).

tensile stress on mesophase fibers is about 20% of that required to break the fiber (see Fig. 2.8), and experimental measurements confirm these predictions. In comparison, during melt spinning the tensile stress developed within a nylon fiber is less than 1% of the breaking strength of the filament. This stability problem is the direct result of two peculiarities of mesophase: its highly temperature-dependent viscosity, and the brittle nature of as-spun mesophase fibers.

Because its viscosity is highly temperature-dependent, mesophase pitch fibers draw down and cool very quickly during fiber formation. In fact, at typical melt-spinning conditions, mesophase fibers are already 100 °C below their glass transition temperature by the time they are 2 cm from the spinneret. As a result, they can break easily during spinning and are extremely difficult to handle before they are carbonized. Although the rheology of mesophase makes control of the melt-spinning process more difficult, its liquid crystalline nature gives this precursor advantages compared to polymeric precursors such as PAN. Unlike polymeric fibers, the molecular orientation within a mesophase precursor fiber can be improved by increasing spinning temperature (Yoon *et al.*, 1994).

3.3 Stabilization of mesophase pitch precursor fibers

Because mesophase pitch is a thermoplastic material, the as-spun structure must be thermoset to prevent relaxation during final heat treatment. Like the PAN carbon fiber process, oxidative stabilization is normally employed to crosslink the as-spun fibers, so the stabilization process involves simultaneous diffusion and reaction. However, unlike PAN precursor fibers, the as-spun structure of mesophase precursor fibers is already highly oriented, so tension does not need to be applied during stabilization. Most mesophase precursor fibers can be stabilized by exposing them to air at temperatures ranging from 230 to 280 °C. Often, the temperature begins near the softening temperature of the mesophase and is increased in a series of steps during the stabilization process. Numerous studies (Lavin, 1992; Drbohlav and Stevenson, 1995; Miura *et al*., 1995) have shown that the rate of oxidative stabilization is affected by the temperature, the concentration of oxygen, and the chemical structure of the mesophase molecules. Most researchers agree that, during the initial stages of oxidative stabilization, the mesophase fiber gains weight; ketones, aldehydes, and carboxylic acids are formed; and water is given off (Drbohlav and Stevenson, 1995; Miura *et al*., 1995). At higher temperatures, the fiber begins to lose weight as CO_2 is evolved. However, the exact nature of the reactions that occur during the stabilization step is still the subject of active research. As in the PAN carbon fiber process, the objective is to uniformly crosslink the precursor fiber as fast as possible with a minimum addition of non-carbon elements. Currently, stabilization is the slowest step in the pitch-based carbon fiber process, taking from 30 minutes to over 2 hours for most mesophase precursors. Therefore, the search continues for new stabilization techniques and new mesophase structures that can be more readily crosslinked.

3.4 Carbonization of stabilized mesophase pitch-based fibers

Once stabilized, the pitch fiber is carbonized at 1,500–3,000 °C in an inert atmosphere (Rand, 1985; Edie, 1990). During this step most of the non-carbon elements within the fiber are volatilized in the form of methane, hydrogen, water, carbon monoxide, carbon dioxide, and various other gases. Because the mesophase precursor fiber is 90% carbon and it gains only 6–8 weight % of oxygen during stabilization, the yield of the pitch-based carbon fiber process ranges from 70% to 80% – considerably higher than that of the PAN-based process. However, the lower mass loss also means that, typically, a 12-micron-diameter precursor fiber must be spun if a 10 micron final diameter is desired. By comparison, a fully-drawn PAN precursor fiber with a diameter of 15 microns would yield the same size carbon fiber after carbonization. Needless to say, smaller as-spun diameters tend to increase processing costs.

Increasing the final heat treatment temperature improves the degree of preferred orientation within the fiber and, thus, the modulus of the pitch-based carbon fibers. As with PAN-based carbon fibers, the various grades of fiber available from a particular manufacturer often are produced by merely changing this temperature.

3.5 Structure of mesophase pitch-based carbon fibers

Ever since mesophase was first melt spun into fiber form, researchers have recognized that, when carbonized, mesophase fibers can develop remarkably high moduli (Barr *et al*., 1976; Singer, 1978; Bacon, 1979; and Otani, 1981). This is the direct result of the transverse microstructure and axial molecular orientation created as the liquid crystalline precursor flows through a capillary and then is extended during fiber formation. Unless relaxation occurs during thermosetting, this transverse microstructure and axial orientation is merely perfected during carbonization. The transverse texture of early commercial mesophase carbon fibers was either radial or flat-layer (see Fig. 2.9). Thus, in the transverse direction the graphene layer planes fan out from the center of the fiber, and in the axial direction the layer planes tend to align parallel to the fiber axis. As Bright and Singer (1979) first demonstrated, the transverse texture can affect fiber graphitizability. Although this early study did not reveal how fiber texture could be varied, a later patent (Nazem, 1984) disclosed that

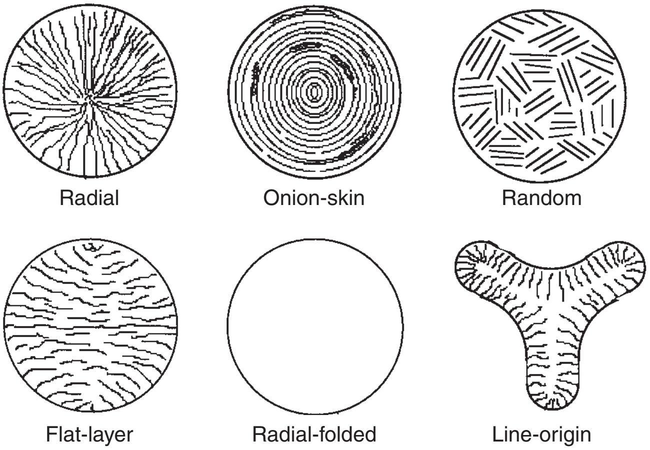

Figure 2.9 Transverse textures of mesophase pitch-based carbon fibers (Edie, 1990).

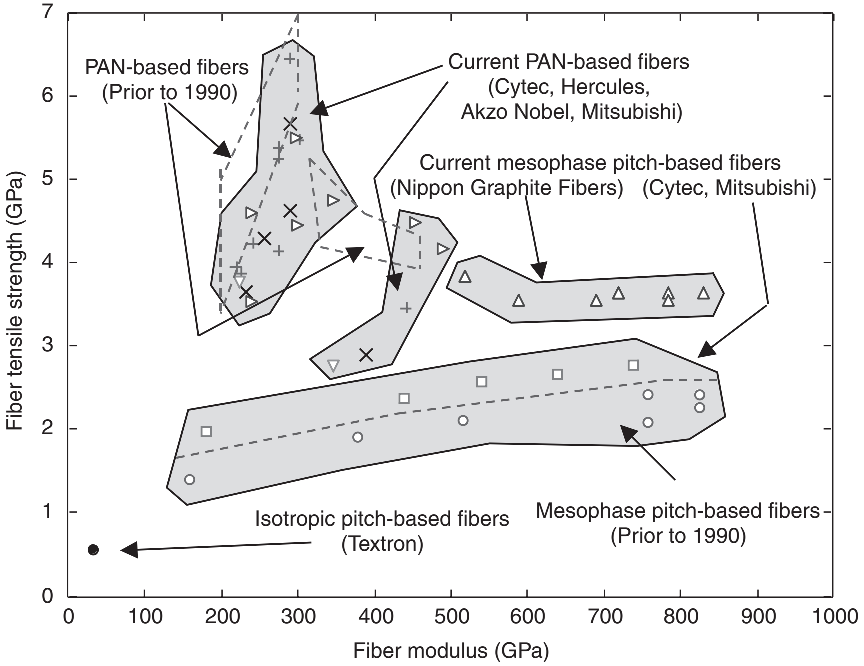

Figure 2.10 Mechanical properties of commercial PAN-based and mesophase pitch-based carbon fibers as of 1989 compared to the properties of current commercial PAN-based and pitch-based fibers (adapted from Edie, 1998). (See Color Plate I.)

fibers with random transverse textures could be produced by disrupting the flow during extrusion.

These initial mesophase-pitch-based carbon fibers with radial and flat-layer transverse textures readily developed three-dimensional crystallinity (see Fig. 2.9). Although this structure made pitch-based carbon fibers more flaw sensitive than PAN-based fibers with their more random, fibril structure, it gave them superior lattice-dependent properties. As Fig. 2.10 shows, prior to 1990, PAN-based carbon fibers were characteristically high strength but low modulus, whereas pitch-based carbon fibers were high modulus but low strength.

4 New developments

Obviously, structure controls the properties of the final carbon fiber (either PAN-based or pitch-based). In this chapter, I have tried to demonstrate that the carbon fiber structure can be controlled by changing the chemistry of the precursor, by controlling the development of structure as the precursor fiber is formed, or by modifying the conditions used to heat treat the precursor fiber. Over the past 10 years pitch-based carbon fiber researchers have focused on these first two factors, and their efforts are beginning to yield results. As Fig. 2.10 shows, new pitch-based fibers are now being introduced with strengths approaching those of PAN-based fibers. Also, new pitch-based fibers with extremely low electrical resistivities (and, thus, high thermal conductivities) are also being introduced for thermal management applications. These improved mechanical and thermal properties appear to be the result of optimizing the transverse textures for a given property and utilizing improved mesophase precursors.

4.1 Control of structure

Several years ago Japanese and US researchers showed that the texture of mesophase fibers was created, and thus could be controlled, during melt spinning (Matsumoto, 1985; Edie *et al*., 1986; and Hamada *et al*., 1987). Hamada *et al*. (1987) changed transverse structure by disrupting the flow profile prior to extrusion, whereas Matsumoto (1985) and Edie *et al*. (1986) used extrusion capillaries with either non-uniform, or non-circular cross sections. Since that time numerous researchers have demonstrated that flow during extrusion can be controlled to create mesophase fibers with a variety of textures, each with certain advantages. Mesophase fibers with random or radial-folded textures tend to exhibit higher tensile and compressive properties (Johnson, 1990; Edie and Stoner, 1993). By comparison, fibers with linear transverse textures appear to develop better lattice-dependent properties, e.g. thermal conductivity (Bright and Singer, 1979; Edie *et al*., 1994).

4.2 Modeling the development of structure

While viscous effects control the rate and distribution of flow during extrusion, elastic effects appear to control the development of structure prior to and during extrusion. Recent research (McHugh and Edie, 1995; Rey, 1995; McHugh and Edie, 1996; Wang and Rey, 1997) shows that continuum theories (such as Leslie–Ericksen's), first developed for rod-like liquid crystals, can be extended to predict the development of structure during the melt spinning of mesophase. Edie and McHugh showed that the mesophase structure observed as mesophase passes through circular capillaries (as well as the transverse texture of

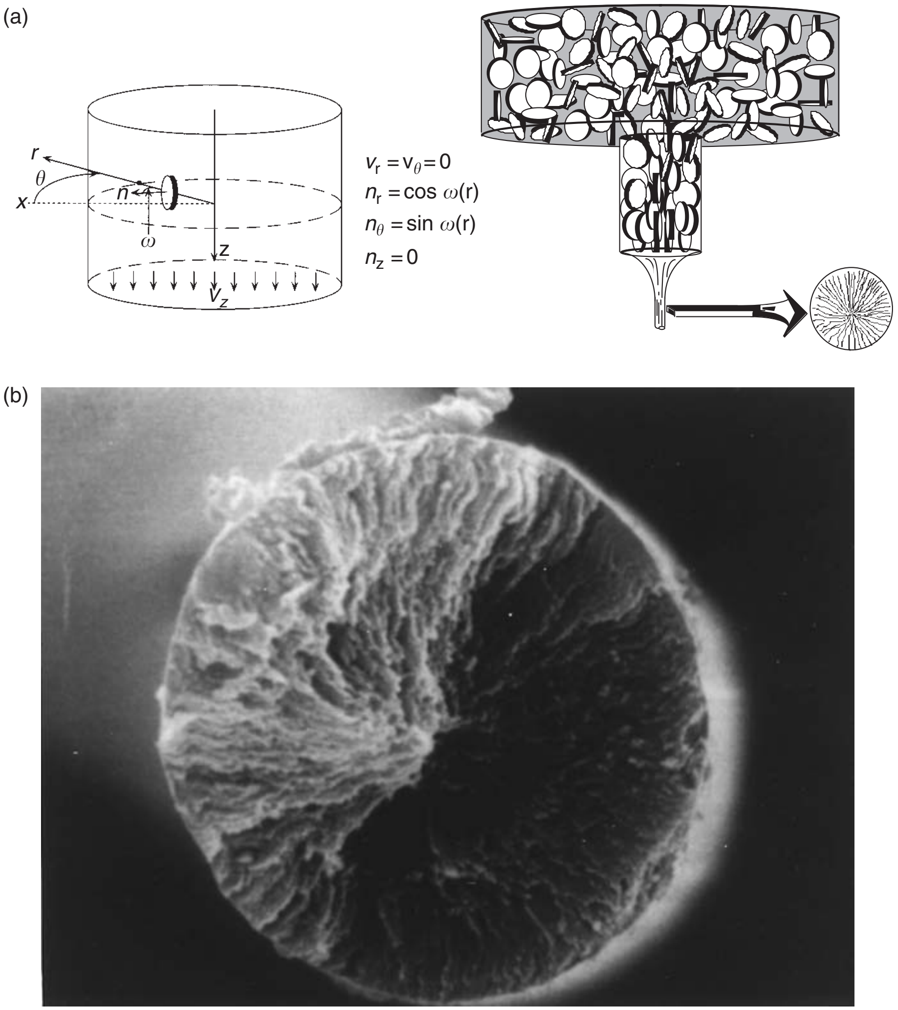

Figure 2.11 Predicted transverse molecular orientation for mesophase pitch flowing through a circular capillary and transverse texture of carbonized mesophase fiber extruded from a circular capillary: (a) predicted transverse molecular orientation and (b) transverse texture of carbonized fiber (McHugh and Edie, 1996).

carbonized fibers) matches that predicted by liquid crystal theory (see Fig. 2.11). Wang and Rey (1997) have shown that both the radial and the onion-skin structure occur naturally (either during flow or in a stagnant fluid). Apparently the stable form depends on the relative size of the elastic constants for bend and splay (see Fig. 2.12). Rey would predict that high temperatures would favor the formation of onion-skin textures, low temperatures would favor radial textures, and random textures would occur at intermediate temperatures.

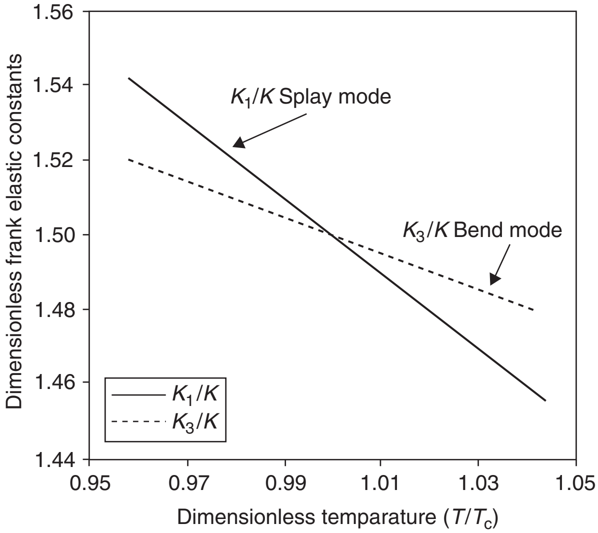

Figure 2.12 Temperature variation in elastic constants for splay, K_1, and bend, K_3 (Rey, 1995). The temperature is scaled by the transitional temperature T_c at which $K_1 = K_3$, and the scaling constant for the Frank elastic constants is K, the cross-over value of K_1 and K_3.

McHugh found that this same liquid crystal theory correctly modeled the development of molecular orientation as mesophase was extruded through rectangular capillaries (see Fig. 2.13) and correctly predicted that converging flow prior to extrusion would linearize the transverse structure of a mesophase fiber. Recent results by Robinson and Edie (1996) prove this to be true. Converging flow prior to extrusion not only linearizes the transverse texture of the fiber (see Fig. 2.14), but it also dramatically improves the thermal properties of the fiber.

Based on these studies, it would appear that the texture of pitch fibers now can be predicted. However, Robinson and Edie (1996) and Mochida *et al.* (1996) have shown that, although this texture represents the gross structure, the microtexture (as the high resolution SEM photo in Fig. 2.15 shows) contains irregular kinks and bends. Oberlin and coworkers have even proposed that mesophase pitch is actually a gel, and that deformation of this gel during fiber formation creates this complex microstructure (Lafdi *et al.*, 1992a–c). Fathollahi and White (1994) contend that this complex substructure is the result of disclinations that are deformed during extrusion and fiber formation. This argument would be consistent with liquid crystal theory. In fact, as Fig. 2.16 shows, Fleurot and Edie (1997) have now demonstrated that the liquid crystal theory of Marruchi successfully predicts the deformation of this disclination structure during the extrusion of mesophase pitch precursors. Thus, in some ways, Fleurot and Edie are using classical liquid terminology to explain observations such as those reported by Oberlin and coworkers. Fleurot and Edie (1997) have already developed "visual" computer models, based on first principles, which can even simulate vortices which can develop prior to flow through the spinneret capillary (see Fig. 2.17).

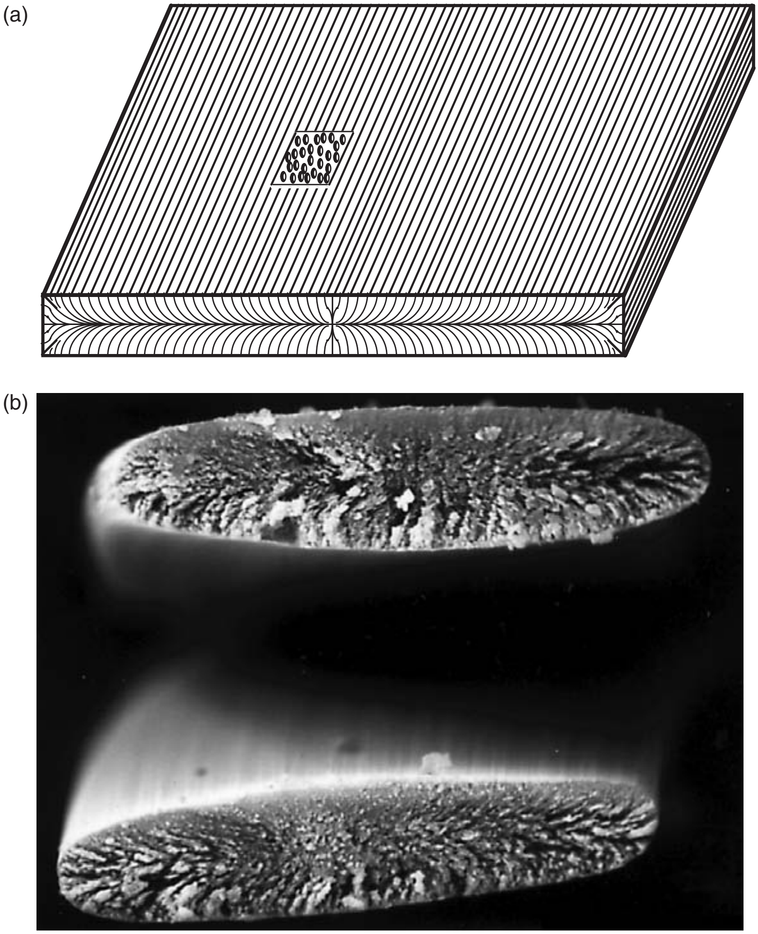

Figure 2.13 Predicted transverse molecular orientation for mesophase pitch flowing through a rectangular capillary and transverse texture of carbonized mesophase fiber extruded from a rectangular capillary: (a) predicted molecular orientation during flow through rectangular capillary and (b) transverse texture of carbonized fiber extruded from a rectangular capillary.

The next objective is to include the development of this substructure, generated by the deformation of the mesophase disclinations.

Although mesophase pitch-based carbon fibers are a newer product than PAN-based carbon fibers, researchers are beginning to develop a far better understanding of how to predict and control their structure. The primary reason for this advance is that, while most PAN-based fiber research has focused on heat treatment, most mesophase pitch-based fiber research has concentrated on precursor chemistry and fiber formation. Once perfected, the ability to predict the development of structure during fiber formation could lead to mesophase-pitch-based carbon fibers with properties engineered for specific applications.

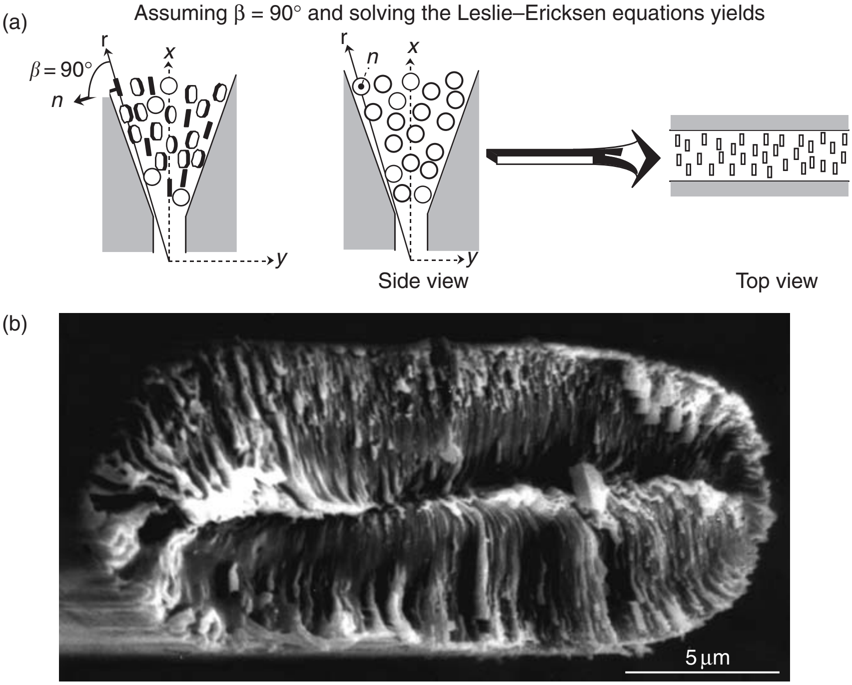

Figure 2.14 Predicted effect of converging flow prior to extrusion through rectangular capillary and transverse texture of carbonized mesophase fiber extruded from a rectangular capillary with a converged entry region: (a) Predicted effect of converging flow on randomly oriented discotic molecules and (b) transverse texture of fiber extruded from rectangular capillary with converging entry.

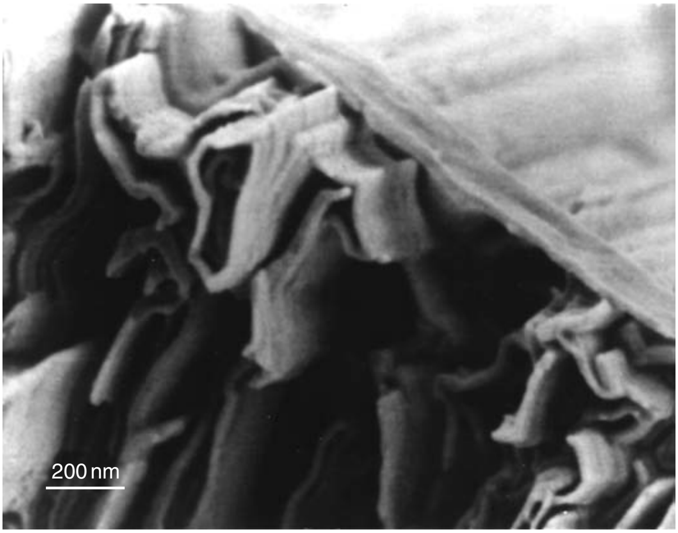

Figure 2.15 High resolution SEM image of near-surface in a mesophase-pitch-based carbon fiber (Robinson and Edie, 1996).

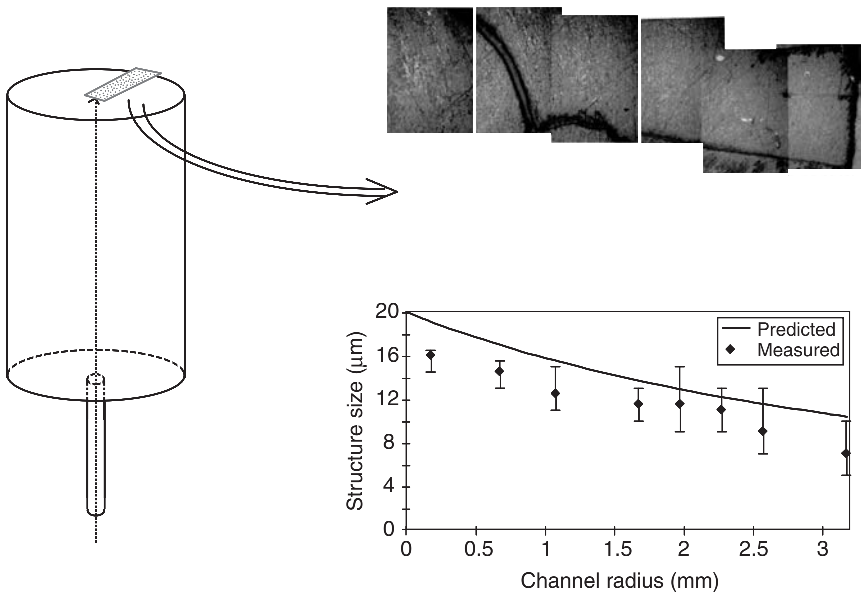

Figure 2.16 Predicted and observed microstructure during flow of AR mesophase through entry region of capillary ($\gamma_{\mathrm{w}} = 3\ \mathrm{s}^{-1}$) (Fleurot and Edie, 1997). (See Color Plate II.)

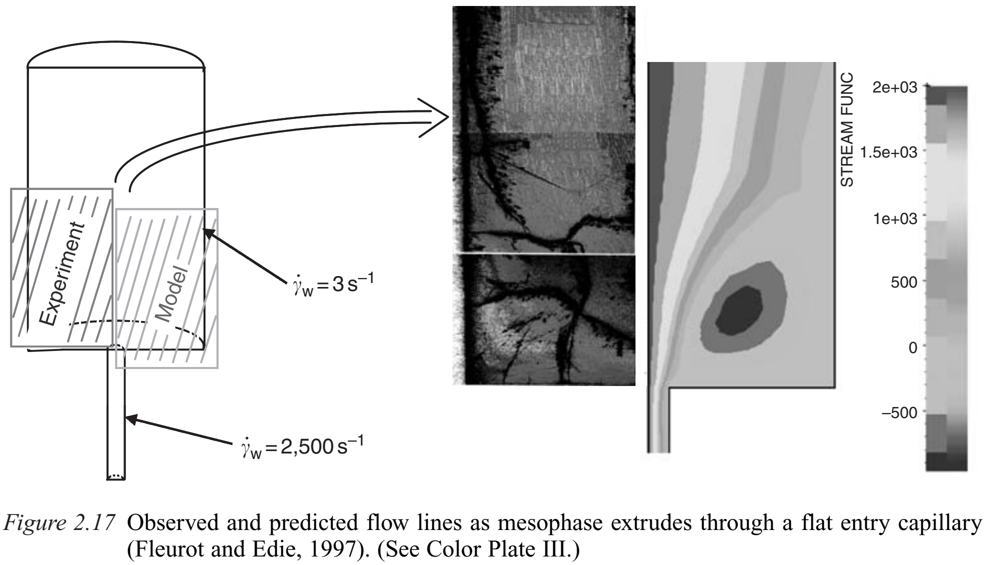

Figure 2.17 Observed and predicted flow lines as mesophase extrudes through a flat entry capillary (Fleurot and Edie, 1997). (See Color Plate III.)

This approach represents the future of materials processing, and it could revolutionize carbon fiber manufacturing.

5 Summary

As Fig. 2.10 indicates, current commercial PAN-based carbon fibers exhibit higher tensile strengths, but lower moduli, than do mesophase-pitch-based carbon fibers. This balance of properties is a direct result of the as-spun structure of the two precursor fibers.

The fibrillar texture of the PAN precursor inhibits the development of graphitic structure during carbonization, making these fibers less flaw-sensitive. By comparison, liquid crystalline mesophase can produce a precursor with an extremely high degree of molecular orientation parallel to the fiber axis. The transverse structure can be disrupted during extrusion to decrease graphitizability and improve strength, or it can be linearized to increase graphitizability and enhance thermal conductivity.

Although it is likely that PAN-based fibers will continue to dominate strength-based applications for the next several years, thermal management applications are likely to create a large market ideally suited for mesophase pitch fibers. Researchers are just beginning to understand how to control mesophase structure during fiber formation and optimize final fiber properties. In the future, this knowledge could lead to pitch-based carbon fibers with mechanical properties equal to or greater than those of PAN-based fibers. However, new low-cost production techniques also must be developed if pitch-based carbon fiber manufacturers hope to compete with PAN-based fibers in strength-related applications.

Acknowledgments

This work was supported in part by the ERC program of the National Science Foundation under Award Number EEC-9731680. Thanks are also due to Elsevier Science Ltd. for permission to publish this chapter, which is based on an article the author published in the journal *Carbon*. The advice and helpful interaction of industrial colleagues at BP Amoco, in particular Drs Roger Bacon, Girish Deshpande, and Chris Levan, is gratefully acknowledged. I would like to thank Dr Rosa Menendez and Professors Erich Fitzer, Brian Rand, Carlos Bernardo, Isao Mochida, Charles Fain, and Mark Thies. Their advice, comments, and ideas have been invaluable. Finally, I would like to thank my current and former graduate students for their dedication, their creativity, and their hard work.

References

Azami, K., Yamamoto, S., Yokono, T., and Sanada, Y. (1991) In-situ monitoring for mesophase formation processes of various pitches by means of high-temperature ^{13}C-NMR, *Carbon*, **29**, 943–947.

Bacon, R. (1979) Carbon fibres from mesophase pitch, *Phil. Trans. Roy. Soc. London Ser. A.*, **294**, 437–442.

Barr, J. B., Chwastiak, S., Didchenko, R., Lewis, I. C., Lewis, R. T., and Singer, L. S. (1976) High modulus carbon fibers from pitch precursor, *Journal of Applied Polymer Science Appl. Polymer Symp.*, **29**, ed. J. Economy, Wiley, New York, 161–173.

Bashir, Z. (1991) A critical review of the stabilisation of polyacrylonitrile, *Carbon*, **29**, 1081–1090.

Bolaños, G. and Thies, M. C. (1996) Supercritical toluene-petroleum pitch mixtures: liquid–liquid equilibria and SAFT modeling, *Fluid Phase Equilibria*, **117**, 273–280.

Bright, A. A. and Singer, L. S. (1979) The electronic and structural characteristics of carbon fibers from mesophase pitch, *Carbon*, **17**, 59–69.

Brooks, J. D. and Taylor, G. H. (1968) The formation of some graphitizing carbons, *Chemistry and Physics of Carbon*, Vol. 4, ed. P. L. Walker, Jr., Dekker, New York, 243–286.

Capone, G. J. (1995) Wet-spinning technology, *Acrylic Fiber Technology and Applications*, ed. J. C. Masson, Marcel Dekker, Inc., New York, 69–103.

Chen, S. S., Herms, J., Peebles, L. H., and Uhlmann, D. R. (1981) Oxidative stabilization of acrylic fibres, *J. Mater. Sci.* **16**, 1490–1510.

Chwastiak, S. (1980) Low molecular weight mesophase pitch, U.S. Patent 4,209,500.

Colman, M. M., Sivy, G. T., Painter, P. C., Snyder, R. W., and Gordon, B. (1983) Studies of the degradation of acrylonitrile/acrylonitrile copolymers as a function of composition and temperature, *Carbon*, **21**, 255–267.

Diefendorf, R. J. and Riggs, D. M. (1980) Forming optically anisotropic pitches, US Patent 4,208,267.

Diefendorf, R. J. and Tokarsky, E. (1975) High performance carbon fibers, *Poly. Eng. Sci.*, **15** (3), 150–159.

Dobb, M. G., Guo, H., Johnson, D. J., and Park, C. R. (1995) Structure-compressional property relations in carbon fibers, *Carbon*, **33**, 1553–1559.

Drbohlav, J. and Stevenson, W. T. K. (1995) The oxidative stabilization and carbonization of a synthetic mesophase pitch, Part I: The oxidative stabilization process, *Carbon*, **33** (5), 693–711.

Edie, D. D. (1990) Pitch and mesophase fibers, *Carbon Fibers Filaments and Composites*, eds J. L. Figueiredo, C. A. Bernardo, R. T. K. Baker, and K. J. Hüttinger, Kluwer Academic Publishers, Dordrecht, The Netherlands, pp. 43–72.

Edie, D. D. and Diefendorf, R. J. (1993) Carbon fiber manufacturing, *Carbon-Carbon Materials and Composites*, eds J. D. Buckley and D. D. Edie, Noyes Publications, Park Ridge, New Jersey, 19–37.

Edie, D. D. and Dunham, M. J. (1989) Melt spinning pitch-based carbon fibers, *Carbon*, **27** (5), 647–655.

Edie, D. D. and Stoner, E. G. (1993) The effect of microstructure and shape on carbon fiber properties, *Carbon–Carbon Materials and Composites*, eds J. D. Buckley and D. D. Edie, Noyes Publications, Park Ridge, New Jersey, 41–70.

Edie, D. D., Fox, N. K., Barnett, B. C., and Fain, C. C. (1986) Melt spun non-circular carbon fibers, *Carbon*, **24** (4), 477–482.

Edie, D. D., Robinson, K. E., Fleurot, O., Jones, S. P., and Fain, C. C. (1994) High thermal conductivity ribbon fibers from naphthalene-based mesophase, *Carbon*, **32** (6), 1045–1054.

Ehrburger, P. and Donnet, J. B. (1983) Carbon and graphite fibers, *Handbook of Fiber Science and Technology: Volume III, High Technology Fibers*, eds M. Lewin and J. Preston, Marcel Dekker Inc., New York, 169–220.

Endo, M. (1988) Structure of mesophase pitch carbon fibers, *J. Mater. Sci.*, **23** (2), 598–605.

Fathollahi, B. and White, J. L. (1994) Flow-induced microstructures in the spinning of carbonaceous mesophase, a discotic nematic liquid crystal, *J. Rheology*, **38** (5), 1591–1607.

Fitzer, E. (1989a) Carbon fibers – present state and future expectations, *Carbon Fibers Filaments and Composites*, eds J. L. Figueiredo, C. A. Bernardo, R. T. K. Baker, and K. J. Hüttinger, Springer-Verlag, New York, 3–41.

Fitzer, E. (1989b) PAN-based carbon fibers – present state and trend of the technology from the viewpoint of possibilities and limits to influence and to control the fiber properties by the process parameters, *Carbon*, **27** (5), 621–645.

Fitzer, E. and Frohs, W. (Sept. 18–23, 1988) The influence of carbonization and post treatment conditions on the properties of PAN-based carbon fibers, *Carbon ’88*, Proceedings of the International Carbon Conference, Newcastle upon Tyne, United Kingdom, 298–300.

Fitzer, E. and Müller, D. J. (1972) Reaktionstechnische Betrachtung der kontinuierlichen Herstellung von Kolenstoff-Fasern aus Polyacrylnitril, *Chemiker-Zeitung*, **96** (1–2), 20–26.

Fitzer, E., Heine, M., and Metzler, W. (June 30–July 4, 1986) Gaseous products during heat treatment of polyacrylonitrile, *Carbon ’86*, Proceedings of Fourth International Carbon Conference, Baden-Baden, Germany, 853–855.

Fitzgerald, J. D., Pennock, G. M., and Taylor, G. H. (1991) Domain structure in MP (mesophase pitch)-based fibres, *Carbon*, **29** (2), 139–164.

Fleurot, O. and Edie, D. D. (July 13–18, 1997) Modeling of structural development during flow of mesophase pitch through capillaries, *Carbon '97*, Extended Abstracts of the 23rd Biennial Conference on Carbon, Penn State University, 416–417.

Guigon, M., Oberlin, A. and Desarmot, G. (1984) Microstructure and structure of some high tensile strength PAN-based carbon fibres, *Fibre Sci. Technol.*, **20**, 55–72.

Gupta, A. and Harrison, I. R. (1996) New aspects in the oxidation stabilization of PAN-based carbon fibers, *Carbon*, **34**, 1427–1445.

Grassie, N. and Hay, J. (1962) Thermal coloration and insolubilization of polyacrylonitrile, *J. Poly. Sci.*, **56**, 189–202.

Hamada, T., Nishida, T., Sajiki, Y., Matsumoto, M., and Endo, M. (1987) Structure and physical properties of carbon fibers from coal tar pitch, *J. Mater. Res.*, **2**, 850–857.

Huang, Y. and Young, R. J. (1995) Effect of fibre microstructure upon the modulus of PAN- and pitch-based carbon fibers, *Carbon*, **33** (2), 97–107.

Hutchenson, K. W., Roebers, J. R., and Thies, M. C. (1991) Fractionation of petroleum pitch by supercritical fluid extraction, *Carbon*, **29**, 215–223.

Johnson, D. J. (1987) Structure property relationships in carbon fibers, *J. Phys. D: Appl. Phys.*, **20** (3), 287–291.

Johnson, D. J. (1990) Structure and properties of carbon fibres, *Carbon Fibers Filaments and Composites*, eds J. L. Figueiredo, C. A. Bernardo, R. T. K. Baker, and K. J. Hüttinger, Kluwer Academic Publishers, Dordrecht, The Netherlands, 119–146.

Knudsen, J. P. (1963) The influence of coagulation variables on the structure and physical properties of an acrylic fiber. *Textile Research Journal*, **33**, 13–20.

Korai, Y. and Mochida, I. (1992) Molecular assembly of mesophase and isotropic pitches at their fused states, *Carbon*, **30** (7), 1019–1024.

Lafdi, K., Bonnamy, S., and Oberlin, A. (1992a) Anisotropic pitch-based carbon fibers – carbonization and graphitization (radial-with-wedge I1 and radial I2 types), *Carbon*, **30** (4), 533–549.

Lafdi, K., Bonnamy, S., and Oberlin, A. (1992b) Mechanism of formation of the texture and microtexture in as-spun then oxidized anisotropic pitch-based carbon fibers – part I: radial with wedge type I1), *Carbon*, **30** (4), 551–567.

Lafdi, K., Bonnamy, S. and Oberlin, A. (1992c) Mechanism of formation of the texture and microtexture in as-spun then oxidized anisotropic pitch-based carbon fibers – part II: radial I2 types, *Carbon*, **30** (4), 569–575.

Lavin, J. G. (1992) Chemical reactions in the stabilization of mesophase pitch-based carbon fiber, *Carbon*, **30** (3), 351–357.

Lewis, I. C. (1977) Process for producing fibers from mesophase pitch. US Patent 4,032,430.

McHugh, J. J. and Edie, D. D. (1995) Orientation of mesophase pitch in capillary and channel flow, *Liquid Crystals*, **18** (2), 327–335.

McHugh, J. J. and Edie, D. D. (1996) The orientation of mesophase pitch during fully developed channel flow, *Carbon*, **34** (11), 1315–1322.

Marsh, H. and Cornford, C. (1976) Mesophase: the precursor to graphitizable carbon, *Petroleum Derived Carbons*, eds M. L. Deviney and T. M. O'Grady, ACS Symp. Ser. 21, Amer. Chem. Soc., 266–281.

Matsumoto, T. (1985) Mesophase pitch and its carbon fibers, *Pure & Appl. Chem.*, **57** (11), 1553–1562.

Miura, K., Nakagawa, H., and Hashimoto, K. (1995) Examination of the oxidative stabilization reaction of the pitch-based carbon fiber through continuous measurement of oxygen chemisorption and gas formation rate, *Carbon*, **33** (3), 275–282.

Mochida, I., Shimizu, K., Korai, Y., Sakai, Y., Fuhiyama, S., Toshima H., and Hono, T. (1992) Mesophase pitch catalytically prepared from anthracene with HF/BF_3, *Carbon*, **30** (1), 55–61.

Mochida, I., Yoon, S. H., Takano, N., Fortin, F., Korai, Y., and Yokagawa, K. (1996) Microstructure of mesophase pitch-based carbon fiber and its control, *Carbon*, **34** (8), 941–956.

Nazem, F. (Nov. 1984) Apparatus for controlling the cross-sectional structure of mesophase pitch derived fibers. US Patent 4,480,977.

Otani, S. (1981) Carbonaceous mesophase and carbon fibers, *Mol. Cryst. Liq. Cryst.*, **63**, 249–264.

Ram, M. J. and Riggs, J. P. (April 1972) Process for production of acrylic filaments. US Patent 3,657,409.

Rand, B. (1985) Carbon fibres from mesophase pitch, *Handbook of Composites, Volume 1: Strong Fibres*, eds W. Watt and B. V. Perov, Elsevier Science Publishers, Amsterdam, 495–576.

Rey, A. D. (1995) Elasticity-driven texture selection mechanism in mesophase carbon fibers, *Phys. Rev. E.*, **51**, 6278–6281.

Riggs, D. M., Shuford, R. J., and Lewis, R. W. (1982) Graphite fibers and composites, *Handbook of Composites*, eds G. Lubin and Van Nostrand Reinhold, New York, 196–271.

Robinson, K. E. and Edie, D. D. (1996) Microstructure and texture of pitch-based ribbon fibers for thermal management, *Carbon*, **34** (1), 13–36.

Singer, L. S. (1977) High modulus high strength fibers produced from mesophase pitch. US Patent 4,005,183.

Singer, L. S. (1978) The mesophase and high modulus carbon fibers from pitch, *Carbon*, **16**, 409–415.

Thorne, D. J. (1985) Manufacture of carbon fibre, *Handbook of Composites, Vol. 1 – Strong Fibres*, eds W. Watt and B. V. Perov, 475–493.

Wang, L. and Rey, A. D. (1997) Pattern selection mechanism in mesophase carbon fibers, *Modelling Simul. Mater. Sci. Eng.*, **5**, 67–77.

White, J. L. and Zimmer, J. E. (1976) Disclination structures in carbonaceous mesophase and graphite, *Surface and Defect Properties of Solids*, Vol. 5, eds M. W. Roberts and J. M. Thomas, Chem Soc., London, 16–35.

Yoon, S. H., Korai, Y., Mochida, I. and Kato, I. (1994) The flow properties of mesophase pitches and derived from methylnaphthalene and naphthalene in the temperature range of their spinning, *Carbon*, **32**, 273–280.

Ziabicki, A. (1976) *Fundamentals of Fibre Formation*, John Wiley and Sons, London.

Zimmer, J. E. and White, J. L. (1977) Disclinations in the carboneaceous mesophase, *Mol. Cryst. Liq. Cryst.*, **38**, 177–193.

Zimmer, J. E. and White, J. L. (1982) Disclination structures in carbonaceous mesophase, *Advances in Liquid Crystals*, Vol. 5, ed. H. G. Brown, Academic Press, New York, 157–213.

3

ELECTRONIC AND THERMAL PROPERTIES OF CARBON FIBERS

J.-P. Issi

1 Introduction

Despite the great deal of attention that carbon nanotubes (CN), the "ultimate" carbon fibers, is attracting because of their fascinating scientific aspects, the physical properties of the macroscopic version of carbon fibers remain a topic of great interest. Transport properties are no exception, since the various structures of carbon fibers and their particular geometry, have lead to interesting observations, which could not be made on bulk carbons and graphites. To this should be added the practical aspects since carbon fibers find unique applications, particularly in the form of composites. Also, as is the case for the bulk material, some carbon fibers may be intercalated with various species leading to a significant modification of their physical properties.

Because of their large length to cross section ratio, DC electrical resistivity measurements are relatively easy to perform on fibrous materials, in contrast to the case of bulk graphites (see Section 2). This allowed to separate the electronic and lattice contributions to the thermal conductivity using the Wiedemann–Franz law (Section 4). It also made possible high resolution electrical resistivity measurements leading to the discovery of quantum transport effects on intercalated (Piraux *et al.*, 1985) and pristine fibers (Bayot *et al.*, 1989). Also carbon fiber-based composites exploit their unique mechanical and thermal properties for which they find applications as light mechanical systems and heat transfer devices.

Transport properties have been reported for all varieties of carbon fibers including single wall (SWNT) and multiwall (MWNT) carbon nanotubes. Among macroscopic fibers, vapor grown carbon fibers (VGCF) are the most adequate for basic studies. They have the highest structural perfection when heat treated at high temperature. In that case, their transport properties are much like those observed for highly oriented pyrolytic graphite (HOPG). They display the highest electrical and thermal conductivities with respect to other carbon fibers. Also, they may be intercalated with donor and acceptor species which results in higher electrical conductivities, as is the case for HOPG. Similarly, their thermal conductivity and thermoelectric power are notably modified by intercalation.

The transport properties of carbon fibers are governed by the in-plane coherence length which mainly depends on the heat treatment temperature (cfr. e.g. Dresselhaus *et al.*, 1988; Issi and Nysten, 1998). Some commercial pitch-derived carbon fibers (PDF) heat treated at high temperature have low electrical resistivities and thermal conductivities close to 1,000 $Wm^{-1}K^{-1}$, which largely exceeds that of copper. These high thermal conductivities associated to the fact that they may be obtained in a continuous form make them the ideal candidates for thermal management applications (Allen and Issi, 1985).

PAN-based fibers (PAN) are also continuous fibers, but they are generally disordered and their conductivity levels are rather low. One exception is the Celanese GY70, which exhibits a room temperature thermal conductivity of almost 200 $\mathrm{Wm^{-1}K^{-1}}$ when it is heat treated at very high temperature (Nysten *et al.*, 1987).

Some carbon nanotubes may have electrical conductivities comparable to VGCF heat treated at high temperature (Issi and Charlier, 1999). The thermal conductivity has not been measured on a single CN, but one may expect for such materials very high values associated to their unique mechanical properties.

VGCF's heat treated at high temperature are semimetallic with very few charge carriers as compared to metals. Also, like HOPG, they have generally more than one type of charge carriers, which complicates the analysis of electronic transport properties data. Owing to the small density of charge carriers, associated with a relatively large lattice in-plane thermal conductivity, heat is almost exclusively carried by the lattice vibrations above the liquid helium temperature range.

Because of the favorable length to cross section ratios (Chieu *et al.*, 1982; Issi, 1992), four-probe electrical DC measurements may be readily performed on intercalated fibers contrary to the case of the bulk material. High resolution electrical resistivity measurements have thus been performed on graphite fibers allowing the investigation of weak localization effects and the separation of the ideal resistivity from the residual resistivity in spite of their very low residual resistivity ratio (RRR) – the ratio of the resistance at 300 K to that at 4.2 K (Piraux *et al.*, 1986a,b).

A few comprehensive reviews have been recently published on the transport properties of pristine and intercalated carbon fibers (Dresselhaus *et al.*, 1988; Issi, 1992; Issi and Nysten, 1998). We shall refer to them when necessary for more detailed information.

In chapter 3, volume 1 of this series, to which we shall refer hereafter as I, we have discussed the basic aspects of the transport properties of carbons and graphites (Issi, 2000). We have pointed out in I that there were no qualitative differences between the basic transport phenomena in bulk and fibrous materials. So, we will mainly concentrate here on the specific aspects related to fibers which were not discussed in detail in I. These are essentially due to their geometry and their very small cross sections. We will also discuss in some detail the thermal conductivity of fibers, since it was not presented in I. We will refer, when necessary, to the basic concepts developed in I. Thus, in this chapter emphasis will be placed on:

- the thermal conductivity of pristine fibers;
- the effect of intercalation on the transport properties;
- the thermal and, to a lesser extent, the electrical conductivity of composites;
- the experimental difficulties associated to measurements on fibrous materials.

The chapter is organized as follows. First, we shall point out some experimental aspects specific to fibrous materials, including CNs (Section 2). Then we shall discuss the electrical conductivity (Section 3) the thermal conductivity (Section 4) and the thermoelectric power (Section 5) of various types of pristine carbon fibers. The effect of intercalation on these transport properties will be discussed in Section 6. Then, after briefly showing how transport measurements may be used to characterize carbon fibers (Section 7), we will consider the situation for carbon fiber composites (Section 8).

2 Experimental challenges

There are some specific problems associated to the measurement of the transport properties on fibrous materials which are not encountered in bulk materials. It is obvious that this should be the case for measurements on individual nanotubes where samples are of submicronic sizes and are quite difficult to handle. For other reasons (cfr. below), it also applies for the measurement of the thermal conductivity on carbon fibers.

For fibers with diameters around 10 μm, electrical resistivity, magnetoresistance, and thermoelectric power measurements do not generally present serious problems. The problems encountered in the case of *electrical resistivity* measurements are due to the nature of the samples. Indeed, the diameters of the fibers are not the same along a given filament and from one filament to another of the same batch. Also, the cross sections of the samples are not always cylindrical. This makes it difficult to calculate the conductivity (or resistivity) from the measured resistance. So, the determination of the fiber cross section introduces large uncertainties in the estimation of the absolute values of the resistivities or conductivities. Since electrical parameters such as electrical current and voltage, may be measured with great accuracy, the data obtained are more accurate with regard to temperature variation than with regard to absolute magnitudes. Fortunately, for the interpretation of the experimental results it is more important to know the temperature variation than the absolute values. These problems are not met in magnetoresistance and thermoelectric power measurements since the knowledge of the samples cross sections is not needed to calculate these transport coefficients.

More generally speaking, it is a rather easy task to measure the electrical resistivity, except for extreme cases of very low or very high values. However, the measurement of samples of submicronic sizes requires a miniaturization of the experimental system, which may in some instances attain a high degree of sophistication. This is particularly true for the case of single CNs, where one has to deal with samples of a few nm diameter and about a μm length (Issi and Charlier, 1999). One has first to detect the sample, then apply to it electrical contacts, which means, in a four-probe measurement, four metallic conductors, two for the injected current and two for measuring the resulting voltage. This requires the use of nanolithographic techniques (Langer *et al*., 1994). Besides, one has to characterize the CN sample which electrical resistivity is measured in order to determine its diameter and helicity, which leads to the knowledge of the electronic structure.

Thermal conductivity is a very delicate measurement to perform on a single fiber and prohibitively difficult on a single CN. This explains why little attention had been paid to the thermal conductivity of carbon fibers until the beginning of the 1980s and while still no data are available on single CNs. More generally, thermal conductivity measurements are time consuming and very delicate to perform. This is particularily true for samples of small cross-sections, as it is the case for carbon fibers (Piraux *et al*., 1987). Indeed, since the fibers are usually of small diameters (~10^{-5} m) it is difficult to make sure that the heat losses in the measuring system do not by far exceed the thermal conductance of the samples measured. The thermal conductance is defined as the heat flow through the sample per unit temperature difference. One may measure a bundle of fibers to increase the thermal conductance with respect to heat losses, but it is not always possible to realize samples in the form of bundles. Moreover, in order to be able to get an insight into the mechanisms of the thermal conductivity of these fibers, it is necessary to measure the temperature variation of this property over a wide temperature range on a single well characterized fiber, as was done for VGCFs (Piraux *et al*., 1984).

In order to measure the temperature variation of the thermal conductivity of a single VGCF or a small bundle of continuous fibers one should use a sample holder specially designed to reduce significantly heat losses. This sample holder, which was designed for measuring samples with very small thermal conductances, is described in detail elsewhere (Piraux *et al.*, 1987). It is based on the principle of a thermal potentiometer, adapted to measure the thermal conductivity of brittle samples of very small cross-sections and low thermal conductances (10^{-6}–10^{-2} WK^{-1}) over a wide temperature range.

In some cases the fibrous geometry presents some advantages with respect to bulk carbons and graphites. In lamellar structures like that of graphites the electrical conductivity is highly anisotropic. This anisotropy is even higher in their acceptor intercalation compounds where it may exceed 10^6. In that case measuring the in-plane DC electrical resistivity on bulk samples presents a real problem, since one needs a sample of extremely large length to cross section ratio to insure that the electrical current lines be parallel. Fibers have very high length to cross section ratios and thus electrical resistivity measurements could easily be realized on them.

3 Electrical resistivity

We have introduced in I what we believe are the most important features pertaining to the electrical resistivity of carbons and graphites. We have insisted on the effect of the semimetallic band structure on the electronic behavior in general, and, more particularly, on electron scattering mechanisms in these materials. This applies also for VGCFs heat treated at high temperatures and to some CNs. We have also discussed in some length the effect of weak localization. Incidentally, the particular geometry and the defect structure of carbon fibers have allowed the observation of these *quantum transport effects* for the first time in carbons and graphites (Piraux *et al.*, 1985).

We have seen that the Boltzmann electrical conductivity for a given group of charge carriers is proportional to the charge carrier density and mobility. Concerning the scattering mechanisms, the main contributions to the electrical resistivity of metals, ρ, consists of an intrinsic temperature-sensitive ideal term, ρ_{i}, which is mainly due to electron–phonon interactions and an extrinsic temperature independent residual term, ρ_{r}, due to static lattice defects.

As is the case for any solid, the temperature dependence of the electrical resistivity of various classes of carbon-based materials is very sensitive to their lattice perfection. The higher the structural perfection, the lower the resistivity. Samples of high structural perfection exhibit room temperature resistivities below $10^{-4}\Omega\,\mathrm{cm}$, while partially carbonized samples exhibit resistivities higher than $10^{-2}\Omega\,\mathrm{cm}$ which generally increase with decreasing temperature. An intermediate behavior between these two extremes is represented by curves which depend less on the heat treatment temperature (HTT) and does not show significant temperature variations (cfr. I).

The first comprehensive measurements of the temperature dependence of the electrical resistivity of pitch-based carbon fibers were performed by Bright and Singer (1979). They investigated radial as well as random samples heat treated at various temperatures ranging from 1,000 to 3,000 °C. They have shown that the magnitude of the resistivity, as well as its temperature variation, depends on the heat treatment temperature. The same kind of observations were made for VGCFs.

In I we have presented the temperature dependence of the electrical resistivity of many carbon materials, including fibers. As an additional illustrative example we show in Fig. 3.1

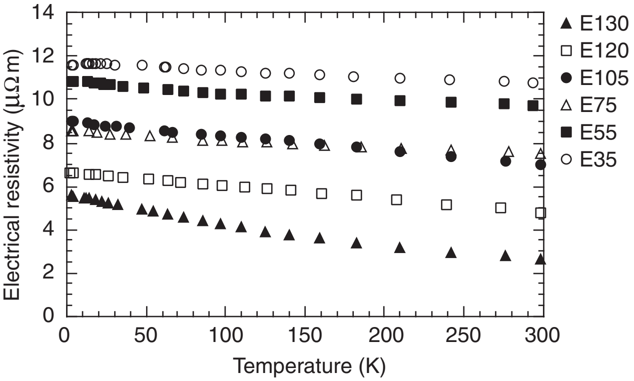

Figure 3.1 Temperature dependence, from 2 to 300 K, of the zero-field electrical resistivity of six samples of pitch-based carbon fibers heat treated at various temperatures (Nysten *et al.*, 1991a).

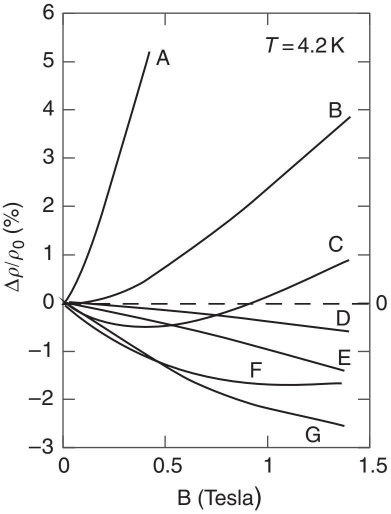

Figure 3.2 Transverse magnetoresistance for ex-mesophase pitch carbon fibers heat treated at different temperatures ranging from 1,700 (sample D) to 3,000 °C (samples ABCF). Samples A, B, C, and F, which were heat treated at the same temperature, exhibit different residual resistivities (measured at 4.2 K): 3.8, 5.1, 7.0, and $6.6 \times 10^{-4}\,\Omega\,\mathrm{cm}$ respectively. Samples G and E were heat treated at 2,500 and 2,000 °C, respectively (from Bright, 1979).

how this temperature dependence may vary with the heat treatment temperature, i.e. with crystalline perfection. In this figure the temperature dependence of the electrical resistivity of six samples of pitch-based carbon fibers heat treated at various temperatures are compared (Nysten *et al.*, 1991a). Except for the E35 fibers, the resistivies of all the samples investigated decrease with increasing temperature. This dependence was also observed on

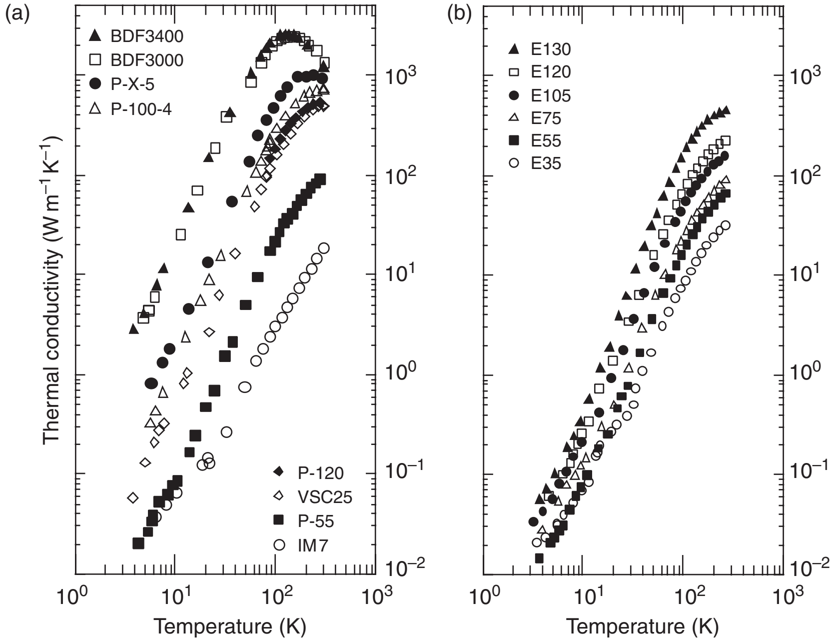

Figure 3.3 (a) Comparison of the temperature variation of the thermal conductivity of pristine carbon fibers of various origins. Since scattering below room temperature is mainly on the crystallite boundaries, the phonon mean free path at low temperatures, i.e. below the maximum of the thermal conductivity versus temperature curve is temperature insensitive and mainly determined by the crystallite size. The largest the crystallites the highest the thermal conductivity. Note that some VGCF and PDF of good crystalline perfection show a dielectric maximum below room temperature. For decreasing lattice perfection the maximum is shifted to higher temperatures (Issi and Nysten, 1998); (b) Temperature dependence of the thermal conductivity of the six samples of pitch-based carbon fibers heat treated at various temperatures, the same fibers with electrical resistivity is presented in Fig. 3.1 (Nysten *et al.*, 1991b).

other carbon fibers (Bayot *et al.*, 1989) and pyrocarbons (cfr. I, Figs 3.3 and 3.4). Such a behavior was explained in the frame of the weak localization theory (Bayot *et al.*, 1989).

As explained in I, weak localization generates an additional contribution to the low temperature electrical resistivity which adds to the classical Boltzmann resistivity. Indeed, in the weak disorder limit, which is also the condition for transport in the Boltzmann approximation, i.e. when $k_F.l \gg 1$, where k_F is the Fermi wave vector and l the mean free path of the charge carriers, a correction term, $\delta\sigma^{2D}$, is added to the Boltzmann classical electrical conductivity, $\sigma^{2D}{}_{\text{Boltz.}}$:

$$\sigma^{2D} = \sigma^{2D}{}_{\text{Boltz.}} + \delta\sigma^{2D} \qquad (1)$$

The additional term $\delta\sigma^{2D}$ accounts for localization and interaction effects which both predict a similar temperature variation (cfr. I).

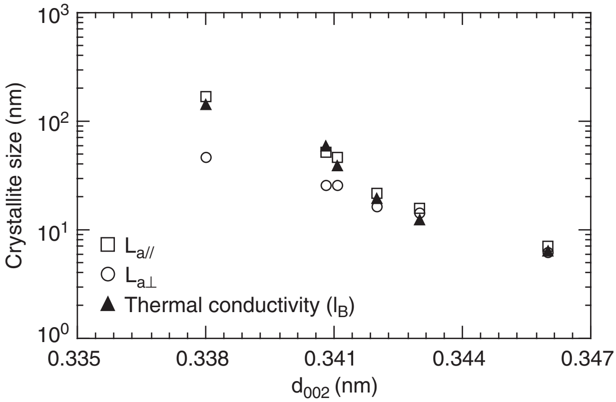

Figure 3.4 Dependence on the interlayer spacing d_{002} of the in-plane coherence lengths and the phonon mean free path for boundary scattering, l_B (Nysten *et al.*, 1991b).

A magnetic field destroys this extra contribution (Bayot *et al.*, 1989) and restores the classical temperature variation predicted by the standard two band model (Klein, 1964). This results in an apparent negative magnetoresistance.

We have briefly discussed in I the positive and negative magnetoresistances in carbons and graphites and the interpretation of the latter in terms of weak localization effects. The positive magnetoresistance at low magnetic fields depends essentially on the carrier mobilities. The *negative magnetoresistances*, which was first observed in pregraphitic carbons by Mrozowski and Chaberski (1956) and later on in other forms of carbons, is a decrease in resistivity with increasing magnetic field. This effect was also observed in PAN-based fibers (Robson *et al.*, 1972, 1973), pitch-derived fibers (Bright and Singer, 1979), and vapor-grown fibers (Endo *et al.*, 1982) and was interpreted later on in the frame of the weak localization theory for two dimensional systems (Bayot *et al.*, 1989).

We present in Fig. 3.2 the results obtained by Bright (1979) for the transverse magnetoresistance at 4.2 K for ex-mesophase pitch carbon fibers heat treated at different temperatures ranging from 1700 °C (sample D) to 3,000 °C (samples A, B, C, and F). It is worth noting that the four samples A, B, C, and F were all heat treated at the same temperature, but exhibited different residual resistivities (measured at 4.2 K); 3.8, 5.1, 7.0, and 6.6, $10^{-4}\Omega$ cm respectively. Higher residual resistivities correspond to higher disorder. Samples G and E were heat treated at 2,500 and 2,000 °C respectively.

It should be also noted that highly graphitized fibers, i.e. those heat treated at the highest temperatures, present large positive magnetoresistances, as expected from high mobility charge carriers. This explains why samples A and B which exhibit the lowest residual resistivities exhibit also large positive magnetoresistances, even at low magnetic fields. With increasing disorder, a negative magnetoresistance appears at low temperature, where the magnitude and the temperature range at which it shows up increase as the relative fraction of turbostratic planes increases in the material (Nysten *et al.*, 1991a).

The results obtained, which are presented in Fig. 3.2, were later confirmed by Bayot *et al.* (1989) and Nysten *et al.* (1991a), who found the same qualitative behavior on different samples of pitch-derived carbon fibers.

4 Thermal conductivity

4.1 Electron and phonon conduction

Around and below room temperature, heat conduction in solids is generated either by the charge carriers as is the case for pure metals or by the lattice waves, the phonons, which is the case for electrical insulators. In carbons and graphites, owing to the small densities of charge carriers, associated with a relatively large in-plane lattice thermal conductivity due to the strong covalent bonds, heat is almost exclusively carried by the phonons, except at very low temperatures, where both contributions may be observed. In that case, the total thermal conductivity is expressed:

$$\kappa = \kappa_E + \kappa_L \tag{2}$$

where κ_E is the electronic thermal conductivity due to the charge carriers and κ_L is the lattice thermal conductivity due to the phonons.

We will show in Section 6.6 that, because of their large length to cross section ratio, it is possible to separate κ_E and κ_L in carbon fibers, when they contribute by comparable amounts as it is the case at low temperature for pristine fibers and at various temperatures for the intercalated material.

In Fig. 3.3a we present the temperature variation of the thermal conductivity of pristine carbon fibers of various origins and precursors. In Fig. 3.3b we compare the temperature dependence of the thermal conductivity of the six samples of pitch-based carbon fibers heat treated at various temperatures (Nysten *et al.*, 1991b). These are the same set of fibers which electrical resistivity is presented in Fig. 3.1.

4.2 Lattice conduction

It was shown that the lattice thermal conductivity of carbon fibers is directly related to the the in-plane coherence length (Nysten *et al.*, 1991b; Issi and Nysten, 1998). Thus thermal conductivity measurements allow to determine this parameter. It also enables to compare between shear moduli (C_{44}) and provide information about point defects.

In Fig. 3.4, the dependence of the in-plane coherence lengths, L_a, and the phonon mean free paths for boundary scattering, l_B, on the interlayer spacing d_{002} is presented (Nysten *et al.*, 1991b). One may see that the phonon mean free path for boundary scattering is almost equal to the in-plane coherence length as determined by x-ray diffraction, L_a. Thermal conductivity measurements may thus be used as a tool to determine this parameter, especially for high L_a values where x-rays are inadequate. One may also observe that the concentration of point defects such as impurities or vacancies, decreases with increasing graphitization.

A naive way to understand how lattice conduction takes place in crystalline materials, is by considering the case of graphite in-plane, assuming that it is a two-dimensional (2D) system, which is not too far from the real situation around room temperature. The atoms in such a system may be represented by a 2D array of balls and springs and any vibration at one end of the system will be transmitted via the springs to the other end. Since the carbon atoms have small masses and the interatomic covalent forces are strong, one should expect a good transmission of the vibrational motion in such a system and thus a good lattice thermal conductivity. Any perturbation in the regular arrangement of the atoms, such as defects or atomic vibrations, will cause a perturbation in the heat flow, thus giving rise to scattering which decreases the thermal conductivity.

In order to discuss the lattice thermal conductivity results of isotropic materials, one generally uses the Debye relation:

$$\kappa_g = \frac{1}{3} C\, v\, l \tag{3}$$

where C is the lattice specific heat per unit volume, v is an average phonon velocity, the velocity of sound, and l the mean free path which is directly related to the phonon relaxation time, τ, through the relation $l = v\,\tau$. For a given solid, since the specific heat and the phonon velocities are the same for different samples, the sample thermal conductivity at a given temperature is directly proportional to the phonon mean free path.

VGCF's heat treated at 3,000 °C, may present room temperature heat conductivities exceeding 1,000 $\mathrm{W m^{-1} K^{-1}}$ (Fig. 3.3a). The thermal conductivity of less ordered fibers may vary widely, about two orders of magnitude, according to their microstructure (Issi and Nysten, 1998). At low temperature, the lattice thermal conductivity is mainly limited by phonon-boundary scattering and is directly related to the in-plane coherence length, L_a.

When scattering is mainly on the crystallite boundaries, the phonon mean free path should be temperature insensitive. Since the velocity of sound is almost temperature insensitive, the temperature dependence of the thermal conductivity should follow that of the specific heat. Thus, the largest the crystallites the highest the thermal conductivity. Well above the maximum, phonon scattering is due to an intrinsic mechanism: phonon–phonon umklapp processes, and the thermal conductivity should thus be the same for different samples.

Around the thermal conductivity maximum, scattering of phonons by point defects (small scale defects) is the dominating process. The position and the magnitude of the thermal conductivity maximum will thus depend on the competition between the various scattering processes (boundary, point defect, phonon, …). So, for different samples of the same material the position and magnitude of the maximum will depend on the point defects and L_a, since phonon–phonon interactions are assumed to be the same. This explains why, by measuring the low temperature thermal conductivity, one may gather information about the in-plane coherence length L_a and point defects. This shows also that by adjusting the microstructure of carbon fibers, one may tailor their thermal conductivity to a desired value.

Some VGCF and PDF of good crystalline perfection show a maximum below room temperature and, with decreasing lattice perfection the maximum is shifted to higher temperatures (Issi and Nysten, 1998).

Recently, the thermal conductivities of ribbon-shaped carbon fibers produced at Clemson University and graphitized at 2,400 °C and those of commercial round fibers graphitized at temperatures above 3,000 °C were measured and the data were compared. It was shown that, in spite of the difference in the heat treatment temperature, the two sets of fibers presented almost the same electrical and thermal conductivities. This clearly shows that, for a given HTT, spinning conditions have an important influence on the transport properties of pitch-based carbon fibers. By modifying these conditions, one may enhance these conductivities, which is important for practical applications since HTT is a costly process (cfr. Part 1, § 2 of this issue).

Oddly enough, though the electrical and thermal conductivities of pristine carbon fibers are generated by different entities, charge carriers for the electrical conductivity and phonons for the thermal conductivity, a direct relation between the two parameters is observed at room temperature (Nysten *et al.*, 1987). This is related to the fact that both transport properties depend dramatically on the structure of the fibers. They both increase with the in-plane coherence length. As a practical result of the direct relation between these transport coefficients for fibers with the same precursor, once the electrical resistivity is measured one can determine the thermal conductivity.

5 Thermoelectric power

We have introduced in I the two mechanisms responsible for the thermoelectric power, a *diffusion and a phonon drag mechanism* and have given an expression for the diffusion thermoelectric power. From this expression, it was found that the diffusion thermoelectric power for a degenerate electron gas varies as the inverse of the Fermi energy, or carrier density. This explains why semimetals like graphites exhibit higher partial diffusion thermoelectric powers than metals or graphite intercalation compounds (GICs). We have also presented in I the temperature variation of the thermoelectric power of a graphite single crystal.

We present in Fig. 3.5 the temperature dependence of the thermoelectric power of six samples of pitch-based carbon fibers heat treated at various temperatures. The samples investigated are the same whose electrical resistivities are presented in Fig. 3.1 and thermal conductivities in Fig. 3.3b. In Fig. 3.6 the earlier results of Endo and co-workers (1977) on the temperature dependence of the thermoelectric power of vapor grown (benzene-derived) carbon fibers are shown. In this figure VGCFs heat treated at two different temperatures are compared to the as-grown material.

It may be seen from all these curves that, as is the case for the bulk material, the thermoelectric power of carbon fibers is very sensitive to lattice perfection. For as grown fibers or fibers heat treated at low temperatures, the thermoelectric power is low and does not vary significantly with temperature; the room temperature thermoelectric power may even be

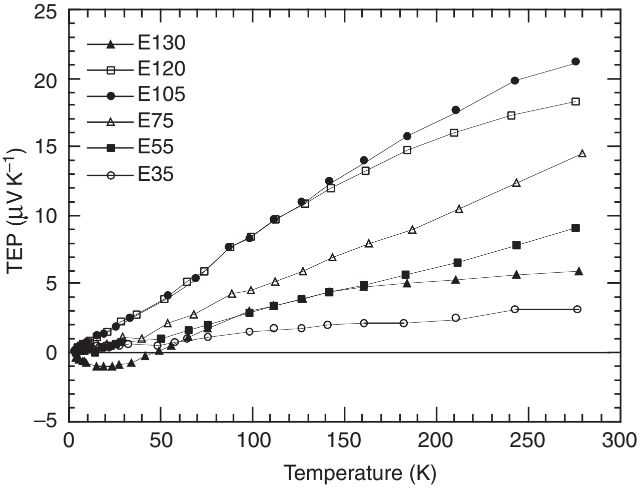

Figure 3.5 Temperature dependence of the thermoelectric power of six samples of pitch-based carbon fibers heat treated at various temperatures, the same fibers with electrical resistivity is presented in Fig. 3.1 and thermal conductivity in Fig. 3.3b (Issi and Nysten, 1998).

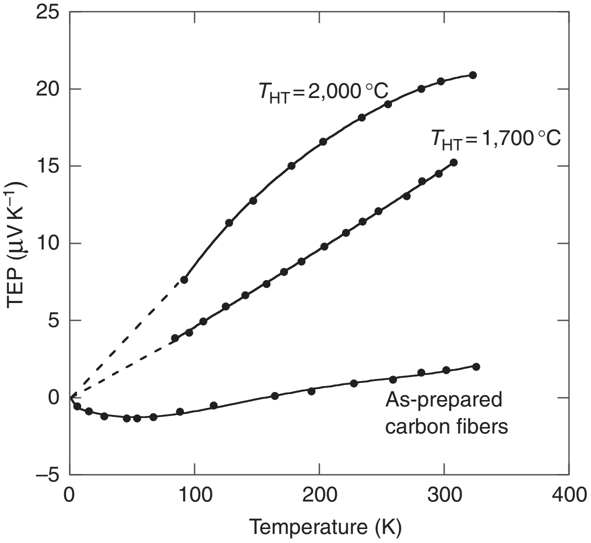

Figure 3.6 Temperature dependence of the thermoelectric power of three VGCFs heat treated at two different temperatures compared to the as-grown material (Endo *et al.*, 1977).

negative. Fibers heat treated at higher temperature exhibit a marked temperature dependence and higher magnitudes for the thermoelectric power. Then, if the heat treatment temperature is further increased the thermoelectric power decreases.

This behavior should naturally be correlated to that of the in-plane coherence length, L_a, or the 2D cristallites sizes, In I we have presented the room temperature thermoelectric power of various experimental pitch-based carbon fibers versus in-plane coherence length, L_a (fig. 3.5b in I). It was shown that the thermoelectric power increases first rapidly with L_a, reaches a maximum, then decreases first rapidly then slowly with L_a. For L_a larger than 300 nm the thermoelectric power is positive around room temperature.

The temperature variation of the thermoelectric power of bundles of SWNTs has been measured from 4.2 to 300 K by Hone *et al.* (1998). They have also reported on the temperature dependence of the electrical resistivity of their samples in the same temperature range. Three samples were investigated, two pristine and one sintered. Their thermoelectric powers exhibited the same qualitative behavior and almost the same magnitudes (Fig. 3.7). They were found to be positive over all the temperature range investigated. They increase first linearly at low temperature, then tend to reach an almost constant value around 100 K, to increase slowly again with temperature around 200 K. The room temperature values, around 50 μVK^{-1}, are considerably higher than that of metallic samples (a few μVK^{-1}), but comparable to those observed in semimetals. Oddly enough, the temperature variation resembles more that observed in graphite intercalation compounds (Fig. 3.12) than in the pristine material, though the room temperature value measured in SWNTs is about twice that reported for GICs.

In general, the interpretation of thermoelectric power data in most materials is a delicate job and this is particularly true for the case of carbons and graphites. We have seen for example that the relation between the thermal conductivity or electrical conductivity versus in-plane coherence length is straightforward. We observe an enhancement of these properties

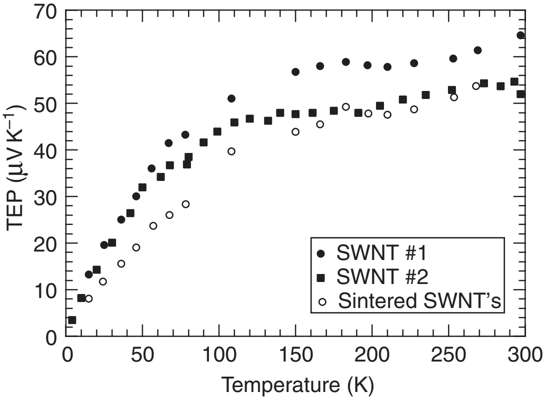

Figure 3.7 Temperature dependence of the thermoelectric power of three single wall carbon nanotube samples (Hone *et al.*, 1998).

with increasing L_a. This is due to the fact that both the electron and phonon mean free paths increase with L_a, i.e. with crystalline perfection. For the thermoelectric power the situation is different. This is due to the fact that the thermoelectric power is much more sensitive to the carrier density than to the scattering mechanism. In addition, when electrons and holes contribute to conduction, they have opposite effects on the thermoelectic power since the latter is negative for electrons and positive for holes. So, unless one knows with some accuracy the band structure of the sample and the scattering mechanism, it is difficult to predict which contribution, electron or hole, will dominate the scene.

6 Fibrous intercalation compounds

6.1 Introduction

Since the early 1980s, a large amount of experimental data has been published on the temperature variation of the electrical resistivity of intercalated carbon fibers of various origins. Fewer results are available on the thermal conductivity of these compounds (Issi, 1992). This is due to the difficulties associated with thermal conductivity measurements on samples of small cross sections that we discussed in Section 2.

The *charge transfer* resulting from intercalation increases the carrier density, while defects due to the intercalation process reduces the electronic mobility, but generally in a smaller relative amount. The net result of intercalation is thus an increase in *electrical conductivity* (Fig. 3.8). Most types of fibers have been intercalated and some fibrous acceptor GIC were found to exhibit room temperature electrical conductivities comparable to that of the best metallic conductors. The situation is different for the *thermal conductivity* which, depending on the compound and the temperature range investigated, may increase or decrease after intercalation.

Acceptor GICs are highly anisotropic electronic systems and their charge carriers, originating from the charge transfer from the intercalate, form 2D hole gases. Their Fermi surfaces consists in circles for stage-1 compounds and in cylinders for higher stage compounds (Blinowsky *et al.*, 1980). It is interesting to note that the same 2D model may be applied for

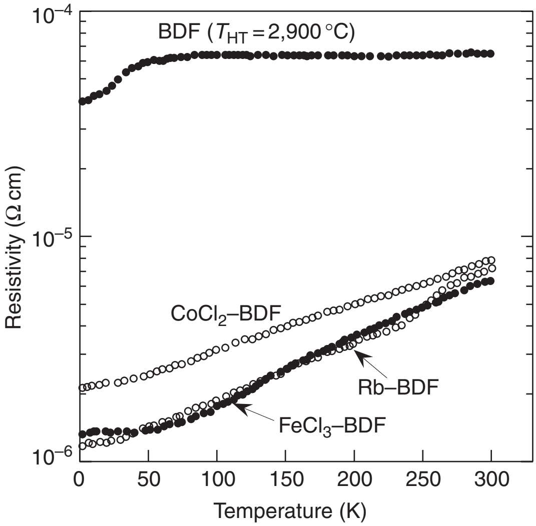

Figure 3.8 Effect of intercalation by a donor (Rb) and acceptor (FeC1$_3$) intercalate on the temperature variation of the electrical resistivity of a benzene-derived VGCF heat treated at 29,000 °C (Chieu *et al.*, 1983).

all acceptor compounds and the value of the Fermi level, which is directly related to the magnitude of the charge transfer, determines the value of the ideal resistivity.

For *donor compounds*, since the anisotropy varies considerably with the intercalated species, and from one stage to another for a given intercalate, the situation is far more complicated. This is why, despite the considerable amount of theoretical work performed on the band structure of donor compounds, the situation is not as clear as it is for acceptor compounds. This has a direct bearing on our understanding of the transport properties of these compounds.

As a direct consequence of the anisotropic band structure, the *electrical resistivity* of acceptor GICs is also highly anisotropic. The ratio of the in-plane conductivity to that along the c-axis may reach six orders of magnitude at room temperature for some acceptor GICs (Dresselhaus and Dresselhaus, 1981).

Since it is dependent on the phonon spectrum, which is less anisotropic than the electron distribution, the *lattice thermal conductivity* is also less anisotropic than the electrical resistivity (Issi *et al.*, 1983). The *thermoelectric power* presents a smaller anisotropy than that of the two other transport properties (Issi, 1992).

6.2 Electrical resistivity

As a typical example among others, we present in Fig. 3.8 the effect of intercalation on the temperature variation of the electrical resistivity of a VGCF heat treated at 2,900 °C (Chieu *et al.*, 1983). We may see that there is a significant decrease in resistivity due to the intercalation of either donor (Rb) or acceptor (FeCl$_3$ and CoCl$_2$) intercalated species. The temperature variation of the intercalation compounds thus obtained exhibit metallic behaviors with a room temperature electrical resistivities 3–4 times that of pure copper.

The in-plane resistivity data in acceptor GICs is interpreted by considering the 2D hole gas in the graphene host layers, which is fully described once its Fermi energy is known. This 2D hole gas interacts with the phonons and defects which are present in the host layers generating a finite resistivity. In the presence of weak disorder hole–hole interaction may also take place at low temperature.

The *ideal electrical resistivity*, which is due to electron–phonon scattering, should vary as T^n with $n = 5$ at very low temperature. Then n should gradually decrease with increasing temperature until it reaches unity around and above the Debye temperature. The temperature dependence of the ideal resistance in GICs was found instead to fit the relation (see e.g. Dresselhaus and Dresselhaus, 1981):

$$\mathrm{R(T) = BT + CT^2} \tag{4}$$

where B and C are constants, which may vary according to the compound considered.

In acceptor GICs the *ideal electrical resistivity* depends on the carrier density, N, and on the phonon spectrum of the host material (Issi and Piraux, 1986), which determines the electron-phonon relaxation time. The amount of charge transfer generating N varies with the nature of the intercalate and with the stage of the compound. The phonon dispersion relations do not vary significantly from one compound to another. Thus, if the same 2D band model is assumed for all acceptor GICs, the differences in ideal resistivities for fibrous GICs samples should be entirely ascribed to different Fermi energies. For metal chlorides GICs, since their Fermi energies are almost the same for a given stage and do not vary significantly from one stage to the other for lower stages, the ideal resistivities are not expected to be much different from one compound to another (cfr. I).

We have discussed in I the electron–phonon interaction in pristine carbons and graphites and concluded that, contrary to 3D metals, the charge carriers interact with subthermal phonons except at very low temperatures. In the case of acceptor GICs the situation is intermediate between that of 3D metals and that of the pristine material. This means that electron–phonon interactions are weaker in GICs than in 3D metals at a given temperature, but stronger than in the pristine material (Issi and Nysten, 1998).

Measurements performed on various low stages fibrous acceptor GICs confirmed the validity of relation (4). An almost linear variation of the ideal resistivity at low temperature and an almost T^2 behavior around room temperature was observed. Oddly enough, contrary to what is generally predicted and observed, a higher power law is found at higher temperature. This is difficult to ascribe to an electron–phonon scattering mechanism all over the temperature range. Instead, in the presence of weak disorder, the relaxation time for 2D hole–hole interactions should vary linearly at low temperatures. Thus, it is reasonable to ascribe the low temperature linear dependence to strong hole–hole interactions.

The *residual resistivity* of acceptor GICs, is due to hole-defect scattering. The defects are those which were initially in the pristine host material to which are added those introduced during the intercalation process. Scattering from the defects of both origins will combine in the temperature region where the mean free paths associated to the two scattering processes are comparable in magnitude. The residual resistivity will then depend on the host material and on the intercalated species. In pristine fibers the defect structure varies widely according to the type of fiber, heat treatment temperature and quality of the precursor for a given type of fiber. Thus, since carbon fibers provide a large variety of host defect structures in GICs, fibrous acceptor GICs are ideal candidates to investigate 2D weak localization and interaction effects (Issi, 1992).

First, acceptor GICs are natural 2D electronic systems, since the 2D behavior results from the distribution of the charge carriers, which are strongly localized in the graphene planes and which may be considered as quasi free carriers – though weakly localized – only for motion along these planes. This leads to the 2D electronic band structure. Second, the possibility of varying the defect structure of the host material over wide ranges in acceptor GICs allows large experimental possibilities for investigating the phenomena of weak localization and electron–electron interactions. Finally, the Fermi level may be modified by varying the nature of the intercalate and its concentration.

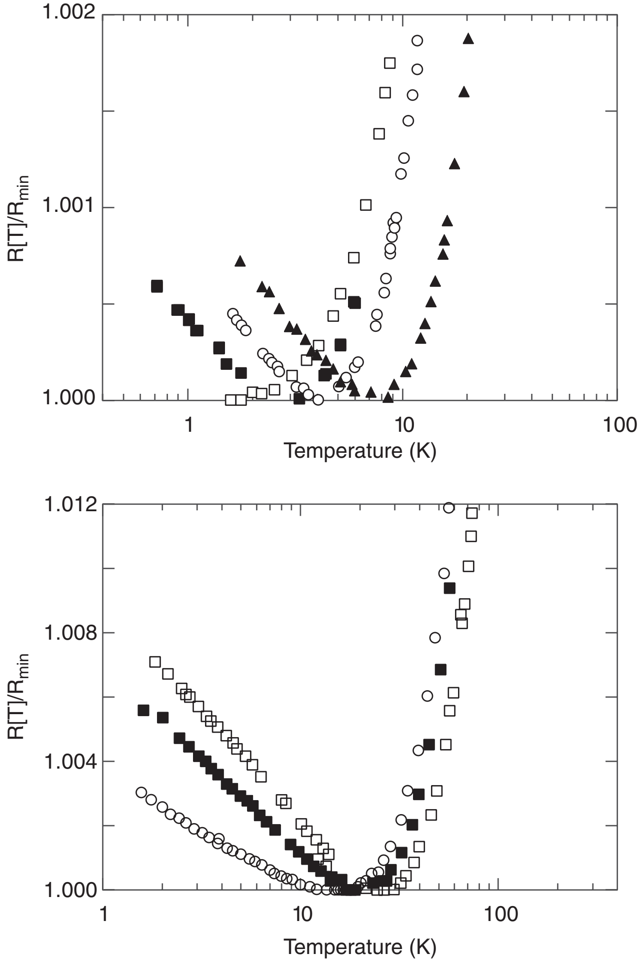

Figure 3.9 Low temperature dependence of the resistance for low-stage fibrous acceptor GICs, with various hosts and intercalates, showing the logarithmic increase in resistivity with decreasing temperature, charateristic of localization and electron–electron interaction effects. All data are normalized to the minimum value of the resistance (Piraux, 1990).

In low stage acceptor graphite fiber intercalation compounds high resolution low temperature resistivity measurements performed by Piraux and co-workers (1985) displayed logarithmic increases of the resistivity with decreasing temperature for different host structures and intercalates. In most cases, 0.1% to 1% increases in electrical resistivities were detected over a decade of temperature in the liquid helium range (Fig. 3.9). Except for the case of fluorine intercalation compounds, the increase in resistivity was thus found to be usually small above 1.5 K, the lowest temperature at which measurements were performed. The better the samples are, the smaller is the increase in resistance due to localization (Piraux, 1990). This increase in zero-field resistivity is accompanied by a negative magnetoresistance.

The most spectacular effects of the localization and Coulomb interaction effects were observed on fiber-based compounds of low crystalline perfection. This is the case for fluorine compounds where intercalation may lead to significant distortion of the graphene layers.

Weak localization effects have been observed in the electrical resistivity of all intercalated carbon fibers of low structural perfection, whether PDFs or VGCFs. The compounds investigated were found to verify the weak disorder condition $k_F l \gg 1$. The temperature dependence of the resistivity increase was found consistent with the 2D electronic structure and the results obtained concerning the temperature and magnetic field dependences of the effect were found to fit the theoretical predictions (Piraux, 1990).

Finally, for comparison, we present in Fig. 3.10 the effect of intercalation by donor (Fig. 3.10a) and acceptor (Fig. 3.10b) species on the temperature dependence of the resistivity of SWNT samples. In both cases, we observe, as for the case of bulk fibers, a decrease of resistivity after intercalation (Lee *et al.*, 1997).

6.3 The limits of electrical conductivity

Earlier work on the electrical resistivity of graphite intercalation compounds was stimulated by the promise of realizing electrical conductors with conductivities that could reach or even exceed that of copper. A question which might be raised now is to what extent one could increase the electrical conductivity of GICs. We now know the answer for the particular case metallic chlorides GICs (Issi, 1992).

In the 2D model derived for acceptor compounds (Blinowski *et al.*, 1980), the carrier density, N, varies as k_F^2 and the effective mass, m*, varies linearly with k_F, the Fermi wave vector. Thus, we may express the 2D electrical conductivity:

$$\sigma_{2D} \sim k_F \cdot \tau(k_F) \qquad (5)$$

and since the relaxation time, $\tau(k_F)$, should decrease with increasing wave number or carrier density:

$$\tau(k_F) \sim k_F^{-a} \qquad (6)$$

One may see from relations (5) and (6) that, if a is larger than 1, the electrical conductivity decreases when the k_F or N increases. Since at room temperature one should expect a value of a equal or higher than 1, the conductivity should either remain constant or decrease when the charge transfer increases, provided we remain in the range where the dispersion relation is linear in k. If scattering by in-plane graphitic phonons is the dominant mechanism, $a = 1$ (Pietronero and Strässler, 1981), then $\tau(k_F) \sim k_F^{-1}$, and in this case one should expect a conductivity independent of charge transfer.

So, at least for metallic chloride GICs, the resistivity could hardly be less than roughly $5 \times 10^{-6} \Omega$ cm, the value of the intrinsic resistivity at this temperature. However, one should add to this intrinsic resistivity that of the residual resistivity. Since the latter is governed by lattice defects and there are defects inherent to the intercalation process, the resistivities of metallic chloride GICs should in practice be higher than $5 \times 10^{-6} \Omega$ cm.

6.4 Thermal conductivity

We have already pointed out in Section 4 the mechanisms which contribute to the thermal conductivity of solids and discussed the case of pristine carbons and graphites. Let us consider now how intercalation is expected to modify the thermal conductivity of pristine fibers.

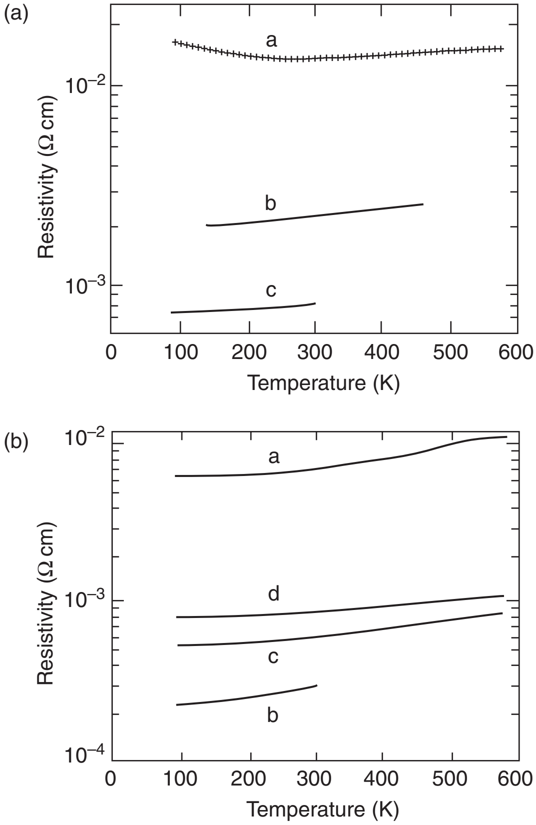

Figure 3.10 (a) The effect of potassium intercalation on the temperature dependence of the resistivity of a bulk SWNT sample. Curve a, pristine material from a different batch than in Fig. 3.6; curve b, after doping with potassium; curve c, after heating in the cryostat vacuum to 580 K overnight; curve d, after 3 days at 580 K (Lee *et al.*, 1997). (b) The effect of Br_2 intercalation on the temperature dependence of the resistivity of a bulk SWNT sample. Curve a, pristine material; curve b, saturation doped with Br_2; curve c, after heating in the cryostat vacuum to 450 K for several hours (Lee *et al.*, 1997).

On one hand, according to the Wiedemann–Franz relation, which relates the electronic thermal conductivity, κ_E, to the electrical conductivity, σ:

$$\kappa_E = L\,T\,\sigma \tag{7}$$

one should expect an increase in the electronic thermal conductivity in intercalation compounds. On the other hand, because of lattice defects introduced by intercalation, the lattice thermal conductivity should decrease. This is what is observed. The net result of intercalation is a decrease of the total thermal conductivity at high temperature and an increase at low temperature with respect to that of the pristine material (Fig. 3.11) (Issi, 1992). Here also, as is the case for the pristine material (cfr. Section 4), from the low temperature lattice thermal conductivity, one may estimate the size of the large scale defects and the concentration of point defects.

It is worth noting that when the electrical conductivity and electronic thermal conductivity may both be expressed in terms of the same relaxation time, the Lorenz ratio, L, takes the value of the Lorenz number ($L_o = 2.44 \times 10^{-8} V^2 K^{-2}$). This holds for a degenerate free electron system which undergoes elastic collisions. Thus $L = L_o$ for metals in the temperature ranges where this last conditions apply. This is the case in the low temperature residual resistivity range when scattering is dominated by impurities and lattice defects. The Wiedemann–Franz law holds also around and above the Debye temperature when large angle intravalley electron–acoustic phonon interaction is the main scattering mechanism.

In Fig. 3.11 we present on a log-log plot the temperature dependence of the thermal conductivity of a benzene-derived carbon fiber (BDF) intercalated with $CuCl_2$ (Piraux *et al.*, 1986). For comparison we have presented on the same figure the temperature dependence of the thermal conductivity of the pristine material heat treated at the same temperature

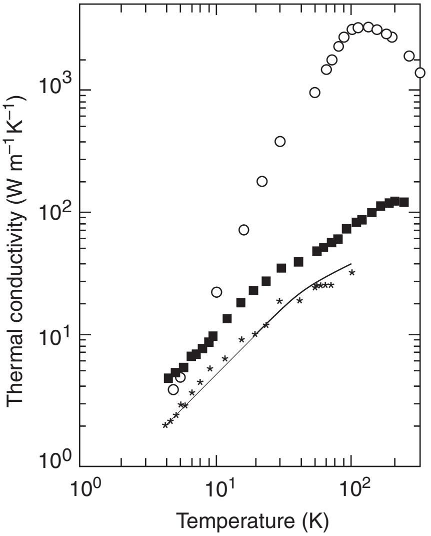

Figure 3.11 Temperature dependence of the thermal conductivity of $CuCl_2$ intercalated benzene-derived carbon fibers compared to that of pristine fibers (open circles) heat treated at the same temperature (3,000 °C). The total measured thermal conductivity of the intercalated sample (black squares) is separated into its electronic (curve) and lattice (crosses) contributions (Piraux *et al.*, 1986).

(3,000 °C). Starting from the liquid helium temperature range, the thermal conductivity increases with increasing temperature up to nearly 230 K. Using the Wiedemann–Franz relation, the total measured thermal conductivity was separated into its electronic and lattice contributions (cfr. Section 6.5).

It may be seen in Fig. 3.11 that, in contrast to the pristine material, electronic conduction in GICs may contribute to heat transport well above the liquid helium temperature range. This is due to the large increase in the charge carrier concentration in GICs resulting from charge transfer and is more pronounced at low temperatures where the lattice thermal conductivity of the pristine material decreases almost quadratically with temperature.

It is worth adding that, contrary to the case of intercalated HOPG, where the thermal conductivity of both acceptor and donor compounds have been investigated, for intercalated fibers, only a few acceptor compounds have been studied. The results obtained with HOPG and fibers as hosts were found to be qualitatively the same.

6.5 Separation of the electronic and lattice contributions

Contrary to the case of pristine fibers where the thermal conductivity is generally dominated by the lattice contribution above the liquid helium temperature range, in GICs an electronic contribution may be important at any temperature. In that case, in order to interpret the results it is necessary to be able to separate the two contributions. One of the great advantages of measuring the thermal conductivity on intercalated fibers is that, contrary to bulk graphites this separation can be done. For that purpose, one has to measure on the same sample the electrical and thermal conductivities. In fibers, this resistivity can be measured by means of a DC method (cfr. Section 2). Then, introducing the values obtained in the Wiedemann-Franz relation (relation 7), one may readily calculate the corresponding electronic thermal conductivity at a given temperature. By subtracting the latter from the total measured thermal conductivity (relation 2), one obtains the lattice contribution. This method is applicable in the temperature range where the Wiedemann–Franz ratio is equal to L_o, the free electron Lorentz number.

Generally, intercalated fiber exhibit high residual resistivities which may dominate the total resistivity up to relatively high temperatures (Issi and Nysten, 1998). In that case the Wiedemann–Franz law is expected to be valid over a wide temperature range. This is particularily true for pitch-derived fibers of poor structural perfection, where the electrical resistivity is very weakly temperature dependent (Issi and Nysten, 1998). In that case the electronic thermal conductivity can be directly computed over a large temperature range from the measured electrical resistivity via the Wiedemann–Franz law using the free electron Lorentz number (Piraux *et al.*, 1985, 1986).

So, the fibers present two major advantages with respect to HOPG when we need to separate the two contributions to the thermal conductivity. First, one can measure electrical and thermal conductivities on the same sample, and second the Wiedemann–Franz law applies over much wider temperature ranges. The result of such a separation for a $CuCl_2$ fibrous compound is presented in Fig. 3.11.

6.6 Thermoelectric power

In Fig. 3.12 we present the temperature dependence of the thermoelectric power of the BDF intercalated with $CuCl_2$ (Piraux *et al.*, 1986), which thermal conductivity is presented

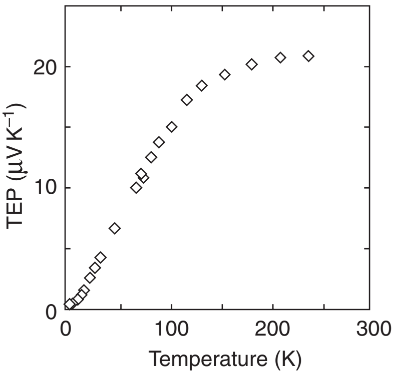

Figure 3.12 Temperature dependence of the thermoelectric power of $CuCl_2$ intercalated benzene-derived carbon fibers, which thermal conductivity is presented in Fig. 3.11 (Piraux *et al*., 1986).

in Fig. 3.11 and discussed in Section 6.4. The thermoelectric power is positive over the entire temperature range, indicating that hole conduction dominates. The temperature dependence is typical of that of all low-stage GICs whether fibrous or bulk. It starts with a linear dependence in the lowest temperature range, then increases more rapidly and finally tends to saturate around 200 K.

From the low temperature linear temperature dependence of the thermoelectric power of stage-2 compounds at low temperatures, Piraux and co-workers (1988) were able to estimate the Fermi energies of a few compounds.

Also, a thorough analysis of the data obtained on the thermoelectric power of various acceptor intercalation compounds lead to the conclusion that there is a dominant phonon drag contribution for low stage acceptor GICs in the high temperature range (Issi, 1992). This is a unique situation which should be attributed to the particular 2D nature of acceptor GICs.

7 Sample characterization

We have recently shown (Issi and Nysten, 1998) how the residual resistivity and the magnetoresistance, provide information about the lattice defects, while the interpretation of the temperature variation of the ideal electrical resistivity shed some light on electron–phonon and electron–electron interactions. We have also seen that thermal conductivity measurements were a useful source of information about lattice defects.

One may characterize and determine the defect structure of various types of carbon fibers, whether pristine or intercalated. This approach usefully complements the information obtained by means of more powerful techniques which probe the material at the microscopic level, such as SEM, high resolution TEM, X-ray diffraction, STM, AFM, … Contrary to these microscopic techniques, which are very localized and thus only probe a very tiny portion of the sample, electrical and thermal transport data give an overall view over the entire macroscopic sample. In addition, in some cases transport data are sensitive to defects which could not be detected by other techniques.

As was seen above, *thermal conductivity* measurements performed in the liquid nitrogen temperature provide a direct way to determine the in-plane coherence length in pristine fibers. This is also true for the intercalation compounds. Thus, from comparative measurements on pristine and intercalated samples, one is in a position to appreciate how the intercalation process affects the in-plane coherence length. *Electrical resistivity* measurements, though they are extremely sensitive to defects revealing very large differences in residual resistivies for samples with different defect structures, are more delicate to analyze in detail in the case of pristine fibers. In principle, *magnetoresistance* measurements probe the mobilities, thus are essentially sensitive to the scattering mechanism. The *thermoelectric power* is very sensitive to the carrier densities, and although it depends on the nature of the scattering mechanism, it is not affected by its intensity. As it is the case for the electrical resistivity, the thermoelectric power data are delicate to interpret in pristine carbons and graphites.

8 Carbon fiber composites

8.1 Introduction

One may look at *Polymer–matrix composites* filled with carbon fibers in two ways. The first approach consists in considering the exceptional mechanical properties or thermal conductivity of carbon fibers associated to their specific geometry and decide to use these properties in order to realize a practical device. Since the tiny and breakable fibers are usually delicate to handle, the solution is to embed them in a matrix which will distribute the mechanical stresses and connect the fibers to the macroworld via the matrix. One may then use the composite wherever lightweight mechanical structures or efficient bulk thermal conductors are needed.

Alternatively, one may think of improving the electrical or thermal properties of polymeric materials, which are generally electrical insulators and poor thermal conductors, by realizing polymer matrix composites filled with conductive fibers.

From the previous sections it was obvious that it is possible to tailor carbon fibers at the microstructural level to obtain specific electrical or thermal conductivities, since these properties are very sensitive to the in-plane coherence length. This was found to be particularly interesting for the case of the thermal conductivity. Indeed, by choosing adequately the precusor and by increasing the heat treatment temperature higher thermal conductivities are obtained. We were tailoring in fact the conductivity at the *microscopic level*. In a similar way, composites allow to tailor the properties of a given material at a *macroscopic level*. By this way, one is able to realize efficient heat transfer devices and in some cases heat hyperconductors, with the highest thermal conductivities which could be attained in a practical material.

8.2 Electrical conductivity

Polymer–matrix composites filled with a high enough percentage of carbon fibers may be *electrically conductive*. To attain this goal, the percentage of fibers should exceed the percolation threshold, which is relatively low for these fillers because of their high aspect ratio, i.e. their high length to cross section ratio. A transition from insulating to electrically conductive behavior occurs at the percolation threshold (see e.g. Carmona, 1988).

The typical dependence of the electrical resistivity of the composite on the fiber volume fraction is as follows (Carmona, 1988; Demain, 1994). For low concentrations, the dilute concentration regime, the fibers are randomly distributed in the matrix forming small aggregates or single inclusions which are separated by the polymer matrix. Since the latter has a very high electrical resistivity, the electrical resistivity of the composite is very high. An increase in the fiber concentration leads to an increase of the number and size of the aggregates. Eventually, some growing aggregates get in contact with their nearest neighbors and merge into larger clusters. For larger concentrations, an "infinite" cluster is formed. Around this concentration, i.e. at the percolation threshold, the electrical resistivity of the composite dramatically drops by 10–15 orders of magnitude. This results from the creation of a continuous path of electrically conductive fibers across the entire sample.

With further increase of the fiber concentration, new electrically conductive paths may be created inside the infinite cluster or may link to this cluster aggregates which were previously isolated. This leads to a monotonic decrease of the composite electrical resistivity with further increase in fiber content.

8.3 Thermal conductivity

The need for high thermal conductivity materials is increasingly recognized nowadays for technical applications. This is true when we need to improve heat exchanges in practical devices or during a manufacturing process. In that context polymeric matrix composites present the great advantage of having very low specific gravity as compared to metals and their alloys. This is particularly interesting for applications in space and airborne systems. To this advantage, one must add their relatively high chemical resistance, their ease of processing and energy saving.

For unidirectional composites with highly conductive continuous pitch-based carbon fibers, room temperature thermal conductivities comparable to that of pure copper are now readily attained (Nysten and Issi, 1990). With chopped fibers, thermal conductivities superior to that of metallic alloys may be obtained in composites, as will be seen below. Thus, with carbon fibers one may tailor at the macroscopic scale the thermal conductivity of composites to the desired values for practical applications.

For the case of composites containing aligned highly conducting *continuous carbon fibers* the result of fiber addition on the total thermal conductivity of the composite is straightforward. It was shown experimentally in that case that the thermal conductivity of the composite along the fiber axis direction obeys the simple law of mixtures. Since the thermal conductivity of the polymer is generally negligible with respect to that of the fiber, this means that it is equal to the product of the fiber volume fraction and thermal conductivity. In order to check that, the thermal conductivity of the fibers were first determined and the result was compared with those obtained for the composite as a function of fiber volume fraction (Nysten and Issi, 1990). With the composites investigated, thermal conductivities higher than that of pure copper were obtained. This result is obvious when we consider that pitch-derived carbon fibers with thermal conductivities exceeding 1,000 $\mathrm{Wm^{-1}K^{-1}}$ are now available.

The case of composites with *chopped fibers* is far more complicated to deal with. In that case, though there is a relation between the thermal conductivity of the fiber and that of the composite, this relation is not staightforward as for the case of unidirectional composites with continuous fibers. In addition to the volume fraction and fiber conductivity, there is

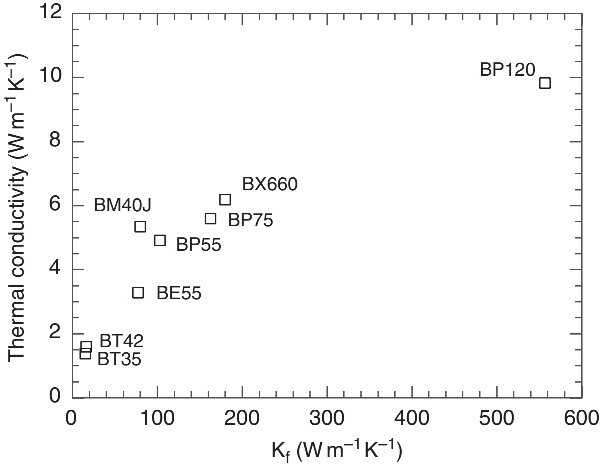

Figure 3.13 Room temperature thermal conductivity of chopped fiber-polycarbonate matrix composites versus the thermal conductivity of the fibers (Demain, 1994) for a given volume fraction. For each experimental point the corresponding type of fiber is indicated.

a large variety of parameters to control in order to improve the thermal conductivity of the composite (Demain, 1994): fiber length, length to diameter ratio, average orientation of the fibers in the composite, the fiber-matrix interface, …

As an example, we present in Fig. 3.13 the room temperature thermal conductivity of chopped fiber-polycarbonate matrix composites versus the thermal conductivity of the fibers (Demain, 1994), all other parameters being almost the same. We may see that for carbon fibers with a thermal conductivity of $550\,\mathrm{Wm^{-1}K^{-1}}$, one may elaborate a composite with a thermal conductivity of $\sim 10\,\mathrm{Wm^{-1}K^{-1}}$, which compares fairly well with that of metallic alloys. Figure 3.14 shows the relation at 300 K between the thermal conductivity of a chopped fiber–polycarbonate matrix composite versus fiber volume fraction for fibers of different lengths. The heat flow is parallel to the plane of the composite which is in the form of a plate.

We have seen above that for the case of electrical conductivity (Section 8.2), the transition from electrically insulating to electrically conductive state, which is explained in the frame of the percolation theory, is abrupt. However, such a rapid transition does not occur in the case of thermal conductivity. The reason for that is that the mechanisms responsible for electrical and thermal conduction are different. Electrical conductivity is always generated by charge transport, while the thermal conductivity of the fibers at room temperature and of the polymeric matrix is due exclusively to phonons. Besides, while the polymeric matrix is an electrical insulator and thus cannot carry electrical current, it may still conduct heat to some extent and thus may still transfer some heat from one fiber to the other.

Thus the dependence of the composite thermal conductivity on the fiber concentration (Fig. 3.14) is expected to be different from that of the electrical conductivity discussed above (Section 8.2). We may tentatively explain this behavior as follows (Demain, 1994). Within the aggregates of fibers, the conductance of the polymer separating the fibers which are very close to them is of the same order of magnitude as that of the fibers, yielding thus highly

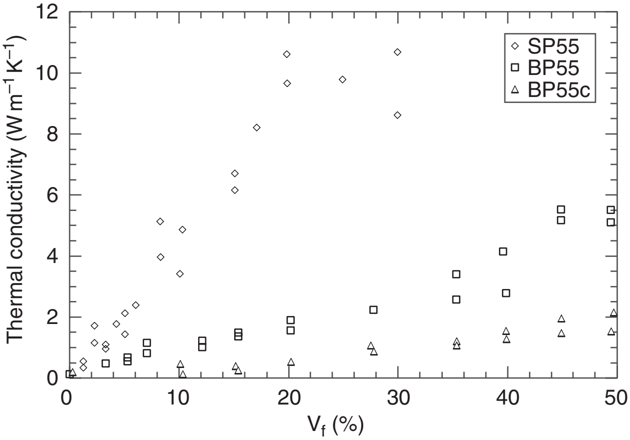

Figure 3.14 Room temperature dependence of the thermal conductivity of a chopped fiber (P55)-polycarbonate matrix composite versus fiber volume fraction (Demain, 1994). The heat flow is parallel to the plane of the composite in the form of a plate. The different sets of experimental points are relative to composites with fibers of different average lengths: roughly 40 gm for BP55c, 100 gm for BP55, and 360 gm for SP55. From this figure one may also appreciate the effect of fiber length on the conductivity for a given volume fraction.

thermally conductive regions inside the composite. At low fiber concentrations, those aggregates are separated from each other by resin rich regions which are less conductive and thus reduce the heat transfer across the sample.

One may consider the polymer loaded with particles whose sizes and geometries are those of the aggregates and whose thermal conductivity is intermediate between that of the polymer and the filler. When the concentration is increased, the average distances between the aggregates decreases thus increasing the conductance of the polymer separating them and hence increasing the thermal conductivity of the composite. Finally, when the fiber concentration exceeds the percolation threshold, an infinite aggregate is formed. In the absence of resin rich regions between the aggregates, the conductance of the polymer close to the fibers dominates the composite thermal conductivity. Any further increase of the fiber concentration increases the number of paths for the heat and areas for heat transfer from one fiber to another.

Hence, the transition from a concentration range where the thermal conductivity of the composite is depending on the conductance of the polymer between aggregates to a concentration range where the conductance within the aggregates dominates, could explain the change from a linear to a non linear $K_c(V_f)$. This interpretation is corroborated by results of electrical resistivity measurements which were used to probe the type of arrays formed by the fibers in the matrix.

When we compare the results relative to *in-plane* and *out-of-plane* thermal conductivities (Demain, 1994), we observe that for the same fiber volume fraction, in-plane thermal conductivities are always much larger than out-of-plane thermal conductivities. Also, both in-plane and out-of-plane conductivities increase linearly with fiber concentrations in the range 0–30%, whereas they generally increase more rapidly for larger concentrations.

Concerning the effect of the *average fiber length* for concentration ranging from 0% to 30%, it was shown that thermal conductivities comparable to that of a composite filled with continuous random in-plane fibers could be attained with samples whose average fiber lengths are around 500 μm.

It is interesting to note that as for the case of fibers, transport measurements may be used to characterize to some extent composites. For example, electrical resistivity and magnetoresistance measurements may be used to gain information on the fiber orientation and the way the fibers are dispersed in the matrix (Demain, 1994).

9 Conclusions

In this chapter our aim was to outline the specific aspects of transport in carbon fibers with respect to bulk carbons and graphites in particular, but also, more generally with respect to other solids. We have considered carbon nanotubes as one variety of fibers, but have refrained in discussing in detail their properties, since they are the object of other chapters in this series.

We have shown that, in addition to practical aspects, the various structures of carbon fibers and their particular geometry have lead to interesting observations, which could not be made on bulk carbons and graphites. This is the case for high resolution electrical resistivity measurements which lead to the discovery of quantum transport effects on carbons and graphites. We have also shown that it was possible to separate the electronic and lattice contributions to the thermal conductivity in intercalated fibrous compounds

Leaning heavily on the basic concepts which we have discussed in I, we have mainly concentrated in this chapter on the specific aspects related to fibers which were not already discussed in detail in I. Emphasis was thus placed on the thermal conductivity of pristine fibers, the effect of intercalation on the transport properties, and the electrical and thermal conductivities of composites. Besides, we have discussed in brief the experimental difficulties associated to measurements on fibrous materials.

Note added in proof

Since this chapter was written the thermal conductivity and thermoelectric power of individual multiwalled carbon nanotubes has been measured (Kim *et al.*, Phys. Rev. Letters, 87 (2001)). As expected, the room temperature thermal conductivity was found to exhibit very high values (3000 $\mathrm{Wm^{-1}K^{-1}}$).

References

Allen, G. and Issi, J.-P. (1985) *Proceedings of ECCM-1*, 447.
Bayot, V., Piraux, L., Michenaud, J.-P., and Issi, J.-P. (1989) Phys Rev. **B40**, 3514.
Blinowski, J. and Rigaux, C. (1980) Synth. Metals **2**, 277.
Bright, A. A. (1979) Phys. Rev. **B20**, 5142.
Bright, A. A. and Singer, L. S. (1979) Carbon **17**, 59.
Carmona, F. (1988) Ann. Chim. Fr. **13**, 395–443.
Chieu, T. C., Dresselhaus, M. S., and Endo, M. (1982) Phys. Rev. **B26**, 5869.
Chieu, T. C., Dresselhaus, M. S., Endo, M., and Moore, M. A. W. (1983) Phys. Rev. **B27**, 3686.
Demain, A. (1994) *Thermal conductivity of polymer-chopped carbon fiber composites*, PhD thesis, Université Catholique de Louvain, Louvain-la-Neuve.
Dresselhaus, M. S. and Dresselhaus, G. (1981) Adv. Phys. **30**, 139.

Dresselhaus, M. S., Dresselhaus, G., Sugihara, K., Spain, I. L., and Goldberg, H. A. (1988) *Graphite Fibers and Filaments*, Springer Series in Materials Science 5, Springer-Verlag.

Endo, M., Tamagawa, I., and Koyama, T. (1977) Jpn. J. Appl. Phys. **16**, 1771.

Endo, M., Hishiyama, Y., and Koyama, T. (1982) J. Phys. D: Appl. Phys. **15**, 353.

Gallego, N. C., Eddie, D. D., Nysten, B., Issi, J-P., Treleaven, J. W., and Deshpande, G. V. (2000) Carbon **38**, 1003–1010.

Hone, J., Ellwood, I., Muno, M., Mizel, A., Cohen, M. L., Zettl, A., Rinzler, A. G., and Smalley, R. E. (1998) Phys. Rev. Letters **80**, 1042.

Issi, J.-P. Heremans, J., and Dresselhaus, M. S. (1983) Phys. Rev. **B27**, 1333.

Issi, J.-P. and Piraux, L. (1986) Annales de Physique, **11**(2), 165.

Issi, J.-P. (1992) "Transport properies of metal chloride acceptor graphite intercalation compounds," in Zabel, H. and Solin, S. A. eds, *Graphite Intercalation Compounds II*, Springer Series in Materials Science, Vol. 18 (Springer-Verlag, Berlin).

Issi, J.-P. and Nysten, B. (1998) "Electrical and thermal transport properties in carbon fibers," in Donnet, J.-B., Rebouillat, S., Wang, T. K., and Peng, J. C. M. eds *Carbon Fibers*, New-York Marcel Dekker, Inc.

Issi, J.-P. and Charlier, J.-C. (1999) "Electrical transport properties in carbon nanotubes," in *Science and Technology of Carbon Nanotubes*, Tanaka, K. ed., Elsevier, London.

Issi, J.-P. (2000) "Electronic Conduction" in Delhaes, P. ed. (1964) *World of Carbon*, Gordon and Breach, UK.

Klein, C. A. (1964) J. Appl. Phys. **35**, 2947.

Langer, L., Stockman, L., Heremans, J. P., Bayot, V., Olk, C. H., Van Haesendonck, C., Bruynseraede, Y. and Issi, J.-P. (1994) *J. Mater. Res.* **9**, 927–932.

Langer, L., Bayot, V., Grivei, E., Issi, J.-P., Heremans, J. P., Olk, C. H., Stockman, L., Van Haesendonck, C. and Bruynseraede, Y. (1996) Phys. Rev. Letters **76**, 479.

Lee, R. S., Kim, H. J., Fischer, J. E., Thess, A., and Smalley, R. E. (1997) Nature, **388**, 255.

Mrozowski, S. and Chaberski, A. (1956) Phys. Rev. **104**, 74.

Nysten, B., Piraux, L., and Issi, J.-P. (1987) in D. W. Yarbrough, ed. *Thermal Conductivity* **19**, Plenum Press, New York, 341.

Nysten, B. and Issi, J.-P. (1990) Composites **21**, 339.

Nysten, B., Issi, J.-P., Barton, R., Jr. Boyington, D. R., and Lavin, J. G. (1991a) J. Phys. D: Appl Phys, **24**, 714.

Nysten, B., Issi, J.-P., Barton Jr., R., Boyington, D. R., and Lavin, J. G. (1991b) Phys. Rev. **B44**, 2142.

Pietronero, L. and Strässler, S. (1981) Synthetic. Metals **3**, 213.

Piraux, L., Nysten, B., Issi, J. P., Salamanca-Riba, L., and Dresselhaus, M. S. (1986) Solid State Commun. **58**, 265.

Piraux, L., Nysten, B., Haquenne, A., Issi, J.-P., Dresselhaus, M. S., and Endo, M. (1984) Solid State Commun. **50**, 69.

Piraux, L., Issi, J.-P., Michenaud, J.-P., McRae, E., and Marêché, J. F. (1985) Solid State Commun. **56**, 567.

Piraux, L., Bayot, V., Michenaud, J.-P., Issi, J.-P., Marêché, J. F., and McRae, E. (1986a) Solid State Commun. **59**, 711.

Piraux, L., Issi, J.-P., Salamanca-Riba, L., and Dresselhaus, M. S. (1986b) Synthetic Metals, **16**, 93.

Piraux, L., Issi, J. P., and Coopmans, P. (1987) Measurement, **5**, 2.

Piraux, L. (1990) Mater. J. Res. **5**, 1285.

Robson, D., Assabghy, F. Y. I., and Ingram, D. J. E. (1972) J. Phys. D: Appl. Phys. **5**, 169.

Robson, D., Assabghy, F. Y. I., Cooper, E. G., and Ingram, D. J. E., J. Phys. D: Appl. Phys.

Part II

CVD/CVI PROCESSES

4

FUNDAMENTALS OF CHEMICAL VAPOR DEPOSITION IN HOT WALL REACTORS

K. J. Hüttinger

1 Introduction

Chemical vapor deposition (CVD) is a process for deposition of a solid on the external surface of a substrate by pyrolysis of a gaseous precursor. Carbon is commonly deposited from light hydrocarbons. CVD on an internal surface of a substrate is called chemical vapor infiltration (CVI). As compared to CVD the CVI process is much more important because it is the optimal technique to fabricate fiber reinforced ceramics and particularly carbon fiber reinforced carbon. CVD and CVI of carbon were developed more than 30 years ago; the developments were completed by review articles of Bokros (Bokros, 1969; Bokros *et al.*, 1973) and Kotlenski (1973).

The interest in CVD and CVI of carbon during the following two decades was small as follows from more recent literature reviews on CVD and CVI (Becker and Hüttinger, 1998a and Benzinger and Hüttinger, 1996a, respectively). It is the scope of this chapter to summarize progresses in understanding CVD and CVI from new research activities since about 1990.

Chemical vapor deposition in hot wall reactors implies that a precursor gas is heated to the deposition temperature by convection resulting in complex gas phase reactions (homogeneous pyrolysis reactions) which are interacting or competing with complex surface reactions (heterogeneous deposition reactions). Gas phase reactions of light hydrocarbons are synthesis reactions in which hydrocarbons (molecules or radicals) of increasing size are formed. Understanding chemistry and kinetics of gas phase reactions is an essential basis for understanding kinetics of carbon deposition.

Surface reactions are accelerated by preceding gas phase reactions, because the deposition rate tends to increase with increasing size of a hydrocarbon. Limiting effects of surface reactions result from saturation adsorption and hydrogen inhibition. Saturation adsorption may occur at increasing partial pressure of any hydrocarbon. Hydrogen inhibition is selective with respect to the nature of a hydrocarbon which may be linear or cyclic and exhibit a high or low carbon to hydrogen ratio. During CVD in a hot wall reactor, precursor gas, intermediates (molecules, radicals), and final products (carbon, hydrogen) always coexist. This coexistence may cause auto-inhibitions by hydrogen, especially if a hydrocarbon with a low carbon to hydrogen ratio such as methane is used as a precursor. During CVI, hydrogen is separated from other products because its diffusion out of a porous material is strongly favored. Therefore, deposition reactions in a porous material are less inhibited which underlines the importance of understanding the special influence of hydrogen on gas phase and particularly on surface reactions.

Gas phase and surface reactions are simultaneous reactions competing with each other. The interactions of these reactions are determined by the ratio of the surface area of the substrate and the free volume of the deposition space (A/V). By variation of this ratio, generally more or less neglected in literature on CVD (Hitchman and Jensen, 1993), a wide range of deposition kinetics can be obtained (Hüttinger, 1998). Porous materials exhibit much higher ratios of internal surface area to pore volume as compared to plane substrates in a CVD reactor. Additionally, the A/V ratio of a porous material continuously increases with progressive infiltration. An understanding and especially a numerical simulation of CVI will not be possible without consideration of the influence of this ratio on the deposition kinetics. Furthermore, it should be considered that changes in deposition chemistry and kinetics also cause changes in the structure of the deposited carbon.

The following sections are concerned with the above and some additional topics: (1) elementary processes of CVD of carbon from light hydrocarbons, (2) hydrogen inhibition and rate limiting step, (3) surface area/volume ratio, (4) saturation adsorption, (5) consequences of complex deposition kinetics for CVI and (6) considerations about the formation of different carbon structures.

2 Elementary processes

A scheme of carbon deposition from methane during flowing along a hot wall is shown in Fig. 4.1. As a consequence of increasing temperature methane undergoes pyrolysis reactions. These reactions lead to hydrocarbons of increasing size; at temperatures around 1100 °C, relevant for CVI, aromatic and polycyclic aromatic hydrocarbons are formed rapidly. Reactive intermediates of homogeneous gas phase reactions may diffuse through the boundary layer, adsorb at the substrate surface and form solid carbon. Hydrogen should be the main volatile product of surface reactions. Thermodynamic calculations show that the solubility of carbon in the gas phase at high temperatures is extremely low (Lersmacher *et al.*, 1967); this is not reflected in the carbon yield, because the deposition rates are low, too. At a low surface area or A/V ratio, respectively, carbon deposition even is an unimportant side reaction. This indicates that surface reactions are strongly inhibited in particular if a hydrocarbon with a high hydrogen/carbon ratio such as methane is used as a precursor.

Chemistry and kinetics of gas phase reactions of hydrocarbons have extensively been studied; evaluated rate constants of hundreds of elementary reactions are available in the literature (Baulch *et al.*, 1994). Open questions are related to dissociation of methane (Palmer *et al.*, 1968; Dean, 1990; Bockhorn, 2000), formation of the so-called first aromatic ring (benzene, phenyl-radical) and its significance in the formation of polycyclic aromatic hydrocarbons (Frenklach and Wang, 1994) as well as the rapid formation of the latter hydrocarbons (Marinov *et al.*, 1996; Feron *et al.*, 1999; Hu and Hüttinger, 2001a).

Dissociation of methane under CVD-conditions occurs much faster as compared to dissociation rates determined on the basis of elementary reactions (Bockhorn, 2000). According to Palmer *et al.* (1968) flow conditions are very important. An influence of wall reactions (substrate surface) may be excluded on the basis of experimental results (Eisenberg and Bliss, 1967; Teubner *et al.*, 2000) as well as because of the low sticking coefficient of methane. On the other hand, dissociation of methane is accelerated by

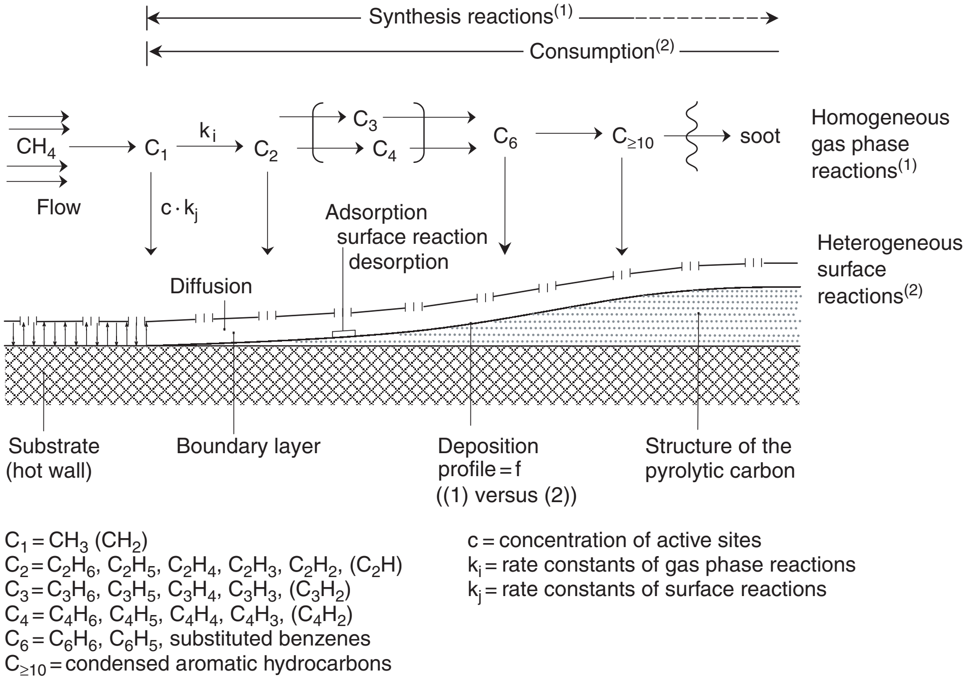

Figure 4.1 Scheme showing elementary processes of carbon deposition in hot wall reactors.

reaction products of consecutive reactions, especially by atomic hydrogen (eq. (1)) (Dean, 1990).

$$CH_4 + H \rightarrow CH_3 + H_2 \tag{1}$$

This effect may not sufficiently be considered in calculations of methane dissociation based on elementary reactions because the knowledge about these reactions is limited to two- and three-membered aromatic rings. A possible reason for high rates of methane dissociation may be a strong back-mixing in CVD-reactors operated at low pressure (Andrä *et al.*, 2000).

Two routes are discussed for the formation of the first aromatic ring, the C_4-route with C_4H_5 at lower and C_4H_3 at higher temperatures (Frenklach and Wang, 1994; Wang and Frenklach, 1997), and the C_3-route with the propargyl radical as the most important intermediate (Marinov *et al.*, 1996; Atakan *et al.*, 1998). Aromatic growth may occur according to the HACA (hydrogen abstraction acetylene addition) mechanism (Frenklach and Wang, 1994) or by aromatic condensation (Sarofim *et al.*, 1994). In both mechanisms atomic hydrogen is needed. This arises the same question as in the dissociation of methane, namely about the source of atomic hydrogen. Aromatic growth could also be based on energetically favored pathways which are still not known. Experimental studies of gas phase chemistry and especially of aromatic growth are a major challenge in the future (Feron *et al.*, 1999).

Provided open questions are solved numerical simulations of gas phase reactions using elementary reactions seem to be extremely difficult because of the high branching ratio in the formation of polycyclic aromatic hydrocarbons. For this reason reduced chemical models are most important; examples were presented recently (Bammidipati *et al.*, 1996;

Birakayala and Evans, 2002). Such models are a precondition for numerical simulation of CVD and CVI of carbon and thus for decisive progresses in these processes.

Understanding surface reactions is similarly unsatisfying, although some facts seem to be known or plausible. The rate of carbon formation from a reactive hydrocarbon species increases with its size (Becker and Hüttinger, 1998b, 1999). Surface reactions may strongly be inhibited (Tesner, 1984; Feron *et al.*, 1998) and especially selectively inhibited by hydrogen (Becker *et al.*, 2000). This problem will be treated in Section 3. Surface reactions should be similar to aromatic growth in the gas phase, because the bond dissociation energy of the C–H bond at aromatic rings does not depend on the size or shape of an aromatic hydrocarbon or a graphene layer (May *et al.*, 2000).

The influence of the size of a hydrocarbon on the deposition rate of carbon at a temperature of 1000 °C is presented in Fig. 4.2 (Becker and Hüttinger, 1999). It shows surface related deposition rates as a function of residence time at a A/V ratio of about 0.2 mm^{-1} and a partial pressure of 4 kPa, normalized to C_1; i.e. the effective partial pressure of C_2-hydrocarbons was 2 kPa, that of propene 1.33 kPa, etc. A comparison of the rates at low residence time shows a clear increase from the C_2-hydrocarbons to the C_3, C_4, and C_6-hydrocarbons. This tendency indicates that the rate of carbon deposition increases with the ability of a hydrocarbon to form aromatic or polycyclic aromatic hydrocarbons. Rates increasing with residence time result from synthesis reactions by formation of hydrocarbons with increasing size, most pronounced in the case of C_2-hydrocarbons. The influence of hydrogen follows from a comparison of the deposition rates from ethene and ethine. Methane is much less reactive; a temperature of at least 1100 °C is necessary to obtain similar deposition rates (Becker and Hüttinger, 1998). As the initial compound of the reaction sequence of Fig. 4.1 the rate increase as a function of residence time is significantly stronger than in the case of the C_2-hydrocarbons.

These results suggest that the reaction sequence of gas phase reactions presented in Fig. 4.1 leads to increasing deposition rates as the gas flows along the substrate (Hu and Hüttinger, 2000, 2001a). The rate increase may be lowered by decreasing pressure because axial diffusion is favored (Hu and Hüttinger 2000, 2001a) and reactive species of gas phase reactions are widely consumed in surface reactions. At strongly increased A/V ratio surface

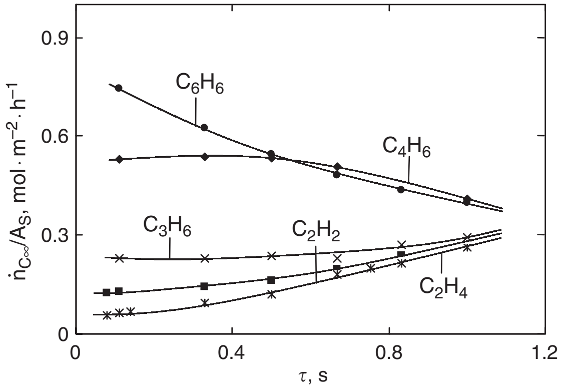

Figure 4.2 Surface-related deposition rates from various hydrocarbons as a function of residence time at 1000 °C and 4 kPa normalized partial pressure (Becker *et al.*, 1999).

reactions are favored on the expense of synthesis reactions in the gas phase resulting in a flat deposition profile (Hu and Hüttinger, 2000, 2001a; Zhang and Hüttinger, 2001a). Interactions of gas phase and surface reactions as influenced by the A/V ratio are discussed in Section 4.

Variation of these parameters including residence time have a significant influence on the major carbon forming species. This may explain that ethine on the one hand (Murphy and Carrol, 1992; Murphy *et al.*, 1997) and benzene (Glasier and Pacey, 2001) or polycyclic aromatic hydrocarbons (Chen and Back, 1979; Lucas and Marchand, 1990) on the other hand are postulated to be the decisive species of carbon deposition. In fact, carbon deposition can be attributed to a wide range of classes of hydrocarbons (see Section 5).

3 Hydrogen inhibition

Inhibition of carbon deposition by hydrogen was reported in several papers (Eisenberg and Bliss, 1967; Tesner, 1984; Feron *et al.*, 1998). In a more recent paper (Becker *et al.*, 2000) it was concluded that the inhibition mainly results from an inhibition of surface reactions which is selective with respect to the C/H ratio of a hydrocarbon and the molecular structure of a hydrocarbon, if small linear hydrocarbons are compared with cyclic, i.e. aromatic hydrocarbons.

An example of hydrogen inhibition obtained at 1000 °C, a normalized hydrocarbon partial pressure of 4 kPa (see Fig. 4.2) and a very short residence time of 0.1 s is depicted in Fig. 4.3 (Becker *et al.*, 2000). It shows deposition rates with added hydrogen related to the deposition rate from the pure hydrocarbon as a function of hydrogen partial pressure. The result for methane (dashed line) was obtained at a temperature of 1100 °C and a partial pressure of 10 kPa. In the case of linear hydrocarbons the inhibition increases with decreasing C/H ratio. Inhibition of carbon deposition from benzene is dramatic although it exhibits the same C/H ratio as ethine. A similar strong inhibition was reported in Feron *et al.*, (1998). The result for methane cannot directly be compared because of the higher deposition temperature and partial pressure.

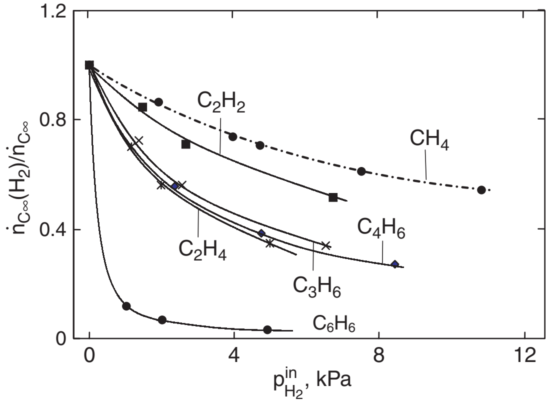

Figure 4.3 Deposition rates from various hydrocarbons as a function of hydrogen initial partial pressure normalized to deposition rates without added hydrogen at a temperature of 1000 °C and 4 kPa normalized partial pressure of hydrocarbons (results for methane correspond to 1100 °C and 10 kPa partial pressure) (Becker *et al.*, 2000).

Hydrogen inhibition is attributed to the stability of the C–H bond at the edges of graphene layers; it exhibits a bond dissociation energy of 461 kJ mol^{-1} (May *et al.*, 2000). The corresponding energy for dissociation of a C–CH_3 bond is lower and amounts to 412 kJ mol^{-1} (zig-zag edges) and 378 kJ mol^{-1} (armchair edges) (May *et al.*, 2000). Activation energies for hydrogen desorption from edge atoms vary from 425 to 460 kJ mol^{-1} (Zhang *et al.*, 2000). The overall activation energy of carbon deposition from methane, determined in several studies, exhibits a similar value of 445 ± 10 (Brüggert *et al.*, 1999; Hu and Hüttinger, 2001a). These values suggest that carbon deposition is controlled by dissociation of the C–H bond. Hydrogen inhibition of carbon deposition from all hydrocarbons of Fig. 4.3 can perfectly be described with Langmuir–Hinshelwood kinetics (Becker *et al.*, 2000).

In the case of carbon deposition from methane an auto-inhibition is possible because large amounts of hydrogen are produced. In CVD formed hydrocarbons and hydrogen always coexisist. In CVI they are separated by preferred diffusion of hydrogen out of a porous material. As a consequence carbon deposition from all hydrocarbons and especially from aromatic hydrocarbons should be less limited resulting in increasing deposition rates.

4 Surface area/volume ratio

Chemical vapor deposition of carbon, like most of the CVD processes in hot wall reactors, is a homogeneous–heterogeneous process. In such a process homogeneous gas phase reactions are interacting or competing with heterogeneous surface reactions (Hüttinger, 1998). It is obvious that surface reactions are favored by a high surface area. Consideration of the surface area of the substrate is not sufficient because gas phase reactions are determined by the free volume of the deposition space. This implies that the competition of gas phase and surface reactions is controlled by the A/V ratio. At a low ratio gas phase reactions leading to hydrocarbons of increasing size are nearly not influenced by surface reactions. At a high ratio these reactions are limited because reactive intermediates of gas phase reactions are consumed in surface reactions.

An example for the influence of the A/V ratio is presented in Fig. 4.4 (Hu and Hüttinger, 2000). It shows surface related deposition rates as a function of substrate length at three different A/V ratios. Surface related rates are not constant but decrease with increasing A/V ratio. It is noteworthy that these differences develop as the gas flows along the substrate. They are not caused by a depletion effect, but by an altered deposition chemistry. A confirmation will be presented in the following Section 5. A direct confirmation of an altered deposition chemistry was obtained in CVD studies of silicon carbide from methyltrichlorosilane showing a significant influence of the A/V ratio on the stoichiometry of the deposited material (Zhang and Hüttinger, 2001b). Strong co-deposition of free silicon, observed at a low A/V ratio, was completely suppressed at a high ratio.

The influence of the A/V ratio on the kinetics of carbon deposition was demonstrated for a wide range of deposition conditions (Antes *et al.*, 1999; Hu and Hüttinger, 2000, 2001a; Teubner *et al.*, 2000; Zhang and Hüttinger, 2001a). The results indicate that nearly any deposition kinetics can be determined just by changing the A/V ratio. A priori this ratio represents a geometric factor. In fact, it is a volume related concentration of active sites which are reaction partners of species from the gas phase. The concentration of active sites per unit area of the surface may vary from one substrate to another or change with a variation of deposition conditions. Therefore, the real A/V ratio may strongly differ from the geometric ratio.

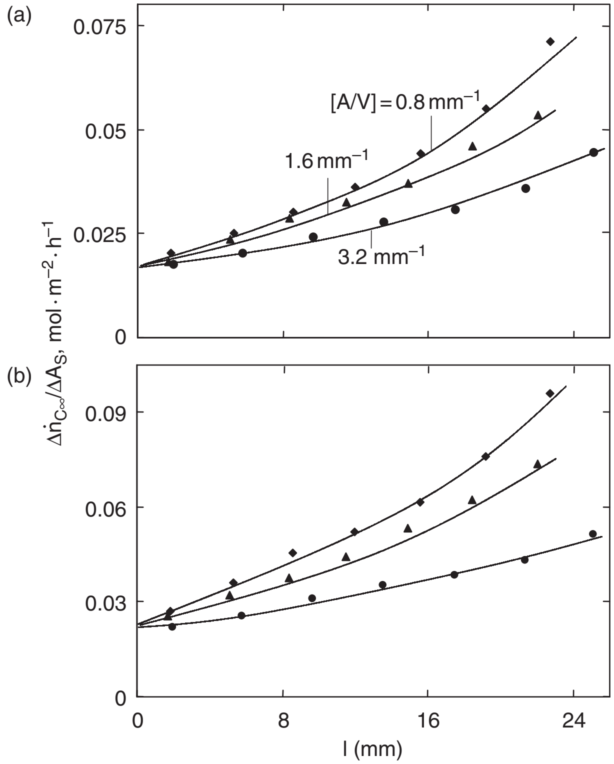

Figure 4.4 Surface-related deposition rates from methane as a function of substrate length at various A/V ratios, a temperature of 1100 °C, and a partial pressure of 10 kPa. (a) residence time of 0.55 s, (b) residence time of 1.1 s, which correspond to a total length of the substrate of about 25 mm (Hu and Hüttinger, 2000).

The A/V ratio is most significant for CVI because the ratio of internal surface area and pore volume changes with progressive infiltration. In the case of a cylindrically shaped pore it increases proportional to the reciprocal diameter. Changing deposition chemistry and kinetics may result in different structures of carbon (isotropic or dark, smooth, and rough laminar). Structural changes observed during progressive infiltration of carbon fiber felt (Pearson and Lieberman, 1975; Loll *et al.*, 1977) can be correlated with changes of A/V ratio (Benzinger and Hüttinger, 1999a).

5 Saturation adsorption

Saturation adsorption is a well known phenomenon of heterogeneous catalysis and heterogeneous gas solid reactions (Yang and Hougen, 1950; Corrigan, 1955). In a simplest case the rate increases with increasing partial pressure of the gas up to a limiting value which does not change with further increasing partial pressure.

Very recent studies of CVD of carbon from methane showed a similar rate increase to a limiting value, but a further rate increase was observed at further increasing methane pressure, additionally (Becker and Hüttinger, 1998b). An example of continued studies is

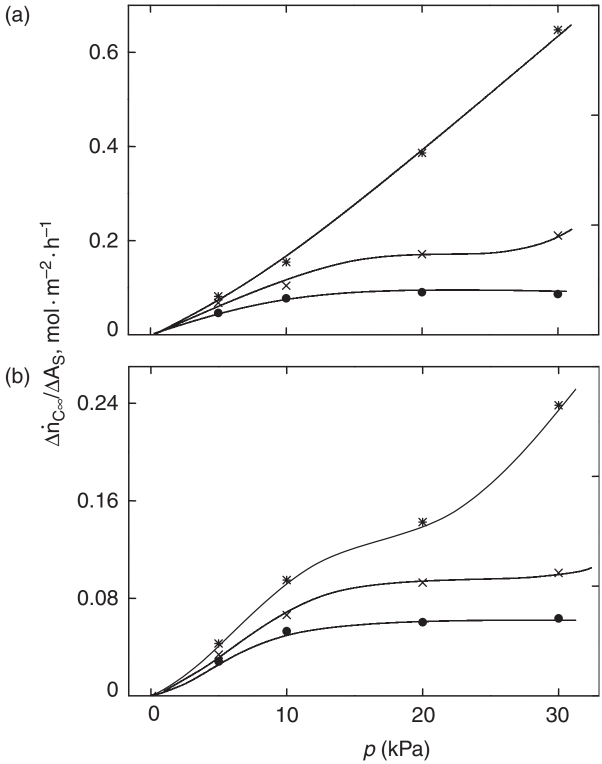

Figure 4.5 Surface-related deposition rates as a function of methane pressure at a temperature of 1100 °C, a residence time of 1 s corresponding to a total length of the substrate of 40 mm, and A/V ratios of 0.79 mm^{-1} (a) and 3.2 mm^{-1} (b). (•), (×), (∗): starting point, middle and final point of the substrate (Hu and Hüttinger, 2001a).

presented in Fig. 4.5 (Hu and Hüttinger, 2001b). It shows surface related deposition rates as a function of methane pressure determined at the initial point (•), the middle (×) and the final point (∗) of substrates with A/V ratios of 0.79 mm^{-1} (a) and 3.2 mm^{-1} (b). Saturation adsorption is perfectly developed at both [A/V] ratios at the initial point of the substrate (•). At the final point of the substrate with the higher A/V ratio a tendency to saturation adsorption is still indicated which is not the case at the lower A/V ratio.

Saturation adsorption implies that all active sites are working. This is only possible at an excess of reactive gas phase species, which obviously also exists at the higher A/V ratio. Lower surface related rates in the state of saturation adsorption at high A/V ratio as compared to a low ratio may thus not be caused by a depletion effect. In fact, they are a result of altered deposition chemistry and kinetics with species of smaller size as the major carbon forming species.

Saturation adsorption is limited by a further rate increase. This indicates a deposition process at which active sites should not play a decisive role. A corresponding model is presented in Section 6.

Saturation adsorption at pressures up to 30 kPa corresponds to a zero order formal kinetics which is extremely important for CVI. In the case of pure Fick diffusion the Thiele modulus is not increased in the case of Knudsen diffusion, important for the infiltration of very narrow pores, or in the case of mixed diffusion it is even decreased if the pressure is increased. A decreasing Thiele modulus corresponds to an increasing pore effectiveness factor and thus to a lowered diffusion limitation (Benzinger and Hüttinger, 1996b, 1998, 1999b). The advantage of an increased pressure on the rate of infiltration and the densification of a porous material was demonstrated by numerical simulations and confirmed by corresponding experimental studies (Hu and Hüttinger, 2001b; Zhang and Hüttinger, 2001c).

6 The role of a complex deposition chemistry for CVI

In the above sections the influence of hydrogen, A/V ratio and saturation adsorption on CVI was already discussed. The most important influence on CVI, however, results from a complex deposition chemistry. Methane is an ideal precursor for CVI for various reasons (Benzinger *et al.*, 1996; Benzinger and Hüttinger, 1996b). It exhibits a high diffusion coefficient, a high thermal stability and is not able to form carbon directly (see Fig. 4.1). Additionally, it shows the most complex deposition chemistry, i.e. the most extended sequence of pyrolysis reactions.

Numerical simulations of CVI of carbon from methane were performed using three models with differently extended reaction sequences (eqs. 2(a)–(c)) (Zhang and Hüttinger, 2001 (c)).

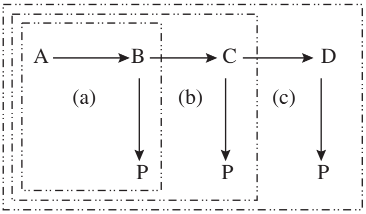

$$A = CH_4$$
$$B \approx C_2$$
$$C \approx C_6 \qquad (2)$$
$$D \approx C_n \ (n \geq 10)$$
$$P = C_\infty$$

First of all, it was demonstrated that the infiltration profiles must increase from the surface to the center. Furthermore, it was shown that the increase of the profiles is enhanced by an extended reaction sequence (eqs. 2(a)–(c)), an increasing infiltration depth and an increasing methane pressure. These calculations were confirmed in corresponding experimental studies (Hu and Hüttinger, 2001b). This revised interpretation of CVI can easily be understood knowing that diffusion of methane into the porous material is not a limiting factor, but diffusion of hydrocarbon species out of the porous material is more difficult at increasing size of the species, increasing depth and increasing methane pressure. It is obvious that a decomposition of methane outside of the porous material has to be avoided. With this technique fiber structures used for manufacturing break discs can be densified to a density above 1.7 $\mathrm{g cm^{-3}}$ within two days (Beinborn, 2000).

7 Considerations about the formation of different carbon microstructures

Carbon deposited by CVD may be isotropic or dark, smooth, and rough laminar microstructure (Dupel *et al.*, 1995). Rough laminar carbon exhibits the highest degree of crystalline preorder, it is graphitizable and preferred for industrial applications.

Models to correlate the various microstructures with deposition conditions or deposition chemistry, respectively, were proposed by several authors (Bokros *et al*., 1973; Pearson and Lieberman, 1975; Feron *et al*., 1995; Benzinger and Hüttinger, 1999a). In Feron *et al*. (1995) the structures were correlated with the size of the major carbon forming species, in Benzinger and Hüttinger (1999a) with the A/V ratio and thus indirectly with the size of the major carbon forming species. According to Feron *et al*. (1995) smooth laminar carbon is formed from small and rough laminar carbon from large hydrocarbon species. The conclusions from Benzinger and Hüttinger (1999a) are opposite, which demonstrates that a general correlation of deposition chemistry and kinetics with microstructures is more complex than postulated in these models.

The results of Section 5 may be used as a basis for a better understanding of structure formation. From low to medium pressures of methane the deposition is determined by Langmuir–Hinshelwood kinetics (Yang and Hougen, 1950; Corrigan, 1955). This implies that active sites are involved in the deposition process. Such sites exist at edges of or defects in graphene layers, respectively. It is self-evident that hydrocarbon species of any size are able to chemisorb at free sites and form carbon. According to the results of Sections 4 and 5 the size or nature of the major carbon forming species are controlled by the A/V ratio. The influence of size or nature of the major carbon forming species on the development of the various microstructures was clarified very recently (Dong and Hüttinger, 2002; Zhang and Hüttinger, 2002).

As soon as saturation adsorption is achieved a simultaneous deposition process which does not depend on the availability of active sites is favored or even dominant. At sufficiently high partial pressure aromatic hydrocarbons may be assumed to adsorb at the basal planes (Vorpagel and Lavin, 1992). An experimental confirmation of a planar adsorption was presented recently (Bouchard *et al*., 2001).

The above considerations are schematically summarized in Fig. 4.6. With respect to deposition of highly preordered carbon the deposition process at basal planes should be important. From the deposition rates it may be concluded that a multi-layer or a film of aromatic hydrocarbons is formed within a few seconds, provided that the rates of condensation reactions of adsorbed aromatics are low. In fact, these rates are low, because of the very high bond dissociation energy of the C–H-bond of about 461 kJ mol^{-1} (May *et al*., 2000). Low surface free energy of the basal planes and transient existence of a 'liquid' film of planarly stacked aromatic hydrocarbons would be optimal preconditions for development of a high preorder and the deposition of a highly textured or rough laminar carbon, respectively.

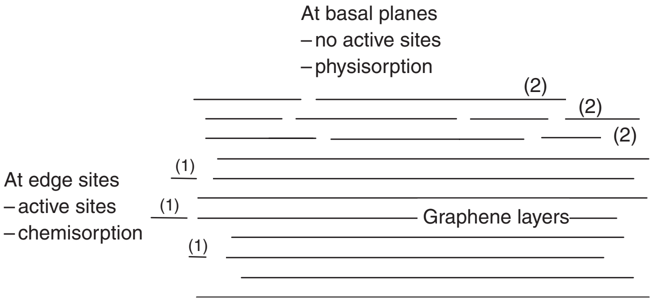

Figure 4.6 Scheme of carbon deposition at edge sites and basal planes. (1) Chemisorbed species (species of any size); (2) physisorbed species (large species).

Such a mechanism is known from the formation of highly preordered cokes involving the polyaromatic mesophase as an intermediate.

8 Summary

Chemical vapor deposition of carbon from light hydrocarbons is summarized with special consideration of CVI as the most important application of CVD. It is shown that CVD from small hydrocarbons is an extremely complex homogeneous–heterogeneous process. Homogeneous reactions lead to the formation of hydrocarbons of increasing size; aromatic and polycyclic aromatic hydrocarbons are dominating carbon forming species and important for the deposition of highly textured rough laminar carbon.

Gas phase reactions leading to hydrocarbons of increasing size are limited by consumption of reactive intermediates in surface reactions. The competition of gas phase and surface reactions is controlled by the A/V ratio; this ratio represents a third parameter of CVD, besides temperature and pressure or partial pressure. A variation of this parameter effects changes of deposition chemistry and kinetics as well as of structure of deposited carbon.

Deposition reactions may occur at active sites existing at edges of or at defects in the basal plane. Reactions at active sites are selectively inhibited by hydrogen depending on the C/H ratio and the molecular structure of a hydrocarbon. Inhibition is attributed to the C–H bond at the edges. Dissociation of this bond should be the rate limiting step of this deposition process the rate of which may also be limited by saturation adsorption occurring at increasing methane pressure. Most of these effects are shown to be advantageous to optimize CVI.

Deposition at active sites may result from hydrocarbon species of any size. Deposition on the basal planes is possible but limited to polycyclic aromatic hydrocarbons. Active sites are not necessary. This process should be important for deposition of highly textured, rough laminar carbon at temperatures relevant for CVI.

Acknowledgments

The assistance of Dr Z. J. Hu and Dr G. Schoch in preparing the manuscript, and discussions with Dr W. G. Zhang are gratefully acknowledged.

References

Andrä, H., Langhoff, T.-A., Schnack, E., and Hüttinger, K. J. (2000) Fuel **80** 1273.

Antes, J., Hu, Z. J., Zhang, W. G., and Hüttinger, K. J. (1999) Carbon **37** 2031.

Atakan, B., Hartlieb, A. T., Brand, J., and Kohse-Höinghaus, K. (1998) Twenty-Seventh Symposium (International) on Combustion/The Combustion Institute 435.

Bammidipati, S., Stewart, G. D., and Elliot, J. R. Jr (1996) AICHE Journal **42** 2123.

Baulch, D. L., Cobos, C. J., Cox, R. A., Frank, P., Hayman, G. Just, Th., Kess, J. A., Murrells, T., Pilling, M. J., Troe, J., Walker, R. W., and Warnatz, J. J. (1994) J. Phys. Chem. Ref. Data **23** 847.

Becker, A. and Hüttinger, K. J. (1998a) Carbon **36** 177.

Becker, A. and Hüttinger, K. J. (1998b) Carbon **36** 213.

Becker, A., Hu, Z. J., and Hüttinger, K. J. (1999) J. Phys. IV France **9** Pr 8–41.

Becker, A., Hu, Z. J., and Hüttinger, K. J. (2000) Fuel **79** 1573.

Beinborn, K. M., Sintec Keramik GmbH, personal communication.

Benzinger, W., Becker, A., and Hüttinger, K. J. (1996) Carbon **34** 957.

Benzinger, W. and Hüttinger, K. J. (1996a) Carbon **34** 1465.

Benzinger, W. and Hüttinger, K. J. (1996b) Carbon **34** 1465.

Benzinger, W. and Hüttinger, K. J. (1998) Carbon **36** 1033.

Benzinger, W. and Hüttinger, K. J. (1999a) Carbon **37** 1311.
Benzinger, W. and Hüttinger, K. J. (1999b) Carbon **37** 187.
Birakayala, N. and Evans, E. A. (2002) Carbon **40** 675.
Bockhorn, H., University of Karlsruhe, personal communication.
Bokros, J. C. (1969) in *Chemistry and Physics of Carbon*, Vol. 5, 1–118, M. Dekker, New York.
Bokros, J. C., La Grange, L. D., and Schoen, F. J. (1973) in *Chemistry and Physics of Carbon*, Vol. 9, 103–72, M. Dekker, New York.
Bouchard, E., Lavenac, J., Roux, J. C., Langlais, F., and Delhaes, P. (2001) Adv. Mater.-CVD **7** 7.3, 125–130.
Brüggert, M., Hu, Z. J., and Hüttinger, K. J. (1999) Carbon **37** 2021.
Chen, C.-J. and Back, M. H. (1979) Carbon **17** 175.
Corrigan, T. E. (1955) Chem. Eng. Fundamentals 199.
Dean, A. M. (1990) J. Phys. Chem. **94** 1432.
Dong, G. L. and Hüttinger, K. J. (2002) Carbon **40** 2575.
Dupel, P., Bourrat, X., and Pailler, R. (1995) Carbon **33** 1193.
Eisenberg, B. and Bliss, H. (1967) Chem. Eng. Progr. Symp. Series **63** 3.
Feron, O., Langlais, F., and Naslain, R. (1999) Adv. Mater.-CVD **5** 37.
Feron, O., Langlais, F., and Naslain, R. (1998) Int. Symp. on Carbon (Tokyo) 54.
Feron, O., Langlais, F., Naslain, R., and Thebault, J. (1995) Carbon **33** 1193.
Frenklach, M. and Wang, H. (1994) in *Soot Formation in Combustion* (H. Bockhorn, ed.), 162–92 Springer, Berlin.
Glasier, G. F. and Pacey Ph.D. (2001) Carbon **39** 15.
Hitchman, M. L. and Jensen, K. F. eds. (1993) *Chemical Vapor Deposition,* Academic Press, London.
Hu, Z. J. and Hüttinger, K. J. (2000) Adv. Mater.-CVD **6** 77.
Hu, Z. J. and Hüttinger, K. J. (2001a) Carbon **39** 433.
Hu, Z. J. and Hüttinger, K. J. (2001b) Carbon **39** 1023–1032.
Hüttinger, K. J. (1998) Adv. Mater.-CVD **4** 147.
Kotlenski, W. V. (1973) in *Chemistry and Physics of Carbon*, Vol. 9, 173–262, M. Dekker, New York.
Lersmacher, B., Lydtin, N., Knippenberg, W. F., and Moore, A. W. (1967) Carbon **5** 205.
Loll, P., Delhaes, P., and Pacault, A. (1977) Carbon **15** 383.
Lucas, P. and Marchand, A. (1990) Carbon **28** 207.
Marinov, H., Pitz, W., Westbrook, C. K., Castaldi, M. J., and Senkan, S. M. (1996) Combustion Sci. and Tech. **116–117** 211.
May, K., Dapprich, S., Furche, F., Unterreiner, B. V., and Ahlrichs, R. (2000) Phys. Chem. Chem. Phys **2** 5084.
Murphy, D. B. and Carrol, R. W. (1992) Carbon **30** 47.
Murphy, D. B., Carrol, R. W., and Kolonowski, J. E. (1997) Carbon **35** 1819.
Palmer, H. B., Lahaye, J., and Hou, K. C. (1968) J. Phys. Chem. **72** 348.
Pearson, H. O. and Lieberman, M. L. (1975) Carbon **13** 159.
Sarofim, A. F., Longwell, J. P., Wornat, M. J., and Mukherjee, J. (1994) in *Soot Formation in Combustion* (H. Bockhorn, ed.), 485–500, Springer, Berlin.
Tesner, P. A. (1984) in *Chemistry and Physics of Carbon*, Vol. 19, 65, M. Dekker, New York.
Teubner, M., Hu, Z. J., and Hüttinger, K. J. (2000) High Temp. – High Press. **32** 725.
Vorpagel, E. R. and Lavin, J. G. (1992) Carbon **30** 1033.
Wang, H. and Frenklach, M. (1997) Combustion and Flame **110** 173.
Yang, K. H. and Hougen, O. A. (1950) Chem. Eng. Progr. **46** 146.
Zhang, W. G. and Hüttinger, K. J. (2001a) J. Mater. Sci. **36** 3503.
Zhang, W. G. and Hüttinger, K. J. (2001b) Adv. Mater.-CVD **7** 173.
Zhang, W. G. and Hüttinger, K. J. (2001c) Carbon **39** 1013.
Zhang, W. G. and Hüttinger, K. J. (2002) Carbon **40** 2529.
Zhang, Z., Lussier, M. G., and Miller, D. J. (2000) Carbon **38** 1289.

5

CHEMICAL VAPOR INFILTRATION PROCESSES OF CARBON MATERIALS

P. Delhaès

1 Introduction

Monolithic carbons as well as thin films or carbon–carbon composites are prepared from pyrolysis and consequent carbonization of an initial organic phase. Compared to bulk pieces these composites present a noncatastrophic failure under severe experimental constraints: this is the basic reason for their broad applications (Delmonte, 1981). Before going into the details of the different processes and the associated composites manufacturing it is noteworthy to remind some basic concepts on carbon deposition. Indeed the structures and properties of a deposited carbon or pyrocarbon are related to the pyrolysis conditions which control the mechanisms of carbon formation. The matrix precursor can be either liquids or gases; in the first case the process is labelled as the impregnation technique starting usually from fluid resins or pitches (Rand, 1993). The second process is the cracking of a hydrocarbon gas at high temperature under an inert atmosphere. The associated coating process on hot bulk surfaces is called the chemical vapor deposition (CVD) and alternatively on porous substrates the chemical vapor infiltration (CVI) technique.

In this chapter, we will examine mainly the thermal decomposition of an hydrocarbon gas, the most versatile deposition process, which is widely used to make carbon–carbon composites; starting from a porous preform made of shopped or continuous carbon fibers, arranged in different bundles arrays, which are usually ex polyacrilonitrile (PAN) type. These composites are realized by filling all the voids of these preforms with an adapted fiber–matrix interaction (Inagaki, 2000).

This presentation will start with a comparison between the CVD and CVI processes including the historical aspects which have been introduced a long time ago.

Both techniques are based on the competition between the chemical reactions and the physical transport properties as discussed in Section 2. Then in Section 3 we present the different processes starting from pioneering works in the sixties until the more recent improved processes. Several new approaches have been developed these last years to optimize the infiltration processes and to understand them keeping in mind that the two key points are to speed up the deposition efficiency and to ameliorate the deposit quality of the matrix.

In Section 4, the approach will deal with the study of the formation of pyrocarbons, their different microstructures described at different length scales and their growing stability.

They are functions of different external parameters that we will analyze to establish a relationship between the deposition mechanisms and the structural and physical properties of the matrix. These pyrocarbons will be defined as a subclass of non-crystalline graphitic carbons (Delhaès, 2000). In Section 5 some basic concepts regarding a few infiltration models are presented; our approach starting with thermodynamics equilibrium at the first level is relevant to out-of-equilibrium modeling. The main emphasis will be about the competition and the interactions between the chemical kinetics and the transport coefficients in a porous medium. Dynamic modeling of CVI processes result from these theoretical works.

Finally the physical properties and the numerous applications of carbon–carbon composites are summarized. They are related to their peculiar characteristics – light weight associated with high mechanical strength including stiffness, wear, toughness, and thermal shock resistance.

2 General background on CVD and CVI processes

2.1 Definitions and outlines

The different types of allotropic forms for crystalline as well as non-crystalline carbons are essentially functions of two basic parameters. They are the nature and phase of the precursor and the experimental method selected to deliver the process energy respectively (Delhaès and Carmona, 1981). Indeed the final product, except hexagonal graphite, is in a metastable thermodynamic state which needs to be defined. Two main classes of precursors exist, either pure solid carbons or various gas and liquid hydrocarbons containing possibly hetero-elements as oxygen, nitrogen or even halogens. In the first case, this is a physical process as produced by thermal or laser beam evaporation, ion-plasma techniques as electrical discharges or sputtering techniques. Starting from hydrocarbon precursors rather complex chemical processes are ocurring including the pyrolysis and carbonization steps to obtain a pyrocarbon coating. In that situation the supplementary energy is also afforded by similar techniques but the control of the complex and numerous chemical reactions is essential. This is the natural approach for CVI processes that we are developing in this chapter. Following a chronological approach it is necessary to remind that the main point is to control both the homogeneous gas phase reactions and the heterogeneous ones at the solid–gas interface, and thereafter the deposition mechanism on a selected substrate. Many studies have been accomplished to understand the mechanism of carbon formation from different gaseous organic compounds (Tesner, 1984) and to establish a relationship between the deposition conditions and the structures of pyrocarbons (Bokros, 1969). Before going into the details of the physical process which can be defined as a balance between chemistry and hydrodynamics we will introduce the basic chemical mechanisms which have been established with some emphasis on the progress gained during these last years.

2.2 Chemistry of carbon formation

We summarize both the mechanisms and kinetics of the overall reactions. In general the precursors are alcanes, usually methane or propane, but also non-saturated hydrocarbons (such as acetylene or propylene) or aromatic molecules (benzene and derivatives) which are decomposed at a lower temperature than the alcanes. From all the experimental studies it results that a general trend can be drawn to furnish an overall reaction modeling which consider two main classes (Hüttinger, 1998).

Homogeneous gas phase reactions The radical processes are favorized, the primary and secondary mechanisms give birth to free radicals which are recombined immediately. In a first step non-saturated species (as allenes, propyne, butadiene) are formed. Following the formation of these aliphatic compounds different cyclization processes occur; there are mainly the C_3 and C_4 cyclization ways and the HACA (H abstraction and C_2H_2 addition) mechanisms (Frenklach, 1996). Aromatics and polyaromatics (HAP) are formed for a longer reaction time (Lucas and Marchand, 1990). This is the so-called maturation effect involving the aromatic route which depends on the residence time of the molecules in the free reacting volume (Ferron *et al*., 1999). In situ spectroscopic analysis have been carried out to follow both the mechanisms and kinetics of these complex reactions (Chen and Back, 1979; Ferron *et al*., 1997). They give valuable information but no definite results for the complete understanding of the pyrocarbon deposition. Indeed the active species are essentially free radicals which are instable (life-time about 0.01 sec). The stable molecules which are side products, not directly transformed in solid carbon, are preferentially detected by these different analytical techniques as mass spectroscopy or gas chromatography.

Heterogeneous surface reactions They are fundamental for the formation rate of pyrocarbons, starting from the nucleation and the growing processes on a given substrate. These interfacial reactions, associated with sticking coefficients and surface migrations, specific for each species, have been investigated for a long time (Tesner, 1984); they are very difficult to analyze and therefore to control. One attempt has been to consider Langmuir–Hinshelwood model for the kinetics of surface reactions (Benziger and Hüttinger, 1999a,b). In particular, the influence of catalysts as transition metals and additive reacting gas are predominant factors. For example, hydrogen but also oxygen or chlorine gas play a role for both the deposition mechanism and the type of deposit.

Starting from the initial works (Diefendorf, 1960; Tesner, 1984) many studies have been done to understand the intrinsic mechanisms but with a rather small insight for the details of the chemical roads which remain a current challenge.

In conclusion, without taking account of the specific nature of the pristine gases, a summary of all the possible generic radical type reactions is given on the schema presented in Fig. 5.1 (Hüttinger, 1998). The chemistry inside the homogeneous gas phase leads to the aliphatic formation (C_2) as ethylene or acetylene, then the aromatic route (C_6) of benzene type species, and the formation of polyaromatics, then droplets in the gas phase (homogeneous nucleation) when the residence time is long enough (Grisdale, 1953).

This is in qualitative agreement with the thermodynamic calculations at thermal equilibrium concerning acetylenic and aromatic species carried out with thermodynamic softwares

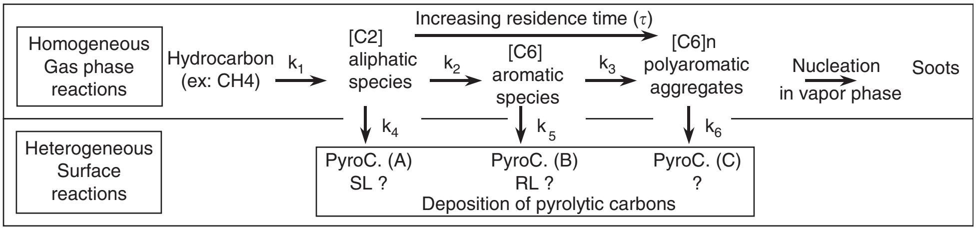

Figure 5.1 Simplified reaction scheme for pyrocarbon deposition; the rate constants are labelled (Ki) (adapted from Hüttinger, 1998).

for methane (Lieberman and Pierson, 1974) and other hydrocarbons (Diefendorf, 1969) and confirmed by experiments in closed systems. The first authors defined an equilibrium ratio $R = C_2H_2/C_6H_6$ function of P and T, which is relevant for further correlation to the type of deposited pyrocarbon (see Section 4).

2.3 Deposition mechanisms

It concerns essentially the condensation of gases on a solid surface, i.e. the nucleus and growing mechanisms. The basic thermodynamic approach for a hemispheric germ indicates that the Gibbs enthalpy for heterogeneous nucleation is always lower than for the homogeneous one, depending on the contact angle and the wetting conditions on a given substrate (Adamson, 1976).

The experimental consequence is that a pyrocarbon should be deposited at a lower T and (or) P than predicted by the classical homogeneous nucleation which gives rise to the formation of carbon blacks (Donnet and Voet, 1976). This is an interfacial property depending on both the nature of the gas phase and the solid surface. It has been shown that the substrate plays a role for the first pyrocarbon layers from the physical (roughness, curvature and surface energy) and chemical (nucleation sites) point of view. In particular it has been demonstrated that the active sites on a graphene surface and the plane edges are the preferential nucleation sites which control the first step for the kinetic deposition (Hoffman *et al.*, 1985). In this chemisorption process the main parameter is the active surface area (ASA) and its percentage with the total area (Ismail and Hoffman, 1991). More recently it has been evidenced by scanning tunneling microscopy (STM) on a pyrographite that the initial deposit is sensitive to the residence time parameter and a sort of wetting transition is detected associated with a morphological change indicating the influence of the gas composition on the adsorption process (Bouchard *et al.*, 2001). This ideal substrate which presents a low surface energy is strongly modified for non-crystalline carbons as fibers; the density of active sites is much more higher and controls the pyrocarbon deposit (Ismail and Hoffman, 1991) and therefore the interfacial strength between fibers and matrix.

Other planar substrates have been used for electron microscopy works as, for example, alumina (Desprez and Oberlin, 1997; Soutric, 1998) or boron nitride (De Pauw *et al.*, 2003); apparently it does not change strongly the kinetics on the growing process after deposit of the first layers. This growing process has also been examined by several authors (Kaae, 1985). Two types of cone structures are usually recognized when the nucleus are created only on the substrate or regenerated at different levels (Diefendorf, 1960). These various features include the structure of nodules under different substrate conditions as presented in Fig. 5.2 (Coffin, 1964). As developed in classical CVD models (Bryant, 1977) the morphology of pyrocarbons with their cone growing structure, and through their density and porosity, are functions of the deposit conditions. In particular when the coating temperature is as high as 1,500 °C a less dense pyrocarbon is obtained which is considered as a non-graphitable carbon (Ford and Bilsby, 1976).

2.4 Comparison between standard CVD and CVI processes

In a standard technique, i.e. under isothermal and isobaric conditions the main difference between CVD and CVI concerns the type of substrate. As pointed out during the early studies (Kotlensky, 1973) there are very strong similarities between the pyrocarbon deposition

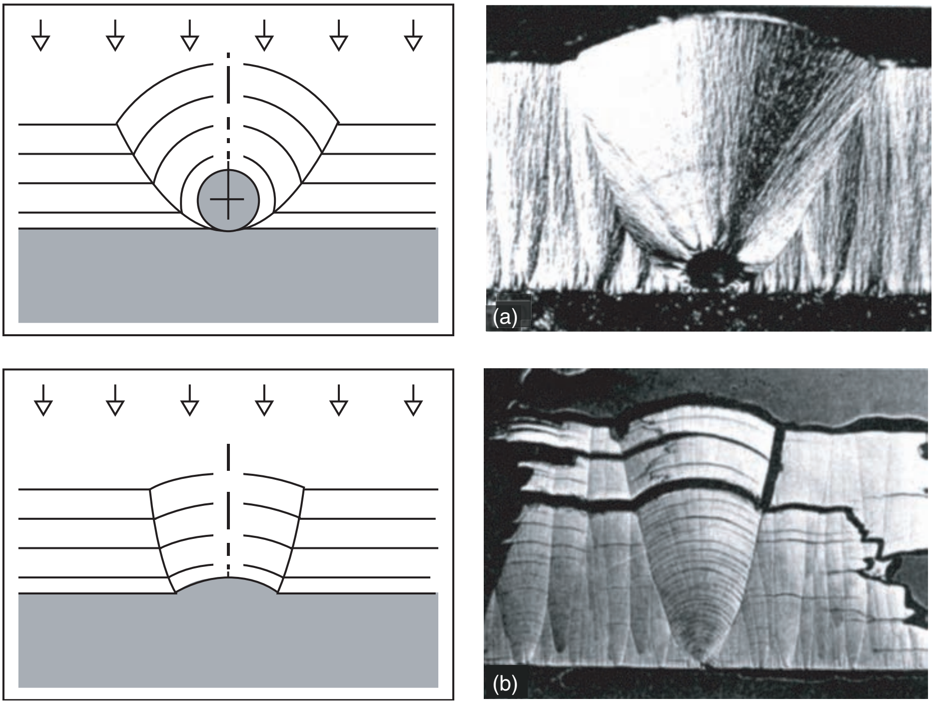

Figure 5.2 Cross sections of a nodule of pyrocarbon with the associated model (from Coffin, 1964): (a) nodule formed from surface asperity; (b) nodule formed from a foreign particle.

on a static substrate or a dynamic bulk surface, the so-called usual fluid bed technique, and the carbon growth inside a porous substrate. The phenomenological competition between the mass and heat transport phenomena and the overall chemical reactions is the basic point to consider. We can enounce two statements which are fundamental in this presentation:

(i) The overall chemistry by itself is mainly related to the local conditions in particular for the surface reactions. For a given precursor, they are supposed very similar in the gas phase for both CVD and CVI processes. However with porous preforms an increase of the surface to volume ratio (S/V) is a novel parameter to take into account (Hüttinger, 1998). As shown on the simplified schema presented Fig. 5.1, the deposits will result from the competition between the rate constants of the homogeneous and heterogeneous reactions.

(ii) The transport phenomena related to the hydrodynamics of fluids and to the energetic supply would be quite different. They are submitted to different scale factors related to the piece and reactor sizes which are sometimes very different (as in classical CVD) or comparable: they have to be examined for each type of process (see Section 3); on a general way the kinetic deposition of pyrocarbons can be represented by an Arrhenius plot which describes the general heterogeneous reactions of gases with porous solids (Hedden and Wicke, 1957). As presented in Fig. 5.3 three different regimes are recognized; they are related by a different rate limiting step. In regime I, at low temperatures the deposition rate (k) is

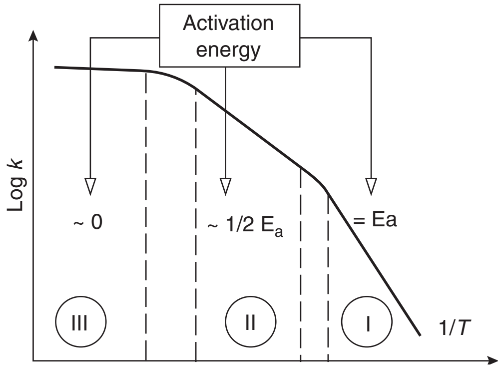

Figure 5.3 Characteristic Arrhenius plot: k versus T^{-1} with $k = k_0 \cdot \exp\,(-\mathrm{Ea}/kT)$, involving a reacting gas and a porous medium (from Hedden and Wicke, 1957).

determined by the kinetics of the chemical reactions with an apparent activation energy (Ea) and the concentration gradient across the porous solid is negligible. At intermediary temperatures, within regime II the mass diffusion through the pores influences the rate of conversion which should correspond to about half-value of Ea. When the temperature is raised the diffusion factor becomes comparable with the rate reactions leading to an internal concentration gradient. Then in regime III at high temperatures the rate deposition becomes almost independant; the diffusion of gases through the stagnant boundary layer which always exists in a laminar flow (Carlsson, 1985), controls the process. In this last case the carbon infiltration inside the pores is not effective; a deposition rate of about a few microns per hour is usually observed. This is the main limitation for the usual making of these C/C composites as we will consider it in the following sections.

3 CVI processes and efficiency

The infiltration and the deposition of pyrocarbons in different porous substrates have been largely investigated starting from the classical isothermal and isobaric process. Its major drawback is the very low infiltration rate related to the diffusion constants. Many developments have been published to improve this situation in this multiparameter technique. As presented in Fig. 5.4, for the system responses we will analyze the matrix characteristics in relation with the following two major requirements, infiltration homogeneity and microstructure control of the matrix.

3.1 The process parameters

The numerous external constraints acting at different scales are divided into three different classes as summarized in Fig. 5.4:

(i) Geometrical and Energetical – considering the sources of heat and their distribution inside the reactor and the preform. The heating method, resistive inductive or radiative, is associated with either hot wall or cold wall reactors. This is a basic difference which

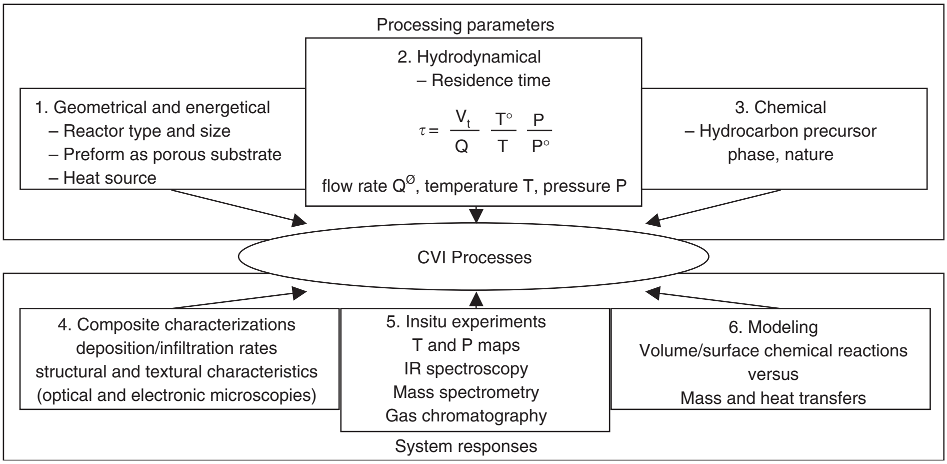

Figure 5.4 Summary of the parameters and system responses in CVI processes.

involves for hot wall technique isothermal and isobaric conditions whereas thermal gradients (Lieberman *et al*., 1975) or pressure gradients and forced flows (Lackey and Starr, 1991) exist in the cold wall approach. This one can be also combined with either laser or DC and RF plasma uses (Lachter *et al*., 1985; Levesque *et al*., 1989).

The preform to densify is also crucial through its nature, orientation, and volumic fraction of the carbon fibers (Delhaès *et al*., 1984); its position and volume occupation inside the furnace are noteworthy.

(ii) Hydrodynamical – the flow regime inside the reactor is related to the nature of the precursor fluid but also the size and the shape of the reactor; usually a low value of the Rayleigh number characterizes this laminar flow. The precursors are in a gaseous phase at different pressures; under isothermal conditions a laminar flow is expected and the residence time (see definition, Fig. 5.4) is the key parameter. However a forced flow will conduct to a quite different behavior as already demonstrated (Vaidyaraman *et al*., 1996).

(iii) Chemical – the nature of the precursor is important even if the generic reactions are recognized (Fig. 5.1). For example natural gas i.e. methane, is the most stable hydrocarbon and the associated decomposition conditions will be specific compared to the other precursors. Besides liquid precursors, as cyclohexane and aromatic derivatives have been also used in a new fast densification technique that we will describe later (David *et al*., 1995).

A complementary approach concerns the system responses as presented in Fig 5.3: the first ones are the material requirements, essentially the type of carbon matrix, the deposition rates, and the overall carbon yield. Its quality has to be optimized with the highest final density and a well defined type of microstructure. The classical “black box” approach which concerns only ex situ relevant parameters (Loll *et al*., 1977) has been recently improved. Both experimental and theoretical approaches have been developed. In situ observations by FTIR in-line mass spectroscopy or gas chromatography, have deepened the gas chemistry (Chen and Back, 1979; Ferron *et al*., 1999) and global modeling of engineering techniques are in constant progress (Ofori and Sotirchos, 1997). They will contribute in the future to the overall process control.

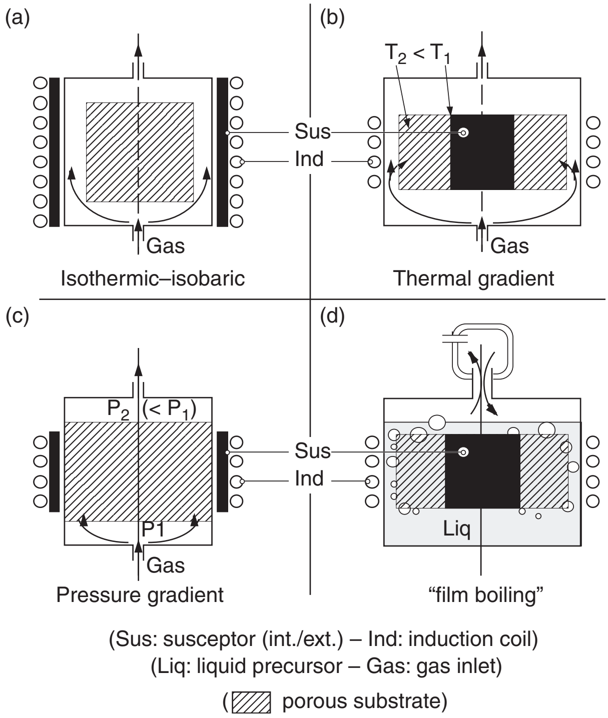

Figure 5.5 Sketches of the basic infiltration techniques (adapted from Kotlensky, 1973).

3.2 Outline of the principal methods

The basic infiltration techniques are schematically drawn in Fig. 5.5. As recently underlined by Golecki the various infiltration methods are at different stages of maturity and understanding (Golecki, 1997). The isothermal and isobaric CVI, the oldest "hot wall" technique, is still widely used both in laboratories and industry. Its main advantage is a good parameter control, in particular for large furnaces where a large number of complex preforms can be densified together. As already indicated a good matrix quality with a selected microstructure and a low residual porosity is obtained (Lackey and Starr, 1991). The main drawback is a quite long processing time, sometimes larger than 500 h with a very slow rate of deposit associated with a very low overall precursor efficiency, a few percent only with the natural gas. New routes to develop rapid infiltration techniques have been explored to increase the process efficiency. We present them, giving some interesting examples:

(i) Derived from the isothermal process, three ways have been explored: the catalytic CVI using transition metals for increasing the rate deposition (McAllister and Wolf, 1993), the plasma enhanced CVI (Levesque *et al.*, 1989), and the pulsed flow where a cyclic evacuation of the reaction chamber and a back filling with reagents is done (Dupel *et al.*, 1994). These approaches appear more interesting for the basic understanding of the infiltration mechanisms than to get an economical and technical gain.

(ii) Pressure gradient and forced flows: Several reactors have been built to control the gas hydrodynamics under isothermal conditions or with thermal gradient (Lackey and Starr, 1991). In particular the forced flow-thermal gradient CVI process (see Fig. 5.6) has been thoroughly developed (Vaidyaraman *et al.*, 1995). The fabrication of valuable C/C composites with a matrix of uniform high thermal conductivity onto conventional size fibers is realized in a few hours under controlled parameters (Lewis *et al.*, 1997).

(iii) Strong thermal gradients under quasi isobaric conditions: this is the case of cold wall reactors with a graphite susceptor inside (see Fig. 5.5d). The precursors are in a gaseous or liquid state; nevertheless in both situations there is a mobile reacting front on which the vapors decompose to produce the carbon deposit. Two main type of reactors have been realized with similar cylindrical geometries, the rapid vapor phase densification and the film boiling technique based on a liquid reservoir (Fig. 5.7). Both techniques are very efficient, a single cycle of densification for a few hours as for the forced flow method is sufficient in the range. A high conversion efficiency is obtained, one order of magnitude higher than is classical processes i.e 20–50%, associated with a good quality of the final products (Golecki *et al.*, 1995). To get a better insight on this type of process a small laboratory reactor equipped with an internal resistive heater has been built up (Rovillain *et al.*, 2001) which can work with various liquid precursors. As shown in Fig. 5.8 this process is based on a mobile reactive front with a steep densification profile which starts from the central part of the preform to the outside. This novel process has been widely investigated these last years concerning the chemical influence with halogen derivatives or iron catalytic effect (Okuno *et al.*, 2001) and the hydrodynamical aspect with a mass barrier effect and the influence of high pressure reagents (Beaugrand, 2000). The essential parameter appears to be the evolutive thermal gradient across the preform which controls both the high infiltration speed and the type of pyrocarbons.

To conclude it should be mentioned that these industrial applications are covered by numerous patents; a comparison between these processes with their advantages and disadvantages are presented in Chapter 6 (Golecki, 2003).

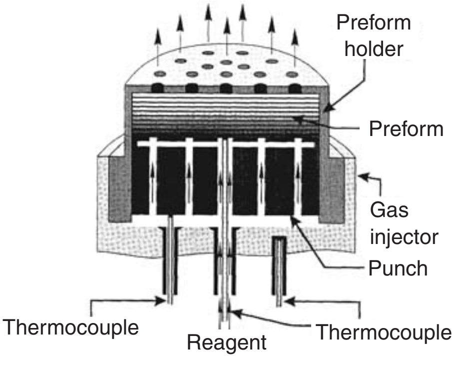

Figure 5.6 Schematic of the preform and the reactor used in forced-CVI process (from Lewis *et al.*, 1996).

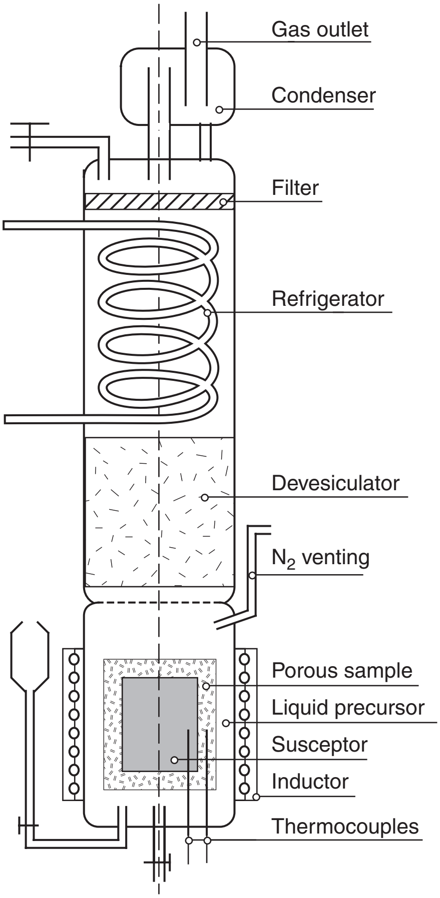

Figure 5.7 Boiling film CVI reactor with induction heating of an internal graphite susceptor immersed in the liquid precursor (from David *et al.*, 1995).

4 Pyrocarbon microstructures

For a long time different types of deposited pyrocarbons have been recognized and well characterized at various length scales. These microstructures are on the one hand dependant on the experimental parameters and techniques and on the other they present reproducible structural and physical characteristics that we will summarize. Indeed it has been observed that typical intrinsic microstructures which are obtained are basically the same for every CVD and CVI process. We will discuss both aspects in the following section.

4.1 The different types of pyrocarbons

In a pioneering work Bokros has identified the experimental conditions favoring the depositions in fluid beds of anisotropic types, i.e. laminar or granular-columnar, and isotropic carbon structures (Bokros, 1969). Following Bokros' work, Lieberman and Pierson in the

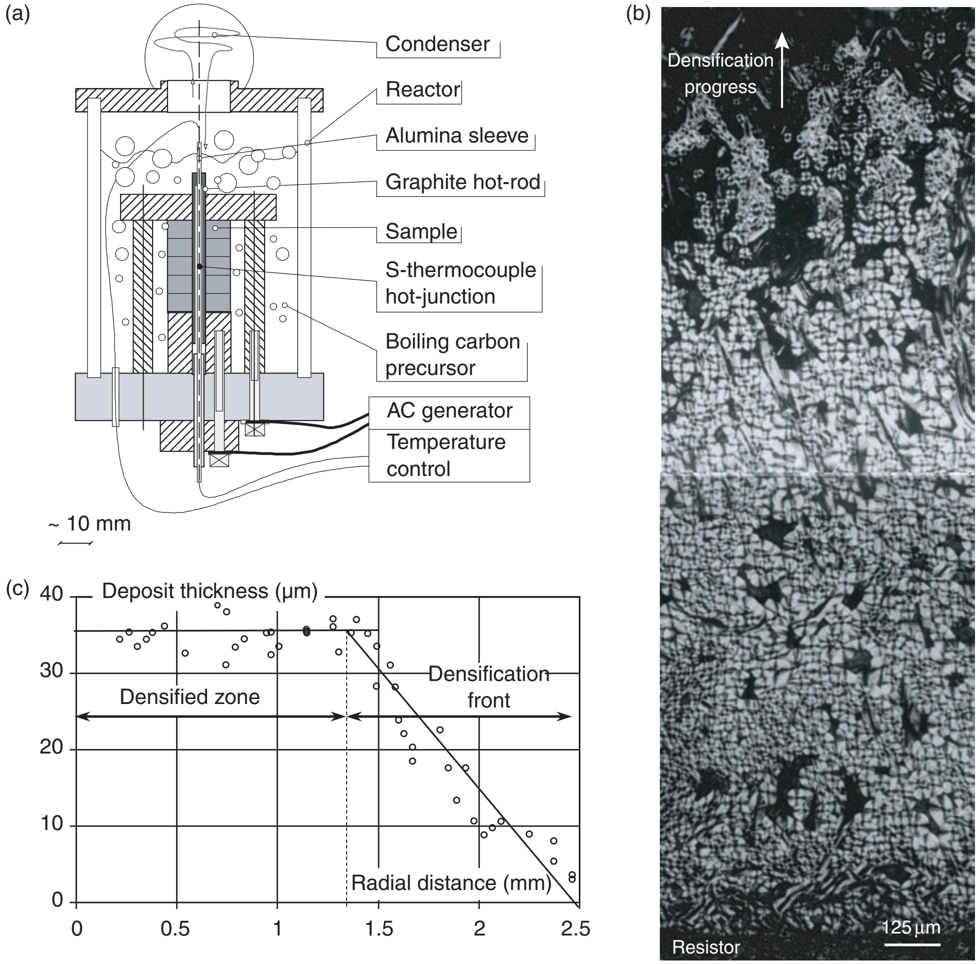

Figure 5.8 Boiling film technique (from Rovillain *et al.*, 2001): (a) Laboratory reactor with resistive heating; (b) cross-section observed by optical microscopy of a partially densified felt (with cyclohexane at T = 1250 °C during 30 min); (c) radial densification profile determined from the photograph presented in (b).

1970s, have proposed a structural classification issued from this optical microscopy observations for the densification process of porous substrates. From polarized optical analysis they defined three main microstructures. They are called smooth laminar (SL), rough laminar (RL), and isotropic (ISO) carbons respectively, based on the shape and contrast of the optical photomicrographs of carbon composites; intermediary state between smooth laminar and isotropic microstructure is also noticed as granular or dark laminar carbon (Lieberman and Pierson, 1974). We will define these structural organizations at different complementary scales, thanks to X-ray diffraction, optical, and electronic microscopies respectively.

The optical texture of these pyrocarbons has been defined from the bireflectance of graphite and graphitic carbons. Several methods have been proposed to quantify the reflectance anisotropy (Bourrat *et al.*, 2000). One usual way is to measure the extinction angle Ae between cross polarizer and analyzer set up perpendicularly to a coated fiber because an axial symmetry is required to observe the Maltese cross. This angle depends on the amplitude of the beam transmitted parallel to the anisotropic plane regarding the normal direction. As presented in Table 5.1 the larger the extinction angle, the higher is the structural anisotropy (the intermediary dark laminar structure is defined for $4° < Ae < 12°$).

A complementary approach is to measure the layer anisotropy by electron diffraction by means of a varieties of transmission electron microscopy techniques (TEM) (Bourrat *et al.*, 2000). The different pyrocarbons are described by the size of the basic structural units (BSU), the mean carbon layers (L2), and the number of these aromatic layers coherently stacked together with a characteristic interlayer distance (d_{002} spacing) and defined with a mean orientation angle. Moreover recent TEM observations have shown that the growing modes are different with a dense columnar type for RL microstructure and a rather non-planar lateral type for SL one (Lavenac, 2000). As summarized in Table 5.1 every microstructure is defined through specific structural and physical properties. The most anisotropic microstructure is RL which presents also the largest specific mass because of both the better nanostructural organization and the absence of any intrinsic porosity as observed by TEM (Goma and Oberlin, 1986). The most significant point is that RL is the only one which is graphitable under further heat treatment (HTT °C), i.e. evoluting toward the stable thermodynamic phase of hexagonal graphite as indicated by the d_{002} spacing in Table 5.1 (for a single crystal of graphite $d_{002} = 3.354$Å at room temperature). Following the same way the electronic, thermal, and mechanical characteristics of each microstructure has been recognized for a long time (Granoff *et al.*, 1973; Loll *et al.*, 1977). They are in favor of the RL microstructure for most of the composite applications. A bulk property as the diamagnetic susceptibility and its anisotropy can be used to relate the preferred orientation of the surface delocalization of π electrons. As in optical birefringence the Landau type diamagnetism depends on the aromatic size, the L2 parameter, and the associated orientation angle (Flandrois, 2000). A relationship exists between this normalized diamagnetic anisotropy and the matrix density as shown in Fig. 5.9 (Delhaès, 1998), and in agreement

Table 5.1 Physical and structural characteristics of the main carbon microstructures (from Delhaès, 1998)

Pyrocarbon microstructure / *Structural and physical characteristics*	*Isotropic (ISO)*	*Smooth laminar (SL)*	*Rough laminar (RL)*
Matrix density	1.8–1.5	1.9–1.7	2.1–2.0
Optical anisotropy	$Ae < 4°$	$12° < Ae < 18°$	$Ae > 18°$
Extinction angle: Ae	dark image	smooth crosses	irregular black crosses
Diamagnetic anisotropy	very weak	weak	strong
TEM experiments	micropores	flattened pores	no pores
Graphitizability	No	No	Yes
d_{002} after HTT = 2800 °C	~ 3.44 Å	<3.44 Å	≂3.37 Å

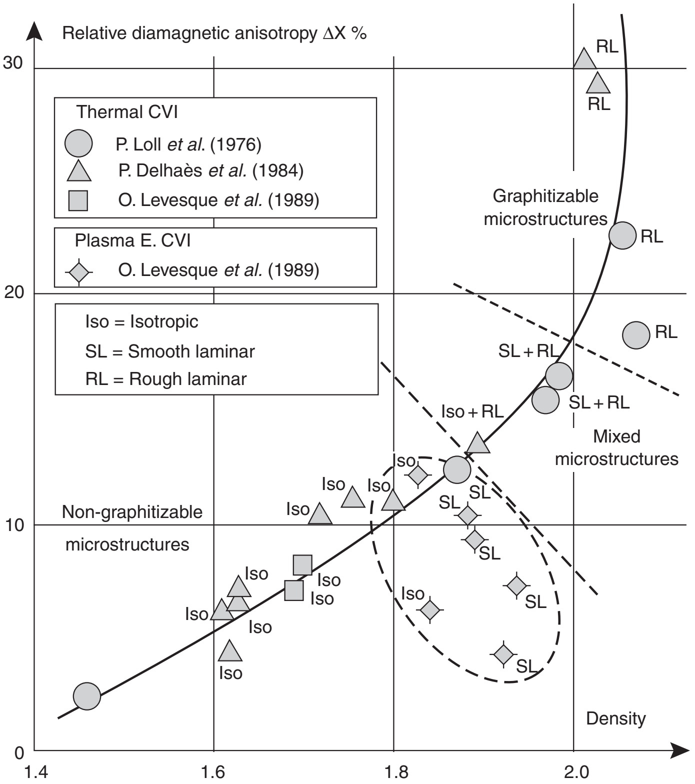

Figure 5.9 Relationship between the relative diamagnetic anisotropy ΔX % and the matrix density for each type of microstructure (from Delhaès, 1998).

with recent TEM observations. Besides the related mean values, upper for the isotropic microstructure than for the anisotropic one, indicates more developed BSU as expected for a longer residence time in gas phase (Fig. 5.1).

These results are confirmed by Raman spectroscopy; indeed in first order Raman spectra, the ideal graphite presents a characteristic single peak at 1580 cm^{-1} (G-band) but for any type of graphitic carbon, a second peak is appearing around 1350 cm^{-1} (D-band) (Lespade *et al.*, 1984). The intensity ratio between these two bands, as already proposed (Truinstra and Koenig, 1970), is a valuable indicator to characterize the local organization occurring in these microstructures. A characteristic behavior is observed for these microstructures which behave as a regular metastable phase with intrinsic characteristics which are not process dependent.

4.2 Existence diagram and phase stability

A correlation between the deposition parameters and the defined microstructures can be drawn for a given experimental set-up working under isothermal and isobaric conditions

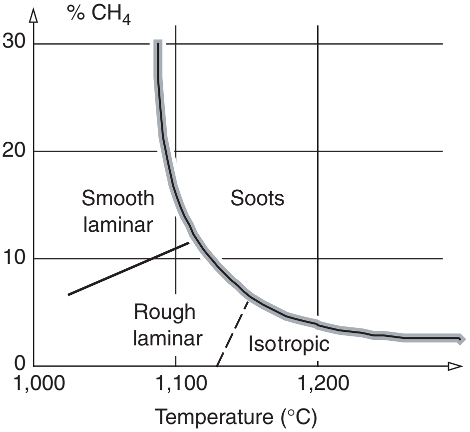

Figure 5.10 Existence diagram of the different microstructures obtained by infiltration inside a carbon felt and playing with two parameters, the proportion of CH_4 in CH_4–N_2 mixture under atmospheric pressure and the temperature of deposition (from Loll *et al*., 1977).

(hot wall reactors). Indeed an existence diagram which represents the different "phases" can be drawn for a given set of experimental constraints. As presented Fig. 5.10 a general boundary is defined between homogeneous vapor nucleation and hetereogeneous one at the gas–solid interface resulting from the competing homogeneous and heterogeneous chemical reaction (see Fig. 5.1). Then for a given set of hydrodynamic parameters, in particular for a fixed gas flow, it is shown that SL is formed at low temperatures and high partial pressure of methane whereas RL is deposited in the medium range and ISO at high temperature with a rather low pressure. The boundary between RL and SL domains is sharp, reminiscent of a first order phase transition, but the change between SL and ISO microstructures is progressive, justifying the introduction of a granular or dark laminar intermediate.

These observations are functions of the experimental parameters as the nature and the initial porosity of the substrate (Delhaès *et al*., 1984) or the nature of the hydrocarbon precursor (Ferron *et al*., 1999). As shown in Fig. 5.10 a sequence SL–RL–SL is observed when the residence time is increasing at a fixed deposit temperature. More generally they do not depend on the used process as for example with the film boiling technique where RL microstructure is preferentially deposited (Bruneton *et al*., 1997).

Besides, a combination of alternative microstructures is quite often detected during the overall infiltration process in particular inside a bundle of single filaments (Pierson and Lieberman, 1975; Loll *et al*., 1977; McAllister and Wolf, 1993; Dupel *et al*., 1994; Benzinger and Hüttinger, 1999b). Sequences of (RL–SL) microstructures are observed by polarized optical microscopy which could result from a change of the local conditions, out of the control of the external parameters. These morphological changes are tentatively interpreted as a bi-stability effect known in non-linear thermodynamics systems (Vignoles *et al*., 2001).

4.3 Deposition and infiltration rates

These process characteristics are strongly dependent on the selected reactor but some global trends can be drawn.

(i) The deposition rate defined as the thickness or locally deposited pyrocarbon per unit of time, on a planar or curved, as a single filament, substrate. It is well known that for the CVI isothermal process because of the rate limiting step due to the diffusion factor (see Fig. 5.1) a very low deposition speed (0.1–0.2 μm h^{-1}) is recorded.

Using the so-called "cold wall" reactors an increase of these deposition rates is obtained. For example, in the case of forced CVI values about 3 μm h^{-1} with propylene as precursor are measured (Vaidyaraman *et al.*, 1996). In presence of thermal gradients with either gas or liquid precursors, higher values are reached up to 50 μm h^{-1} in the case of the boiling technique with a very reactive hydrocarbon (Rovillain *et al.*, 2001) these deposition rates measured under controlled conditions can be related to the apparent activation energy (Ea) and the associated chemical. Indeed it has been shown (Ferron *et al.*, 1999). That the observed structural transitions are related with a kinetic regime change as presented in Fig. 5.11. In the literature many (Ea) values are found which are more or less dependant on the experimental conditions and difficult to compare directly. In the present case however this significant change is attributed to a different mechanism involving interfacial effects (Lavenac, 2000).

(ii) The infiltration rate related to the kinetic of mass uptake which is the primary response examined by almost all the authors. In most of the cases a first order type reaction is used to fit these data (Palmer and Cullis, 1965); one example of comparative study with different porous substrates under constant temperature (Marinkovic and Dimitrijevic, 1985) has shown that the infiltration rate is determined by the open pore volume rather than the total surface area. This result means the homogeneous reactions are more efficient than the heterogeneous ones on the pore walls. One way to get a deeper insight on the infiltration mechanism is to work with model pores of various diameters and lengths. After some earlier attempts (Bickerdike *et al.*, 1961), two recent works have led to interesting results. First, Dupel *et al.* (1994) have used straight pores with rectangular cross-sections (widths: 60–320 μm) under pulsed CVI conditions. The deposits present both a thickness and

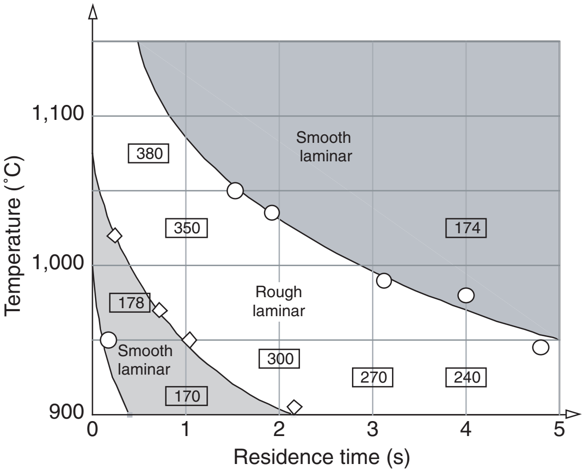

Figure 5.11 Plot of the deposition temperature versus the residence time under isobaric conditions, furnishing the existence diagram with the microstructure domains and the associated activation energies expressed in kJ mol^{-1} (from Feron *et al.*, 1999).

a texture profile, as shown in Fig. 5.12 for a selected range of parameters (Dupel, 1993). For different residence times with an increasing depth inside the pore we observe a decrease of thickness and a change of microstructure. At the pore entrance a RL microstructure is detected which is changed in SL type at a deeper level. As indicated by the authors this is the signature of a local change in the deposition mechanism. Secondly, Hu *et al.* (2000) carried out similar experiments with different circular pores. In particular for a given capillary (1 mm in diameter and 17 mm in length) with low pressure methane decomposed at 1,100 °C they show an increase of the deposition rate from the mouth to the depth of the pores. This opposite result dependant also of the residence time is explained by the competition between heterogeneous and homogeneous reactions and the control of the A/V ratio (see Fig. 5.1).

At the contrary the reaction–diffusion competition is not so critical in the presence of a T or P gradient. The infiltration rate is governed by the displacement of the reacting front inside the porous subtrate (see Section 5). It has been established for the film boiling technique that a relation exists between the deposition on a single filament and the bulk infiltration rate with a proper account of the thermal gradient (Rovillain *et al.*, 2001) (Fig. 5.7).

(iii) Comments about the mechanisms–microstructures relationship in hot walls reactors. Two points are relevant concerning both the hydrodynamic and the chemistry. The hydrodynamic

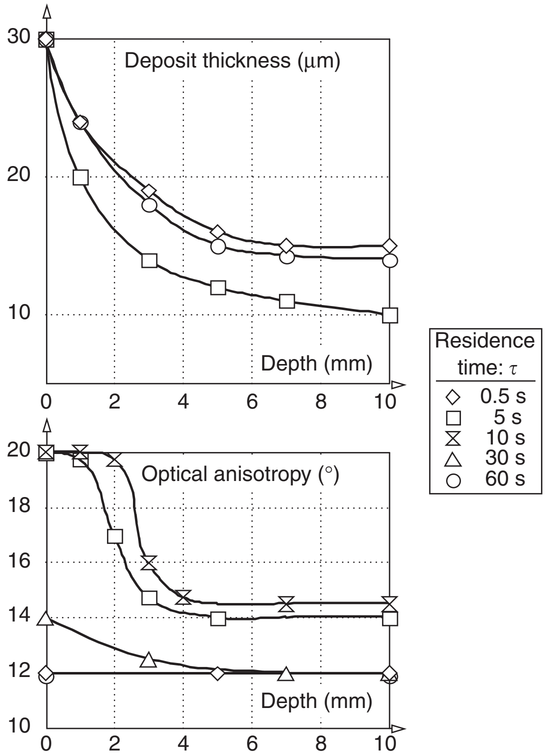

Figure 5.12 Pyrocarbon infiltration with the associated deposit thickness (a) and the optical anisotropy coefficient Ae (b) along a 60 µm model pore, as a function of the pore depth and for different residence times (r); the experimental conditions are T = 1,050 °C, P = 1kPa and propane used as pristine gas (adapted from Dupel, 1993).

flow is characterized by the residence time (Fig. 5.4) which is defined in a free space for a laminar flow in piston mode. This parameter is neither concerned by the chemical reactions nor the transport in porous media. The so-called maturation influence for homogeneous reactions (Marinkovic and Dimitrijevic, 1985; Dupel *et al*., 1994) is valid as long as the furnace reacting volume is large compared to the preform one and the associated residence time is a valuable parameter. Inside a porous substrate characterized by the ratio A/V, and its apparent density the situation is quite different. When it constitutes a large volumic fraction of the reaction (Hüttinger, 1998) the residence time definition is not so straightforward.

For the chemistry it seems that in some cases the increase of ratio $\mathrm{R} = (C_2H_2/C_6H_6)$ established for thermodynamic equilibrium (Lieberman and Pierson, 1974), is related to the observed microstructure sequence, i.e. SL–RL–I (Benzinger and Hüttinger, 1999a,b). However this is not in disagreement with other series of results (Ferron *et al*., 1999; Lavenac, 2000; Bouchard *et al*., 2001) for which SL type deposit is related to a majority of aliphatics and RL one mainly to aromatics (note that in presence of polyaromatics after maturation, the isotropic phase is supposed to be deposited in agreement with the magnetic measurements already discussed in Section 4.1). To get a better understanding, the detection of the more active species, in particular the free radicals, at the interface is obligatory and is the control of their chemical gradients inside the pores which has to be determined for a better insight. The last remark concerns the observed morphological changes during a given infiltration which indicates a coupling effect between the hydrodynamic and chemical effects (De Pauw *et al*., 2003).

5 Physical models

All the reactors are open thermodynamic systems with matter and heat exchanges; their overall balance controls both the deposition rate on a substrate and the infiltration mechanism inside a porous preform. Several models have been developed at different levels of complexity to understand these processes that we will present in relationship with the experiments. For clarity it is still useful to distinguish between the isothermal–isobaric reactors and those working under a strong thermal gradient, alternatively with either forced or pulsed flows.

5.1 Isothermal "hot wall" reactors

In CVD technique a large volume reactor is used where a laminar flow in a free medium is expected for the gases. As it has been demonstrated the film growth rate on a flat surface is dependant on the slower mechanism of either the molecular diffusion or the surface reactivity. It has been shown (Van Den Brekel and Bloem, 1977) that the deposition state is characterized by a dimensionless number which is for example the Sherwood number:

$$N_{\mathrm{sh}} = k \cdot d / D \qquad (1)$$

where k is the kinetic constant for mass deposition, D is the molecular diffusion constant, usually considered to be Fickian ($D = -\mathrm{grad}\, C$, where C is the molecular concentration), and d is a characteristic distance, e.g. the boundary layer thickness in the gas phase (Carlsson, 1985) which is extrapolated to a typical length in the case of a porous substrate with defined pore sizes.

In classical CVD the situation is described by defining $N_{\mathrm{sh}} < 1$, this is the mass transport regime presented in Fig. 5.2 which allows also a homogeneous deposition inside the pores. Besides morphological instabilities are associated with this competition; in particular a realistic model for controlling growth conditions has been proposed (Bales *et al.*, 1989). Introducing also mass transport along the surface driven by capillary forces, this kind of model leads to different morphologies as for example observed on ramified amorphous filaments of carbon (Banhart, 1997). This approach is reminiscent of the different type of microstructures which are observed both by CVD and CVI techniques (see Section 4.2) even if no clear comparison could be drawn so far.

Concerning CVI, the modeling analysis is more complex and one of the simplest but efficient model is issued from Thiele's work (Thiele, 1939) used initially for heterogeneous catalysis problems. It is assumed that the pores are independent and cylindrical with a given diameter, and the chemical reaction giving rise to the carbon formation is of the first order. The overall process is defined through a dimensionless number called Thiele modulus:

$$\phi \alpha (k/d)^{1/2} \tag{2}$$

which is analogous to the square root of N_{sh}.

The efficiency of the process is defined by the infiltration factor inside a pore ($\eta = \mathrm{tgh}\phi/\phi$) as already defined (Fitzer and Hegen, 1979) which can be compared with the experimental results using pore models. To ameliorate the infiltration rate it is possible to increase the chemical reactivity by plasma enhanced CVI for example but a strong deposit gradient is observed (Levesque *et al.*, 1989), which corresponds to a regime change when $\phi \approx 1$. A 3D percolation model where the connectivity between pores whithout any tortuosity factor is taken into account to explain this result (Delhaès, 1998). The infiltration is controlled, in absence of any effective convection, by the diffusion processes which are not only the classical Fick term but also the Knudsen one which introduces the collisions with the solid surfaces. Usually the Knudsen number is indicating the predominant term:

$$K_n = \lambda / d \tag{3}$$

where λ is the molecular mean–free path for a given molecule (from Fick and Knudsen terms) and d the characteristic length is the mean pore diameter which is progressively reduced during the process. At a given stage K_n is lower than 1, the diffusion regime becomes ballistic and the carbon deposit can be affected by this effect which normally occurs is the nanometric range. This is an empirical approach because we are in presence of a multicomponant and evolutive system due to the complex chemistry; indeed the light species as hydrogen are playing a crucial role in such a confined space which is not fully elucidated.

To overcome all these difficulties it is necessary to develop a mathematical model which describes the dynamic behavior of isothermal CVI: the so-called dusty gas model (Sortichos, 1991). The equations for momentum, heat, and mass balances of the whole process including the interfacial hydrodynamic problems, a simplified chemical path, the multicomponent diffusion, and the tortuosity factor for the porous substrate have to be established. A few theoretical works have attempted to solve this difficult problem (McAllister and Wolf, 1993; Vignoles *et al.*, 2001) which are out of the scope of this chapter.

5.2 Non-isothermal or (non-isobaric) conditions: "cold wall" reactors

As has been described in Section 3.2 temperature or pressure gradient generally results in shorter process time than isothermal operation. This is due to the existence of a gradient field which enhances the driving force associated with the thermal and mass transports from the cold face to the hot one inside the preform (Bristow and Hill, 1975). A spatial separation between the chemistry and the transport zones results with the existence of a mobile reacting front. This is a new class of phenomenon that we introduce in a first approach before discussing about the mechanisms which are involved in the presence of a steep thermal gradient.

(i) *The related phenomena* This class of non equilibrium systems is defined when a pressure or thermal front is associated with interfacial chemical reactions. Such a situation is encountered for example when a shock wave is created for making artificial diamonds but most of the cases are related to thermal effects. A drastic thermal front exists for the degradation of carbon materials by oxidation or by ablation effects occuring in spacecraft aerodynamic during the atmospheric re-entry or in gaseous combustion including the models of flame front (Clavin and Linan, 1984). Another similar system is the dynamics of a frontal polymerization associated with exothermic reactions (Posman *et al.*, 1998). Their common point is a coupling effect between the chemistry and the hydrodynamics which is delicate to handle theoretically.

(ii) *Fast densification processes* The film boiling chemical vapour infiltration technique has been mainly investigated by either inductive (Bruneton *et al.*, 1997) or resistive heating (Rovillain *et al.*, 2001) but strong similarities exist with other thermal gradiant furnaces working with gas precursors (Golecki *et al.*, 1995). A comparison between the experimental situations with a combustion front in the case of a subsonic premixed flame

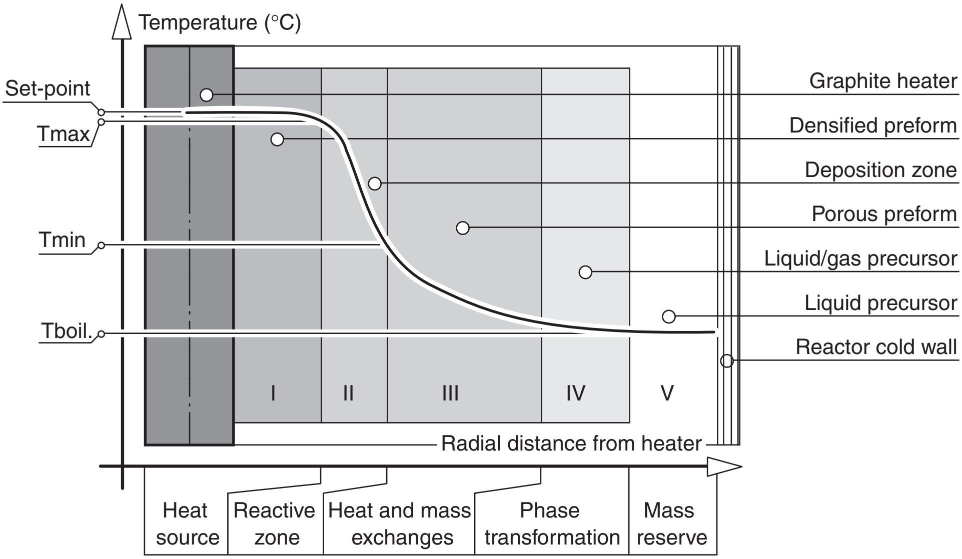

Figure 5.13 Process modelization for the film boiling technique: sketch of the temperature radial profile for a bench reactor with the main different functionalized parts (Rovillain *et al.*, 2001).

has been proposed (Rovillain *et al*., 2001). This model leads to a process analysis presented in Fig. 5.13 starting from the center, where the resistance heater is located. The temperature profile of the radial section of the reactor can be divided into five parts. As shown on the drawing each of them is characterized by a specific function:

- Part I is the graphite heater and the already densified preform. This is the heat source controlled at a constant temperature T and the heat transfer is due to the thermal conduction of the composite.
- Part II, the reacting front characterized by a deposition thickness and a large thermal gradient. All the chemical reactions are confined inside this narrow space so possibly described from flame theory.
- Part III, the porous preform where the complex heat and mass exchanges are located. The heat transfer inside this multiphasic system is due to the solid thermal conduction, to the diffusion–convection mechanism of the gases and the radiation effects. The mass transfer is related with the respective molecular gradient (Fick law) and eventually with the temperature gradient (Soret effect).
- Part IV, the felt external portion where the precursor is boiling and the liquid and gas phases coexist; the calefaction effect is observed inside this biphasic regime.
- Part V, outside the preform, the precursor is boiling at a constant temperature: this is the mass reservoir for carbon deposit.

From the experimental deposition rates on each fiber and the associated front propagation rate inside the preform (Rovillain *et al*., 2001) which can reach 2–3 mm per hour an estimation of the mass transport coefficient is possible. In steady-state conditions it is possible to calculate from the classical diffusion equation for an ideal binary mixture (e.g. cyclohexane and hydrogen) the Fick coefficient which is about the correct order of magnitude. It means this is apparently the main driving force; the effect due to the steep thermal gradient and the influence of the porosity (Knudsen term) are not crucial, at least with a felt used as a light preform (apparent density: 0.1). In any case a complete modeling of these CVI processes with resistive or inductive heating is the next work to accomplish for a better insight and efficiency. It turns out that by comparison with the other related phenomena, the interaction between chemistry and hydrodynamics has to be taken in account to develop a valuable model for infiltration.

6 Carbon–carbon composites

The current purpose is not to fully describe their applications but rather their intrinsic characteristics together with the associated interfacial properties which are dependant of the type and the nature of used preforms. For the industrial uses we will just mention selected examples which emphasize their peculiar properties.

6.1 Composite quality

Two types of requirements have to be considered, the matrix quality by itself and the associated interfacial behavior. The type of microstructure, with its bulk density which is related to the voids, residual porosity and cracks, is first examined. The rough laminar (RL) pyrocarbon is usually searched because of its good thermal and mechanical characteristics associated to the higher grain density and graphitability (see Section 4.1). Therefore the type of process for a selected preform is of primary importance to get a stable and robust RL "phase" with a low residual porosity (Granoff *et al.*, 1973; Delhaès *et al.*, 1984). A complementary characteristic is the high temperature behavior, high thermo-mechanical properties stay up to 2,000 °C except under oxidizing atmosphere. To increase the oxidation resistance of carbons several approaches have been done. One is to dope the matrix to boron which modifies the microstructure and induces an inhibition mechanism against the oxidation (Jacques *et al.*, 1996). An alternative way is to protect the pyrocarbon with a ceramic coating as, for example, silicon carbide (Bines, 1993).

Indeed the type of carbon fiber and its surface characteristics control the composite behavior:

(i) Choice of the space distribution: the different fiber bundle arrays are characterized by their dimensionality as felts, unidirectional bundles, weave patterns, and tri- or multidirectional arrays. The fiber volume fraction is increasing with the arrays dimensionality and the mean pore size is decreasing giving rise to changes in the infiltration process.

(ii) Control of the fiber surface: its choice, rayonne, PAN, or mesophase based and a preliminary treatment will give rise to different works of adhesion which depend on the surface energy as for the wettability characteristics (Vix and Ehrburger, 2003). The shape, curvature, and roughness of the fiber as also its graphene surface with the presence of nucleation sites are influent for the type of physical or chemical interactions. Following this difficult analysis the sort of dry (plasma) or wet treament (chemical or electrochemical attack) can radically change its behavior (Manocha *et al.*, 1989). The type of deposited pyrocarbon will be controlled as for example when an interphase is introduced to improve the mechanical properties in a unidirectional model composite (Naslain *et al.*, 1999).

The mechanical applications are based on the transfer of fiber properties to the matrix which depends on different mechanisms as just discussed above and including the residual thermal stress due to the anisotropy of the thermal expansion coefficient. A compromise between strong and weak bonding at the interface is necessary to optimize the efficiency and the fracture toughness; ultimately a catastrophic type of failure with a brittle behavior is observed but by making use of the fiber surface treatment a pseudo plastic failure mode is

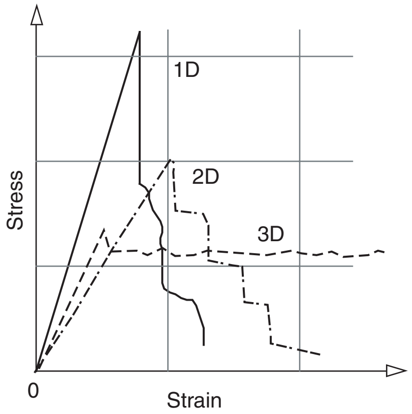

Figure 5.14 Schematic mechanical properties with a strain–stress plot of unidirectional (1D), bidirectional (2D) and tridirectional (3D) composites (from Fitzer, 1987).

obtained. One generic example is presented in Fig. 5.14 where the effect of the bundle orientation on the tensile strength is presented (Fitzer, 1987). When the strain is applied in the bundle directions the 3D composites exhibits a lower but isotropic value accompanied with a pseudo-plastic behavior (McEnaney and Mays, 1993).

Other examples have been published relative to standard flexural tests when the type of deposited microstructure is controlled (Kimura *et al.*, 1981; Delhaès *et al.*, 1984; Oh and Lee, 1989). The influence of the matrix concerning the bending strength and the associated modulus have been recognized in particular for weave preforms.

6.2 Applications overview

The carbon–carbon composites are used for different applications where combined properties are always involved. We summarize three of them (Fitzer, 1987) illustrating valuable examples.

(i) Heat shields of space reentry vehicles and thermo-mechanical properties. A figure of merit for thermal shocks and ablation can be defined as the high thermal stress resistance (TSR) (Lieberman *et al.*, 1975):

$$\mathrm{TSR} = \sigma \cdot K/E \cdot \Delta \tag{4}$$

where σ is the tensile stress, K the thermal conductivity, E the Young's modulus, and Δ the linear thermal expansion coefficient.

As pointed out (Thomas, 1993) this coefficient is very high in C/C composites compared to standard alloys and still valuable at elevated temperatures up to 2,000 °C.

(ii) Brakes for aircrafts and terrestrial vehicles (race cars, trucks, and fast trains); tribological properties are involved combining surface and bulk characteristics. The graphitic carbons present a low coefficient of friction which is used for many applications involving mobile pieces. For brakes the frictional behaviour is associated with its ability to absorb and conduct away large quantity of heat. In presence of different atmospheres complex physico-chemical interactions are superimposed to the mechanical ones. This mixed effect is explained by the role of surface debris forming the third body composed of fine powder involved in the sliding speed; the resulting wear and associated efficiency are explained with the presence of this transfer film (Diss and Brendle, 1997). It is interesting to quote that this situation is similar to those described for depositive phenomena exhibiting a steep thermal gradient (see Section 5.2).

(iii) Biocomposites for prostheses and implants: the carbon presents the best biocompatibility with blood, tissues, and bones. This can be associated with adapted mechanical characteristics for ankles and knee prostheses or plates in ostheosynthesis (Fitzer, 1987). In the recent years, however, these chirurgical applications have not been actively developed because other ceramics or alloys are currently employed.

7 Conclusion and outlook

Our approach is based on the relationship between processes and materials. On one hand the process analysis concerns both the principles and the techniques, i.e. a comparison between the different types of reactors (Sections 2 and 3). On the other hand the deposited pyrocarbons where the established structure–property correlations have been presented; it leads to reproducible type of microstructures necessary for the applications including high temperature behavior and graphitation (Sections 4 and 6). Finally the logical link between them is through the physical models which should explain the whole process if all the chemical, thermal, and hydrodynamical components are included (Section 5). In particular it will be necessary to define a minimum set of indispensable reactants to modelize correctly the overall chemistry.

The formation mechanisms in confined media are rather complex but a general description is given which covers from the deposition on a bulk surface to the soot nucleation in the gas phase. It appears that a better knowledge of the interfacial physics and chemistry is necessary for both the deposition mechanism and the resulting composite characteristics. Coupled with the development of local sensors to measure the effective constraints it turns out that the observed morphological instabilities could be analyzed and controlled.

As noticed before, these CVI processes are characterized by different scale factors and also by different time scales. Indeed the surface reactions are usually fast with a characteristic time about a microsecond, the residence time in the gas phase is the range of several seconds or more and the processing time is at least ten thousand times longer. For the industrial CVI reactors the main difficulty is to control both these different length and characteristic times for making the desired type of metastable phase of pyrocarbon (in general the RL microstructure) under robust experimental constraints to obtain an homogeneous bulk piece. This is one blocking point of development of the fast densification techniques that we have presented in this review.

In conclusion, the new pressure or thermal gradient reactors, as developed for the fast boiling technique, lead to a shorter processing time and an increased process efficiency which need to be extended to an industrial scale. An economical gain could be expected as long as the matrix quality and the interfacial interactions are optimized in these C/C composites.

References

Adamson, A. W. (1976). Physical chemistry of surfaces (Third edition, Wiley-interscience editor).

Bales, G. S., Redfield, A. C., and Zangwill, A. (1989). Phys. Rev. Lett. **62**, 776–779.

Banhart, F. (1995). Phys. Rev. E **52**, 5156–5162.

Beaugrand, C. (2000). PhD thesis, University of Orleans (France).

Benziger, W. and Hüttinger, K. J. (1999a). Carbon **37**, 181–193.

Benziger, W. and Hüttinger, K. J. (1999b). Carbon **37**, 1311–1322.

Bickerdike, R. L., Brown, A. R. G., Hugues, G., and Ranson, H. (1961). Fifth International Carbon Conference, 575–582.

Bines, E. B. (1993). In *Essentials of Carbon–Carbon Composites* (Ed. by C. R. Thomas, Royal Society of Chemistry), ch. 8, 204–227.

Bokros, J. C. (1969). *Chemistry and Physics of Carbon* (Ed. by P. L. Walker), Vol. 5, 1–118.

Bouchard, E., Lavenac, F., Roux, J.-C., Langlais, F., and Delhaès, P. (2001). Advanced materials-CVD **7**, 125–130.

Bourrat, X., Trouvat, B., Limousin, G., Vignoles, G., and Doux, F. (2000). J. Mater. Res. **15**, 92–101.

Bristow, H. A. S. and Hill, J. (1975). I. Chem. E. Symposium Series No. 43, 5/1–5/11.

Bruneton, E., Narcy, B., and Oberlin, A. (1997). Carbon **35**, 1593–1598 and 1599–1611.

Bryant, W. A. (1997). J. Mater. Sc. **12**, 1285–1300.

Carlsson, J. O. (1985). Thin solid films **130**, 261–282.

Chen, C. J. and Back, M. H. (1979). Carbon **17**, 175–180.

Clavin, P. and Linan, A. (1984). In *Non-equilibrium Cooperative Phenomena in Physics and Related Fields* (Ed. by M. G. Velard, NATO ASI series B) **116**, 291–338.

Coffin, L. F. (1964). J. of Amer. Chem. Soc. **47**, 473–478.

David, P., Narcy, B., Lulewicz, J. D., Ravel, F., and Schulmann, S. (1995). Proceedings of ICCM-10, Vol. 4, 611–616.

Delhaès, P. and Carmona, F. (1981). In *Chemistry and Physics of Carbon* (Ed. by P. L. Walker and P. A. Thrower) Vol. 17, 89–174.

Delhaès, P., Trinquecoste, M., Pacault, A., Goma, J., Oberlin, A., and Thebault, J. (1984). J. de Chimie-Physique **81**, 809–817.

Delhaès, P. (1998). Proceedings of Euro CVD-11 (Ed. by M. D. Allendorf and C. Bernard), part 4, 486–495.

Delhaès, P. (2000). In *World of Carbon*, "Graphite and precursors" (Ed. by P. Delhaès, Gordon and Breach Science Publishers), Vol. 1, 1–24.

Delmonte, J. (1981). *Technology of Carbon and Graphite Fiber Composites* (Van Nostrand Reinholt company, USA).

De Pauw, V., Reznik, B., Kalhofer, S., Gerthsen, D., Hu, Z. J., and Hüttinger, K. J. (2003). Carbon **41**, 71–77.

Desprez, J.-F. and Oberlin, A. (1996). Tanso, **17**, 2–12.

Diefendorf, R. J. (1960). J. de Chimie-Physique **57**, 815–821.

Diefendorf, R. J. (1969). In *Reactivity of Solids* (Ed. by J. W. Mitchell, R. C. De Vries, R. W. Roberts, and P. Cannon) 471–473.

Diss, P. and Brendle, M. (1997). *Wear* 203–204, 564–572.

Donnet, J.-B. and Voet, A. (1976). *Carbon Black* (Ed. by M. Dekker).

Dupel, P. (1993). PhD thesis, University of Bordeaux I (France).

Dupel, P., Pailler, R., Bourrat, X., and Naslain, R. (1994). J. Mater. Sci. **29**, 1056–1066.

Ferron, O., Langlais, F., Naslain, R., and Thebault, J. (1999). Carbon **37**, 1343–1353.

Fitzer, E. and Hegen, D. (1979). *Angew. Chem. Int.* English Edition **18**, 295–304.

Fitzer, E. (1987). Carbon **25**, 163–190.

Flandrois, S. (2000). In *World of Carbon*, "Graphite and Precursors" (Ed. by P. Delhaès, Gordon and Breach Science Publishers), Vol. 1, ch. 4, 71–86.

Ford, L. H. and Bilsby, C. F. (1976). J. of Nuclear Materials **60**, 79–88.

Frenklach, M. (1996). Twenty-sixth International Symposium on Combustion (Pittsburgh, USA), 2285–2293.

Golecki, I., Morris, R. C., Narasimhan, D., and Clement, N. (1995). Appl. Phys. Lett. **66**, 2334–2337.

Golecki, I. (1997). Materials Science and Engineering **R20**, 37–124.

Golecki, I. (2003). In *World of Carbon*, "Fibers and composites" (Ed. by P. Delhaès, Taylor and Francis), Vol. 2, ch. 6.

Goma, J. and Oberlin, A. (1986). Carbon, **24**, 135–142.

Grisdale, R. O. (1953). J. of Applied Physics **24**, 1082–1091.

Granoff, B., Pierson, H. O., and Schister, D. N. (1973). J. Composite Materials **7**, 36–52

Hedden, K. and Wicke, E. (1957). Third Biennial Carbon Conference (Buffalo, USA), 249–256.

Hoffman, W. P., Vastola, F. J., and Walker, P. L. (1985). Carbon **23**, 151–161.

Hu, Z. J., Schoch, G., and Huttinger, K. J. (2000). Carbon **38**, 1059–1065.

Hüttinger, K. J. (1998). Advanced Materials CVD **4**, 151–158.

Inagaki, M. (2000). *New Carbons: Control of Structures and Functions* (Ed. Elsevier).

Ismail, M. K. I. and Hoffman, W. P. (1991). Carbon **29**, 587–594.

Jacques, S., Guette, A., Bourrat, X., Langlais, F., Guimon, C., and Labrugere, G. (1996). Carbon **34**, 1135–1143.

Kaae, J. L. (1985). Carbon **23**, 665–673.

Kimura, S., Yasuda, E., Takase, N., and Kasuya, S. (1981). High Temp. High Press. **13**, 193–199.

Kotlensky, W. V. (1973). In *Chemistry and Physics of Carbon* (Ed. by P. L. Walker and P. A. Thrower), Vol. 9, 173.

Lachter, A., Trinquecoste, M., and Delhaès, P. (1985). Carbon **23**, 111–116.

Lackey, W. J. and Starr, T. L. (1991). In *Fiber Reinforced Ceramic Composites* (Noyes Publ. Park Ridge, USA), 397–449.

Lavenac, J. (2000). PhD thesis, University of Bordeaux I (France).

Lavenac, J., Langlais, F., Feron, O., and Naslain, R. (2001). Composites Science and Technology **61**, 339–345.

Lespade, P., Marchand, A., Couzi, M., and Cruège, F. (1984). Carbon **22**, 375–385.

Levesque, O., Ricci M., Trinquecoste, M., and Delhaès, P. (1989). J. de Physique C5 **50**, 269–279.

Lewis, J. S., Lackey, W. J., and Vaidyaraman, S. (1997). Carbon **35**, 103–112.

Lieberman, M. L. and Pierson, H. O. (1974). Carbon, **12**, 233–241.

Lieberman, M. L., Curlee, R. M., Braaten, F. H., and Noles, G. T. (1975). J. of Composite Materials 337–346.

Loll, P., Delhaès, P., Pacault, P., and Pierre, J. (1977). Carbon **16**, 390–395.

Lucas, P. and Marchand, A. (1990). Carbon **28**, 207–219.

McAllister, P. and Wolf, E. E. (1993). AIChE Journal **39**, 1196–1209.

McEnaney, B. and Mays, T. (1993). In *Essentials of Carbon–Carbon Composites* (Ed. by C. R. Thomas, Royal Society of Chemistry), ch. 6, 143–173.

Manocha, L. M., Bahl, O. P., Singh, Y. K. (1989). Carbon **27**, 381–387.

Marinkovic, S. and Dimitrijevic, S. (1985). Carbon **23**, 691–699.

Naslain, R., Lamon, J., Pailler, R., Bourrat, X., Guette, A., and Langleis, F. (1999). Composites; Part A. **30**, 537–547.

Ofori, J. Y. and Sortichos, S. V. (1997). Proceedings of Euro CVD-11 (Ed. by M. D. Allendorf and C. Bernard), Vol. 97–25, 536–543.

Oh, S. M. and Lee, J. Y. (1989). Carbon **27**, 423–430.

Okuno, H., Trinquecoste, M., Derre, A., Monthioux, M., and Delhaès, P. (2002). J. of Materials 17, 1904–1913.

Palmer, H. B. and Cullis, C. F. (1965). In *Chemistry and Physics of Carbon* (Ed. by P. L. Walker), Vol. 1, 265–325.

Pierson, H. B. and Lieberman, M. L. (1975). Carbon **13**, 159–166.

Posman, J. A., Gunn, G., Patterson, C., Owens, J., and Simmons, C. (1998). J. Phys. Chem. **B102**, 3927–3929.

Rand, B. (1993). In *Essentials of Carbon–Carbon Composites* (Ed. by R. C. Thomas, Royal Society of Chemistry), ch. 3, 67–102.

Rovillain, D., Trinquecoste, M., Bruneton, E., Derre, A., David, P., and Delhaès, P. (2002). Carbon **39**, 1355–1365.

Sortichos, S. V. (1991). AIChE Journal **37**, 1365–1378.

Soutric, F. (1998). PhD thesis University of Toulouse (France).

Tesner, P. A. (1984). In *Chemistry and Physics of Carbon* (Ed. by P. L. Walker and P. A. Thrower), Vol. 19, 65–162.

Thiele, E. W. (1939). Industrial and Engineering Chemistry **31**, 916–920.

Thomas, C. R. (1993). In *Essentials of Carbon–Carbon composites* (Ed. by C. R. Thomas, Royal Society of Chemistry), ch. 1, 1–36.

Truinstra, F. and Koenig, J. L. (1970). J. of Composite Materials **4**, 492–499.

Van Den Breckel, C. H. J. and Bloem, J. (1977). Philips Res. Repts. **32**, 134–146.

Vaidyaraman, S., Lackey, W. S., Agrawal, P. K., Starr, T. L. (1996). Carbon **34**, 1123–1133.

Vignoles, G. L., Baconneau, O., Brauner, C. M. (2001). In ECS Proceedings, Vol. 13 (N. T. Switart, M. D. Allendorf, M. Meyjapan, and S. Seal Editions).

Vix-Guterl, C. and Ehrburger, P. (2003). In *World of Carbon* “Fibers and composites” (Ed. by P. Delhaès, Taylor and Francis), Vol. 2, ch. 9.

Zi Jun Hu and Hüttinger, K. J. (2002). Carbon **40**, 624–628.

6

INDUSTRIAL CARBON CHEMICAL VAPOR INFILTRATION (CVI) PROCESSES

I. Golecki

1 Introduction

Carbon–Carbon (C–C) fiber-matrix composite materials – C–Cs (Buckley and Edie, 1993; Savage, 1993; Thomas, 1993) possess several extraordinary sets of properties. Foremost, C–Cs have densities in the range of 1.6–2.2 $\mathrm{g\,cm^{-3}}$, much lower than those of most metals and ceramics. Lower densities can be translated into lower component weights, an important consideration, especially for applications in flying platforms. C–Cs also have excellent mechanical and thermal properties. The mechanical strengths of C–Cs *increase* with temperature, in contrast to the strengths of the majority of other fiber–matrix composites and those of metals and ceramics, which *decrease* with increasing temperature. C–Cs evidence high toughness and graceful failure under load, as do some other fiber-matrix composites, in contrast to the more abrupt brittle behavior of most monolithic materials. No melting occurs in C–Cs at increasing temperatures, although carbon evaporates above ≈ 2,500 °C. Appropriately processed, pitch-fiber based C–C's possess higher thermal conductivities than copper and silver and they exhibit, by far, the highest thermal conductivity per unit density among thermal management materials, e.g. $400\,(\mathrm{Wm^{-1}\,k^{-1}})/(\mathrm{g\,cm^{-3}})$ (Golecki *et al.*, 1998). In addition, the thermal expansion coefficient of C–Cs in the fiber direction at 20 °C to ≈1,000 °C is between -1 and 1 ppm/°C, much lower than that of most other structural materials. Consequently, thermal stresses in C–C articles are, in principle, also lower. All of these properties of C–Cs can be tailored by design, using different fibers, matrices, processing methods and schedules. While C–C articles can be used from cryogenic temperatures to over 3,000 °C, and in severe and chemically aggressive environments, they require protection from oxidation for continuous use above ≈350 °C. The practical effect of oxidation is to diminish the structural and functional integrity of the article. Effective engineering solutions for protecting C–C articles from oxidation have been demonstrated for different types of articles and different temperature-time envelopes (Buckley and Edie, 1993; Savage, 1993; Sheehan *et al.*, 1994; Golecki *et al.*, 2000). Current and potential future applications of C–Cs include disc brake pads for commercial and military airplanes and racing cars, uncooled engine parts, rocket leading-edge sections, furnace heating elements, heat sinks for high-power electronics, heat exchangers, and bipolar plates for proton-exchange-membrane fuel cells.

Carbon–Carbon articles generally comprise (a) continuous or chopped carbon fibers produced from rayon, polyacrilonitrile (PAN) or pitch precursors and (b) one or more types of carbon matrices (Savage, 1993). One of the most common fabrication methods of C–C articles is densification of a porous preform having the desired shape, so-called near-net processing. The preform consists only or principally of fibers. The initial geometrical density of such preforms varies in the range 10–80% of the theoretical value at full density. Preforms may be fabricated using e.g. weaving of continuous fibers, lay-up of fibrous mats or fabrics, needle-punching, or mixing of chopped fibers with resins and powders, followed, as needed, by thermal treatment in the 200–1,000 °C range to evaporate organic binders or residues (Savage, 1993). Fabricating, cutting and machining a porous preform is easier and faster than machining a fully-dense C–C bar, which often requires diamond tooling. The densification of the preform can be achieved either from the vapor phase, conventionally by means of isothermal isobaric chemical vapor deposition and infiltration (CVD/CVI), or by liquid-phase resin infiltration and annealing, or by a combination of these two approaches. Both approaches involve heating the preforms to about 1,000 °C, either during CVI or after resin has been placed inside the preforms. Conventionally, in either densification approach, several steps are required to effect sufficient densification of the preforms. Minimum final density values are necessary for achieving the desired mechanical and thermal properties. All densification methods leave typically 1–10% of voids in the composite. The average density of a composite article, ρ_{av}, is equal to:

$$\Sigma\rho_i X_i = \rho_{\mathrm{f}} X_{\mathrm{f}} + \rho_{\mathrm{m1}} X_{\mathrm{m1}} + \rho_{\mathrm{m2}} X_{\mathrm{m2}} + \cdots \tag{1}$$

where the X_i denote the respective volume fractions ($\Sigma X_i = 1 - X_{\mathrm{v}}$) and the subscripts f, mi, and v denote fiber, matrix no. i, and void, respectively. After densification is complete, the C–C article may just need to be lightly machined to final tolerances. Additional processing steps involved in the manufacture of C–C articles often include high-temperature (1,000–3,000 °C) annealing in an inert ambient, called graphitization, in order to achieve desired properties, and oxidation protection treatment.

In this chapter, a brief review is provided of CVI routes to the densification of C–C's, from an industrial perspective, with emphasis placed on published approaches demonstrated to reduce the processing time of functional components or that show potential for the same; a more extensive review of this subject was published recently (Golecki, 1997).

2 Overview of carbon CVI

CVI and CVD (Pierson, 1992; Hitchman and Jensen, 1993) involve flowing one or several streams of precursor vapors containing the desired element or compound, e.g. methane (CH_4), over and around the porous parts, while keeping these parts in a furnace at a sufficiently high temperature to decompose the precursor. Each flow rate is usually controlled by means of an electronic mass flow controller and the total pressure in the furnace can be controlled independently by means of a throttle valve, which varies the flow conductance to the vacuum pumps. The terms CVD and CVI are often used interchangeably, but strictly speaking, they denote different processes. The purpose of CVD is to deposit a functional, thin coating on a dense substrate; e.g. the coating may serve as the active part of an electronic device or as a protective layer. The coating produced by CVD generally adds less than 1% of weight to the substrate and the deposition time is of the order of a few minutes to a few hours. The primary purpose of CVI, on the other hand, is to increase the density of a porous body by 100–900%, in order to obtain a material with desirable properties. In addition to achieving the desired density, a specific carbon matrix microstructure may be required, which is a function of the CVI process conditions. The infiltration time in conventional CVI methods is therefore much longer than the deposition time in CVD.

The most important quantity describing a CVD process is the *deposition rate* of the coating, r, which may vary from $\approx 10^{-2}$–10^{3} μmh^{-1}. The most important parameter influencing the deposition rate for a given material system is the *substrate temperature*. The deposition rate can be expressed (Grove, 1967) as:

$$r = C_g[k_s h_g/(k_s + h_g)]/N_s, \tag{2}$$

where C_g is the chemical concentration in the gas phase, k_s is the rate constant for heterogeneous decomposition of the chemical into the film on the surface of the substrate, h_g is the gas-phase mass-transfer coefficient of the chemical to the substrate, and N_s is a normalizing constant. This chemical may be, but often is not the input precursor (e.g. CH_4) introduced into the reactor. Often a complex series of chemical reactions lead from the input gas to the solid film. The gas-phase mass-transfer coefficient can be expressed as $h_g = D/d_b$, where D is the gas-phase diffusivity and d_b is the thickness of the boundary layer. When $k_s \ll h_g$, $r \approx k_s C_g/N_s$ and the process is *surface-reaction controlled*. Under these conditions, the reaction rate constant k_s and hence the deposition rate r usually increase exponentially with temperature according to the Arrhenius law:

$$k_s = k_{so}\exp(-\mathrm{E_a}/kT), \quad r = (k_{so}C_g/N_s)\mathrm{p}^{\mathrm{n}}\exp(-\mathrm{E_a}/kT), \tag{3}$$

where $\mathrm{E_a}$ is the activation energy for the controlling surface reaction, T is the absolute temperature in K, and Boltzmann's constant $k = 1.3805 \times 10^{-16}$ ergK^{-1} $= 8.614 \times 10^{-5}$ eVK^{-1} (see Fig. 6.1). For carbon, $\mathrm{E_a} \approx 2 - 4$ eV/molecule. Pressure signifies the pressure in the reactor chamber.

At higher temperature, when $k_s \gg h_g$, $r \approx h_g C_g/N_s$ and the process is *gas-phase diffusion controlled*. Under these conditions, transport of the precursor through the gas phase to the substrate becomes the limiting factor, while the surface chemical kinetics are relatively more rapid. In this regime, the deposition rate increases with temperature much more slowly, as $r = AT^{\mathrm{b}}$, where $\mathrm{b} \approx 0.5 - 1$, due to the temperature dependence of the gas-phase diffusivity. At still higher temperature, the deposition rate decreases with increasing temperature, due to competing reactions, such as homogeneous gas-phase nucleation or powder formation and sometimes etching of the surface of the film. Generally, lower temperatures, lower pressures, increased dilution, and higher flow rates (i.e. milder CVD conditions) minimize undesirable processes at the expense of growth rate. The choice of precursor may also influence the deposition rate and the properties of the deposited coating (Tesner, 1984; Duan and Don, 1995; Hüttinger, 2001).

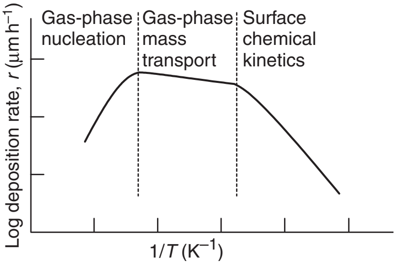

Figure 6.1 Three temperature regimes in chemical vapor deposition.

To sum, the basic steps in CVD are: (1) transport of the gaseous precursor from the center of the gas stream to the boundary layer, (2) diffusion of the precursor across the boundary layer to the surface of the substrate, and (3) decomposition of the precursor on the surface of the substrate to form the solid coating. The last step includes adsorption of precursor-derived moieties on the surface, desorption of other moieties from the surface, surface diffusion and chemical reactions. The conditions during CVD are usually far from thermodynamic equilibrium. Only a few systems, such as Si and GaAs, have been studied in relative depth. An accurate description of the CVD mechanism requires numerically solving the combined chemical and flow equations for the particular reactor configuration. In spite of the progress achieved, quantitative modeling of CVD processes in general cases is limited. Porting of a process from one reactor to another reactor of different geometry and/or size may not be trivial. Therefore, reliable data must be acquired experimentally.

In CVI, an additional gas-phase diffusion step needs to occur after the second step in CVD, namely diffusion from the surface of the preform into the interior pore. Such diffusion may be driven by a concentration gradient (isobaric CVI) or by a pressure gradient (forced-flow CVI). Porous fiber preforms generally have a complex pore size distribution, which may consist of several median size ranges. Continuous fibers, with diameters of 5–15 μm, are arranged in bundles or tows, with 500–3,000 or more fibers per bundle (Lovell, 1995). Pore sizes between individual fibers are of the order of 1–15 μm, those between fiber bundles and between cloth layers are typically 50–500 μm. Because flow conductances are proportional to the opening diameter to the third or fourth power, the partial pressure of a precursor inside a small pore in a preform may be different than its value in the reactor. Also, the characteristic dimensions(s), a, for the reactor (1–500 cm) and for the interior of the preform (1–500 μm) differ by many orders of magnitude. For example, for a mean free path $\lambda = 17\,\mu\text{m}$ (methane molecules at 1,000 °C and 10 Torr $= 1.3 \times 10^3$ Pa), and assuming the same pressure in the pore as in the reactor, the flow would be laminar outside the preform ($\lambda \ll \text{a}$) and laminar, mixed or molecular inside a pore in the preform. Therefore, both the gas-phase diffusion and the CVD deposition mechanisms may differ in the reactor and inside a pore: while on the surface of the preform, the CVD process may be in the surface-reaction controlled regime, within an interior pore there may be significant depletion of the precursor due to slow gas-phase diffusion in the molecular regime and the process may be gas-phase diffusion controlled. This state of affairs may lead to non-uniform densification observed in isothermal, isobaric CVI of thick preforms, where the outer surface of the preform has a higher density than the interior regions.

A helpful dimensionless number in CVI is the Thiele modulus (Thiele, 1939):

$$\theta = (k_s L^2/Da)^{0.5} \tag{4}$$

where a and L are the pore diameter and length, respectively. The Thiele modulus gives the relative importance of chemical reaction rate versus gas-phase diffusion. Solution of the pertinent differential equations for mass transfer, diffusion and change of pore geometry under simplifying assumptions results in the following expression for the concentration profile, $C(z)$, of the precursor species along the pore ($0 \leqslant z \leqslant L$):

$$C(z)/C(0) = \cosh[(1 - 2z/L)\theta]/\cosh\theta. \tag{5}$$

As shown in Fig. 6.2, the gas-phase concentration within the pore and therefore the deposition rate of the solid will be more uniform the smaller the Thiele modulus, i.e. the larger the gas-phase diffusivity compared to the surface reaction rate, and the smaller the aspect ratio L/a. It is generally preferable in CVD and CVI to operate in the surface-reaction controlled

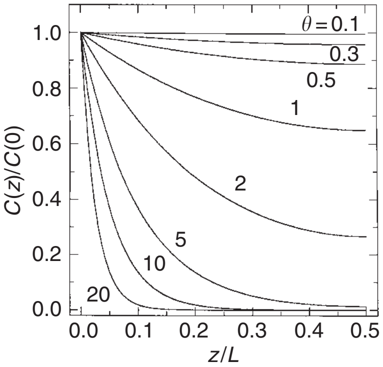

Figure 6.2 Calculated relative deposition rate along a pore axis, *z*, for different values of the Thiele modulus, θ; *L* = pore length.

regime, where D/k_s is large. For Fickian diffusion, the diffusivity *D* is inversely proportional to pressure and thus operating at lower pressures will decrease θ and result in a more uniform infiltration profile (Kotlensky, 1973; Naslain *et al.*, 1989; Pierson, 1992; Savage, 1993) and a more uniform microstructure (Pierson and Lieberman, 1975) in the pore. The value of the Thiele modulus will change during infiltration, because both the gas-related quantities and the aspect ratio of the pore will change. The above simplifying assumptions include a first-order chemical reaction with no change in volume and no homogeneous gas-phase reactions; solutions for other cases were published (Thiele, 1939). In many CVI processes, including carbon CVI, there is a net increase in the volume of the gaseous materials due to the decomposition of the precursor. Thus, fresh precursor species have to diffuse into the pores against an opposite, higher flow of by-product species. For carbon CVI, temperatures can vary, e.g, in the 600–2,000 °C range, depending on the particular chemistry and system; total pressures in the reactor are generally in the range $0.13 - 1.3 \times 10^5$ Pa ($10^{-3} - 10^3$ Torr).

CVI has several advantages compared to other densification methods. CVI allows penetration of the desired atoms or molecules into the smallest pores of the preform and does not require post-densification treatment to remove organics. CVI produces uniform and conformal coatings around each accessible fiber and surface in the preform. The matrix produced by CVI is purer than that obtained by hot pressing. The final shape of an article densified by CVI is closest to the desired shape. CVI minimizes the mechanical damage to the fibers as a result of the much lower pressures and temperatures employed. The published methods described here of infiltrating composites using CVI are listed in Table 6.1 and depicted schematically in Fig. 6.3 (Golecki, 1997). These CVI methods can be divided into several categories, depending on:

(i) spatially uniform temperature (isothermal) or not (thermal gradient);
(ii) heating method – radiative or inductive;
(iii) type of reactor – cold wall or hot wall;
(iv) method of extraction of heat from the preform (e.g. radiative, convective, conductive);
(v) pressure regime – atmospheric or low pressure;
(vi) uniform pressure (isobaric) or pressure gradient (forced flow, pulsed pressure);
(vii) whether a plasma is used;
(viii) whether immersion in a liquid is required.

Table 6.1 Published characteristics of different chemical vapor infiltration methods used to densify C–C composite articles and described in this chapter

CVI process (Section no.)	*Preform*		*Process*			*Reactor*	
	Multiple	*Thick/large size (>2.5 cm in all directions)*	*Densification time (w/r to perform thickness)*	*Pressure adjustable*	*Precursor efficiency*	*Cost of capital*	*Special fixturing*
Isothermal isobaric (2.2)	Yes	Yes	Very long	Yes	Low	High	No
Early thermal-gradient inductively-heated isobaric (2.3.1)	No	Yes	Long	Yes			Yes
Recent thermal-gradient inductively-heated isobaric (2.3.2)	Yes	Yes	Short	Yes	High	Low	No
Liquid-immersion thermal-gradient inductively-heated isobaric atm. pressure (2.4)	No	No	Short	No			
Forced-flow thermal-gradient (2.5)	No	No	Short	Very limited	High	Low	Yes

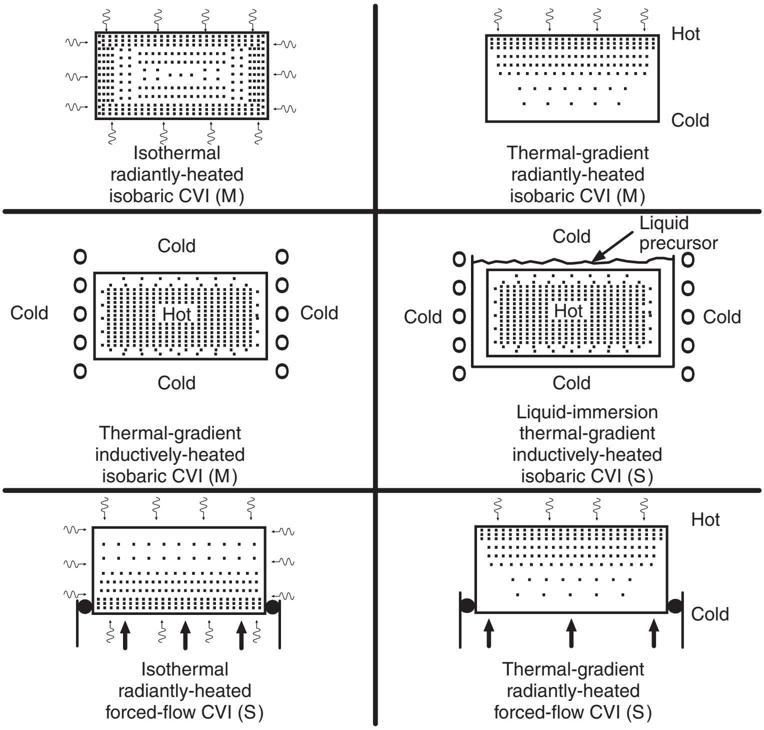

Figure 6.3 Principles of the main chemical vapor infiltration methods (Golecki, 1997); M = multiple preforms, S = single preform per run.

Different CVI methods are at different stages of technological and industrial maturity. Much data on infiltration of composites are unpublished or unavailable. Thus, the comparisons provided in this chapter are based on printed, public-domain studies, and patents. In the next sections, more detailed consideration is given to specific CVI methods used in fabrication of C–C articles.

3 Chemical vapor infiltration processes

3.1 Isothermal isobaric carbon CVI

Isothermal isobaric CVI is in wide use since the 1960s for densification of C–Cs and other refractory composites (Kotlensky, 1971; Savage, 1993; Golecki, 1997). In a common application, a large number of porous carbon disk brake-pad preforms, typically 15–55 cm in outer diameter (o.d.) by 2–3 cm in thickness, are placed in a hot-wall reactor, i.e. a furnace uniformly heated by radiation, at a temperature in the range 1,000–1,100 °C and exposed to a flow of reactant gas, e.g. CH_4 at 5–100 Torr $= 6.6 \times 10^2 - 1.3 \times 10^4$ Pa (Thomas, 1993); see Fig. 6.4. In isothermal isobaric CVI, the densification kinetics of a thin (e.g. 1–2 mm thick) preform with initial density ρ_o follow an exponential approach with time to a "final" density value, ρ_f (Loll *et al.*, 1977; Marinkovic and Dimitrijevic, 1987; Naslain *et al.*, 1989):

$$\rho(t) = \rho_o + (\rho_f - \rho_o)[1 - \exp(-t/\tau)] \tag{6}$$

where τ is the time constant of the process; τ decreases with increasing temperature according to an exponential (Arrhenius) relationship in the surface-reaction limited regime. For such a thin preform, ρ_f may equal the desired final density, but in a thicker preform the surface pores become clogged well before that density value is reached, requiring several interruptions of the infiltration to allow grinding the external surfaces in order to open the pores and enable further infiltration; see Fig. 6.5. The total densification time is thus a strong supra-linear function of the thickness of the preform. For >2 cm thick preforms, 600–2,000 h may be required to achieve the desired density.

Since from an economic viewpoint, it is desirable to minimize the densification time, higher temperature and precursor pressure would seem to be the direction to follow. However,

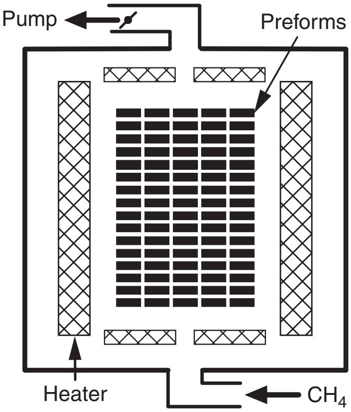

Figure 6.4 Simplified schematic diagram of a hot-wall, isothermal–isobaric chemical vapor infiltration reactor (not to scale).

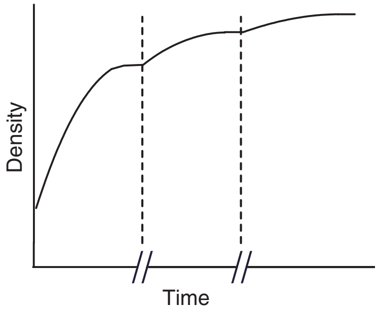

Figure 6.5 Schematic illustration of the densification kinetics of a thick preform in isothermal isobaric chemical vapor infiltration.

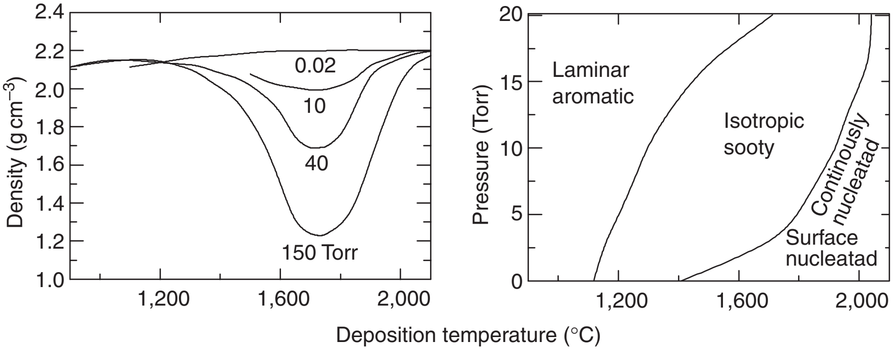

Figure 6.6 Density and microstructure of infiltrated carbon versus temperature and pressure (Kotlensky, 1971; reprinted by permission of the Society for the Advancement of Materials and Process Engineering).

doing so may also lead to more premature closure of surface pores. Conversely, lower temperatures and pressures may reduce undesirable gas-phase nucleation and formation of tar and soot by-products. Lower pressure corresponds to higher gas-phase diffusivity, leading to more uniform distributions of density and microstructure within the composite. For example, the density minimum observed in carbon CVI (Kotlensky, 1971) – see Fig. 6.6 – was interpreted as resulting from the incorporation of soot particles formed in the gas phase into the carbon deposited in the pores of the preform. If the pressure was reduced sufficiently, this density minimum could be eliminated. C–C composites having larger crystallite size, L_a, and improved thermal and electrical conductivities were produced at lower pressures (Stoller and Frye, 1972). Rough-laminar (anisotropic) carbon, which is generally desired for many applications, was obtained at 35 Torr (4.7×10^3 Pa), but not at 100–760 Torr ($1.3 \times 10^4 - 1.0 \times 10^5$ Pa). Rough-laminar carbon can be rendered more graphitic, i.e. more ordered microstructurally, by high-temperature treatment (graphitization) at ≥ 2,000 °C (Loll *et al*., 1977) and this may result in improved composite properties. Lower pressures also allow lower inlet precursor flow rates.

The effect of different precursors on the carbon densification rate of 7.6 × 7.6 × 1.6 cm carbon preforms was studied (Duan and Don, 1995). Randomly oriented pitch-fiber tow preforms were impregnated with phenolic resin and densified at 1,000–1,150 °C and 15 Torr

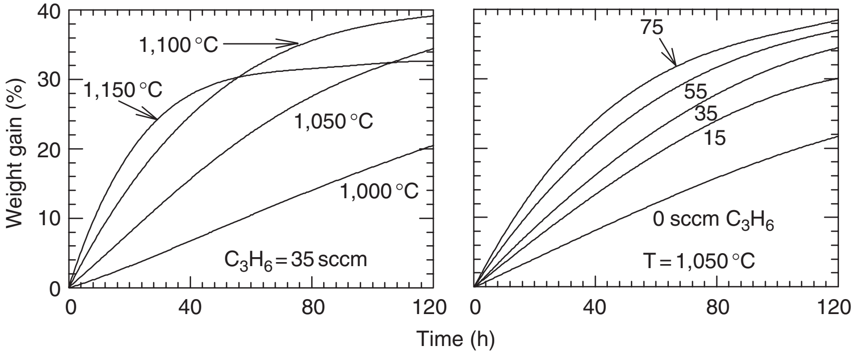

Figure 6.7 Relative weight gain versus time in isothermal isobaric carbon CVI from CH_4 and H_2, showing the effects of temperature and C_3H_6 additions (Duan and Don, 1995; reprinted with the authors' kind permission).

(2.0×10^3 Pa). The initial density and open porosity of the preforms were 1.25 g cm^{-3} and 38 vol%, respectively. The preform weight was continuously recorded by means of an in-situ balance. CH_4 at 400 sccm was the primary precursor, with additions of 100 sccm H_2 and 0–75 sccm propylene, C_3H_6. The hot zone of the furnace was 15.2 cm in diameter by 30.5 cm long. The curves of fractional weight gain versus time had an exponential-type behavior and were fitted to the equation $\Delta m/m = a_1(\rho_{CVD}/\rho_o)\ln\{1 + a_2[\exp(-a_3t - a_4t^2)] - 1\}$, where the a_j's were constants. At 1,050 °C, the addition of increasing fractions of C_3H_6 resulted in increases of the initial deposition rate and of the final density, shown in Fig. 6.7. The microstructure of the deposited carbon changed from isotropic in the absence of C_3H_6 to anisotropic when 35 sccm C_3H_6 was added. With 35 sccm C_3H_6, increasing the temperature from 1,000 to 1,100 °C also increased the initial densification rate and the final density, whereas at 1,150 °C, premature surface pore closure and non-uniform deposition through the thickness were seen.

Thus, the operating conditions of a hot-wall, isothermal isobaric CVI process involve a compromise which results in materials with the desired properties in the shortest possible time and with the minimum amount of labor, supplies, and energy.

Advantages of isothermal isobaric CVI include:

- The method is well-established and relatively well-understood.
- A large number of preforms can be densified simultaneously.
- The densification time per preform is relatively low for heavy loading of the reactor.
- Preforms of different and complex shapes and sizes can be readily densified in the same run, although the minimum dimension (usually the thickness) needs to be similar.
- The energy expenditure per part is relatively low.

Disadvantages of isothermal isobaric CVI include:

- Premature surface crusting occurs before the desired bulk density is reached, necessitating several interruptions in the CVI process to grind surfaces.
- Very long hot processing time, typically 600–2,000 h per batch (but the time does not depend on the number of parts being densified in a given reactor).
- The density within the article is generally highest at the surfaces and lowest in the interior regions.

- Overall precursor conversion efficiency is low, of the order of 1–2%.
- Preforms having different minimum dimensions (usually the thickness) densify at very different rates.
- Capital cost is relatively high.
- Cost of inventory and potential re-work can be high.
- Process development or process changes may be slow to implement.

From the previous sections, it follows that in order to significantly speed up the densification process of relatively thick parts, either the temperature or the pressure during CVI has to be increased, yet without clogging surface pores or degrading material properties. The next section describes approaches using a thermal gradient to achieve this goal.

3.2 Thermal-gradient inductively-heated isobaric CVI

3.2.1 Early thermal-gradient isobaric CVI studies

In an early thermal-gradient CVI process (Stoller and Frye, 1972; Lieberman and Noles, 1973; Stoller *et al.*, 1974; Lieberman *et al.*, 1975), intended for rocket components (Thomas, 1993), a porous carbon felt was mounted around a truncated-conical graphite susceptor; see Fig. 6.8. This electrically conductive susceptor was heated by a conical-shaped induction coil (frequency and power levels not provided). The felt was fabricated using 5 cm long, chopped oxidized PAN fibers, which were carded into batts (Lieberman *et al.*, 1975). Alternate carded batts were cross-plied when they were felted by means of a needle loom, in an effort to achieve isotropic properties in the plane. The felts were nominally $118 \times 118 \times 3.2$ cm in size and had a density of $0.14 \pm 0.02\,\mathrm{g\,cm^{-3}}$. Each felt, which was initially flat, was made into a truncated hollow cone by sewing a single seam along the entire length of the cone with a rayon-based carbon yarn. After carbonization in flowing Ar to 1,300 °C to remove volatiles, the weight loss was 44% and the linear shrinkage 13.5–14.6%. The carbon deposition conditions of one preform were (Lieberman *et al.*, 1975): susceptor temperature = 1,325 °C, total pressure = 8.4×10^4 Pa (= 630 Torr = 1 atm in Albuquerque, NM), CH_4 flow rate = $61\,\mathrm{l\,min^{-1}}$, Ar flow rate = $205\,\mathrm{1 min^{-1}}$ and free gas space between shroud and preform = 2.5 cm. From the description given (Lieberman and Noles, 1973; Stoller *et al.*, 1974; Lieberman *et al.*, 1975) it appears that the felt did not initially couple electrically to the coil, so there was no induced electrical current flowing around the circumference of the felt. The sewn construction of the felt may have resulted in a very high electrical resistivity in the circumferential direction and thus a lack of initial electromagnetic coupling. The heating of the felt therefore occurred initially by thermal radiation. It was stated (Stoller *et al.*, 1974) that carbon was deposited first at the surface of the felt adjacent to the susceptor and then deposition progressed radially through the preform as the densified preform became inductively heated. However, as reported (Stoller and Frye, 1972; Stoller *et al.*, 1974), a reduction by a factor of two only was achieved in the overall densification cycle time, compared to isothermal CVI, and this technique was limited to densifying one preform at a time. Gas analysis data (Lieberman and Noles, 1973) indicated that densification times were equal to or longer than 130 h; infiltration times of six weeks (1,000 h) were reported (Lackey, 1989). This process also suffered from soot formation due to the combination of the very high temperature and high pressure employed. Spatial density distributions were obtained from samples cored through the thickness of the frustum. There was a density gradient from the inner

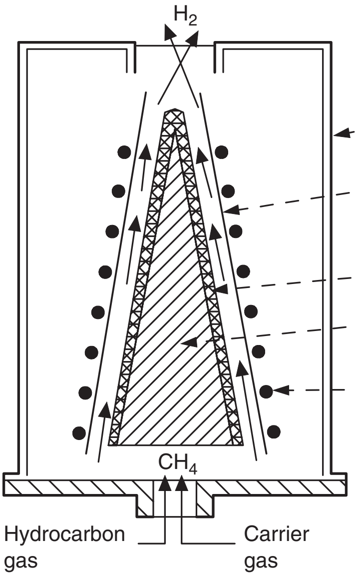

Figure 6.8 Schematic diagram of an early thermal-gradient CVI system (Stoller and Frye, 1972; *reprinted by permission of the Society for the Advancement of Materials and Process Engineering*). The axially sewn preform did not couple to the coil or its coupling was very inefficient and it was thus initially heated by thermal radiation from the inductively-heated conical susceptor.

half (1.73–1.84 g cm^{-3}) towards the outer half (1.87–1.89 g cm^{-3}) of the wall thickness (Lieberman *et al*., 1975), as in isothermal isobaric CVI, indicating possible surface crusting. Significant density gradients were measured for infiltrations performed at lower temperatures (Stoller *et al*., 1974). The microstructure, as measured in polarized-light microscopy, was rough-laminar in 70–100% of the outer half of the wall thickness; the remainder was smooth-laminar, which also comprised an outer, 0.2 cm crust (Lieberman *et al*., 1975). In the inner half, 40–60% of the matrix was rough-laminar.

Advantage of early inductively heated thermal-gradient isobaric CVI process is:

- A decrease of the infiltration time by a factor of about two, compared to isothermal isobaric CVI.

Disadvantages of early inductively-heated thermal-gradient isobaric CVI process include:

- A relatively long infiltration time.
- Spatial gradients in density and microstructure within the thickness of the preform.
- No easy control of deposition and infiltration conditions.
- Large, expensive, specifically machined graphite susceptor was required because of lack of inductive coupling between the induction coil and the preform at the start of infiltration.
- Only one preform densified per run.
- Possible need to machine the cooler, insufficiently-infiltrated surface after the run.
- Preforms having significantly different shapes or dimensions may require different coil and susceptor configurations.

In the next section, recent developments are described which demonstrated at least a ten-fold reduction in the densification time of multiple, thick C–C composites through efficient electromagnetic coupling to an induction coil.

3.2.2 Recent inductively-heated thermal-gradient isobaric CVI studies

Recently it was demonstrated that three 10.8 cm o.d. × 4.4 cm i.d. (internal diameter) × 3.0 cm thick PAN-carbon-fiber preform disks, having an initial density of 0.4–0.6 g cm^{-3}, could be directly heated by electromagnetic induction and simultaneously densified in 1 to 2 days (Golecki *et al.*, 1994; Golecki *et al.*, 1995a). A novel, in situ, densification-rate monitor was also developed (Golecki and Narasimhan, 1998). The thermal-gradient C–C CVI system is shown schematically in Fig. 6.9. The main part of the water-cooled, stainless steel deposition chamber was 38 cm i.d. × 43 cm high. A 38 cm high conical flange allowed access from the top of the chamber. The chamber was pumped by means of a Roots blower, backed by a chemically resistant rotary forepump. The exhaust from the forepump was connected to an oxidation furnace. Flowing cyclopentane, C_5H_{10}, was delivered to the bottom of the chamber as a vapor through a mass-flow-controlled gas line maintained at 70 °C. C_5H_{10} is a liquid at 25 °C with a vapor pressure of 4.3×10^4 Pa (321 Torr) and a boiling point of 50 °C; in large quantities it costs about \$0.44 kg^{-1}. Being a liquid, it occupies significantly less storage space than a gaseous carbon precursor. The total pressure in the deposition chamber was measured using a diaphragm pressure gauge and controlled by means of electronically operated throttle valves. The process ranges were: total pressure = $20-100$ Torr ($2.7 \times 10^3 - 1.3 \times 10^4$ Pa) and C_5H_{10} flow rate = $170 - 540$ sccm.

The three thick carbon preforms were placed around a 4.4 cm o.d. molybdenum or alumina (Al_2O_3) centering mandrel and vertically spaced about 1 cm apart. The preforms and

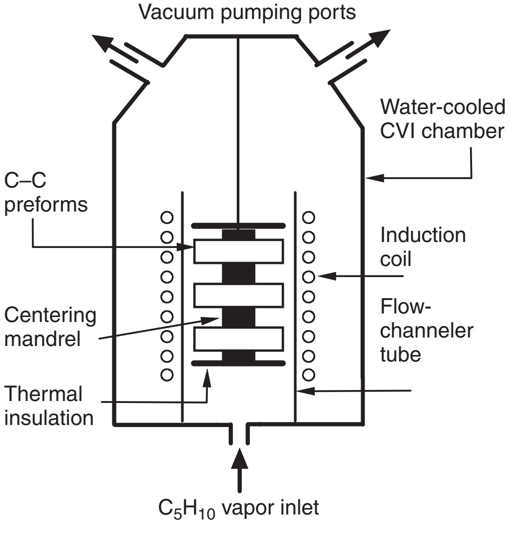

Figure 6.9 Simplified schematic (not to scale) of recent, patented, inductively heated thermal-gradient CVI reactor (Golecki *et al.*, 1994; Golecki *et al.*, 1995a,b), depicting, as an example, three C–C disk-shaped preforms mounted around a centering mandrel inside an induction coil.

mandrel assembly was centered inside a 15 cm i.d. × 22 cm long, helical, water-cooled copper induction coil placed inside the deposition chamber. An electrically conductive mandrel was not required, as the electrical conductivity of these preforms in the undensified state was sufficiently high to couple directly to the electromagnetic field induced by the energized coil. This was evidenced both by inductively heating such preforms in the coil without any mandrel, by using the electrically insulating alumina mandrel during rapid densification runs, and by densifying other, 5.6 cm thick carbon preforms with no mandrel (Golecki and Narasimhan, 2001).

In order to reduce radiative heat losses from the outer surfaces of the top and bottom preforms, several 11 cm o.d. × 0.06 cm thick grafoil plates were placed above and below the bottom surfaces of the mandrel. In some runs, a 47 cm high × 14.1 cm o.d. × 13.5 cm i.d. quartz tube was inserted between the C–C preforms and the coil, in order to act as a flow channeler for the C_5H_{10} vapor. In other runs, an 11.4 cm high quartz tube was placed between the bottom of the chamber and the coil, so that in this case the surfaces of the C–C preforms were in direct optical communication with the coil and chamber walls. The turnaround time for substrate loading and unloading was very short. The temperatures of the C–C disks were measured directly with 0.25 mm diameter, Pt-13%Rh/Pt thermocouples inserted at different radial locations half-way through the thickness of the disks. Pyrometry measurements were also performed.

The induction coil was energized with an audio-frequency power supply; the power, voltage and frequency could be read from panel meters and recorded electrically during CVI runs. The current in the induction coil was monitored during CVI runs via a device termed the "vacuum thermocouple" (VTC), which was part of the power supply. The VTC readout was derived from a pick-up coil placed around a lead within the power supply, which was connected to the induction coil in the chamber. Therefore, the readout of the VTC was directly related to the current in the coil. The parameter ranges of the power supply were: power = 8.8 − 13.2 kW, frequency = 4.9 − 8.6 kHz.

Figure 6.10 illustrates overall gross densification rates measured by interrupting CVI runs (Golecki *et al.*, 1994, 1995a). Average carbon pick-up rates per disk of $9.5\,g\,h^{-1}$ or $10.6\%h^{-1}$ were obtained. The whole-disk density was increased from 0.41 to $1.54\,g\,cm^{-3}$ in just 26 h, representing an average rate of increase of $0.044\,g\,cm^{-3}\,h^{-1}$. Overall disk densities of 1.68 $g\,cm^{-3}$ were obtained, with $1.84\,g\,cm^{-3}$ in regions, depending on process conditions (PAN carbon fiber density is $1.73\,g\,cm^{-3}$). Importantly, the shape of the density vs. time curves was sigmoidal-linear rather than the much slower exponential approach to final density observed in isothermal isobaric CVI. Generally, the highest density was found in the middle disk in the stack, due primarily to lower temperatures at the outer surfaces of the two extremal disks. Optimized end-insulation and coil design can reduce such axial disk-to-disk variations, especially in a scaled-up stack containing, e.g. 30–60 disks. The density uniformity within a disk, as measured from cored and sliced samples, was within ± (5–8)%. The overall conversion efficiency of the precursor, i.e. the amount of carbon added to the disks divided by the amount of carbon which flowed as C_5H_{10}, was 20–30%, over ten times higher than reported for isothermal isobaric CVI, and also higher than published for forced-flow thermal-gradient CVI of carbon (Lackey *et al.*, 1995; Vaidyaraman *et al.*, 1995b), described in Section 2.5.

Figure 6.11 illustrates the variation of temperature at three radial locations in the middle C–C preform disk during a CVI run. Initially the i.d. region of the disk was hottest, all three temperatures increased as a function of time, and the temperature difference between the i.d. and o.d. decreased as a function of time. Temperatures inside the disk reached almost

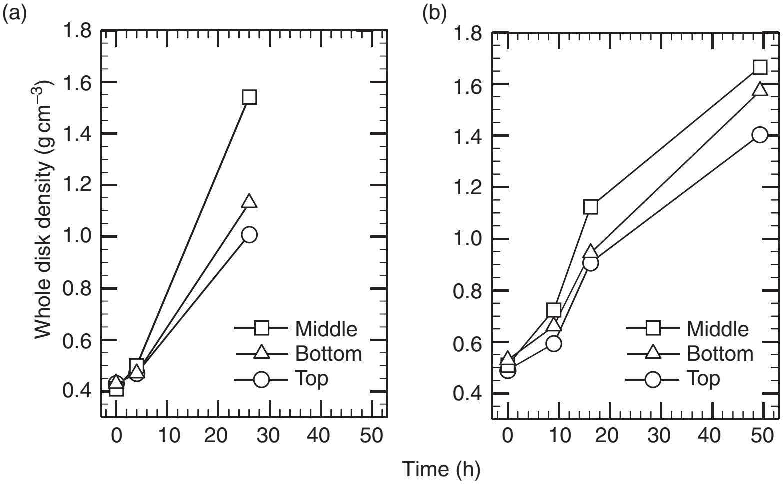

Figure 6.10 C–C disk density versus time in inductively-heated thermal-gradient CVI (Golecki *et al.*, 1994): (a) One set of disks, without grafoil insulation, with long flow channeler tube; run was interrupted to weigh the preforms; (b) Three sets of disks in three separate runs, with grafoil insulation, without flow channeler tube. Lines are intended as an aid to the eye.

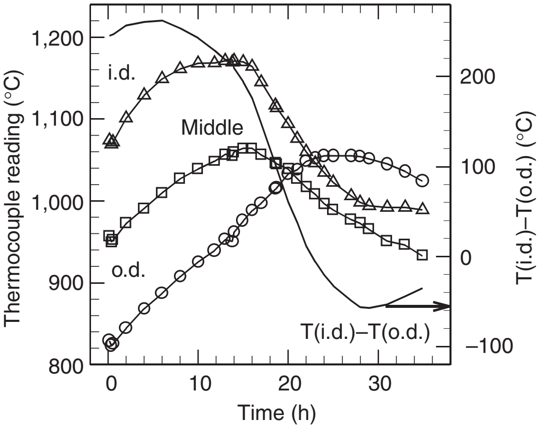

Figure 6.11 Temporal variation of the temperatures at three radial locations in the middle carbon preform disk in a three-disk stack during inductively-heated thermal-gradient CVI (Golecki *et al.*, 1995a). Thermocouple inserted: Δ = near inner diameter (i.d.) of preform disk, □ = mid-way between inner and outer diameters, ○ = near outer diameter (o.d.). Solid line without symbols represents the difference between the readings of the inner diameter and the outer diameter thermocouples.

1,200 °C, ≈ 200 °C higher than in isothermal isobaric CVI of carbon. Some surface crusting occurred and yellow vapors were observed in the chamber towards the end of this particular run but these effects were absent in CVI runs stopped earlier. The total amount of liquid tar was significantly smaller in such runs, compared to the estimated 1–3% of the incoming C_5H_{10} for runs which were continued past surface crusting. No solid or powdery soot was found in any of the runs.

Spatial density distributions in C–C disks as a function of infiltration time were obtained from the geometrical dimensions and weights of cored and sliced samples. The measured densities in a middle disk from a three-disk run interrupted intentionally after 9.0 h (approximately quarter-way through the run) are plotted in Fig. 6.12. The densities were highest in the *interior* regions of the disk, both radially and axially. Figure 6.13 shows spatial density distributions measured in a different disk from another run which was intentionally interrupted after 16.2 h (approximately mid-way through that run). Again, the densities were highest in the *interior* regions of the disk and lower near all outside surfaces, whether on the circumferences or on the top and bottom surfaces. Furthermore, the difference between the highest and lowest densities here was only 10%. As the CVI run progressed, regions which had densified less tended to catch up with regions which had densified more.

The microstructure of the deposited carbon was determined by measuring the extinction angle of the Maltese cross in a polarized-light microscope (Savage, 1993). Depending on processing conditions, rough-laminar (19–23°), smooth-to-rough-laminar (13–15°) or smooth-laminar (10–12°) microstructure was obtained. The rough-laminar structure has the highest density and is generally desired for braking applications. Isotropic carbon (0°) was not found. The compressive strength, measured for 6.6 mm diameter × 7.9 mm long samples, increased steeply with increasing density (Golecki *et al.*, 1995b). At 1.79 $\mathrm{g\,cm^{-3}}$ the value of the compressive strength was 268 MPa (39 ksi), considered very good.

In this inductively-heated thermal-gradient isobaric CVI process, the substrates were Joule heated by circumferential induced currents flowing inside them. In this geometry, the induced power was initially highest near the o.d. and diminished to zero in $\approx 3\delta$, where the skin depth $\delta = 5(\rho_{\mathrm{el}}/f)^{0.5}$ (Brown *et al.*, 1948), with δ in cm, the electrical resistivity ρ_{el} in $\mathrm{m\Omega\,cm}$ and the frequency f in kHz. For example, for a material with an initial uniform electrical resistivity $\rho_{\mathrm{el}} = 10\,\mathrm{m\Omega\,cm}$, $\delta = 5\,\mathrm{cm}$ at 10 kHz. The substrate temperatures increased with power to the coil. The temperature distribution in the substrates was dominated by the radiation losses, Q, to the water-cooled coil and walls, $Q = \varepsilon\sigma_{\mathrm{o}}(T^4_{\mathrm{os}} - T^4_{\mathrm{wall}})$, where ε is the emissivity, $\sigma_{\mathrm{o}} = 5.67 \times 10^{-8}\,\mathrm{J\,K^{-4}m^{-2}s^{-1}}$, T is in K and the subscript 'os' denotes outside surface. The temperature would thus initially be highest in the interior regions of the preforms, lower at the top and bottom surfaces and lowest at the o.d., the latter surfaces having the largest view factors of the water-cooled coil and chamber walls.

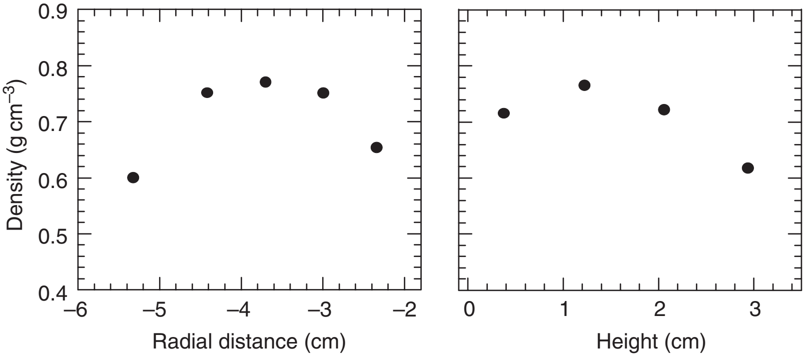

Figure 6.12 Radial and axial density distributions in the middle C–C preform disk in a three-disk stack infiltrated for 9.0 h by inductively-heated thermal-gradient isobaric CVI (Golecki *et al.*, 1996).

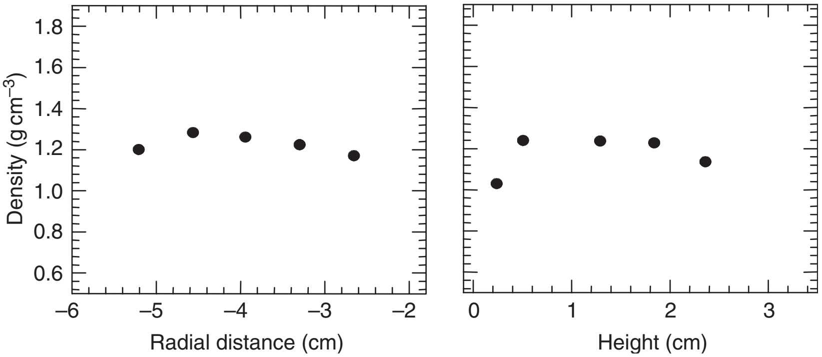

Figure 6.13 Radial and axial density distributions in the middle C–C disk in a three-disk stack infiltrated for 16.2 h by inductively-heated thermal-gradient isobaric CVI (Golecki *et al.*, 1996).

The gas-phase diffusivity of the precursor was high, due to the low deposition pressure, ensuring that the initial densification rate would be highest in those hottest interior regions, consistent with the measured spatial density distributions. As densification progressed, the electrical and thermal conductivities of the preform increased. A higher electrical conductivity resulted in a shallower skin depth and improved coupling to the coil, i.e. higher induced current and higher temperatures near the exterior surfaces of the preform, as measured, other conditions being equal. Thus a spatial "inside-out" densification front existed in the preforms. As the pores inside the disk became smaller and finally the surface started crusting, the carbon deposition rate decreased, due to the much smaller available surface area, and the temperature distribution became more uniform.

In situ densification-rate measurements. The rate at which carbon mass was added to the carbon fiber preforms and the total carbon mass added were determined in real time by measuring the current in, or the voltage across, the induction coil; see Fig. 6.14 (Golecki and Narasimhan, 1998). When the induction power supply is run in the constant-power mode, the coil current and voltage will be adjusted to compensate for changes in the coupling to the load, which comprises the carbon-fiber preforms. When the coupling improves, less current (and voltage) is required in the coil to transfer the same amount of power to the preform disks. Referring to Fig. 6.14, both the VTC voltage (which increases with coil current) and the coil voltage decrease with time during inductively-heated thermal-gradient CVI. The initial slopes are approximately constant in this example. At about 14 h into the process, there is a noticeable break in both slopes and from that point on, both slopes are slightly less than one-third of their previous values. The time at which the break in either slope occurs coincides with the time when the i.d. and middle temperatures of the middle disk peak (Fig. 6.11). In CVI runs which were stopped close to the time of the break in slopes, no surface crusting of the preforms was observed. In runs which were continued well beyond the time of the break in the slopes, some surface crusting of the preforms was noted. Furthermore, the amount of liquid tar (a by-product of any carbon CVI process) was significantly reduced in runs terminated at the slope breakpoint. Note, however, that the amount of tar in inductively heated thermal-gradient CVI is generally significantly lower than that in equivalent runs done by conventional, isothermal isobaric CVI. Another point is that even

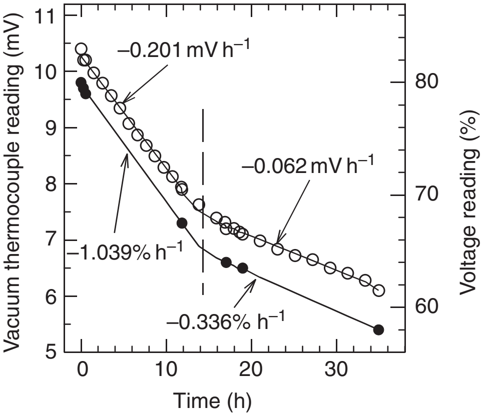

Figure 6.14 Variation of the vacuum thermocouple voltage (○) and coil voltage (•) during inductively-heated thermal-gradient isobaric CVI of three carbon-fiber preforms, each 10.8 cm o.d. × 4.4 cm i.d. × 3.0 cm thick (Golecki and Narasimhan, 1998). Data are for the same run as in Fig. 6.11.

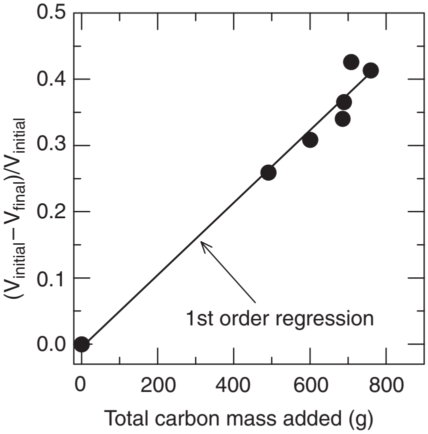

Figure 6.15 Dependence of relative change in vacuum thermocouple readings on the total measured carbon mass added to the three nonwoven PAN-based carbon-fiber preform disks by inductively-heated thermal-gradient isobaric chemical vapor infiltration (Golecki and Narasimhan, 1998). Each point denotes a separate densification run with a different set of preforms.

though the spatial temperature distribution within the preforms changes with time during densification, the intrinsic electrical conductivity of pure carbon or graphite as a function of temperature is constant to better than 4% from 800 to 1,200 °C. Thus, the measured changes in coil current and voltage are due to the increase in carbon mass. Therefore, the slope of either the VTC voltage or the coil voltage as a function of time is a measure of the densification rate. This method is intrinsically very sensitive; e.g. for the case of three carbon preform disks described here, the sensitivity factor is about 0.1 g carbon, or 0.01% of the total mass of carbon added, per μV output of the VTC. When the densification of the bulk of the preforms is complete and surface crusting starts, there is a significant decrease in the slope of both coil current and coil voltage, which can be used as an input signal to terminate the CVI run.

Figure 6.15 illustrates another useful aspect of this novel monitoring and control method. Referring to the rapid densification of the three carbon-fiber preform disks, there is a visual linear relationship between the relative change in VTC readings and the total carbon mass added by CVI to the three disks. This relationship can be used as a calibration curve that makes it possible to apply predictive control of both the densification rate and the process end-point in real time. For example, a preset value of added mass may be identified at the beginning of the densification process. By monitoring the VTC voltage or the coil voltage throughout the process, and using one or the other voltage as an input signal to a feedback control loop, one can control the rate at which the densification proceeds and also end the densification run at exactly the desired time.

Both this thermal-gradient inductively-heated densification process and the densification rate monitoring method described here can be used with different materials systems, article shapes, CVI methods and other processes, for a variety of applications.

Advantages of this recent inductively-heated thermal-gradient isobaric CVI include (Golecki *et al.*, 1994; Golecki and Narasimhan, 1998):

- Single-cycle densification – no need for intermediate sanding.
- At least 10 times faster than isothermal isobaric CVI.
- Multiple preforms can be readily densified in one run.
- Thick preforms (>3 cm in thickness) can be densified readily with very good density uniformity.
- Multiple preforms having different thicknesses can be densified in the same run.
- The process is run at low pressure, which results in higher gas-phase diffusivity and is more conducive than atmospheric pressure CVI to obtaining uniform density profiles and formation of matrices and composites with desirable properties.
- All CVI process conditions, including pressure, flow rate, precursor type, precursor dilution, and temperature are fully adjustable in real time.
- High precursor conversion efficiency (20–30%) is obtained without forced flow.
- No solid by-products (only a small amount of liquid tar) are formed.
- Continuous real-time monitoring and control of densification rate and process end-point.
- No fundamental technical barriers exist in scaling up both the preform size and the number of preforms per run.
- Well suited for small or medium batch size for “just-in-time” production with turn-around time of less than one week, reducing inventory and potential scrap rate.
- No special fixturing is required.
- No extra machining is needed.
- There is no need to immerse the preforms in a flammable liquid and the reactor can be located in a normal industrial setting, without the need for an explosion-proof room.

Disadvantage of recent inductively-heated thermal-gradient isobaric CVI is:

- Preforms having significantly different shapes or lateral (not thickness) dimensions may require different coil configurations.

3.3 Liquid-immersion thermal-gradient atmospheric pressure isobaric CVI

A method for rapid densification of a single porous carbon preform per run was described (Houdayer *et al.*, 1981, 1984), in which the preform was placed around a cylindrical, electrically conducting graphite susceptor, this assembly was immersed in a liquid precursor, preferably cyclohexane, C_6H_{12} (boiling temperature = 80 °C), and the reactor was heated by electromagnetic induction via a coil connected to a high frequency generator, to a temperature in the range 1,000–1,300 °C, sufficient to cause the liquid to vaporize and deposit carbon inside the pores of the preform; see Fig. 6.16. The reactor vessel is assumed to have been electrically insulating (i.e. made of glass, quartz, etc.), since the induction coil was located outside the reactor. The pressure in the reactor was essentially atmospheric. A similar approach had been previously described (Nieberlein, 1968, 1971) for the rapid deposition of SiC coatings on resistively heated, refractory metal filaments.

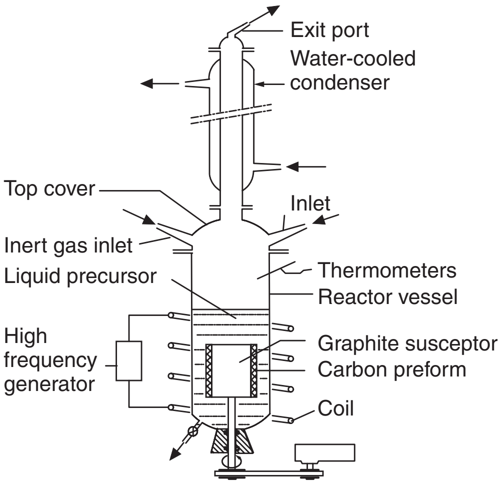

Figure 6.16 Liquid-immersion thermal-gradient inductively-heated chemical vapor infiltration reactor (Houdayer *et al.*, 1984).

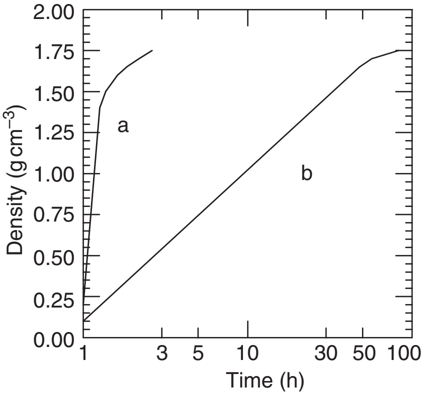

Figure 6.17 Density versus time for (a) a carbon fabric densified by liquid immersion thermal-gradient inductively-heated chemical vapor infiltration and (b) a carbon felt densified by isothermal isobaric chemical vapor infiltration, both preforms having an initial density of 0.1 g cm^{-3} (Houdayer *et al.*, 1984).

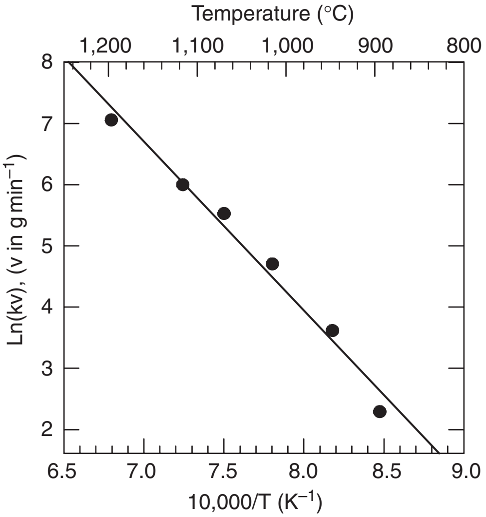

Figure 6.18 Relative rate of mass gain of C–C composite sample versus temperature in liquid-immersion inductively-heated thermal-gradient chemical vapor infiltration reactor (Narcy *et al.*, 1995a; reproduced with permission of the American Ceramic Society).

Using this method, a densification time of ≈3 h was needed to reach 1.75 g cm^{-3} from an initial density of 0.1 g cm^{-3}, compared to 80 h in isothermal CVI; see Fig. 6.17. Shape, dimensional, or physical data for the densified preform or the reactor components were not provided. The electrical continuity of the preform, which has important significance regarding its coupling to the electromagnetic field, was not specified. It appears that the electromagnetic field coupled to and heated the central graphite mandrel but it is not obvious that the porous preform also coupled to the field. Preforms densified using this liquid C_6H_{12} immersion method were stated to exhibit no surface pore plugging and to have a texture and physical characteristics identical to those obtained according to the prior art; the stated application of the carbon parts was as friction materials in disk brake pads. It was stated that since carbon was first deposited in contact with the susceptor, a densification gradient was obtained from the interior to the exterior of the porous preform.

Physical properties of 2.2 cm o.d. × 1.6 cm i.d. (wall thickness 0.3 cm) × 6.5 cm long C–C composites, made from RVC 2000 carbon felt, and densified (one per infiltration run) by this method at 900–1,200 °C were recently published (Narcy *et al.*, 1995a, b). The initial density was ≈ 0.1 g cm^{-3} and the final fiber fraction was <6%; these fibers were not graphitizable. The increase in mass was linear with time at each temperature. The thermal kinetics (Fig. 6.18) yielded an apparent activation energy of 2.3 eV/molecule. Final densities of 1.4–1.8 g cm^{-3}, depending on the preform used, were reached in a few hours. The deposited carbon was rough-laminar as determined by polarized-light optical microscopy and the structure was reported to be homogeneous. The matrix deposited at the lowest temperature, 930 °C, was more likely to produce a "graphite-like structure" after annealing at 2,450 °C, based on the crystallite sizes determined from X-ray diffraction.

The above immersion principle was recently used (Carroll *et al.*, 1995; Thurston *et al.*, 1995; Scaringella *et al.*, 1996) for densification of C–C, SiC–SiC, and SiC–Si_3N_4 composites. Examples given of precursors for C infiltration were cyclohexane, n-hexane, benzene, cyclopentane, cyclohexene, 1-hexene, gasoline, methyl cyclohexane, and toluene. Here the water-cooled copper coil was located inside the reaction chamber, which was fabricated from a non-magnetic material (e.g. quartz, glass, stainless steel, ceramic). Continuous replacement, filtering (using ceramic or charcoal filter) and cooling of the liquid precursor during densification was described. An annular 4.0 cm o.d. × 3.8 cm i.d. (wall thickness 0.1 cm) × 15.2 cm high carbon preform with an initial bulk density of 1.3 g cm^{-3} was placed around a central graphite susceptor core and densified in cyclohexane liquid. The preform was made of a plurality of overlapping sheets of conventional carbon/phenolic material in a format called involute wrap and was carbonized by heating in excess of 650 °C. The power supply was run at 30 kW and 160 kHz and preform temperatures between 900 and 1,500 °C were achieved. After 4 h, the bulk density was 1.83 g cm^{-3} (mercury porosimetry gave 2.01 g cm^{-3}); the porosity was 6.2%. From these data, a bulk mass pick-up rate of 2.5 g h^{-1} is calculated. The tube had a compressive strength of 179 MPa (26.3 ksi) and a modulus of 300 GPa (44.1 Msi). An alternate means of heating a bar-shaped preform was described, using direct-contact, d.c. or a.c. Joule heating, with the bar clamped between two copper electrodes and the whole assembly immersed in the liquid precursor. Such resistive heating results in a very different spatial power density profile compared to inductive heating (Brown *et al.*, 1948; Jackson, 1962). All descriptions referred to infiltration of only one preform at a time; the precursor conversion efficiency was not provided.

A 33 cm o.d. (by ≈ 18 cm i.d. by ≈ 1.5 cm thickness, both estimated from the published photograph) C–C aircraft brake disk pad was stated to have been densified in a single 8 h cycle to a “uniform” density of 1.85 g cm^{-3} (Textron, 1994). The initial density of the disk was not provided. The refurbishment by means of densification of worn C–C rotor brake pads from F-16 military aircraft was described (Scaringella *et al.*, 1996). Each rotor was a 30.5 cm diameter annular disk which was ground to half its original thickness (value not provided). Each such disk was densified by being heated between two pancake-shaped induction coils while both disk and coils were immersed in liquid C_6H_{12} (one disk per run). Heating the worn disk to an internal temperature of 950–1,100 °C for 2.0–3.5 h was generally observed to be sufficient to refurbish it to a density at least equal to that of an original equipment. The surface temperature of the disk was estimated to be approximately 800–1,100 °C during the densification runs. Total process run times were 48 h or less. Initial and final densities were not provided, but a deposited carbon matrix density of at least 1.85 g cm^{-3} was claimed. Friction coefficients, wear rates and carbon microstructures (“preferably substantially non-isotropic”) at least equivalent to those in unused or conventionally refurbished brake pads were obtained. The friction and wear data were acquired using subscale (3.2 cm o.d. × 2.2 cm i.d.) test specimens. A post-densification, 2 h annealing in flowing Ar at 2,100 °C reduced the wear rate without changing the average friction coefficient.

The thermal conditions determining the preform temperature distribution in this type of liquid-immersion reactor are quite different compared to those in a flowing vapor, inductively-heated, thermal-gradient CVI reactor described in Section 2.3.2. In the liquid immersion reactor, significant convection currents exist in the boiling liquid, which cool the exterior of the preform, and significant additional cooling of the heated preform takes place during liquid immersion through the boiling of the liquid (Thurston, 1995). Axial non-uniformities in the heat transfer out of the preform may occur due to variations in the velocity and amount of vapor generated from the liquid along the length of the preform.

Advantages of liquid-immersion thermal-gradient atmospheric-pressure CVI include:

- Infiltration time of single preform is short.
- Single-cycle densification.

Disadvantages of liquid-immersion thermal-gradient atmospheric-pressure CVI include:

- Scale up to simultaneous infiltrations of multiple preforms may be challenging, due, e.g. to the "vapor lock" effect (Thurston *et al.*, 1995; Scaringella *et al.*, 1996). If the preforms are too close to one another, or if the walls of the reaction vessel are too close to a preform, vapor may build up, thereby displacing the liquid, greatly reducing convective heat extraction from the preform and creating a thermal hot spot and non-uniform densification.
- The precursor pressure is 1 atm or above and practically fixed, resulting in a very low gas-phase diffusivity and potentially degraded density profiles (Kotlensky, 1973; Naslain *et al.*, 1989; Pierson, 1992). Atmospheric pressure CVI can additionally result in significant formation of soot and other undesirable by-products.
- Complete immersion of the preform in liquid precursor(s) is required, raising safety concerns associated with handling large amounts of flammable and/or toxic liquids which are boiling in extremely close proximity to parts maintained at 900–1,500 °C.
- Preforms having significantly different shapes and lateral dimensions may require different coil configurations.
- The preform needs to be preferably placed in a support fixture (Thurston *et al.*, 1995; Scaringella *et al.*, 1996), in order to firmly hold the preform within the boiling liquid with respect to the reactor and coil.

In the next section, we describe CVI using a combination of forced-flow and thermal gradient.

3.4 Forced-flow thermal-gradient atmospheric-pressure CVI

In forced-flow thermal-gradient CVI (Kotlensky, 1973; Lackey and Caputo, 1986), there is a pressure gradient impressed across one of the dimensions (usually the thickness) of the porous preform and an inverse temperature gradient across the same dimension. The temperature is coldest at the surface exposed to the high pressure (about 1–2 atm = 100–200 kPa) of the precursor and hottest at the opposing surface. The preform is heated by thermal radiation. All the precursor vapor is made to flow through the preform and the process is finished when the pressure gradient across the preform becomes too large, 0.7–1.4 atm = 70–140 kPa (Besmann *et al.*, 1991), due to the closure of the flow passages through the pores. In a study of forced-flow, thermal-gradient CVI from the 1960s (Kotlensky, 1973), 0.64 cm thick, layered carbon preforms were densified for 6 h at 1,700 °C in CH_4. The densities of these preforms increased from 0.075 $g\,cm^{-3}$ (felt) or from 0.5 $g\,cm^{-3}$ (fabric) to 1 $g\,cm^{-3}$. In a later patent, the deposition of matrix material was stated to occur progressively from the hot surface towards the cold surface (Lackey and Caputo, 1986). This process is best suited for densification of relatively thin-walled tubes and disk-shaped preforms (one preform per run). The specially designed apparatus required is relatively complex and high-temperature fixturing and gasketing are needed. This process has been applied to the densification of SiC–SiC composites (Lackey and Caputo, 1986), including, e.g. 3.7 cm o.d. × 2.5 cm i.d. × 20 cm long SiC-Nicalon-fiber tube preforms (Stinton *et al.*, 1995) and 23 cm o.d. × 0.3–1.3 cm thick T-300 carbon, SiC–Nicalon, and Nextel 480 mullite fibrous disk preforms (one preform per run) infiltrated with SiC or Si_3N_4 (Gulden *et al.*, 1990).

This process was applied to the densification of 4.76 cm diameter × 0.8–1.0 cm thick carbon preforms (one preform per run), fabricated by stacking 40 layers of plain-woven T-300 carbon fiber cloth (fiber diameter 7 μm, fiber density 1.77 g cm^{-3}, 3,000 fibers/bundle) in 0°–30°–60°–90° orientation inside a perforated graphite holder (Lackey *et al.*, 1995; Vaidyaraman *et al.*, 1995a,b). The lay-up was compressed in a graphite punch at ≈ 900 N (91 kgf); fiber content was 46–60%vol. Preform temperature and thermal gradient could be varied by altering the height of the preform holder or the preform thickness. CH_4, C_3H_8 (propane), or C_3H_6 (propylene) diluted in H_2 were used as precursors; Ar was made to flow in the region outside the reaction chamber to protect the furnace heating elements. All infiltration runs were carried out at atmospheric pressure and terminated once the back pressure, p_b, reached 172 kPa (≈ 1.7 atm). The bottom temperature of the disk, T_{bot}, was measured with a type K thermocouple, while the initial value of the top temperature, T_{top}, was obtained from a calibration chart relating the latter to furnace power. The rate of weight gain was much higher using C_3H_6 or C_3H_8, compared to CH_4, even though CH_4 runs were carried out at higher temperatures. This was explained by the higher stability of radicals produced in methane pyrolysis. Comparing two CVI runs with (a) 50 sccm CH_4 and 50 sccm H_2, T_{top} = 1,320 °C, T_{bot} = 1,050 °C and (b) 100 sccm C_3H_6 and 100 sccm H_2, T_{top} = 1,200 °C, T_{bot} = 850 °C, the rates of weight gain, infiltration times, final densities and precursor efficiencies were (a) 0.25 g h^{-1}, 38.5 h, 1.51 g cm^{-3}, 15.4% and (b) 1.1 g h^{-1}, 8 h, 1.69 g cm^{-3}, 11.4%. The rate of weight gain increased with precursor concentration. The carbon coating thickness in micropores (around the fibers within each bundle) and macropores (between bundles and between cloth layers) was measured by means of scanning electron microscopy (SEM); see Fig. 6.19. A SiC marker was introduced (e.g. at 2, 4, 6, and 8 h) by CVI during short interruptions in the flow of C_3H_6, allowing later visualization in the SEM. The micropore coating thickness did not depend on distance from the bottom (cooler) face of the preform, although the scatter was ±30% (Fig. 6.19). The macropore coating thickness, on the other hand, was lowest at the cooler face and increased by 200% with distance towards the hotter face. No SiC was seen inside the fiber bundles, signifying that intra-bundle infiltration

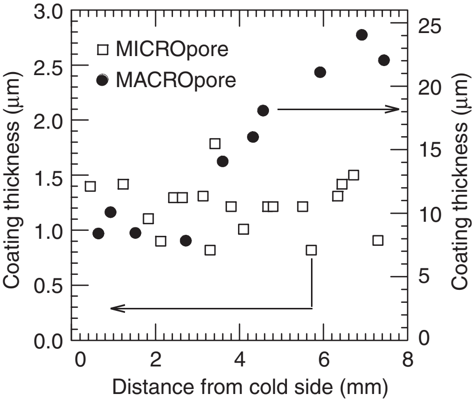

Figure 6.19 Axial variation of carbon coating thickness in micro-(□) and macro-(●) pores in 4.76 cm diameter × 1.0 cm thick C–C disk preform densified by forced-flow radiantly-heated thermal-gradient CVI (Vaidyaraman *et al.*, 1995a; reproduced with kind permission from the Materials Research Society). T_{top} = 1,200 °C, T_{bot} = 850 °C (at start of run); H_2/C_3H_6 = 1.

was completed in less than 2 h and the passages within the bundles were blocked early. The highest deposition rate in the macropores, obtained in the runs with 50% C_3H_6 and 50% C_3H_8, was stated to be similar to that obtained for forced-flow thermal-gradient CVI of SiC–SiC composites and more than an order of magnitude larger than the deposition rate of 0.1–0.25 $\mu m\,h^{-1}$ for isothermal CVI of C or SiC. The large variation in deposition rate for a given processing condition was attributed to variations in fiber spacing and uneven distribution of macropores, apparently as a result of nonuniform pressure during preform compaction. The precursor conversion efficiencies were 5–24% for C_3H_6, 3–14% for C_3H_8, and 10–15% for CH_4, much higher than the typical 0.8–1.5% reported for isothermal isobaric CVI. Stopping C_3H_6/H_2 runs when $p_b = 142$ kPa (1.41 atm), the shortest densification times for a 0.75 cm thick composite were 2.75 and 3.50 h, resulting in final bulk densities of 1.64 and 1.70 $g\,cm^{-3}$, total porosities of 9.8% and 7.2% and precursor efficiencies of 18.2% and 24.4%, respectively (Vaidyaraman *et al.*, 1996a,b). Using C_3H_8/H_2 and stopping the runs when $p_b = 136$ kPa (1.34 atm), the corresponding values were 7 h, 1.68 $g\,cm^{-3}$, 8.3%, and 9.0%. In the 2.75 h run, T_{bot} first increased rapidly from 820 to 950 °C within 0.5 h (attributed to reduced thermal conductivity of the gas mixture as C_3H_6 was added to H_2), stayed at 950 °C to 1.5 h, then decreased to ≈ 870 °C and increased again to 940 °C. The infiltration time decreased with increasing T_{bot} and with higher precursor concentration, and in the case of C_3H_6/H_2 runs, also with increasing total flow rate. The effect of flow rate was interpreted to indicate a CVD regime intermediate between surface reaction and gas-phase diffusion control. Density measurements of slices at different locations within the composites indicated generally lower densities at the cooler side, the effect being more pronounced (≈ 10%) for C_3H_6/H_2 runs. The measured exponential – up to 800% – increase in carbon coating thickness in macropores with distance from the cooler side of the composite was not reflected in a correspondingly large density variation (only 8–24% measured) because the majority of initial porosity was in micropores within the bundles. It was stated that p_b was a reliable indicator of the final bulk density since, for one set of experiments, these densities, in the range 1.58–1.71 $g\,cm^{-3}$, were fairly independent of the temperatures, pressures, and flow rates. However, premature crusting of the cooler preform side seen in one run, resulted in high p_b as well, even though the top 60% of the preform was not densified. SEM showed a two-layer structure of the CVD carbon matrix in some composites, but no information on whether the deposited carbon was isotropic or laminar was provided.

Advantages of forced-flow radiantly-heated thermal-gradient atmospheric-pressure CVI include:

- short densification time;
- one step densification – no intermediate grinding (Matlin *et al.*, 1995);
- high precursor conversion efficiency, 3–24% for C.

Disadvantages of forced-flow radiantly-heated thermal-gradient atmospheric-pressure CVI include:

- unsuitable for complex-shaped performs;
- one preform per CVI run – scale up to multiple parts considered challenging;
- spatial density gradients may exist within the perform;
- temperature within preform varies in a complex way during densification, depending on preform architecture (Vaidyaraman, 1996a);
- requires final machining, due to deformation of the preform in the exhaust areas and to the preform becoming attached to the graphite fixturing (Matlin *et al.*, 1995);
- very complex apparatus;

- requires expensive graphite fixturing; new fixturing must be made for preforms of different dimensions.

4 Summary

The CVI methods described in this review are grouped together with respective advantages and disadvantages in Table 6.1. Certain criteria for capability were chosen, for instance the published ability to densify more than one preform per run and the ability to densify relatively thick (>2.5 cm thick) preforms. Additional published CVI densification approaches, not covered here due to space limitations, were described recently (Golecki, 1997). Since different methods are at different stages of technological development, this information should be viewed as a snapshot, based on the demonstrated concepts in the literature cited herein. Certain methods may be more suitable than others for particular applications, materials (fibers and/or matrix), article shape, dimensional tolerances, intended use environment, production volume, and cost. The fields of C–C composite materials and densification of such composites continue to provide exciting and active opportunities for research and development, driven by the superior physical properties of C–Cs.

Disclaimer

To the best knowledge of the publisher, the author and the author's institution, the information contained in this chapter, which is based on published papers and patents, is accurate; however, the publisher, the author, and the author's institution assume no responsibility nor liability for errors or any consequences arising from the use of the information contained herein. Final determination of the suitability of any datum, information, idea, procedure, method, process, equipment, or product for use contemplated by any user, and the manner of that use, is the sole responsibility of the user. Materials and processes described herein could be potentially hazardous and due caution should always be exercised in the handling of materials and equipment. Expert advice should be obtained at all times when implementation is being considered. Mention of manufacturers' trademarks or trade names does not constitute endorsement by the author, the author's institution or the publisher.

Acknowledgment

Financial support by Honeywell International Inc. (formerly AlliedSignal, Inc.) of the work performed there is acknowledged.

References

Besmann, T. M., Sheldon, B. W., Lowden, R. A., and Stinton, D. P. (1991) "Vapor-phase fabrication and properties of continuous-filament ceramic composites," *Science*, **253**, 1104–1109.

Brown, G. H., Hoyler, C. N., and Bierwirth, R. A. (1948) *Theory and Application of Radio-Frequency Heating*, Van Nostrand, NY.

Buckley, J. D. and Edie, D. D. (eds) (1993) *Carbon–Carbon Materials and Composites*, Noyes Publications, Park Ridge, NJ.

Carroll, T. J., Connors, D. F., Jr., Suplinskas, R. J., and Thurston, G. S. (1995) "Method for densifying porous billets," US Patent No. 5,397,595.

Duan, Z. and Don, J. (1995) "CVI densification of Carbon–Carbon composites," *Proc. 22nd Biennial Conf. on Carbon*, American Carbon Society, San Diego, CA, July 1995, 80–81.

Golecki, I., Morris, R. C., and Narasimhan, D. (1994) "Method of rapidly densifying a porous structure," US Patent No. 5,348,774.

Golecki, I., Morris, R. C., Narasimhan, D., and Clements, N. (1995a) "Rapid densification of porous carbon–carbon composites by thermal-gradient chemical vapor infiltration," *Appl. Phys. Lett.*, **66**, 2334–2336.

Golecki, I., Morris, R. C., Narasimhan, D., and Clements, N. (1995b) "Rapid densification of Carbon–Carbon by thermal gradient chemical vapor infiltration," *Cer. Eng. & Sci. Proc.*, **16**, No. 4, 315–322.

Golecki, I., Morris, R. C., Narasimhan, D., and Clements, N. (1996) "Carbon–Carbon composites inductively heated and rapidly densified by thermal gradient chemical vapor infiltration: density distributions and densification mechanism," *Ceramic Transactions*, **79**, 135–142.

Golecki, I. (1997) "Rapid vapor-phase densification of refractory composites," invited review paper, *Materials Science and Engineering: Reports*, **R20**, No. 2, 37–124.

Golecki, I. and Narasimhan, D. (1998) "Method for measuring the deposition, densification or etching rate of an electrically conductive body," US Patent No. 5,747,096.

Golecki, I., Xue, L., Leung, R., Walker, T., Anderson, A. F., Dewar, D. M., Duncan, C. K., and van Horik, J. (1998) "Properties of high thermal conductivity Carbon–Carbon composites for thermal management applications," in I. Golecki, E. Kolawa, and B. Gollomp (eds), *Proc. 1998 High Temperature Electronic Materials, Devices and Sensors Conference*, San Diego, CA, February 1998, IEEE, Piscataway, NJ, 190–195.

Golecki, I., Xue, L., Dewar, D. M., Anderson, A. F., Duncan, C. K., van Horik, J., Fuentes, K., Rahman, F., and Walker, T. (2000) "Oxidation study of bare and protected Carbon–Carbon composites for accelerated lifetime testing," in S. Loud, V. Karbhari, D. O. Adams, and A. B. Strong (eds), *Proc. 45th International SAMPE Symposium and Exhibition*, Long Beach, CA, May 2000, Society for the Advancement of Material and Process Engineering, 671–682.

Golecki, I. and Narasimhan, D. (2001) "Novel real-time method for measuring the densification rate of Carbon–Carbon fiber-matrix composites and other articles," invited paper, in M. Singh and T. Jessen (eds), *Ceramic Engineering & Science Proc*. **22**, 3, 103–114.

Grove, A. S. (1967) *Physics and Technology of Semiconductor Devices*, John Wiley, New York, ch. 1.

Gulden, T. D., Kaae, J. L., Norton, K. P., and Thompson, L. D. (1990) "Forced-flow thermal-gradient chemical vapor infiltration (CVI) of ceramic matrix composites," *Electrochem. Soc. Proc.*, **90–12**, 546–552.

Hitchman, M. L. and Jensen, K. F. (eds) (1993) *Chemical Vapor Deposition – Principles and Applications*, Academic Press, London.

Houdayer, M., Spitz, J., and Tran-Van, D. (1981) "Increasing the density of a porous structure," French Patent No. 81 22163–26/11/81.

Houdayer, M., Spitz, J., and Tran-Van, D. (1984) "Process for the densification of a porous structure," US Patent No. 4,472,454.

Hüttinger, K. J. (2003) "Fundamentals of chemical vapor deposition in hot wall reactors," ch. 4, in P. Delhaès (ed), *World of Carbon*, Vol. 3, *Fibers and Composites*, Taylor and Francis, London.

Jackson, J. D. (1962) *Classical Electrodynamics*, John Wiley and Sons, Inc., New York.

Kotlensky, W. V. (1971) "A review of CVD carbon infiltration of porous substrates," *Proc. 16th National Symposium of the Society of Aerospace, Materials & Process Engineers (SAMPE)*, Anaheim, CA, April 1971, 257–265.14.

Kotlensky, W. V. (1973) "Deposition of pyrolytic carbon in porous solids" in P. L. Walker, Jr. and P. A. Thrower (eds), *Chemistry and Physics of Carbon*, Marcel Dekker Inc., New York, **9**, 173–262.

Lackey, W. J. (1989) "Review, status, and future of the chemical vapor infiltration process for fabrication of fiber-reinforced ceramic composites," *Ceram. Eng. Sci. Proc.*, **10**, No. 7–8, 577–584.

Lackey, W. J. and Caputo, A. J. (1986) "Process for the preparation of fiber-reinforced ceramic composites by chemical vapor deposition," US Patent No. 4,580,524.

Lackey, W. J., Vaidyaraman, S., Freeman, G. B., Agrawal P. K., and Langman, M. D. (1995) "Rapid fabrication of carbon–carbon composites," *Ceram. Eng. Sci. Proc.*, **16**, No. 4, 299–306.

Lieberman, M. L. and Noles, G. T. (1973) "Gas analysis during the chemical vapor deposition of carbon," *Proc. 4th International Conference on Chemical Vapor Deposition*, Electrochemical Society, Boston, MA, Oct. 1973, 19–29.

Lieberman, M. L., Curlee, R. M., Braaten F. H., and Noles, G. T. (1975) "CVD/PAN felt carbon/carbon composites," *J. Composite Materials*, **9**, 337–346.

Loll, P., Delhaès, P., Pacault, A., and Pierre, A. (1977) "Diagramme d'existence et propriétés de composites carbone-carbone," *Carbon*, **15**, 383–390.

Lovell, D. R. (ed.) (1995) *Carbon and High Performance Fibres Directory and Databook*, 6th edn., Chapman & Hall, London.

Marinkovic, S. and Dimitrijevic, S. (1987) "Process of infiltration of porous carbon bodies by CVD carbon and properties of resulting composites," *Journal de Chimie Physique*, **84**, 1421–1430.

Matlin, W. M., Stinton, D. P., Besmann, T. M., and Liaw, P. K. (1995) "Optimization of bundle infiltration in the forced chemical vapor infiltration (FCVI) process," *Mat. Res. Soc. Symp. Proc.*, **365**, 309–315.

Narcy, B., Guillet, F., Ravel, F., and David, P. (1995a) "Characterization of carbon–carbon composites elaborated by a rapid densification process," *Ceramic Transactions*, **58**, 237–242.

Narcy, B., David, P., and Ravel, F. (1995b) "Elaboration of C/C and C/BN composites by a rapid densification process," *Silicates Industriels*, **7–8**, 199–202.

Naslain, R., Langlais, F., and Fédou, R. (1989) "The CVI-processing of ceramic matrix composites," *J. de Physique*, **50**, *Colloque C5, Suppl. to No. 5*, 191–207.

Nieberlein, V. A. (1968) "Deposition of silicon carbide from liquid compounds," *SAMPE Journal*, **4**, No. 6, 72–74.

Nieberlein, V. A. (1971) "Method for depositing carbide compound," US Patent No. 3,554,782.

Pierson, H. O. (1992) *Handbook of Chemical Vapor Deposition (CVD)*, Noyes Publications, Park Ridge, NJ.

Pierson, H. O. and Lieberman, M. L. (1975) "The chemical vapor deposition of carbon on carbon fibers," *Carbon*, **13**, 159–166.

Savage, G. (1993) *Carbon–Carbon Composites*, Chapman & Hall, Cambridge, UK.

Scaringella, D. T., Connors, D. E., Jr. and Thurston, G. S. (1996) "Method for densifying and refurbishing brakes," US Patent No. 5,547,717.

Sheehan, J., Buesking, K. W., and Sullivan, B. J. (1994) "Carbon–carbon composites," *Ann. Rev. Matls. Sci.*, **24**, 19–44.

Stinton, D. P., Besmann, T. M., Matlin, W. M., Starr, T. L., and Curtain, W. A. (1995) "Forced chemical vapor infiltration of tubular geometries: modeling, design and scale-up," *Mat. Res. Soc. Symp. Proc.*, **365**, 317–324.

Stoller, H. M. and Frye, E. R. (1972) "Processing of Carbon–Carbon composites – an overview," *SAMPE Quarterly*, **3**, No. 3, 10–22.

Stoller, H. M., Butler, B. L., Theis, J. D., and Lieberman, M. L. (1974) "Carbon fiber reinforced-carbon matrix composites," in J. Weeton and E. Scala (eds), *Composites: State of the Art*, Met. Soc. of AIME, *Proc. 1971 Fall Meeting of the Metallurgical Society of AIME*, Detroit, MI, 69–136.

Tesner, P. A. (1984) "Kinetics of pyrolytic carbon formation," ch. 2 in P. A. Thrower (ed.), *Chemistry and Physics of Carbon*, Marcel Dekker, Inc., New York, **19**, 65–161.

Textron Specialty Materials (1994) "Brake disc technology," news release, *Aerospace Products*, Fall 1994, 10.

Thiele, E. W. (1939) "Relation between catalytic activity and size of particle," *Industrial and Engineering Chemistry*, **31**, 916–921.

Thomas, C. R. (ed.) (1993) *Essentials of Carbon–Carbon Composites*, Royal Society of Chemistry, Cambridge, UK.

Thurston, G. S., Suplinskas, R. J., Carroll, T. J., Connors, D. F., Jr., Scaringella, D. T., and Krutenat, R. C. (1995) "Apparatus for densification of porous billets," US Patent No. 5,389,152.

Vaidyaraman, S., Lackey, W. J., Agrawal, P. K., Freeman, G. B., and Langman, M. D. (1995a) "Rapid processing of Carbon–Carbon composites by forced flow-thermal gradient chemical vapor infiltration (CVI)," *Mat. Res. Soc. Symp. Proc.*, **365**, 325–330.

Vaidyaraman, S., Lackey, W. J., Freeman, G. B., Agrawal, P. K., and Langman, M. D. (1995b) "Fabrication of Carbon–Carbon composites by forced flow-thermal gradient chemical vapor infiltration," *J. Mater. Res.* **10**, 1469–1477.

Vaidyaraman, S., Lackey, W. J., Agrawal, P. K., and Miller, M. A. (1996a) "Carbon/carbon processing by forced flow-thermal gradient chemical vapor infiltration using propylene," *Carbon*, **34**, 347–362.

Vaidyaraman, S., Lackey, W. J., and Agrawal, P. K. (1996b) "Carbon/carbon processing by forced flow-thermal gradient chemical vapor infiltration (FCVI) using propane," *Carbon*, **34**, 609–617.

7

LIQUID IMPREGNATION TECHNIQUES FOR CARBON–CARBON COMPOSITES

R. Menéndez, E. Casal, and M. Granda

1 Introduction

Carbon fiber reinforced carbon composites (C–C composites) are unique in providing materials with the highest possible specific thermal-mechanical properties. They have an additional value in that at high temperatures their excellent properties are not only retained but also improved as a result of a better structural order. However, the main problem with C–C composites, apart from their reactivity to oxygen at high temperatures, is their high cost due to the complexity and length of the fabrication processes. Consequently, C–C composites are currently used only in high-technology applications where no other materials are available. In recent years the search for ways to improve properties, reduce costs, and increase the efficiency of the processes involved in the preparation of C–C composites has been intensified. Unfortunately, easily available information is very limited because of confidentiality agreements, most of it being in patent form (Plotzker *et al.*, 1988; Hocquellet and Chenier, 1993).

The type and architecture of the fibers and the microstructure of the supporting matrix determine the physical properties of C–C composites. It is, therefore, important to understand the mechanisms that control the formation of the microstructure and its interaction with the fibers in order to be able to achieve the desired composite properties at the lowest possible cost and make full use of the electrical, thermal, and mechanical properties of the fibers (Meyer, 1994).

Two methods are at present used for the preparation of C–C composites: (i) liquid impregnation; and (ii) carbon vapor infiltration (CVI). A combination of the two methods is also used. Both have been described in detail in the literature (Savage, 1993a). Liquid impregnation, the topic covered in this chapter, is a two-stage method. Basically, in the first stage the fibers are impregnated with an organic precursor, giving rise to what is called a prepreg. Afterwards, the precursor is transformed into a carbonaceous matrix by thermal treatment (650–1,000 °C) in an inert atmosphere via a carbonization process. Depending on the application of the material, graphitization ($>$2,500 °C) may also be required. These stages have to be repeated until the desired density is obtained (Fig. 7.1). The other method, CVI, implies the cracking of a gas and the deposition of carbon onto the fiber substrate (Chapter 7 of this book). In general, liquid impregnation is considerably quicker and cheaper than CVI processing, and the equipment required, in an ambient pressure fabrication route, is not limited

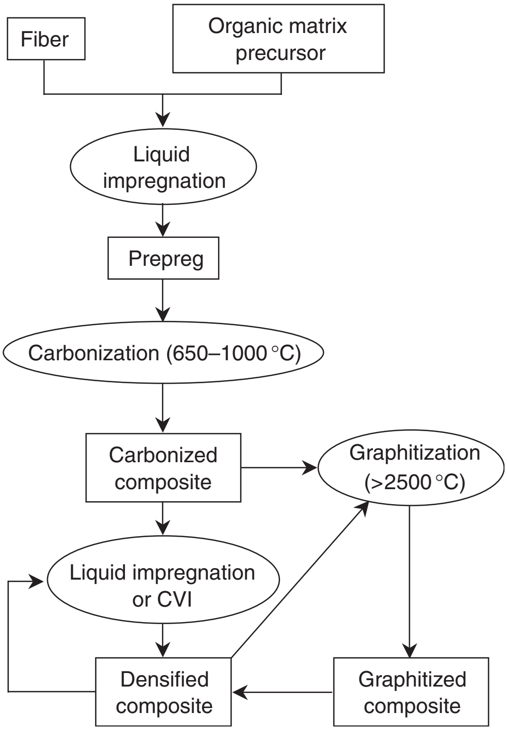

Figure 7.1 Flow diagram of C–C composite preparation by liquid impregnation.

by size or by the need for a large initial capital investment. The main advantage of the liquid impregnation procedure, however, concerns the great variety of matrix microstructures which can be produced, with the subsequent impact on composite properties.

The aim of this chapter is to offer a general view of the fundamentals of the liquid impregnation procedure and to point out the technical problems which may arise through eyes of the authors concerned. Special emphasis is given to the role of matrix precursors and the selection of the correct processing conditions for producing the desired microstructural features and composites with optimum properties. At the same time care is taken not to underestimate the important role of fiber in the properties of the composite. Ways of enhancing these properties through the carbon matrix precursor by means of preliminary treatment or by acting on the prepreg are also considered.

2 Impregnation technology

The technologies available for the impregnation of carbon fibers using a carbonaceous matrix precursor are similar to those used for fiber-reinforced plastics. Depending on the matrix precursor and the type of reinforcement (discontinuous, linear, planar, or n-D) many alternatives are available. Essentially, the procedures include: (i) passing continuous fibers through a solution of the matrix precursor; (ii) infiltration of a liquefied matrix precursor in a fibrous skeleton assisted by vacuum or pressure; and (iii) hot pressing of sandwiched fiber/matrix precursor mixtures.

2.1 Wet-winding technique

This is the most common technique used for preparing unidirectional C–C composites at laboratory scale (Fig. 7.2a). Basically, a continuous fiber bundle is made to pass through a bath which contains a liquefied matrix precursor. The impregnated fibers are then wound onto a mandrel under controlled tension. The winding processes differ from each other in the impregnation conditions chosen and the reinforcement scheme and type of winding path used (Borokh *et al*., 1995). Depending on the impregnation conditions, winding can be wet

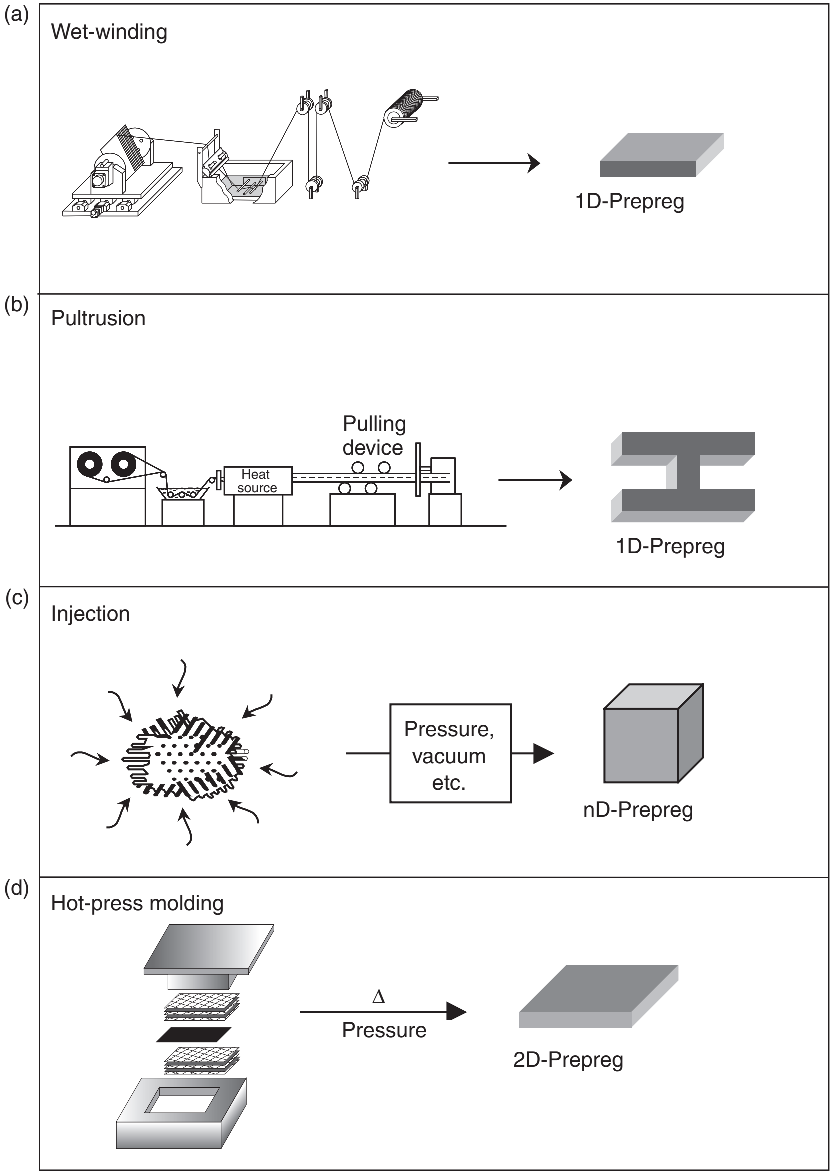

Figure 7.2 Impregnation techniques.

(impregnation is carried out during winding) or dry (winding is carried out on a preimpregnated, dried tape). Winding can also be performed with non-impregnated fibers followed by impregnation.

When using wet winding techniques, the impregnation conditions vary depending on the matrix precursor (Hirano *et al.*, 1993), i.e. a mixture of polymers and a plasticizer, melt pitch, liquid resins, pitch, or resin dissolved in an organic solvent, or fine particles suspended in the form of an emulsion (Hocquellet and Chenier, 1993). Two fundamental factors which must be controlled in this step and borne in mind when selecting the optimum conditions are: the alignment of the fibers and the homogeneous distribution of the matrix precursor. Correct fiber alignment is very important because small variations in the orientation of the fibers can mean additional stresses, which may lead to premature failure of the material. As an example, impregnation is relatively easy with solutions at low concentrations of the organic precursor. However, complete removal of the solvent is hard to achieve and it may produce fiber misalignment, as well as the generation of porosity during solvent removal.

The next step, after the impregnation process, involves curing and/or hot-pressing (depending on the matrix precursor), and then carbonization/graphitization. After this, other techniques (CVI, injection) are required in order to reduce the final porosity and obtain a high density material.

2.2 Pultrusion

This technique is derived from wet-winding. In this case, after being impregnated in a bath, the fibers are pulled through a heated die specifically shaped to produce the desired cross-section (Fig. 7.2b). Partial or complete curing occurs during the passage through the die.

2.3 Hand lay-up

Fibers are placed by hand into a mould covered by a released substance and then impregnated with a liquid precursor by means of painting or spraying and rolling. Rolling compacts the material and ensures the effective impregnation of the fiber by the matrix precursor, homogeneous distribution and the removal of air. The fibers may be in the form of random mats or woven fabrics. Layers of impregnated fibers are stacked up (lay-up) until the desired thickness is achieved. Carbonization is then carried out to obtain a stable porous structure. Again additional techniques are needed to obtain the desired final density.

2.4 Injection technique

This method (Fig. 7.2c) is generally used to impregnate preforms of carbon fibers produced by dry winding or braiding and also as a way to increase the density of the composite prepared by other techniques. The preform is dipped into the liquefied precursor or alternatively the precursor is forced into the pores of the preform by means of surface tension, gravity, atmospheric pressure or external forces such as gas pressure, centrifugal force, mechanical vibration, etc. (Borokh *et al.*, 1995). In some cases this is achieved with the help of a vacuum. Pore distribution in the preform and the rheological properties of the matrix precursor are the main factors that control this process.

2.5 Hot-press molding

This technique is frequently used at laboratory scale to prepare bidirectional C–C composites (Arianoutsos *et al.*, 1990). Woven mats of carbon fibers are stacked in a mold and sandwiched by the matrix precursor powder (Figure 7.2d). The mold, matrix precursor and fibers, are heated together until the matrix precursor is thoroughly melted. At this point mechanical pressure is applied in order to place the melted precursor inside the mats and so ensure an effective impregnation. During pressurization, trapped air and excess precursor are forced out of the mold. After cooling, carbonization is required. Infiltration/carbonization cycles are repeated several times to achieve the desired density.

Unidirectional C–C composites are prepared in a similar way, using a powder coating process (Klett and Edie, 1995). Fiber bundles are separated by a vacuum spreader and then the individual fibers are coated with fine polymer particles in a fluidization chamber. The coated tow thus formed (tow-preg) is heated until the particles are fused to the individual filaments. Next the tow-pregs are cut, stacked and hot-pressed to form the final composite. This procedure may be specially desirable when using pitches with a high softening point and low solubility as matrix precursors.

Hot-press molding is also used as part of the process of preparation of unidirectional C–C composites by wet-winding. Laminated prepregs are stacked and then hot-pressed at specific temperatures, depending on the characteristics (chemical composition and rheological properties) of the precursor (Figueiras *et al*., 1995; Casal *et al*., 2001).

3 Densification efficiency

The preparation of C–C composites with the right density currently requires several impregnation/carbonization cycles, as mentioned above. This is because in the initial stages of the carbonization process of the organic precursor there is a major weight loss of volatiles which continues, to a lesser extent, throughout the process as the temperature increases, giving a porous material. The pores are produced, either in the initial stages of the preparation of the composite (impregnation process and molding), or during subsequent carbonization. Pores of the first type are usually open (Fig. 7.3a), whereas those developed on carbonization may be either open or closed (Fig. 7.3a). Carbonization pores may be developed either while the matrix precursor is still plastic or as a result of stresses (cracks) due to structural rearrangements or thermo-mechanical effects (Fig. 7.3b). Several studies have been carried out in relation with the characterization of porosity in C–C composites (Jortner, 1986; Granda *et al*., 1998). All of these structural imperfections have an adverse effect on the bulk properties.

A knowledge of the parameters which control the efficiency and effectiveness of densification is essential for the optimization of the process. Experience shows that the first step of impregnation is not enough to ensure that all of the empty pores in a C–C composite are filled by the matrix precursor (Fig. 7.3c and d). An impregnation efficiency parameter, Y_i, can be defined as the relationship between the volume of impregnant introduced into the pores of the composite and the volume of the open porosity of the composite (eq. (1)). This parameter can be calculated from the increase in weight gain of the composite during the impregnation, ΔW_i, and the volume fraction of open porosity of the composite before impregnation, θ:

$$Y_i = \frac{\textit{Volume of impregnant introducted}}{\textit{Volume of initial empty pores}} = \frac{\Delta\, W_i}{\rho_p} \cdot \frac{\rho\,(0)}{\theta} \tag{1}$$

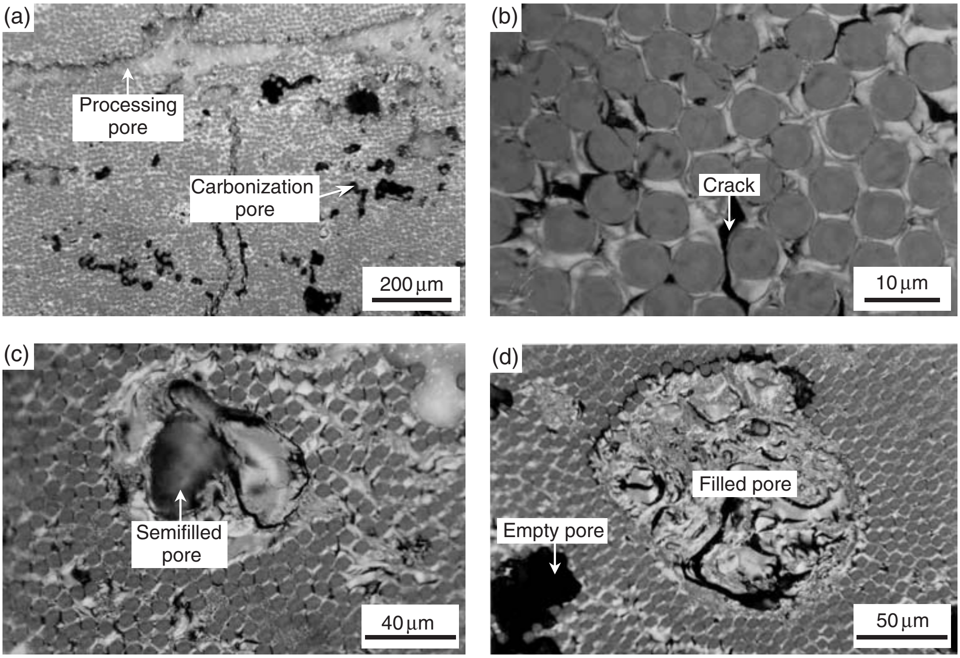

Figure 7.3 Polarized-light micrographs of cross sections of unidirectional C–C composites showing different types of pores: (a)–(b) undensified; and (c)–(d) densified composites. (See Color Plate IV.)

where ρ_p is the density of the impregnant at room temperature, and $\rho(0)$ the bulk density of the empty C–C composite. This expression can be generalized for the *n*-th step of impregnation as follows:

$$Y_i(n) = \frac{\Delta W_i(n)}{\theta(n-1)} \cdot \frac{\rho(n-1)}{\rho_p} \tag{2}$$

Several factors, related not only to the experimental conditions used but also to the characteristics of the network of pores developed in the composite (Fig. 7.3a) and the characteristics of the impregnant, affect the values of this parameter (Oh and Park, 1994; Granda *et al*., 1998).

The density of the carbon matrix of the final composite depends on the experimental conditions used in the carbonization step and may differ somewhat from the density obtained when the matrix precursor is carbonized alone under the same conditions. This is because in the composite the thermally induced stresses tend to promote additional graphitization and densification of both fiber and matrix (Rellick, 1990).

Another aspect that should be mentioned is the relationship between the weight gain of the composite in the impregnation and the absolute increase in weight due to the *n*-th cycle of densification. One might expect the ratio of these magnitudes to be the carbon yield of the matrix precursor under the processing conditions. However, this is not completely true, because when carbonization takes place after impregnation, the phenomenon of matrix bloating may occur as a consequence of the release of volatiles. As a result, matrix yields will be lower than anticipated knowing carbon yields from the impregnant, when carbonized alone. The physico-chemical properties of the precursor, the number of pores, the structure of the pore networks in the composite (size, shape, and orientation), and the experimental conditions used are the main controlling factors.

Studies of the densification efficiency of C–C composites with pitches (Oh and Park, 1994; Granda *et al*., 1998) have led to the conclusion that impregnation efficiency increases, as the process is repeated due to a decrease in porosity, while retention efficiency follows an inverse trend due to the changes in the shape of the pores, as densification proceeds. Overall densification efficiency depends on impregnation efficiency and the effective carbon yield of the impregnating pitch. Pitch fluidity is the main factor controlling impregnation efficiency. Additionally, the tortuosity of the pores also plays an important role during the impregnation process. The use of pressure during carbonization reduces the release of volatiles and pitch bloating, leading to an increase in the effective carbon yield (Granda *et al*., 1998). It also reduces pore closure, thereby improving densification efficiency. It has also been shown that closed porosity may be transformed into open porosity via graphitization (Savage, 1993b).

4 Matrix precursors

The matrix of a C–C composite acts as a binder by maintaining the alignment and position of the fibers, and protects them from damage. It also distributes stresses, transferring the external load to single reinforcing filaments. The structural characteristics of the matrix and their interaction with the fibers contribute significantly to the properties of the composite. These characteristics depend on the chemical composition and physical properties of the precursor, as well as on the processing conditions. As the preparation of C–C composites involves heat treatment in an inert atmosphere to transform the matrix precursor into carbon form, the chemical and rheological behavior of the matrix precursor on pyrolysis is of considerable importance for selecting the optimum processing conditions. Generally speaking, a good matrix precursor should have a high carbon yield while at the same time retaining its fluidity and ability to wet the fibers. Moreover, low volumetric contraction is necessary in order to avoid fiber damage and matrix shrinkage cracks. It is not easy to find a product which fulfills all of the requirements at the same time. As an example, a high carbon yield is usually associated with high organic precursor viscosity, which may impede infiltration and wetting. On the other hand, a high carbon yield may be accompanied by an adequate viscosity but also by considerable matrix bloating on carbonization. Two main types of matrix precursors are currently used in the preparation of C–C composites by liquid impregnation: one is based on resins and polymers and the other is based on pitches.

4.1 Resin precursors

In this group, phenolic and epoxy resins are the most commonly used and both are thermoset and need curing prior to carbonization (Fig. 7.4a). Apart from the above mentioned matrix requirements, it is necessary that the resin cures rapidly at low temperature (without the evolution of volatiles). The carbon yield in commercially available resins usually ranges from 50 to 70 wt%, depending on the type of resin and the processing conditions (Murdie *et al*., 1992). These yields cannot be increased by the application of pressure during carbonization. New resin precursors (Fig. 7.4b) have been developed with carbon yields of up to 85 wt% (800 °C) (Savage, 1993c), but the price of these products is extremely high and in some

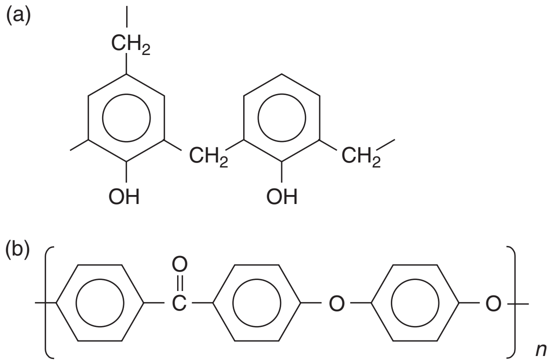

Figure 7.4 Chemical structure of (a) thermosetting phenolic resin precursor; and (b) PEEK thermoplastic resin precursor.

cases the preparation procedures for bulk resin production are difficult to scale up. Furthermore, the resins tend to form closed porosity on carbonization, preventing further densification.

The processing of resin composites includes initial partial curing for polymerization to take place and thereby increase the carbon yield. This is followed by hot-pressing (150–300 °C) or curing in an autoclave to produce a rigid solid via three-dimensional cross-linking. Then pyrolysis and a series of infiltration/carbonization cycles are carried out. The processing conditions used in the preparation of the composite depend on the time/viscosity properties of the resin. In general, the carbonization of composites to temperatures of about 800–1,000 °C is carried out slowly in order to prevent the rapid evolution of gases (H_2O, CH_4, CO, H_2). The carbonization step may take many hours or even days to be completed. During carbonization, the resin is converted into a glassy, isotropic carbon (shrinkage stresses in the vicinity of the fibers may cause graphitization at temperatures $>2{,}500\,^\circ$C). The shrinkage of the resin during curing and carbonization produces slit-shaped pores which need to be filled by a liquid matrix precursor for subsequent carbonization if the density and mechanical properties of the composite are to be improved. The fine micropore network developed during the carbonization of the resin cannot be easily reinfiltrated even when the pores are open (Rand, 1993).

The density of resin-based carbons is relatively low. So, when using resin, the number of densification cycles is higher than with other precursors. As an example, six cycles were required to achieve a density of $1.65\,\mathrm{g\,cm^{-3}}$ in order to process multidirectional cylinders with phenolic resin (Mullen and Roy, 1972). Unfortunately, none of the resins available at the moment, even the more recent ones with high carbon yields, can fulfill all the requirements of an optimum carbon matrix precursor.

4.2 Pitch precursors

4.2.1 Pitch composition

Pitches offer good possibilities as carbon matrix precursors, mainly because of the wide range of pitch products with different characteristics that are available, their relatively low price, easy manipulation, and the possibility of achieving high carbon yields. Pitches come primarily from coal and petroleum. Both petroleum-derived and coal-derived pitches (so called coal-tar pitches) are residues from the distillation or heat treatment of petroleum fractions and coal-tar, respectively, and contain a large range of aromatic molecular types and sizes (Zander, 1997). These pitches differ from one another in their chemical composition (aromaticity, aromatic condensation degree, molecular size, functionality, etc.), physical properties and consequently, in their pyrolysis behavior (Pérez *et al.*, 2000). This is because of differences in their origin. Figure 7.5 shows two average molecular structures for coal-tar and petroleum pitch proposed by Kershaw and Black (1993). Coal-tar pitches are more aromatic, with a higher degree of ring condensation than petroleum pitches and they contain carbonaceous particles (<1 μm) called primary Quinoline Insolubles (QI). These particles are generated during the coke oven operation and are entrained by gases to form part of the tar. Consequently they remain in the pitch which is obtained by tar distillation. Two types of commercial coal-tar pitches are produced mainly for the aluminum and steel industry: binder pitches and impregnating pitches. These pitches differ in their specifications (softening point, carbon yield, QI content, toluene insoluble content, etc.) depending mainly on the preparation process used (vacuum distillation, thermal treatment, etc.). However, the composition of the tar will also have some influence.

In general, pitches are extremely complex in composition. They are composed of several hundreds and even thousands of aromatic compounds which are present in different concentrations and differ in molecular size and topology. These compounds cover a very wide

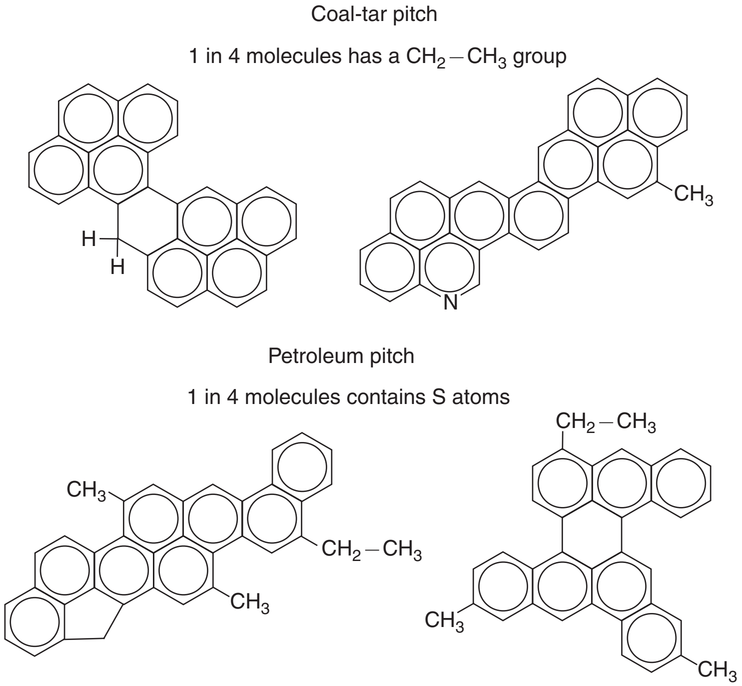

Figure 7.5 Average molecular structures for coal-tar and petroleum pitch (Kershaw and Black, 1993).

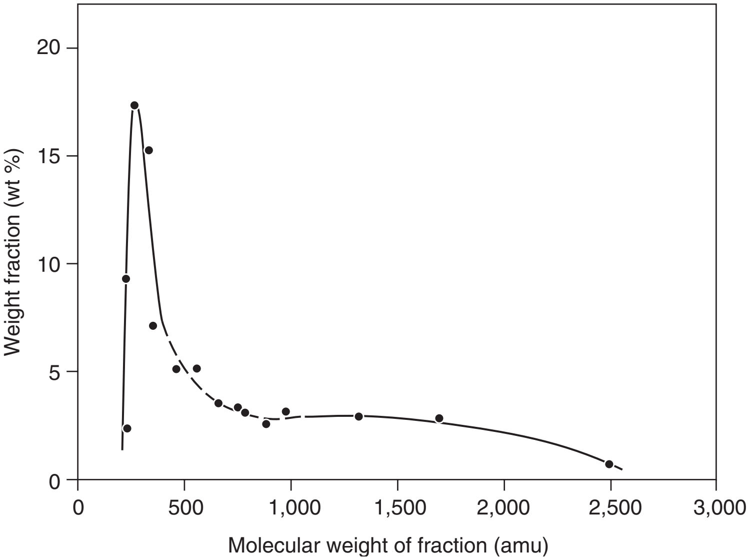

Figure 7.6 Molecular weight distribution of the pyridine-soluble part of coal-tar pitch (Boenigk *et al.*, 1990).

range of molecular weight from ~200 to >3,000 amu (Zander, 1997). As an example, Fig. 7.6 shows the molecular weight distribution determined by preparative size exclusion chromatography (SEC) of the pyridine-soluble fraction (95 vol%) of a coal-tar pitch (Boenigk *et al.*, 1990). From results obtained by preparative SEC and other techniques, these authors conclude that a typical coal-tar pitch consists of ~40 wt% of compounds with a molecular mass of ≤330 amu, ~50 wt% of compounds with a molecular mass ~330–1,500 amu, while 10 wt% of the remaining pitch consists of high-molecular weight material (between ~1,500 and > 3,500 amu).

Coal-tar pitches are mainly composed of polycyclic aromatic hydrocarbons (PAH) and to a lesser extent of polycyclic aromatic compounds containing alkylsubstituents and/or heteroatoms (O, S, and N). These compounds can be compiled into categories by fractionation by means of extrography (Granda *et al.*, 1990). This technique is able to distinguish between pitches differing in origin (coal-tar or petroleum), their uses (binding or impregnating) and also the preparation process (thermal treatment, vacuum distillation, etc.). Thus impregnating and binder pitches mainly differ in the distribution of PAH and the amount of basic polycyclic aromatic compounds (Bermejo *et al.*, 1994). A typical impregnating pitch has a higher content in both PAH of lower molecular weight and basic nitrogen compounds.

There is also what is considered to be a third generation of pitches. Some of these are commercially available (Mitsubishi Gas Chemical and Mitsubishi Oil) and others are still under development. This third group includes the mesophase pitches (from organic precursors and from the pyrolysis of commercial pitches) and isotropic pitches of high carbon yield (from the direct treatment of tar, commercial pitches, and other tar distillation fractions such as anthracene oil). These will be discussed in Section 5 of this chapter.

4.2.2 From pitch to carbon matrix

The processing of pitch-based composites involves a carbonization step (650–1,000 °C) which transforms the pitch into a graphitizable carbon, through a liquid crystal stage called mesophase. The conditions used are strongly dependent on the chemical composition and the rheological behavior of the pitch.

All pitches, petroleum- and coal-based have in common the fact that their constituents are polycyclic aromatic compounds. But, their differences in molecular structure lead to different behaviors during carbonization (Pérez *et al.*, 2000), thereby influencing the properties of the resultant composite.

In the initial stages of carbonization, the lightest compounds are released and the remaining polycyclic aromatic compounds polymerize and condense. The generation of gases, as a consequence of polymerization reactions, and the dimensional shrinkage that accompanies pitch carbonization, leads to the development of open and closed porosity in the composites. The improvement of the density and mechanical properties of the composites requires the elimination or reduction of this porosity by subsequent liquid impregnation (or CVI) followed by carbonization (Section 3 of this chapter).

A knowledge of the temperatures at which all the physico-chemical changes involved in pitch carbonization occur is of great importance for the selection of an adequate precursor and optimum conditions for the preparation of a pitch-based C–C composite. The main factors that must be borne in mind are the temperature of volatiles removal on pitch pyrolysis (Bermejo *et al.*, 1994), viscosity/temperature history (Rand *et al.*, 1989), and temperature interval between mesophase development and solidification, all of which can be monitored by thermogravimetric analysis, rheometry, and hot-stage microscopy, respectively. The information obtained is useful even if the experimental conditions used in the preparation of a C–C composite are rather different. For example, a reduction in the porosity (as determined by optical microscopy) of undensified unidirectional C–C composites, prepared by a wet-winding procedure, from 12 to 4 vol%, was achieved by the adjustment of the operational parameters (heating rate, molding temperature, duration of molding) to the characteristics of the binder pitch that was used as matrix precursor (Casal *et al.*, 1998).

Carbon yields of commercial coal-tar pitches are about 50 wt% under atmospheric conditions, but these can be substantially increased to 80 wt% by reducing the carbonization heating rate or by using pressure. Carbonization under high pressure (100 MPa) results in yields of 90 wt%. The use of a pressure of up to 207 MPa reduces the temperature associated with thermal degradation and improves the carbon yield by reducing the loss of volatiles. McAllister and Lachman (1983) have shown that high pressure impregnation/carbonization of multidirectional fiber preforms with pitch increases the yield and density of the final composite. After six cycles of pitch impregnation/carbonization under pressure, a composite of about 1.9 $\mathrm{g\,cm^{-3}}$ was obtained.

4.2.3 The optical texture of the matrix

The morphology, size, and orientation of the microcrystalline structures which constitute the optical texture of the carbon matrix can differ greatly depending on the composition of the pitch. As shown in Fig. 7.7, they can vary from a very small size ($<10\,\mu$m), mosaic-like structures, to large size ($>60\,\mu$m) domains (Marsh and Latham, 1986). Pitches which contain compounds with a higher capacity of hydrogen transfer, i.e. hydroaromatics and naphthenics, tend to produce better ordered structures of a larger size. The same tendency

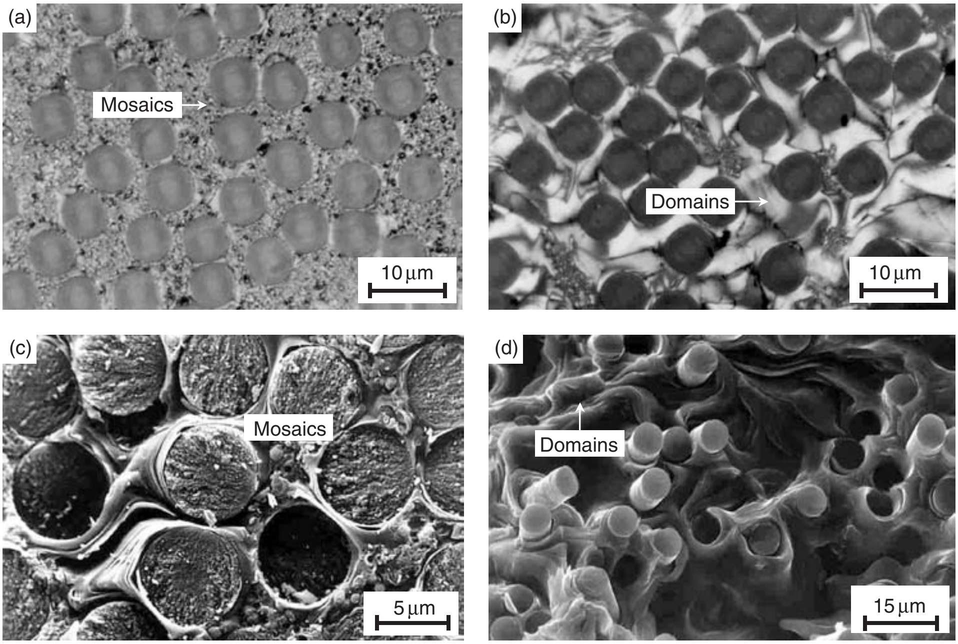

Figure 7.7 Pitch-based unidirectional C–C composites exhibiting different (a)–(b) optical textures; and (c)–(d) SEM fracture surfaces. (See Color Plate V.)

was observed for those containing basic-nitrogen compounds. However, the presence of oxygen functional groups (phenolic, carbonyl, etc.) has a negative effect on the optical texture (Menéndez *et al*., 1997), generating small size textures and even destroying pitch graphitizability when occurring in high concentrations. Primary QI, present in coal-tar pitches, also yield optical textures of a small size (Fig. 7.7). These differences are related to the thermal reactivity of the compounds and the viscosity of the pyrolysis system which addresses the development of mesophase and finally the carbon microstructure. Moreover, for a given pitch the optical texture of the resultant carbon can be modified by variations in the carbonization conditions (heating rate, use of pressure).

When dealing with C–C composites, the presence and characteristics of the fiber through fiber–matrix interfacial effects also yield preferential orientations of the matrix with respect to the fiber (Appleyard *et al*., 1995) as shown in Fig. 7.7.

The wide range of optical textures which can be generated is of special relevance to the properties of the C–C composites. Large-size optical textures are currently associated in coke with high electrical conductivity, while small sizes are associated with improved mechanical strength. However, recent studies have shown that domain-like structures (from petroleum pitches) can also give high strength carbon materials (Pérez *et al*., 2000). This suggests that other factors related to packing or interlaminar bonding/interactions also play a role. But it is not only the microstructure of the matrix, but also the strength of the fiber–matrix bonding that is critical in the behavior of the C–C composite under mechanical loading, and this can be influenced by the optical texture of the matrix. Matrices with a dominant mosaic texture exhibited stronger bonding with AS4k fibers than those with domains. Whereas the former resulted in a pure brittle failure mode (Fig. 7.7c), the latter was pseudoplastic (Fig. 7.7d). It has also been observed that matrices with domain textures, which mainly develop in pitch containing aliphatic hydrogen, have a higher propensity to form intramatrix and interface cracks (Figueiras *et al*., 1995).

The presence of primary QI particles in coal-tar pitches restricts the development of mesophase during pyrolysis, producing matrices with a smaller size of optical texture, a lower amount of cracks and stronger fiber–matrix bonding (Figueiras *et al*., 1998). Figure 7.8 illustrates how the QI affects the mechanical properties and failure mechanism of the material. For an undensified composite prepared from a pitch with 11 wt% of QI (Fig. 7.8a) the flexural strength is higher than for a composite prepared from a free QI pitch (Fig. 7.8b). The increase in the strength of the composites containing QI is accompanied by a change in the mode of failure. Composite from QI free pitch shows a classical multiple fracture mode

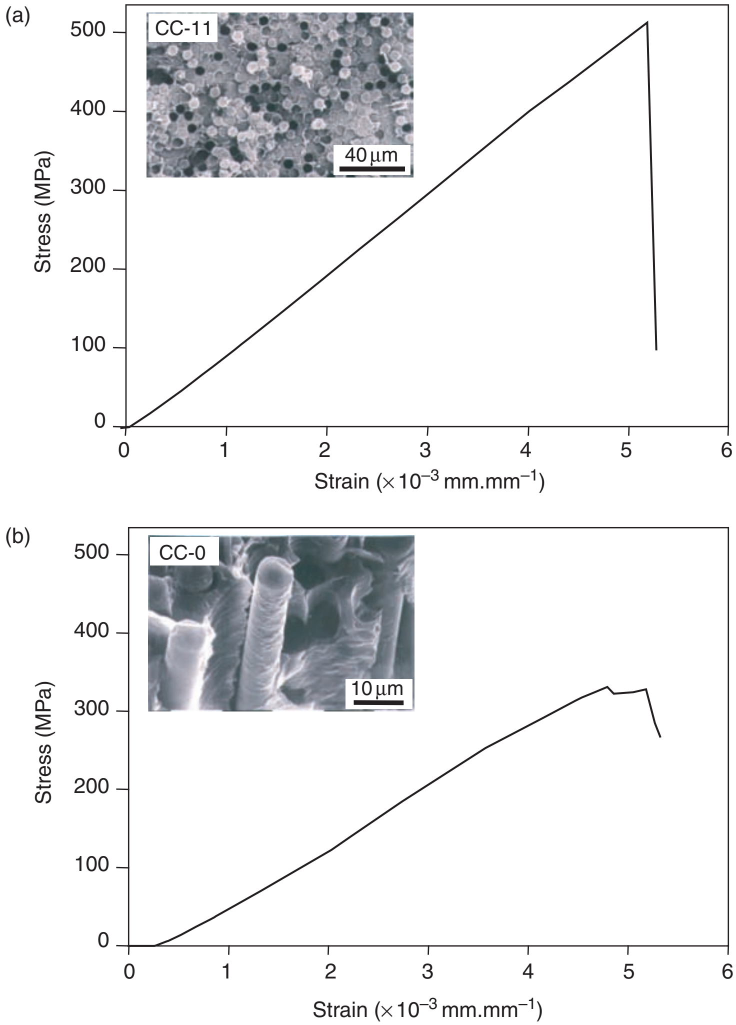

Figure 7.8 Stress–strain curves and fracture surfaces for (a) composite from a pitch with 11 wt% of QI and (b) composite from a QI free pitch.

of failure (pseudoplastic behavior) leading to the relative movement of the two phases as the load is transferred to the fibers. However, composite from pitch with 11 wt % of QI (Fig. 7.8a) failed in a catastrophic way (brittle behavior). In this case, the stronger fiber– matrix bonding increases the transfer of the load to the fiber, which in turn increases the overall strength of the composite, causing the composite to fail in a catastrophic-like tensile fracture (Fig. 7.8a).

As an improvement in the strength of the material is accompanied by an increase in its brittleness, possible ways to overcome this problem could be the use of matrix precursors prepared from two individual components in order to obtain a blend which gives on pyrolysis a carbon with a combined optical texture, yielding both strength and capability of fracture propagation. The mechanical properties of the composite could also be improved by using the appropriate fiber, depending on the type of carbon matrix.

5 New developments in C–C composites

Alternatives to the use of pressure and extended impregnation/carbonization cycles for preparing high density composites are the new developments in high carbon yield pitch-based matrix precursors or the application of oxidative stabilization treatments at the prepreg stage.

Some pitches can be pre-treated to induce the polymerization of the components of the pitch in order to obtain high density C–C composites (in the range of 1.6–1.8 g cm^{-3}), without the need for applying further impregnation/carbonization cycles or reducing the number of those currently applied. Densities may be even higher than the above mentioned values when using blends of thermally treated pitch powder and phenolic resin as matrix precursor of unidirectional C–C composites (Tsushima *et al.*, 1993). In this way, the use of pressure, which substantially increases the price of the composite, can be avoided. However, an increase in carbon yield is the result of an increased content in high molecular weight compounds, which may lead to greater viscosity. The new pitches can be expected to have a high beta resin (toluene insolubles/quinoline solubles) content. This entails large molecules that do not distil on carbonization, thereby giving rise to high carbon yields but a low enough viscosity for the penetration and wetting of the carbon substrate. The use of thermal treatment to remove volatiles and promote dehydrogenative polymerization reactions, either individually or combined with coking accelerators, such as sulfur (Fernández *et al.*, 1998; Oh and Park, 1999) or $AlCl_3$ (Mochida *et al.*, 1985) has been tested mainly at laboratory scale. However, in recent years considerable attention has been given to air-blowing, because of its effectiveness and for economic reasons. The oxygen in the air acts as a polymerization promoter, increasing the molecular size of light compounds through dehydrogenative polymerization reactions (Barr and Lewis, 1978; Zeng *et al.*, 1993; Fernández *et al.*, 1995), thus preventing their distillation and removal during the carbonization stage. The result is an increase in viscosity and a more disordered orientation of the lamellar aromatic molecules, limiting the growth and coalescence of mesophase, but still giving graphitizable or partially graphitizable carbon. With air-blown impregnating pitches (250 °C, 18 h) and AS4k carbon fibers, unidirectional composites of bulk densities up to 1.59–1.60 g cm^{-3} were achieved without any further densification. Composites showed high flexural strength, but fiber–matrix bonding was too strong, leading to a brittle failure. A possible way to overcome this problem could be the use of untreated fibers which yield weaker fiber–matrix bonding.

Other recent developments, designed to reduce costs by avoiding the pre-treatment step, include the direct oxidative stabilization of impregnated carbon preforms or pitch-based

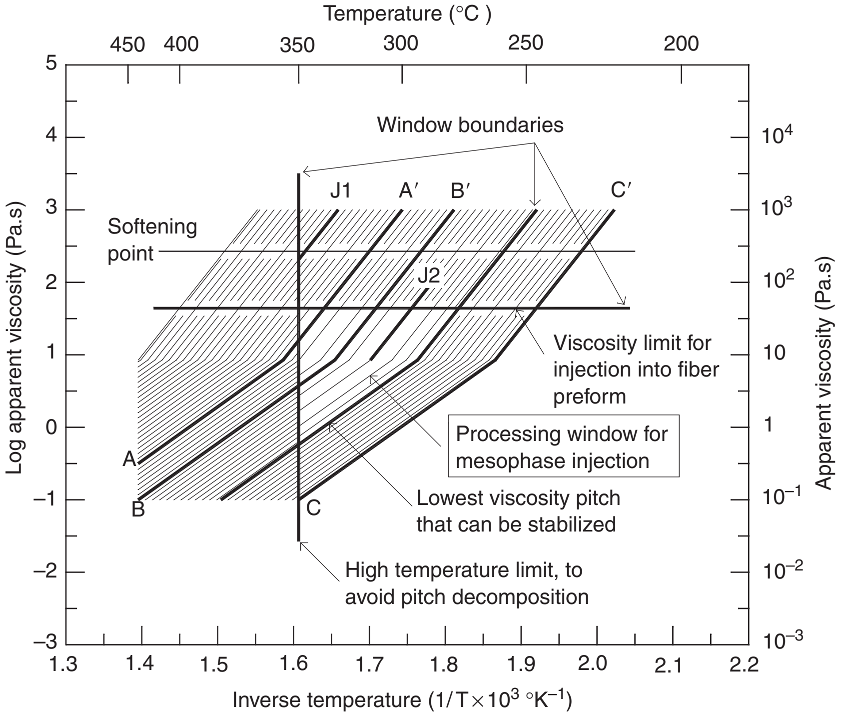

Figure 7.9 Processing window for mesophase injection (White *et al*., 1994).

tow-pregs (Casal *et al*., 1999), in order to obtain composites with a total absence of pores (after carbonization at 1,200 °C) and a graphitic matrix excepting the edges of the laminate.

A remarkable achievement in recent years has been the development of synthetic mesophase pitches from aromatic compounds (Mochida *et al*., 1988; Mochida *et al*., 2000). Mesophase pitches were initially prepared by thermal treatment of isotropic pitch (Singer *et al*., 1987). These pitches have no light compounds which makes it possible to obtain high carbon yields and shorter processing times on carbonization. Moreover, they also have a low enough viscosity for infiltration purposes. In relation with this, White *et al*. (1994) developed a processing window for the injection of mesophase pitch into fiber preforms (Fig. 7.9). This processing window, expressed in terms of apparent viscosity and temperature, illustrates three competitive requirements: (i) the pitch must be sufficiently fluid to flow without any excessive distortion of the preform; (ii) possess the required thermal stability for completing the injection process; and (iii) be sufficiently viscous to retain the shrinkage-crack porosity essential for stabilization in depth by oxidation. If these requirements are fulfilled, a preliminary evaluation of the flow properties of a candidate pitch for a specific preform can be achieved.

The oxidative stabilization mentioned above is related to the problem of matrix bloating on carbonization when using mesophase pitches. The oxidative stabilization of preforms and woven fabrics impregnated with mesophase pitch, prior to the carbonization process, has been shown (White and Sheaffer, 1989; Christ and Hüttinger, 1993) to be an efficient way of preventing bloating, while preserving the matrix microstructure. However, further research is needed to make it more efficient and economical.

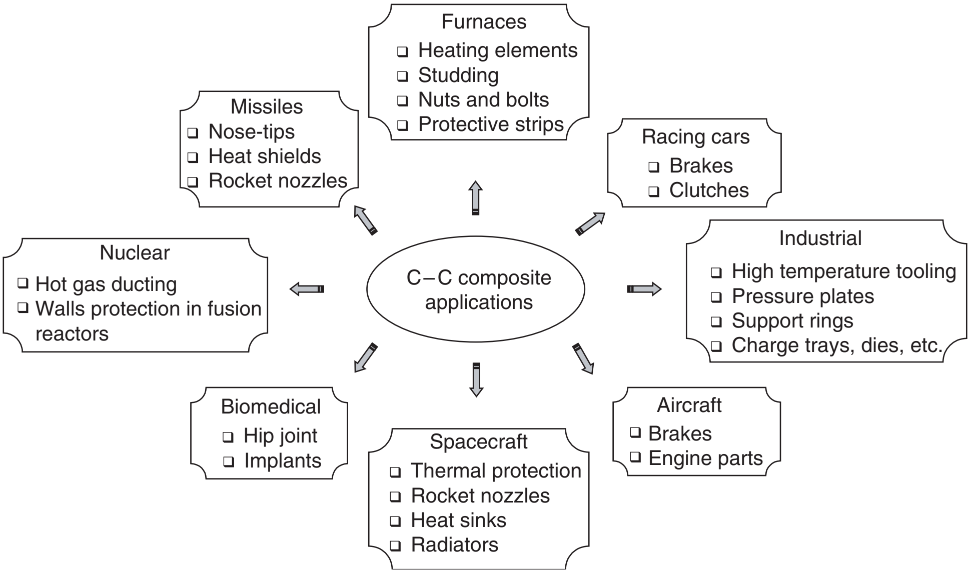

Figure 7.10 Main applications of C–C composites.

6 Summary and conclusions

C–C composites have a great potential for a wide range of applications (Fig. 7.10), not only for high-technology but also for industrial uses (Savage, 1993d; Walker, 1993). However, to exploit the full potential of the excellent properties of these materials requires the overcoming of drawbacks such as price, brittleness, and oxidation resistance. This would be possible only with the combined multidisciplinary effort of expertise from different fields, such as chemists, physicians, engineers, etc.

Further research into new aspects concerning the technology involved in the preparation of C–C composites by liquid impregnation is needed before they can be industrially applicable, in addition to a deeper understanding of the mechanisms involved in the formation of the matrix microstructure and its interaction with the fiber.

However, the development of new matrix precursors of high carbon yield with optimum viscosity, and the use of blends which individually yield different microstructures offers a promising future for these materials.

References

Appleyard, S. P., Rand, B., and Ahearn, C. E. (1995). “Processing, structure and properties of pitch-based carbon–carbon composites,” *Abstracts of Papers of the American Chemical Society*, ed. American Chemical Society, Washington, 209: 53-Fuel, Part 1, 260–264.

Arianoutsos, S., Murdie, N., Takano, S., and Ju, C. P. (1990). “Processing of pitch based carbon–carbon composites,” *Extended Abstracts of 6th Annual Conference on Materials Technology* (*Composite-Technology*), ed. M. Genisio, PhD, Southern Illinois University at Carbondale (USA), 134–145.

Barr, J. B. and Lewis, I. C. (1978). “Chemical changes during the mild air oxidation of pitch,” *Carbon* **16**, 439–444.

Bermejo, J., Granda, M., Menéndez, R., and Tascón, J. M. D. (1994). "Comparative analysis of pitches by extrography and thermal analysis techniques," *Carbon* **32**, 1001–1010.

Boenigk, W., Haenel, M. W., and Zander, M. (1990). "Structural features and mesophase formation of coal-tar pitch fractions obtained by preparative size exclusion chromatography," *Fuel* **69**, 1226–1232.

Borokh, G. R., Grechishkin, V. A., Gorokhovich, A. I., and Tikhonov, A.I (1995). "Forming of parts and components of fibre composites by winding," in *Composite Manufacturing Technology*, eds A. G. Bratukhin and V. S. Bogolyubov, Chapman & Hall, London (UK), 77–124.

Casal, E., Granda, M. Bermejo, J., and Menéndez, R. (1998). "Voids development during processing of unidirectional C/C composites," *Extended Abstracts of Eurocarbon'98*, Strasbourg (France), vol. I, 515–516.

Casal, E., Bermejo, J., Prada, V., Granda, M., and Menéndez, R. (1999). "Oxidative stabilization of C/C tow pregs studied by light microscopy", *Journal of Microscopy* **196**, 237–242.

Casal, E., Granda, M., Bermejo, J., and Menéndez, R. (2001). "Monitoring unidirectional C/C composite processing by light microscopy", *Journal of Microscopy* **201**, 324–332.

Christ, K. and Hüttinger, K. J. (1993). "Carbon-fiber-reinforced carbon composites fabricated with mesophase pitch," *Carbon* **31**, 731–750.

Fernández, A. L., Granda, M., Bermejo, J., Bernad, P., and Menéndez, R. (1998). "Carbon precursors from anthracene oil. Insight into the reactions of anthracene oil with sulfur," *Energy & Fuels* **12**, 949–957.

Fernández, J. J., Figueiras, A., Granda, M., Bermejo, J., and Menéndez, R. (1995). "Modification of coal-tar pitch by air-blowing – I. Variation of pitch composition and properties," *Carbon* **33**, 295–307.

Figueiras, A., Fernández, J. J., Granda, M., Bermejo, J., Casal, E., and Menéndez, R. (1995). "Influence of matrix precursors on the microstructure and mechanical properties of C/C composites," *Journal of Microscopy* **177**, 218–229.

Figueiras, A., Granda, M., Casal, E., Bermejo, J., Bonhomme, J., and Menéndez, R. (1998). "Influence of primary QI on pitch pyrolysis with reference to unidirectional C/C composites," *Carbon* **36**, 883–891.

Granda, M., Bermejo, J., Moinelo, S. R., and Menéndez, R. (1990). "Application of extrography for characterization of coal tar and petroleum pitches," *Fuel* **69**, 702–705.

Granda, M., Patrick, J. W., Walker, A., Casal, E., Bermejo, J., and Menéndez, R. (1998). "Densification of unidirectional C/C composites by melted pitch impregnation," *Carbon* **36**, 943–952.

Hirano, K., Narita, N., and Mukai, K. (1993). "Development of high performance coal tar pitch based C/C composites," *Proceedings 4th "Nippon Steel Corporation" Symposium on High-Performance Materials for Science Environments*, Nagoya (Japan), pp. 124–132.

Hocquellet, D. and Chenier, J. P. (1993). "Procédé de fabrication d'une pièce en matériau composite carbone/carbone utilisant de la poudre de mesophase," *European Patent No. 0558 417 A1*.

Jortner, J. (1986). "Macroporosity and interface cracking in multi-directional carbon–carbons," *Carbon* **24**, 603–613.

Kershaw, J. R. and Black, K. J. T. (1993). "Structural characterization of coal-tar and petroleum pitches," *Energy & Fuels* **7**, 420–425.

Klett, J. W. and Edie, D. D. (1995). "Flexible towpreg for the fabrication of high thermal conductivity carbon/carbon composites," *Carbon* **33**, 1485–1503.

Marsh, H. and Latham, C. (1986). "The chemistry of mesophase formation," *Petroleum Derived Carbons – ACS Symposium Series No 303*, ed. M. J. Comstock, American Chemical Society, 1–28.

McAllister, L. E., and Lachman, W. L. (1983). "Multidirectional carbon-carbon composites," in *Fabrication of Composites*, eds A. Kelly and S. T. Mileiko, Elsevier Science Publ. Co. Inc., Northholland, Amsterdam, New York, 109–175.

Menéndez, R., Granda, M., and Bermejo, J. (1997). "Relationships between pitch composition and optical texture of cokes," *Carbon* **35**, 555–562.

Meyer, R.A. (1994). "Overview of international carbon–carbon composite research", *Materially Speaking*, Southern Illinois University at Carbondale, Carbondale (USA), vol. 9, No. 3.

Mochida, I., Sone, Y., and Korai, Y. (1985). "Preparation and properties of carbonaceous mesophase. II Highly soluble mesophase from ethylene tar modified using aluminum chloride as a catalyst," *Carbon* **23**, 175–178.

Mochida, I., Korai, Y., Wang, Y. G., and Hong S. H. (2000). "Preparation and properties of mesophase pitches," in *Graphite and Precursors – World of Carbon*, ed. P. Delhaès, Gordon and Breach Science Publishers, Amsterdam (The Netherlands), chapter 10, 221–248.

Mochida, I., Shimizu, K., Korai, Y., Otsuka, H., and Fujiyama, S. (1988). "Structure and carbonization properties of pitches produced catalytically from aromatic hydrocarbons with HF/BF_3," *Carbon* **26**, 843–852.

Mullen, C. K. and Roy, P. J. (1972). "Fabrication and properties description of AVCO 3-D carbon–carbon cylinder materials," *Proc. 17th Nat. SAMPE Symp.* (SAMPE, Azusa), III–A-2.

Murdie, N., Ju, C. P., Don, J., and Wright, M. A. (1992). "Carbon–carbon matrix materials," in *Carbon–Carbon Materials and Composites*, eds J. D. Buckley and D. D. Edie, NASA Reference Publication 1254, 105–167.

Oh, S. M. and Park, Y. D. (1994). "An analysis of densification process of carbon/carbon composites," *Mat. Res. Soc. Symp. Proc. Vol.* **349**, 93–97.

Oh, S. M. and Park, Y. D. (1999). "Comparative studies of the modification of coal-tar pitch," *Fuel* **78**, 1859–1865.

Pérez, M., Granda, M., García, R., Moinelo, S.R., Menéndez, R., and Romero, E. (2000). "Petroleum pitches as an alternative to binder coal-tar pitches," in *Light Metals*, 531–536.

Plotzker, I. G., Cranmer, J. H., Uhlmann, D. R., and Peebles, L. H. Jr. (1988). "Process for car-carbon composite fabrication," *United States Patent No. 4,745,008*.

Rand, B. (1993). "Matrix precursors for carbon–carbon composites," in *Essentials of Carbon–Carbon Composites*, ed. C. R. Thomas, Royal Society of Chemistry, Cambridge (UK), 67–102.

Rand, B., Hosty, A. J., and West, S. (1989). "Physical properties of pitch relevant to the fabrication of carbon materials," in *Introduction to Carbon Science*, ed. H. Marsh, Butterworths, London (UK), 75–106.

Rellick, G. (1990). "Densification efficiency of carbon–carbon composites," *Carbon* **28**, 589–594.

Savage, G. (1993a). "Gas phase impregnation/densification of carbon–carbon and other high-temperature composite materials," in *carbon–carbon composites*, Chapman & Hall, London (UK), 85–116.

Savage, G. (1993b). "The properties of carbon–carbon composites," in *Carbon–Carbon Composites*, Chapman & Hall, London (UK), 277–322.

Savage, G. (1993c). "Thermoplastic matrix precursors," in *Carbon–Carbon Composites*, Chapman & Hall, London (UK), 157–191.

Savage, G. (1993d). "Applications of carbon–carbon composites," in *Carbon–Carbon Composites*, Chapman & Hall, London (UK), 323–359.

Singer, L. S., Riffle, D. M. and Cherry, A. R. (1987). "High temperature centrifugation: application to mesophase pitch," *Carbon* **25**, 249–257.

Tsushima, T., Takayasu, J., Taniguchi, K., Kobayashi, H., and Sindo, A. (1993). "Physical properties of pitch-based carbon-fiber reinforced carbon composites using pitch-powder and phenolic resin mixture as matrix precursor," *Proceedings 4th "Nippon Steel Corporation" Symposium on High-Performance Materials for Science Environments*, Nagoya (Japan), 115–123.

Walker, E. J. (1993). "The importance of fibre type and fibre surface in controlling composite properties," in *Essentials of Carbon–Carbon Composites*, ed. C. R. Thomas, Royal Society of Chemistry, Cambridge (UK), 37–66.

White, J. L. and Sheaffer, P. M. (1989). "Pitch-based processing of carbon–carbon composites," *Carbon* **27**, 697–707.

White, J. L, Gopalakrishan, M. K., and Fathollahi, B. (1994). "A processing window for injection of mesophase pitch into a fiber preform," *Carbon* **32**, 301–310.

Zander, M. (1997). "Pitch characterization for industrial applications," in *Introduction to Carbon Technologies*, eds H. Marsh, E. A. Heintz, and F. Rodríguez-Reinoso, Universidad de Alicante, Alicante (Spain), 425–459.

Zeng, S. M., Maeda, T., Tokumitsu, K., Mondori, J., and Mochida, I. (1993). "Preparation of isotropic pitch precursors for general purpose carbon fibers (GPCF) by air blowing – II. Air blowing of coal tar, hydrogenated coal tar and petroleum pitches," *Carbon* **31**, 413–419.

Part III

PROPERTIES OF MATRICES AND COMPOSITES

8

STRUCTURE OF PYROCARBONS

X. Bourrat

1 Introduction

Pyrocarbon is the solid form of carbon deposited on a hot surface by cracking of gaseous or liquid hydrocarbons. Pyrocarbon is made up with small or extended graphene layers of sp^2 hybridized carbons more or less saturated with hydrogen. But what makes his a unique character is that these graphene layers can be piled in a high anisotropic way along the deposit surface. The *anisotropy* of the texture and the *density* are the key parameters characterizing this material with also the *size distribution of the layers* and the *hydrogen content*.

Three main events have boosted researches in the second half of the twentieth century: the discovery of carbon/carbon composites at the end of the fifties and their application as strategic material (Lamicq, 1984; Buckley, 1993). Pyrocarbon is the major matrix material. Then pyrocarbons were developed to be used as coating in nuclear fuel industry in the sixties for which the fluidized bed processing was widely developed, that is the chemical vapor deposition (CVD) of high temperature pyrocarbons (Bokros, 1969; Lefevre and Price, 1977). Finally, the strong development of carbon brakes in the last two decades of the twentieth century has focused the interest on infiltration of low temperature pyrocarbon (chemical vapor infiltration, CVI). Many other applications are existing. But the expansion of the carbon/carbon brakes, market the necessity to lower the prices (for fast train and truck markets) and the emergence of new comers has intensified the research all other the world at the turn of the century.

Nowadays the main issue is a fine control of structure with more and more accuracy. The main interest is focused on low temperature pyrocarbon for CVI with the highest deposit rate at lowest price. Local probes are needed to measure the main properties as, e.g. the elastic properties, thermal conductivity and naturally nanostructure parameters, i.e. anisotropy, density, graphene structure or closed porosity, etc.

First, this chapter will rationalize the very different pyrocarbon types following the two major transitions: *low* and *high temperature transitions*. Then in the next part, the recent efforts achieved to relate the structure (and texture) to the processing conditions in the case of low temperature pyrocarbons will be documented: carbon layer, cones and regenerative features. Finally, is a review of the growth mechanisms in relation with structure development and various approaches to quantify the structural parameters: density and anisotropy.

2 The various pyrocarbons

Bokros (1965, 1969) introduced a first comprehensive distinction among pyrocarbons by means of optical microscopy. At that time four structural groups were distinguished based on their appearance when observed under polarized light (on polished sections). The main concern was the deposition using the fluidized-bed CVD in a broad range of temperature.

Then, Kotlensky *et al*. (1971), Granoff and Pierson (1973), and principally Lieberman and Pierson (1974, 1975) documented the case of carbon composite infiltration at low temperature ($T < 1400\,^\circ\mathrm{C}$) and low partial pressure of hydrocarbon. They were the first to study the texture in relation with the processing conditions: matrix texture fall into three major types identified as rough laminar (RL), smooth laminar (SL), and isotropic pyrocarbons (I). They were the first to establish the important low temperature transition between rough and smooth laminar for infiltration process.

2.1 The low temperature transition: SL ↔ RL (800–1,400 °C)

Nowadays, the transition between high and low density pyrocarbons is well established. It is under control of the gas phase species, itself controlled by the residence time (Dupel *et al.*, 1995), the temperature or pressure. Transition is due to a change in the heterogeneous growth mechanisms in the range of 800–1,400 °C (Féron *et al.*, 1999). These transitions could be called the CVI transitions because it is of major concern in 3D preform infiltration (Lavenac *et al.*, 2000). A progressive passage from SL to a low-density I was also clearly established at very short residence time (and/or lower temperature and pressure) (Lavenac *et al.*, 2001). This passage occurs through the intermediate of dark laminar (DL) (Doux, 1994) by a progressive increase of disclination defects in the hexagonal lattice, the *pentagons* (Bourrat *et al.*, 2001):

SL ↔ RL

2.1.1 Smooth laminar pyrocarbon (SL)

When observed by reflected light SL is characterized by a medium reflectance (see Fig. 8.1). (Reflectance measures the ratio of light reflected by the polished surface.) Under cross-polars SL exhibits a large and well defined extinction cross known as the “Maltese-cross” (around fiber cross-sections). When rotating the stage, the rolling extinction parallel to the polars is smooth, thus this texture is called “smooth” laminar pyrocarbon. An example of this texture is provided on Fig. 8.1a. When measured, the density is found to be intermediate $1.8 < d < 1.95$. The anisotropy is medium too: extinction angle, Ae, measured in cross-polarized light is $12^\circ < \mathrm{Ae} < 18^\circ$ on a scale which goes up to 22 (see Section 5.3). The orientation angle, OA, measured by electron diffraction is $40^\circ < \mathrm{OA} < 70^\circ$. OA measures the disorder along the anisotropy plane which decreases down to 15°.

2.1.2 Rough laminar pyrocarbon (RL)

This texture has a high reflectance. When observed with the polarizer alone and because of carbon dichroism, a gray branch parallel to the polarizer appears around fiber cross-sections: reflectance is higher parallel to the graphene planes. Under crossed polars a highly contrasted Maltese-cross appears around the fiber cross sections (Fig. 8.1b). The extinction of the branches is irregular. For that reason it is called “rough” laminar. The roughness is provided by the prismatic texture due to the formation of fine cones generated on fiber

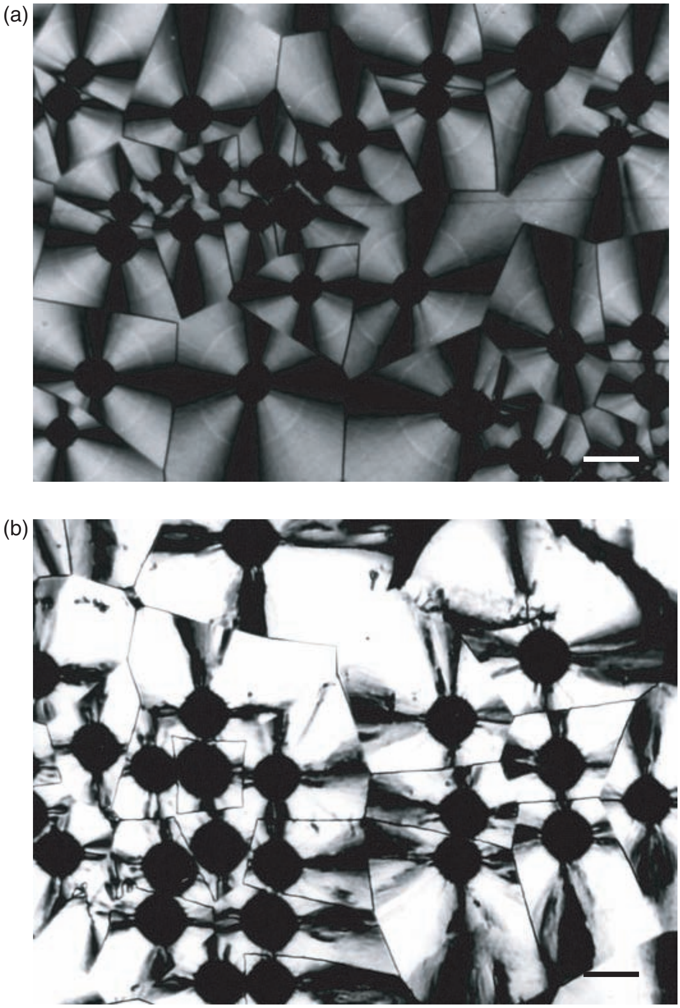

Figure 8.1 Low temperature transition in CVI conditions: (a) SL: smooth laminar pyrocarbon and (b) RL: rough laminar pyrocarbon (Cross-polarized light, bar is 10 μm, after Doux, 1994).

surface asperity and transmitted across the whole deposit (see Section 3.2). RL density is high : $2.0 < d < 2.2$. Anisotropy is high too: $Ae > 18°$ up to the maximum (app. 22°) and OA the disorder is low $<25°$ (typically 15°).

2.1.3 Isotropic pyrocarbon (I)

Isotropic texture has a low reflectance and a very weak anisotropy (or not). Under cross-polars a faint Maltese-cross can hardly be seen. It shows very fine grains with a poor brightness. This texture is often mingled with "isotropic-sooty" pyrocarbons (Section 2.2). The later can have a high density whereas isotropic (ISO) of low density systematically exhibits a low density: $d \sim 1.6$. The measure of the extinction angle gives values lower than 4°.

2.1.4 Dark laminar pyrocarbon (DL)

Dark laminar has no particular interest, it is only an intermediate in the passage between isotropic and smooth laminar pyrocarbons (SL). As isotropic, it does not seem to be resulting from a different mechanism but the same heterogeneous mechanism as smooth laminar (Bourrat *et al.*, 2001). It is defined by a faint anisotropy and intermediate density: $4° < \mathrm{Ae} < 12°$ and $1.6 < d < 1.8$.

2.2 The high temperature transition: L ↔ G ↔ IS (1,400–2,000 °C)

In the CVD range of 1,400–2,000 °C, as processing temperature is increased, density decays and then restores again. This characterizes the high temperature transition reported by many authors in the case of surface deposition (see Fig. 8.2). This second transition towards an "isotropic" grade grown at high temperature was first reported by Brown and Watt (1958). Diefendorf (1970) observed that what is responsible is the "soot" nucleated in gas phase and that it can be avoided by decreasing the hydrocarbon partial pressure (Diefendorf, 1960) as shown in Figs 8.2 (bold line) and 8.3. All these experimental data have been confirmed by many authors in fluidized bed (Bokros, 1965) or static one (Tombrel and Rappeneau, 1965).

Later on, Loll *et al.* (1977) have shown that this transition from laminar (L) to granular (G) and isotropic sooty (IS) pyrocarbon was also existing in the case of CVI (of felt) as shown in Fig. 8.4 under the form of an existence diagram.

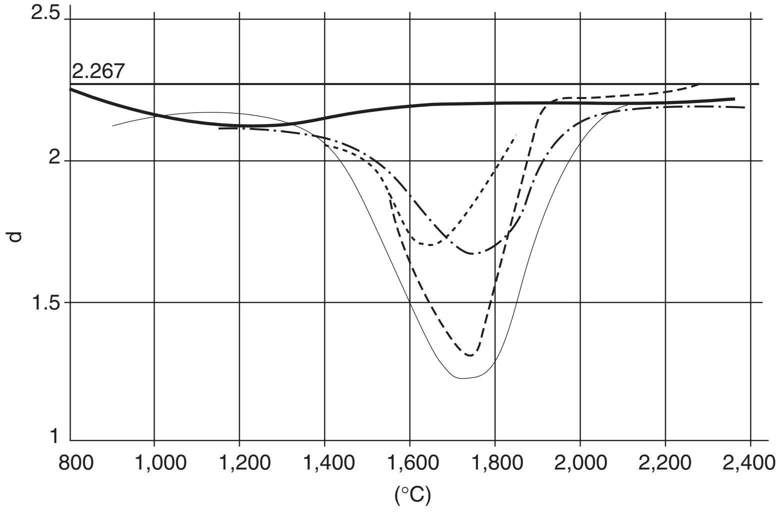

Figure 8.2 High temperature pyrocarbon transition: density versus processing temperature. Full bold line: Diefendorf (1960) 2.3 Pa CH_4; fine dash and dot: ibid., 5.3 kPa CH_4; full fine line: Brown *et al.* (1959) 20 kPa CH_4 or C_4H_4; dashed fine line: Blackman *et al.* (1961) CH_4 and bold dot and dash: Mayasin and Tesner (1961): 100 KPa H_2 and 2 to 10 % CH_4.

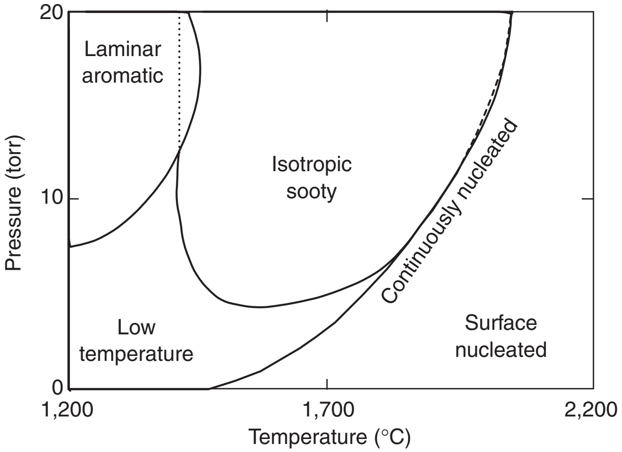

Figure 8.3 High temperature transition after Diefendorf (1970).

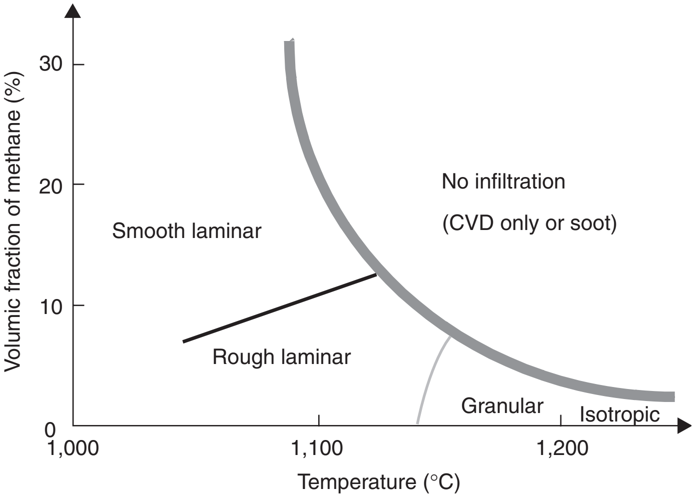

Figure 8.4 Existence diagram of the low temperature transition demonstrated in infiltration of a felt. After Loll *et al*. (1977).

The structural aspects of the growth mechanisms were studied by Kaae *et al*. (1972) and Kaae (1975, 1985). With increasing temperature, laminar pyrocarbon is more and more regenerated by gas-phase nucleated particles as shown in sketch of Fig. 8.5. Transition occurs from regenerated laminar (Fig. 8.6a) to granular (Fig. 8.6b) and to isotropic sooty (Fig. 8.6c, d).

2.2.1 *Granular pyrocarbon*

It results from a mechanism where most of the carbon still grows directly onto the surface (molecular condensation) but gas phase-grown particles regenerate continuously

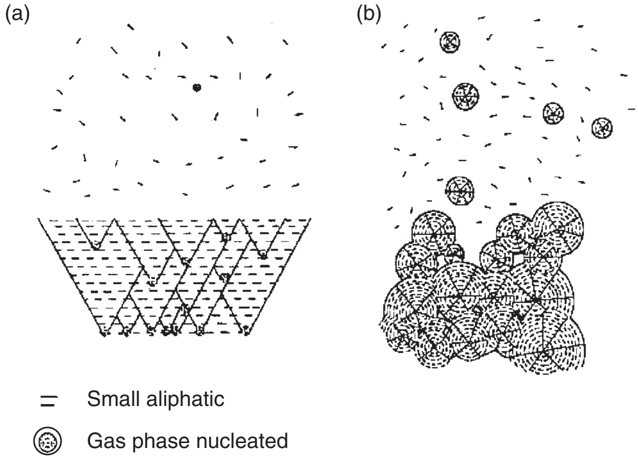

Figure 8.5 Model of the mechanism controlling the high temperature transition: (a) Low depositing rate: regenerated-laminar and granular pyrocarbon; (b) High depositing rate: isotropic sooty (case of high density represented after Kaae, 1985).

small cones (Kaae, 1985). Figure 8.5b gives a sketch to rationalize the mechanism (see Section 3.4).

2.2.2 Isotropic sooty

At higher temperature a sort of "isotropic" deposit is observed (Fig. 8.6c) which was named "isotropic sooty" (IS) by Diefendorf (1970). At the beginning, it has a high density ($\rho = 2.0$). The lack of preferred orientation is provided by the size of the gas phase nucleated particles, these free-floating particles are much larger meanwhile too small to be resolved by optical microscopy: deposits look "isotropic" with optical microscopy. As temperature is increased, density progressively decays down to $\rho = 1.6$ (and even 1.5). Kaae shows that the change in density from high to low, is due to the molecular deposition and not to the particles structure which are still dense in most cases. If the molecular deposition is dense, then the density remains high: $\rho = 2$. If this pyrocarbon is porous, the dense core is surrounded by a tangled structure close to that of glassy carbon: then the density drops down to a minimum ($\rho = 1.6$). At higher temperature the density increases again because the tangled structure becomes coarser and then disappears. It is to note that concentration of hydrocarbon can be increased at a given bed temperature with the same effect. With a too low concentration of precursor this transition was not seen (Fig. 8.2).

Results obtained at General Atomic by Kaae were confirmed at CEA by Pelissier and Lombard (1975). As a matter of fact, the high temperature transition appears as a dramatic drop in density together with the occurrence of an isotropic structure. In this range textures are resulting from a different mechanism for which the particles grown in gas phase have a crucial role. Most of the authors agree with Kaae distinguishing L, G, or IS in-between 1,400 and 2,000 °C:

$$L \leftrightarrow G \leftrightarrow IS$$

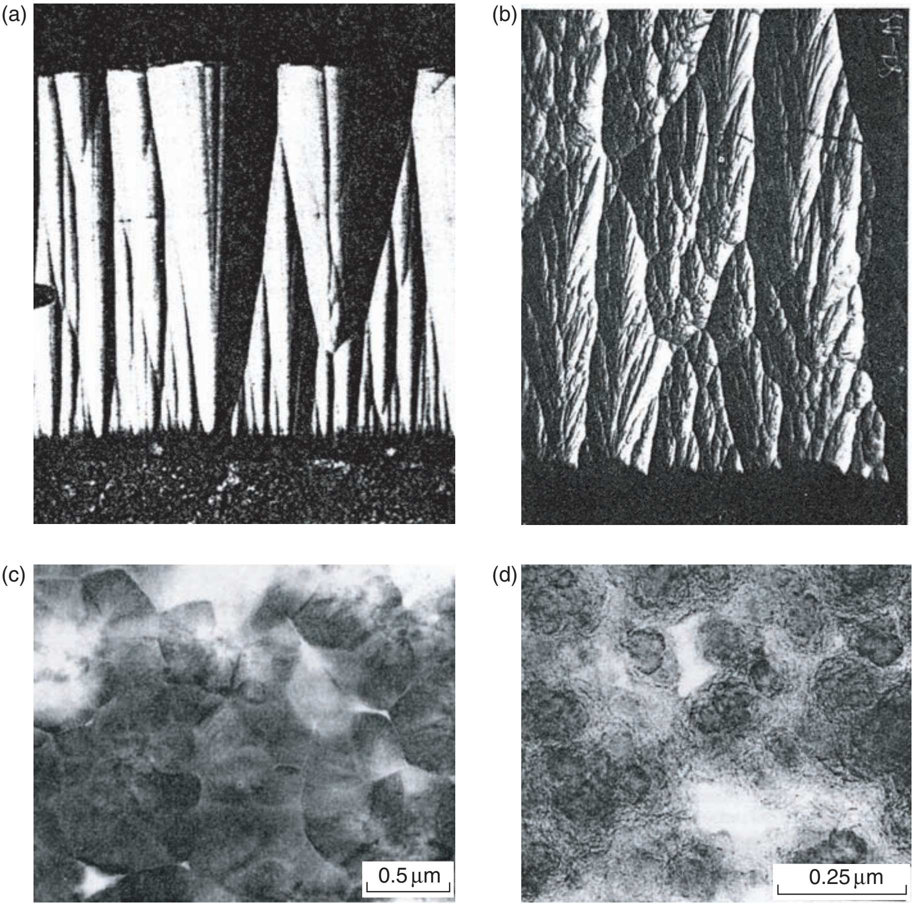

Figure 8.6 Structure evolution during the high temperature transition. (a) Pyrocarbon laminar (few small gas phase-grown particles); (b) Granular pyrocarbon (abundant gas phase-grown particles); (c) IS of high density (abundant dense particles co-deposited with homogeneous pyrocarbon); (d) IS of low density (abundant and dense particles co-deposited with glassy carbon-like pyrocarbon) (a and b: cross-polarized light, bar is 20 μm, after Tombrel and Rappeneau (1965); (c) and (d): TEM after Kaae, 1985).

The high temperature transition has no more been studied till the seventies, in our knowledge.

2.3 Very high temperature pyrocarbons

"Oriented" pyrocarbons used as conductive and gas-tight coating are deposited by CVD of methane at temperatures between 2,000 and 2,500 °C (e.g. 2 kPa of methane at 2,000 °C with a deposition rate of 100 $\mu m\, H^{-1}$, Le Carbone Lorraine, 1975). At higher temperature, works performed (Guentert, 1962; Tombrel and Rappeneau, 1965; Hirai and Yajima, 1967; Bokros, 1969; and Goma *et al*., 1985) have shown by XRD and TEM that the deposit is highly oriented with a regenerated texture (Fig. 8.7c). It was shown by XRD that they grow with

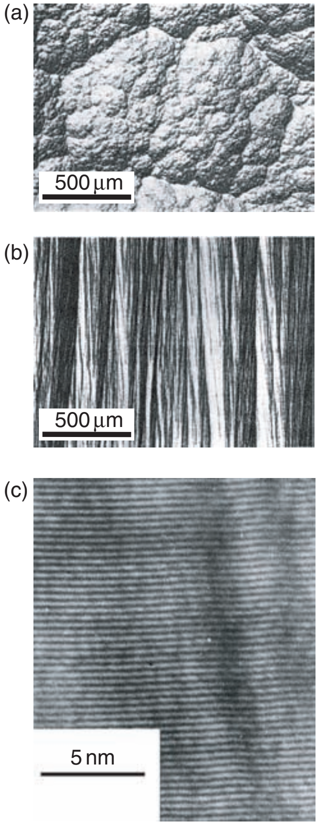

Figure 8.7 Very high temperature pyrocarbon (processing temperature: 2,100 °C): (a) Cross-polarized light on polished surface ($PCH_4 = 0.5$ KPa); (b) Same in cross section (after Tombrel and Rappeneau, 1965); (c) Same pyrocarbon in high resolution TEM (after Goma and Oberlin, 1985).

a turbostratic structure and a high degree of preferred orientation (Guenter, 1962; Tombrel and Rappeneau, 1965). In this case authors speak about direct deposition of carbon with a perfectly oriented turbostratic structure.

2.4 Pyrocarbons issued from new rapid densification processes

The new processes as thermal gradient (Golecki *et al.*, 1995) or pressure-pulse-CVI (Dupel *et al.*, 1994) or film boiling (David *et al.*, 1995; Bruneton *et al.*, 1997), all provide classical textures or combinations of classical features known in CVD, except the possible mixed structures in the case of liquid immersion in the rapid densification process: mosaic pitch-based- and pyrolytic-type carbons (Rovilain, 1999; Beaugrand, 2000) as shown in Fig. 8.8c. It is noteworthy that rough laminar is much easily produced by I-CVI than by any other process. In most cases, regenerative laminar (REL) (see Section 3.3) is obtained with the new rapid densification processes.

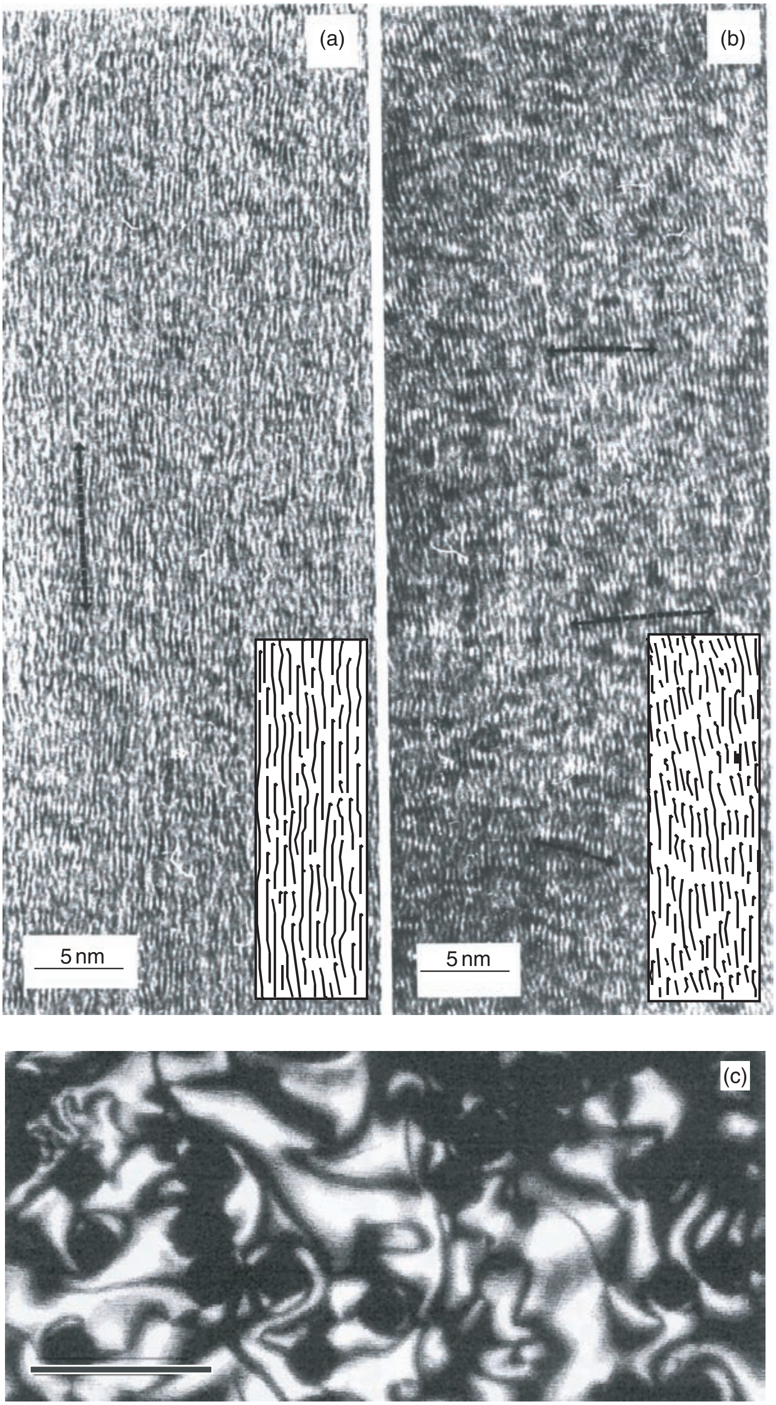

Figure 8.8 New rapid densification processing. (a) Comparison of laminar textures (LRE) obtained by pulse-CVI with a lateral growth of long defective layers with (b) rough laminar pyrocarbon obtained by I-CVI with a good stacking of small and straight layers (Dupel *et al.*, 1995); (c) Mosaic structure that can occur in the film boiling process aside classical laminar textures (after Beaugrand, 2001, bar is 1 μm).

3 Cones and regenerative features

Among the distinctive growth-features of pyrocarbon is the cone generation. These features are important in considering the anisotropy of structure and thermo-mechanical properties, as well as in-service properties (e.g. tribology). Three main mechanisms and their mix have been recognized:

- substrate-generated cones or primary cones;
- secondary cones, self-generated within the deposit;
- secondary cones generated by gas-phase nucleated particles.

Coffin (1964) has modeled the cone formation mechanism. He has definitely shown that they come from a simple roughness transmission effect due to the stacking, layer after layer. It is not the result of a nucleation/growth process.

3.1 Cones formation

Flatness defects which can be transmitted come first from the support roughness. All laminar pyrocarbons possess primary cones generated onto the surface. Rough laminar pyrocarbon alone keeps its primary cones exclusively all across the deposit.

Let us suppose that the surface defect is a sphere lying on the support (Fig. 8.9). Coffin (1964) has shown that the laminar growth propagates the defect layer after layer. At the beginning all asperities at the surface are transmitted exactly with a parabolic shape (2). On both sides of this "paraboloid" surface, the layer direction sharply changes by an angle α as for twinned crystals. This sharp bend when observed on a polished surface perpendicular to the deposit, appears as a parabolic curve with a drastic contrast variation related to the change of the layers direction. This stage lasts more or less depending on surface defects density. Then, the interference of adjacent growing cones leads to a honeycomb structure visible when looking down on the deposit surface. In cross section it shows a prismatic texture (3). The higher the surface roughness, the higher the α angle. This prismatic texture responsible for the rough extinction of the Maltese-cross branches was also called "columnar structure" by Bokros or fibrous structure by Tombrel and Rappeneau (1965) who have extensively studied the generation of cones as a function of temperature during the high temperature transition: laminar–granular transition.

3.2 Surface-generated cones

Rough laminar appears to keep its primary cones across the full deposit. The more probable reason is because rough laminar does develop a highly oriented growth. The superposition of regenerative cones on the primary ones results in the progressive disappearance of them. So the pending question is: why rough laminar does not develop a regenerative growth as all laminars?

Because Rough Laminar pyrocarbon is not regenerative, then primary cones survive providing its prismatic texture. Bourrat *et al.* (2002) have shown that the α angle in-between adjacent columns controls the future "grain boundaries" limiting the lateral graphitization of the crystallites. More importantly they point out that these boundaries control a unique transverse reinforcement in the weakest direction of the matrix (stacking). This is a very important property exclusively known in RL.

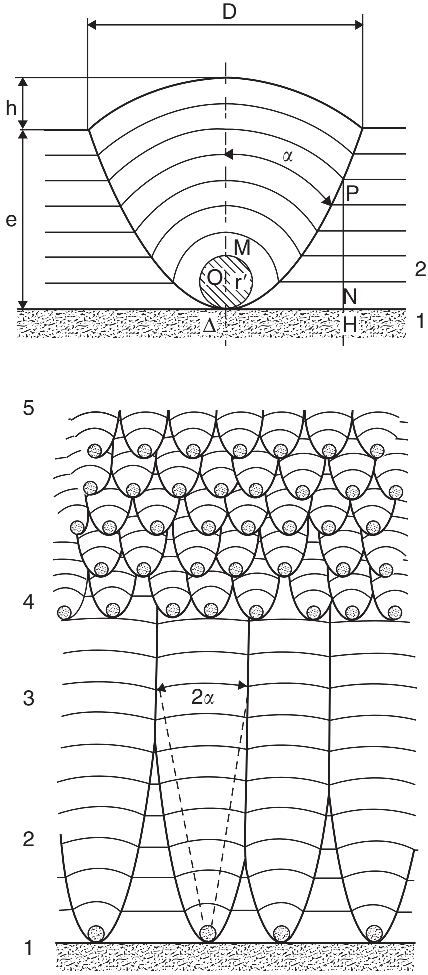

Figure 8.9 Schematic model of cone generation starting from a spherical defect on surface: 1 – surface; 2 – paraboloid zone; 3 – prismatic texture (e.g. RL); 4 – secondary cones as in SL and 6 deposit surface (after Tombrel and Rappeneau, 1965).

3.3 Self-generation of secondary cones

Except rough laminar, all other laminars are regenerative pyrocarbons. Regenerative pyrocarbons appear "smooth." Regeneration and cones growing mechanism are key features to understand the pyrocarbons, their texture and properties.

3.3.1 Smooth and dark laminar pyrocarbons regeneration

Cones are nucleated within the deposit: *self-generated*. These pyrocarbons develop large layers often convex. Curvatures are related to the presence of pentagons (Fig. 8.10a)

(Bourrat *et al.*, 2001). Thus self-generated growth features, call Ω-like growth features, are formed within the deposit (nanoporosity). They constitute spheroid defects with large radius, *r*, responsible for the generation of cones as shown in Fig. 8.10b. Because "*r*" is large, the opening of the cone is large, too. The development of a cone stops when a new one generates especially when *r* is large; for that reason most of the surface-generated cones rapidly disappear (4 in model of Fig. 8.9). Thus, the prismatic columns do not form and the Maltese-cross branches appear "smooth." This is typically a *self-generation cone mechanism*. This phenomenon is important in controlling the transition:

RL ↔ SL

As the development of these large cones stops when a new one generate, if the Ω-like features production increases, cones are less and less visible in the passage SL ↔ DL. At the limit, I is exclusively produced by cone nuclei. As a consequence structure is isotropic, nanoporosity very high and thus density poor.

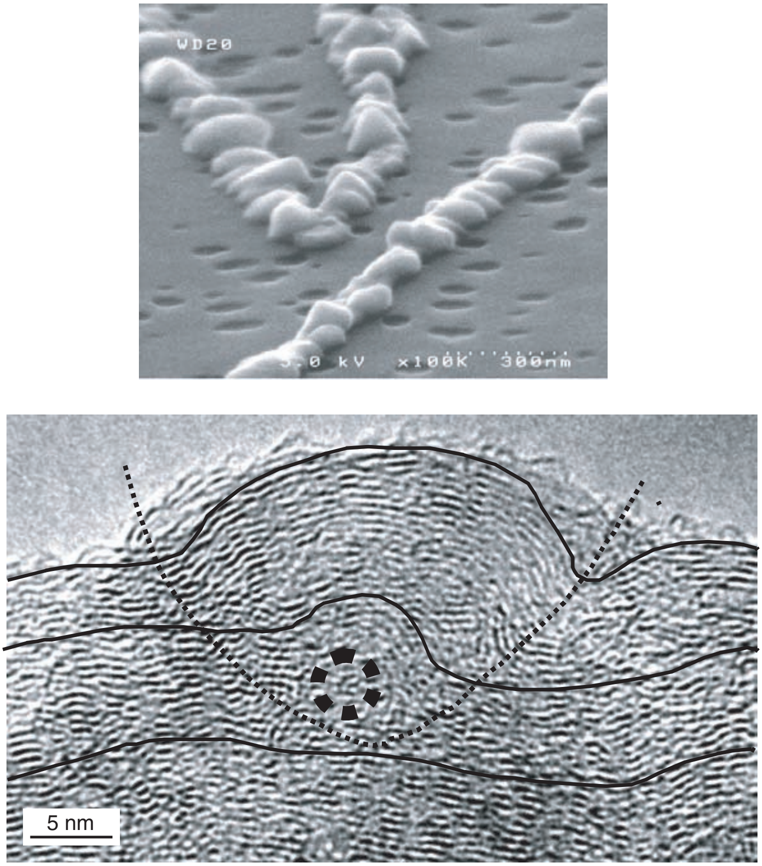

Figure 8.10 Smooth laminar pyrocarbon. (a) Nucleation of curved graphene layers on active sites at the surface of HOPG (Bourrat *et al.*, 2001); (b) Large cones generated by a curved graphene layer (HR-TEM, after Fillion, 2000).

The regeneration of cones produced by the Ω-like growth features gives the smooth aspect to the laminar together with its lower anisotropy and density (Bourrat *et al*., 2002).

3.3.2 Regenerative rough laminar pyrocarbons (REL)

In most of the processes another self-generation of cones occurs, based on a different mechanism. Contrarily to smooth laminar, the cones are generated by small layer defects: α angles measured by TEM darkfield are weak: $15° < \alpha < 18°$ (Fig. 8.11b). The defects in concern lies at nanometric scale, as lattice defects for example. It is assumed that the layer growth mechanism change for a "lateral" mechanism and thereafter the deposit acquires a higher capability to transmit defects. This is referred to as "covering efficiency" of layers (Bourrat *et al*., 2002).

REL pyrocarbon is formed in different processes that have been alternatively developed: e.g. pulse-CVI (Dupel *et al*., 1997) or related to the mother molecule, e.g. toluene (Bourrat *et al*., 2002) or from boron-doped process (Tombrel and Rappeneau, 1965; Jacques *et al*., 1997). In these processes the layer diameter, L_2, is systematically larger while the density keeps high. Layers are larger, highly densely packed but paradoxically the coherent lengths are smaller (e.g. pulse-CVI in Fig. 8.8b). It can be assumed that the growth mechanism is mixed: layers grow following the "atom by atom" (or small species) after diffusion onto the surface, with speculative forms as phenyl radical or monocyclic aromatic in the case of toluene. The transition is not precisely known at that time.

3.3.3 Regenerative features of very high temperature laminar pyrocarbons

Far from CVI conditions, deposits obtained at very high temperature exhibit the superposition of primary cones and regenerative cones within the deposit (Fig. 8.7b). Thus polished surface of deposit get a fractal appearance known as "cauliflower-like" texture of high temperature pyrocarbon (Fig. 8.7a). The vanishing of previous cones does not occur because the size of the defects are very small and in the same time the hexagonal lattice is perfect and supple enough to transmit any defect at long distance without fading. Goma *et al.* (1985) have shown that layer diameters are indeed very large (Fig. 8.7c). It is probably resulting from a lateral growth mechanism. The covering effect is much higher; the cones are very sharp related to very small defects in the lattice, and transmitted on long distance.

3.4 Secondary cones generated by gas-phase nucleated particles

As pointed out very soon by Tesner (1984), blacks and pyrocarbon growth have to be considered as competitive mechanisms but in a given domain of high pressure/temperature. This competition is well documented in the case of granular pyrocarbons for which the nucleation and growth of solid particles in the gas phase is a key step in their growth. These particles by depositing on the growing surface are responsible for the generation of cones (Fig. 8.5a). The different processes, as fluidized bed or static CVD, offer many different combinations. A very wide and open transition occurs, just based on the size of the gas phase particles (improperly called soot), their density and the accessible surface, i.e. surface/volume ratio different on fluidized bed or static surface. All these combinations give rise to the many different granular types reported in the literature.

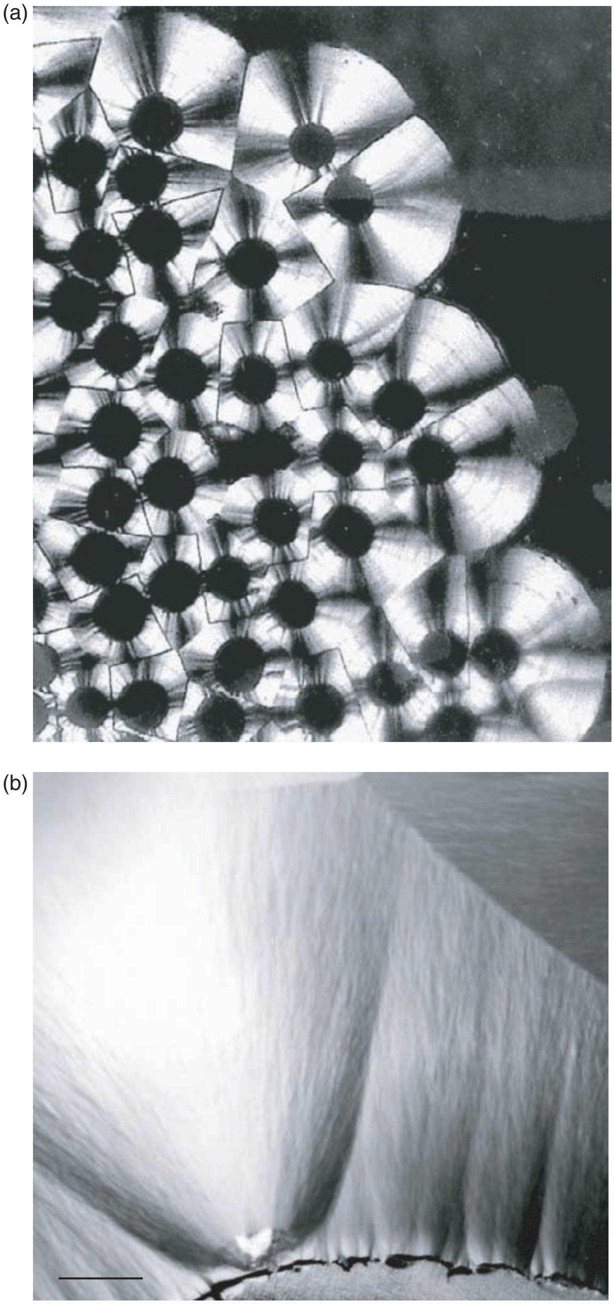

Figure 8.11 Regenerated laminar (P-CVI, toluene 2 kPa, 1,000 °C and residence time $t = 2$s) (a) Cross-polarized light: high reflectance and smooth branches of the Maltese-cross, bar is 10 μm; (b) TEM darkfield: fiber surface-generated cones vanish as secondary cones generate (self-generation); only large cones survive, bar is 1 μm. After Bourrat *et al*. (2002).

4 Carbon layer diameter and growth mechanisms

4.1 Nucleation and heterogeneous mechanisms

The heterogeneous aspect of the pyrocarbon growth mechanism has been very soon the focal point of many experimental and theoretical works. Three different groups of theories have been developed to explain how graphene layers deposit onto the surface. Today the polymorphism of pyrocarbons is clearly related at least to three different heterogeneous mechanisms, controlled by the species present in the gas phase. These species are depending on the mother molecule, the processing pressure, temperature, residence time, and also factors controlling the maturation as diffusion, surface on volume ratio, etc.

- First the Grisdale's droplet theory: formulated by Sweitzer and Heller (1956), after Parker and Wolfhard (1950), Stokes (1951), and Grisdale (1953), developed by Thomas (1962), and reformulated by several authors. This theory has had a lot of success because of the haze visible in the reactor and attributed to the droplets' diffraction. In fact this haze is more likely the diffraction of solid aerosol particles grown in the gas phase or even HAP molecules. It is admitted, now, that granular pyrocarbons are grown by a mechanism in which solid particles nucleated and partly grown in the gas phase, aggregate in the deposit (Kaae, 1985). This theory is abandoned.
- A second group of theories was based on the direct deposition by a mechanism of chemisorption. The main author of this speculated model is Tesner, then more recently Benzinger and Hüttinger (1999). This mechanism was recently pointed out as one of the main mechanism by Féron *et al*. (1999), Lavenac (2001), Bourrat *et al*. (2001): it takes place in CVI and CVD conditions for the low maturation of the gas phase and probably at very high temperature.
- Finally, authors who postulate that two mechanisms are competitively involved as Diefendorf (1960) or Féron *et al*. (1998) were in the right direction. At low temperature in CVI conditions, the direct deposition of small species by chemisorption on layer edge sites and the molecular condensation of HAP molecules is the best model to match with the transition from smooth to highly anisotropic laminar (Féron *et al*., 1998). At higher temperature the competition with homogeneous nucleation and growth as speculated by Tessner was also verified by TEM works (Pellissier and Lombard, 1975; Kaae, 1985).

Aa a summary, according to structural works published in the open literature, three main mechanisms can be considered, based on graphene layer sizes distribution L_2 and the anisotropy of their distribution. Kaae (1985) was more interested by the high temperature transition whereas Bourrat *et al*. (2001) recently documented the low temperature transition. In the following only the two mechanisms related to the low temperature transition will be reviewed.

4.2 Mechanisms controlling the low temperature transition (I-CVD processing)

To evidence this double mechanism, Bourrat *et al*. (2001), have achieved the deposit directly on a TEM carbon grid. All the processing parameters are kept constant except "*t*" the residence time in the hot zone. When "*t*" is very short, dark laminar pyrocarbon is obtained. High resolution TEM shows that the growth occurs out of line in all directions (Fig. 8.12a).

In that case thinning is not necessary; sample is seen "as received." Layers are extended. The mean fringes lengths L_2 was seen to be high: $<L_2> = 5.8$ nm with a maximal length of 20 nm. Such large layers are resulting from a direct deposition mechanism of small species. Because the residence time is very short, it is concluded that smooth laminar pyrocarbon grows from small species. Indeed, mainly small aliphatic are analyzed by in-situ Infra Red for that residence time (Féron *et al*., 1999). If the smooth laminar pyrocarbon is deposited on a cleaved surface of HOPG (pyrographite), the deposit occurs only on substrate sites: (00.2) growth steps and grain boundaries as shown in Fig. 8.12 and sketch of Fig. 8.13a. In absence of active sites the growth of smooth laminar does not occur (Bouchard *et al*., 1999; as seen by STM, Lavenac *et al*., 2001). So it is concluded that heterogeneous reactions comprising a chemisorption and a dehydrogenation step on active sites are required. Last point is that this mechanism gives rise to large layers with a very low hydrogen content (about 1.5 atomic %) and many curvatures in the layers, induced by the presence of pentagons entrapped in the lattice. Growth of the hexagonal lattice with pentagons disturb the anisotropy and increases the nanoporosity: $d < 2$ (Bourrat *et al*., 2001).

On the other side, when the residence time of the gas phase is long before reaching the substrate ($t = 4$ s in Fig. 8.12e) the carbon deposit on the carbon grid is different. The mechanism has changed completely due to the maturation of the gas phase. In those conditions highly oriented rough laminar pyrocarbon is deposited. Layers are short, flat and deposited parallel to the anisotropy plane. Fringes length are three times shorter in average: $<L_2> = 1.7$ nm. More importantly, there is no layer larger than 5 nm and no curvature. The deposit is also characterized by a higher stacking coherence L_c. When HOPG is used as a substrate, the whole surface is rapidly and uniformly covered by a flat coating. There is no need for a reaction on any substrate active site to grow the first layers of RL on the substrate (Bouchard *et al*., 2001). It is deduced from this key experience that the deposit occurs mainly by a step of physisorption of conjugated aromatic polycyclic species (PAH) directly on the surface (Fig. 8.13b). Layer growth still occurs at the edge but mainly by diffusion of large neighboring species. Such a growth mechanism results in a residual hydrogen content higher than that of smooth laminar pyrocarbon (about 3.5 atomic %). Dehydrogenation step is not a critical step in the carbon deposit.

As soon as species are produced with the ability to condense on the surface this mechanism with a higher depositing rate dominates on lateral growth (still active but kinetically much slower). The only control on this sharp transition from one mechanism to the other is the presence in the gas phase of PAH and their capability to condense on the surface with sufficiently high rate to block the chemisorption sites (and lateral growth) on the underlying layers (Bourrat *et al*., 2001): this is the transition from smooth to regenerative laminar.

5 Density and anisotropy of pyrocarbons

5.1 Pyrocarbon density

Density is a key specification for pyrocarbon. The reason is the very high sensitivity of density to the structure. During the high temperature transition, e.g. a large variation of density can occur depending on processing conditions, i.e. temperature, partial pressure and residence time of the hydrocarbon source. Density is resulting from the growth mechanism controlled by these major processing conditions. But different densities have first to be distinguished.

The *apparent density* is that of the material: mass/geometrical volume.

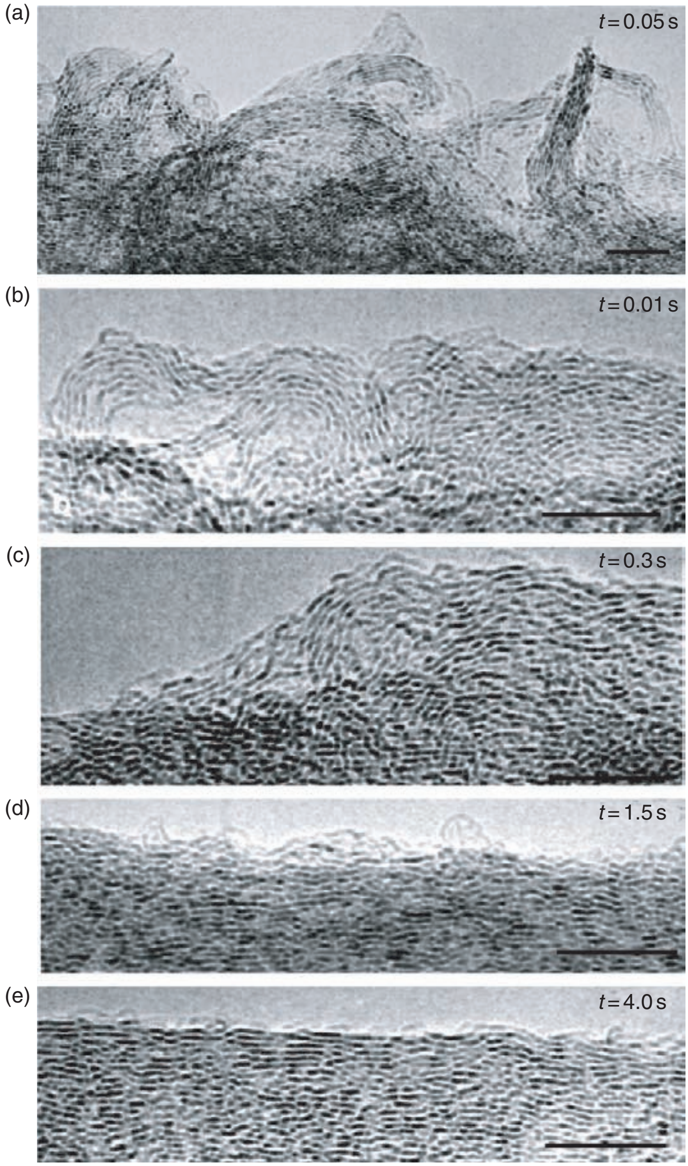

Figure 8.12 Low temperature transition. High resolution TEM micrographs of the growing carbon layers as a function of gas phase residence time "*t*" from dark laminar (a) to smooth laminar pyrocarbon (b)–(d) to highly oriented laminar (e). Bar is 10 nm. After Bourrat *et al*. (2001).

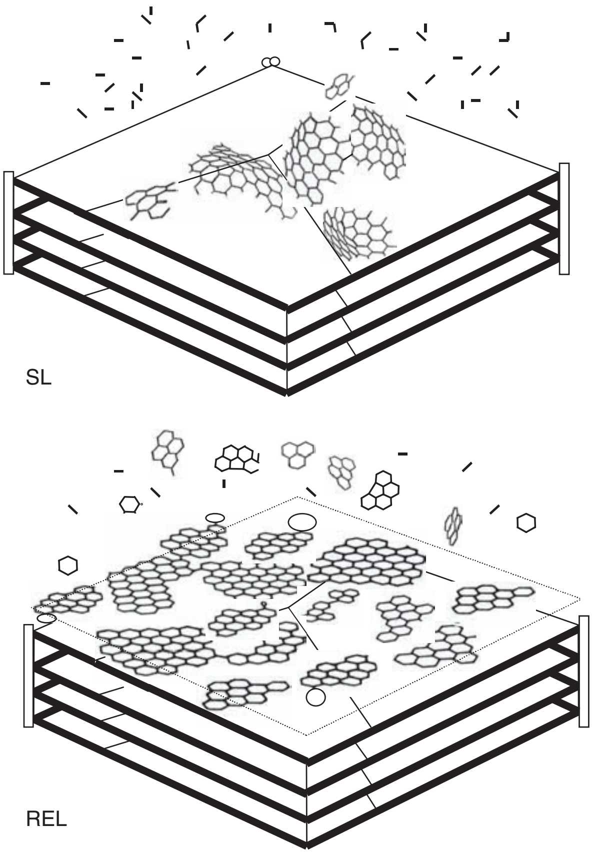

Figure 8.13 Deposition model diagram of smooth (SL) and rough laminar pyrocarbon (RL) on highly oriented pyrographite (HOPG). SL: chemisorption of small species on growing layer edges, dehydrogenation/reaction (according to Bourrat, 2000). REL: molecular condensation on surface and reaction by an edge to edge mechanism.

The *crystallographic density* can be drawn from the lattice parameters: $a = \text{cte} = 245.6\,\text{pm}$ and d_{002}-spacing increases as follows:

- graphite value: $d_{002} = 335.4\,\text{pm}$ $d_{\text{cry}} = 2.267$
- heat-treated dense pyrocarbon: $d_{002} = 342\,\text{pm}$ $d_{\text{cry}} = 2.23$
- as-processed dense pyrocarbon: $d_{002} = 344\,\text{pm}$ $d_{\text{cry}} = 2.21$

This calculation does not take into account hydrogen and boundaries in-between the carbon graphene piles in the as-processed pyrocarbon. Anyway, the very high values obtained following this calculation readily show that the paracrystalline structure of pyrocabon is not easily modeled.

The *helium density* based on the displacement of this very small molecule (helium pycnometry) is a very popular technique. Helium density is often considered as the experimental approach of the crystallographic density: nanoporosity is non accessible by helium. Thus it is used as a specification to characterize the various textures. In the case of CVI textures rough laminar with the highest anisotropy is measured: $2.0 < d < 2.2$ (as-processed). Smooth laminar has a much lower density: $1.8 < d < 2.0$. Then isotropic textures exhibit values as low as 1.6. The methanol or butanol displacement density is used as a standard in Japan (R 7212).

Water density is a very convenient technique for large pieces. It is also known as the triple weighing technique. (i) First the composite is weighed dry, the mass M_0 is obtained; (ii) an Archimede weighing is then performed in the water providing M_1; and (iii) a third weighing of the sample just out of water (no more pouring water) gives M_2. It can be drawn from these three values the so-called water density, d, and the open porosity, $V\mathrm{p}$, of the pyrocarbon as follows:

$$d = M_0/(M_0 - M_1)$$
$$V\mathrm{p} = (M_2 - M_0)/(M_2 + M_1)$$

Also are used techniques as *sink-float density*. Such techniques involve a mixture of dense liquors as bromoform and methanol (Lieberman and Pierson, 1974). Density is determined by suspending ground sample in the density gradient columns.

5.2 Anisotropy as measured by X-ray diffraction

The very high preferred orientation of pyrocarbon is the attractive feature of this form of carbon. The quantification of the anisotropy was recently discussed (Bourrat *et al.*, 2000). Graphene layers tend to align parallel to the surface deposition. Pyrocarbons grow with the hexagonal form of carbon. Unlike graphite, its structure is limited to two dimensions, i.e. the hexagonal lattice of the aromatic layer (graphene). The layers are stacked one on the other with a rotational disorder (no 3D-graphitic order: turbostratic structure (Warren, 1941)). In this stacking, a chance parallel layer occurs giving rise to a local coherent scattering even if not perfectly parallel. The diffracted spots observed in the reciprocal space are not the 00.l graphite spots, but the so-called 00l turbostratic interlayer interference (strongest peak: 002). Coherent lengths parallel and perpendicular to the basal plane (La and Lc, respectively) are more or less extended, depending on the perfection of the layers.

The different pyrocarbons can be characterized by the size distribution of the carbon layers "L_2" (as defined in the schematic of Fig. 8.14) and the anisotropy of the texture. When they are highly anisotropic, all the layers are parallel to the anisotropy plane. As the anisotropy decreases, more and more layers are misaligned with respect to the anisotropy plane. In the reciprocal space, this gives rise to the polar distribution of the 002 spots. A schematic representation of the preferred orientation is represented in Fig. 8.15 following Pappis and Blum (1961): this is a pole figure. The specimen, e.g. a film of pyrocarbon deposited on a flat surface, is placed in the center of a sphere and the orientation of each coherent domain is indicated by a normal to its basal planes. Wherever this normal penetrates the top surface of the sphere a point is marked. In a case of pyrocarbon, the points gather with a density maximum around the point marking the deposit plane. A continuous decrease is observed as the equator region is approached. Pyrocarbon can thus be described exactly as a polycrystalline material which exhibits preferred orientation.

The easiest experimental conditions require a thick pyrocarbon deposit and a transmission setup. As proposed by Guentert (1962), Tombrel and Rappeneau (1965), or Hirai and Yajima (1967), a small cylinder is drilled across the deposit with its axis parallel to the deposit plane

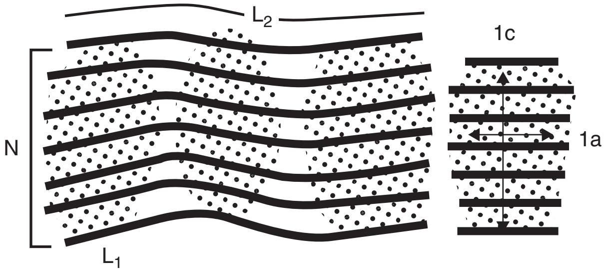

Figure 8.14 Model of turbostratic piles of carbon layers (according to Bourrat *et al.*, 2000).

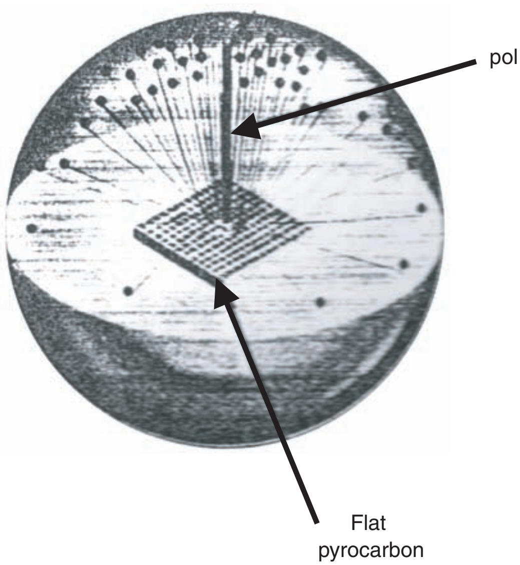

Figure 8.15 Pole figure of pyrocarbon film deposited on a flat support (after Pappis and Blum, 1961).

as shown in Fig. 8.16. Few tenth of millimeters in diameter. This small cylinder is placed on the specimen holder at the center of a regular diffractometer. It is mobile above the θ–2θ axis of the diffractometer with an angle referred to ϕ. At the starting point, ϕ is adjusted in order to place the anisotropy plane approximately in the plane of the tube and detector. A first step consists to fix θ and 2θ positions (tube and detector, respectively), for the maximum intensity of the 002 peak (around 2θ B 25–26° for a Cu anticathode). Then the intensity I(ϕ) is recorded step by step for the different ϕ angles of the sample on its axis. ϕ is equal to 0° for the maximum of intensity. The result is a bell-like curve as represented on Fig. 8.17. Tombrel and Rappeneau compare four different pyrocarbons with lower and lower preferred orientation as the HWHH increases. All the processing computers contain different fitting functions to get the accurate parameter needed to compare the different pole distributions.

When the thickness of the deposit does not allow the sampling of a cylinder, a Euler attachment is required to record the pole figure directly from the flat film. In this case an extra rotation mobility of sample known as the polar χ angle, allows the sample to rotate

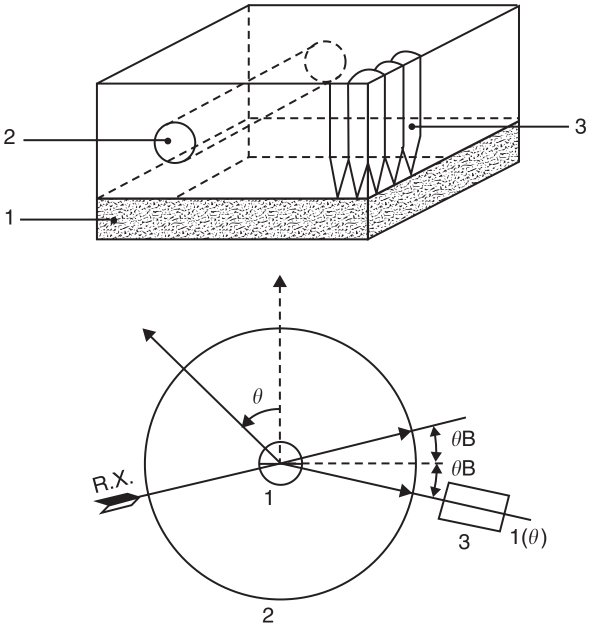

Figure 8.16 Experimental set up in the case of thick deposit and transmission XRD device (after Tombrel and Rappeneau, 1965).

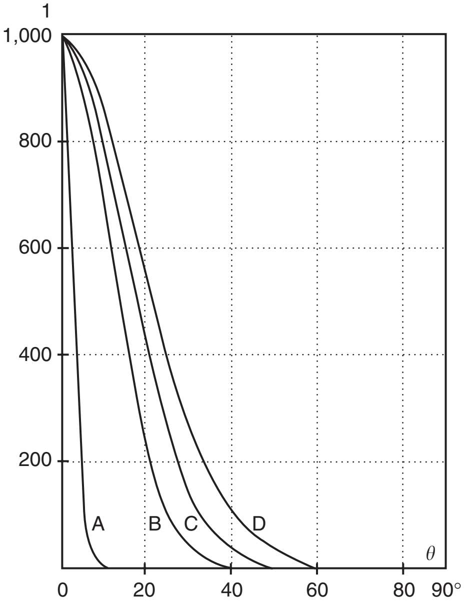

Figure 8.17 XRD anisotropy curves normalized for: A: Regular 2,100 °C pyrocarbon with 0.5 KPa of methane, annealed under compression (0.5 GPa) 1 h at 2,800 °C ($\Delta\theta = \pm 6°$); B: Boron-doped pyrocarbon (0.8 %) deposited at 2,100 °C ($\Delta\theta = \pm 13°$); C: Regular pyrocarbon deposited at 2,100 °C with 0.5 KPa of methane ($\Delta\theta = \pm 16°$); D: Super Temp Corp. sample deposited at 2,100 °C from 0.5 KPa of methane ($\Delta\theta = \pm 23°$) (after Tombrel and Rappeneau, 1965).

above the eucentric point as represented in Fig. 8.18. This case is a reflection setup known as the Schulz setup which allow to record pole figure up to $\chi < 65°$ without too much aberrations. This technique allows a direct recording of the pole figure in reflection mode.

5.3 Optical anisotropy (Ae)

This optical method is based on the measurement of the apparent reflectance ratio of the pyrocarbon (Bourrat *et al.*, 2000). (The best way is to use a photo-multiplier (PM) (Rouzaud and Oberlin, 1983).) When it is not possible method involves the rotation of the analyzer of a polarization device. It has the advantage to be easily performed. Meanwhile, it requires a deposit at least 2 μm-thick and an optical polishing of high quality. This measurement is only semi-quantitative but it enables to separate the different pyrocarbons of a same family on the basis of anisotropy.

This measure is obtained on polished sections perpendicular to the deposit plane. The simplest technique requires a reflected-light microscope equipped for polarization with a rotative analyzer. An example of the measurement is provided on Fig. 8.19. A fiber with a thick coating is selected. Under cross-polars a Maltese-cross can be observed. When the analyzer is rotated (special attachment) the branches of the Maltese-cross fuse together on the bisector (arrow in Fig. 8.19). The first quadrant gets completely dark and then becomes bright again. At the position of complete darkness the extinction angle "Ae" can be read directly on the vernier micrometer of the analyzer. Ae is giving a good approximation of the reflectance anisotropy ratio R_o/R_e, by the relation $R_o/R_e = tg^2\ (45 + Ae)$. The intrinsic value are probably not exactly that of graphite: different electronic structure, heteroelement as H abundance, etc. Also because of the subjective assessment of compensation and discrepancies between polarizers it is best to consider the Ae value directly: the scale generally ranges from $0° < Ae < 4°$ for I, $12° < Ae < 18°$ for SL and $Ae > 18°$ for rough and regenerated laminar pyrocarbons. The highest values obtained are in the range of 22°–24° (depending on the microscope).

5.4 Optical retardation method

A second optical approach can be derived from the classical measurement of birefringence in the field of mineralogy. The cross section (highest birefringence) is observed under cross polars. Because of the strong birefringence of carbon the two reflected beams impinging the analyzer (ordinary and extraordinary beam) produce an interference color. This color is a grey yellowish of the first order. For reflection, retardation has not the same origin as in transmission: phase shift is low while the interference colors indicate higher values (by using the two-beam approximation given by Michel Levy chart). It can be assumed that the anisotropy is responsible of these color changes. The experimental retardation values that can be measured by different means are effectively changing with the anisotropy: RL is observed with more than 250 nm whereas SL gives values about 150–180 nm and DL is much less (isotrope is 50–80 nm). This technique is still under development.

5.5 Anisotropy as measured by electron diffraction (OA)

The electron diffraction technique is irreplaceable to analyze pyrocarbon infiltrated in preforms or very thin coatings. Coupled to an image analysis software, it gives the following structure parameters: (i) the orientation angle, OA, of the scattering domains which is a measurement of the "geometric" anisotropy; (ii) the interlayer spacing d_{002} which is a basic measurement of the

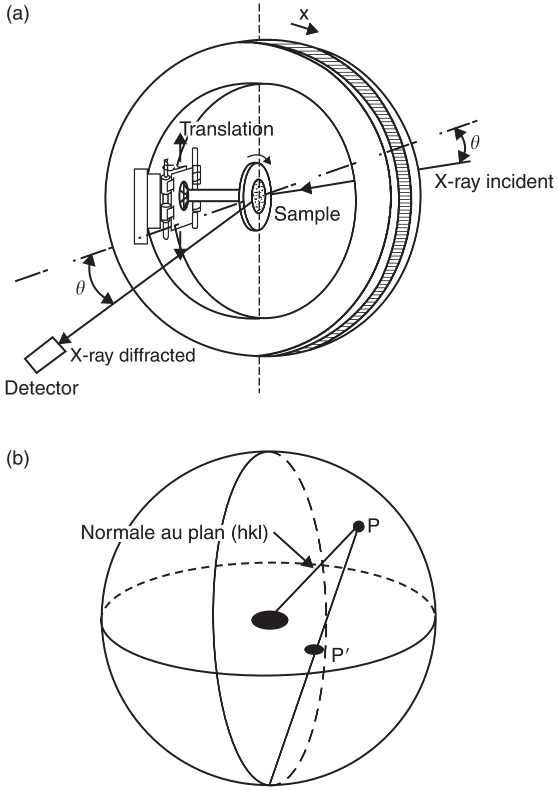

Figure 8.18 Schulz setup for an XRD Euler attachment: (a) for recording the pole figure on thin film (flat support). The pole figure is obtained following the projection shown in (b).

short distance ordering of the carbon turbostratic structure. Other pieces of information can be extracted from the diffraction pattern; (iii) L_c, the turbostratic pile thickness; (iv) L_a the coherent extent of the carbon layer; or (v) P_1 the ratio of graphite stacking in the turbostratic pile.

Orientation angle is determined by selected area diffraction (SAD). The measurement of the azimuth opening of the 002 arcs along the Debye–Scherrer ring is proposed as the OA. The volume which can be analyzed this way is as low as the selected area used to perform the diffraction pattern (100 nm in diameter and few hundred nms thick). The counterpart is the difficulty to get the sample thinned to electron transparency. First the software scan the intensity across the diagram (Fig. 8.20b) passing through the center. The center of the diagram is previously found automatically, provided that the central spot is systematically saturated by the previous intensity correction operated on the image. The program finds out the two 002 maxima, so the "Debye–Scherrer" ring can be drawn, superimposed on the pattern. If the operator agrees with the result, then the intensity is extracted versus the azimuth angle (Fig. 8.20c). The program fits these peaks to two Gaussian curves and the anisotropy OA is given as the mean value of the two widths at half height. The mean full-width at half-height is call "OA" the orientation angle. Physically, it represents the miss-orientation, the disorder of layers along the anisotropy plane (see Bourrat *et al.*, 2000 for more details).

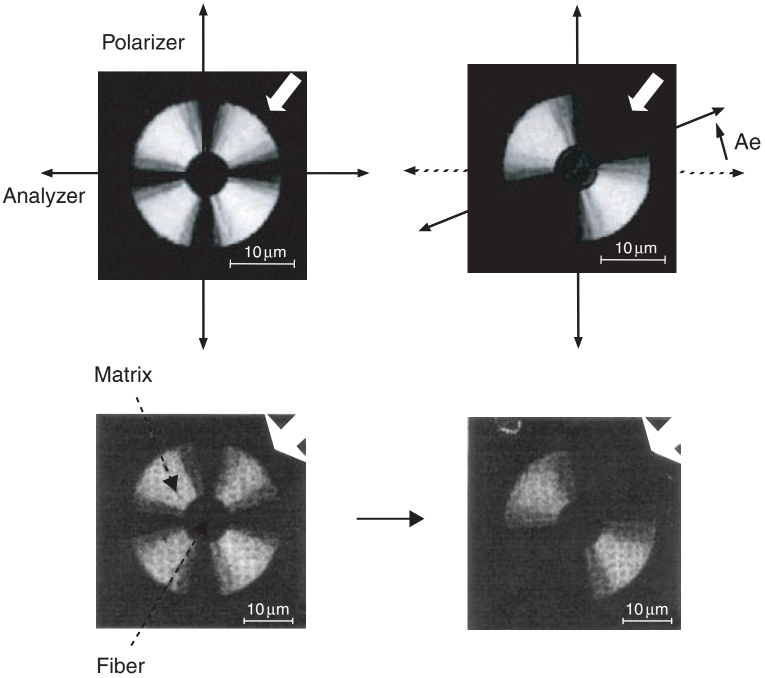

Figure 8.19 Measurement of the extinction angle, Ae, in a pyrocarbon matrix with reflected polarized light (example of a coated fibre) (after Bourrat *et al.*, 2000).

Their exists a linear relationship between OA and Ae for most of the laminar pyrocarbons analyzed by these two techniques as shown in Fig. 8.21. The value of the interlayer spacing (d_{002}) can be obtained as well, after a previous standardization with a graphite pattern, in similar conditions (Fig. 8.20d). Thinning the sample relax the internal stress and thus artifacts are numerous with this d_{002} value.

6 Conclusions

- Structural characterization of the pyrocarbon deposit is an essential requirement before discussing all other data as kinetics, or growth mechanisms or even properties. An abundant literature exists which presents no interest because the pyrocarbon structure was not previously defined: the two main properties are *density* and *anisotropy*.
- Survey of structural studies of pyrocarbons, whatever the process and among the whole range of temperature (800–2,500 °C) show that the different growth mechanisms are not so numerous, even if many different microstructures are existing.
- These few mechanisms are controlled by the concentration in gas phase of key species. For that reason, residence time “*t*” and more generally the so-called maturation of the gas phase is an important parameter. As far as we know, the key species are: small radicals, PAH molecules and solid particles nucleated (and grown) in the gas phase.

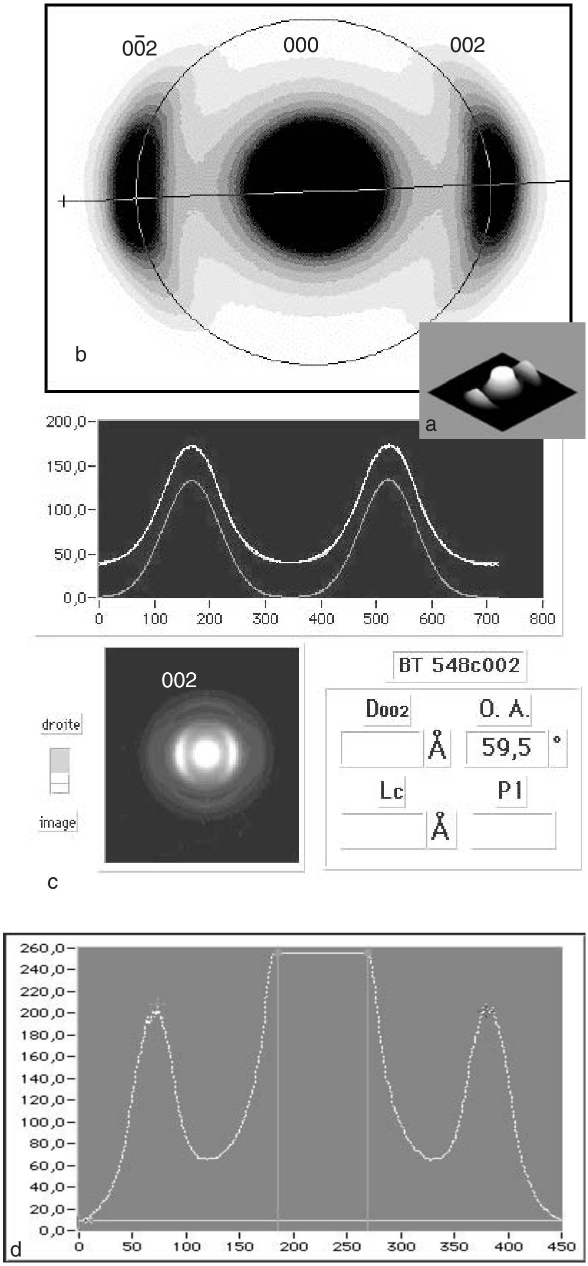

Figure 8.20 Electron diffraction: OA measurement. (a) Experimental pattern; (b) processing of the image analysis; (c) Azimuth plot (white) to be analyzed and Gaussian fit (down) of the experimental intensity. OA is the mean width at half height of the two Gaussian curves; (d) the optional measure of the d_{002}-spacing (after Bourrat *et al.*, 2000).

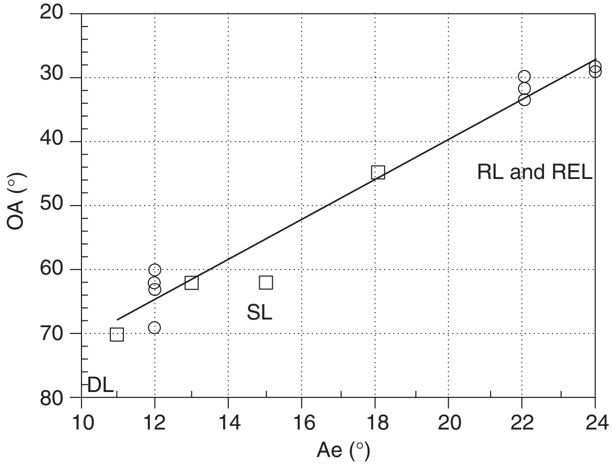

Figure 8.21 Plot of Ae (optical technique) versus OA (electron diffraction technique) (squares after Bourrat *et al*., 2000; open circles after Féron, 1998).

- At low temperature for the isobaric/isothermal CVI processing of aliphatic hydrocarbons (800–1,400 °C) a competition between two mechanisms controls the transition between the two main textures developed for carbon/carbon composites: (i) the direct growth from small species (lateral growth mechanism); or (ii) the molecular condensation and reaction of PAH. If gas phase maturation is poor, pyrocarbon is a smooth laminar or progressively dark laminar (and finally isotropic). Anisotropy is progressively lost because the over-growth of layers (lateral growth mechanism) concentrates pentagons (buckling of layers). On contrary; if the gas phase maturation is higher, then laminar pyrocarbons can develop as small hydrogenated flat graphene layers (REL):

  I ↔ DL and SL ↔ REL

  Gas phase depletion for very high "*t*," leads to the smooth laminar again in the case where the surface/volume ratio is high for a given residence time.
- At high temperature in the CVD domain (1,400–2,000 °C) the competition occurs between particle growth in the gas phase and direct deposition. This range is still in use by means of fluidized-bed for pyrocarbon (medical biomaterials). If temperature and/or saturation is high enough, maturation is prompt and gas-phase nucleation of particles occurs. Competition arises between the direct deposition of solid particles and PAH: a regeneration of cones is produced by particles with the granular structure. In both processes, fluidized-bed and static CVD, a strong drop in density is observed as the amount of particles increases. In fluidized-bed the structure turns to sooty-isotropic. This transition is existing in CVI (Loll *et al*., 1977). The low density is related to the development of a fine porosity of the pyrocarbon directly deposited in competition with the particles (Kaae, 1985). This sooty-I is still gas-tight but not graphitizable.
- At very high temperature (2,000–2,500 °C) a laminar pyrocarbon characterized by extended layers is observed with a regenerative texture. This is probably a self-regeneration related to the very high anisotropy and high density.

References

Bacon, G. E. (1956). J. Appl. Chem., **6**, 477–481.

Blackman, L. C. F., Saunders, G., and Ubbelohde, A. R. (1961). *Proc. Royal Soc. G.B.*, **264A**, 1316, 19–40.

Beaugrand, S. (2000). "Etude du procédé de densification rapide par caléfaction pour l'élaboration de composites carbone/carbone," Univ. Orléans (France).

Bokros, J. C. (1965). "Variation in crystallinity of carbons deposited in a fluidized bed," Carbon, **3**, 201–211.

Bokros, J. C. (1969). "Deposition, structure and properties of pyrolytic carbon," in *Chemistry and Physics of Carbon*, Vol. 5, p. 1, P. L. Walker, Jr ed., Marcel Dekker New York.

Bomar, E. S., Gray, R. J., and Eatherly, W. P. (19xx) "A technique for measuring preferred orientation in pyrolytic carbon coating using plane-polarized light," Oak Ridge Nat. Lab. internal Report, 885.

Bourrat, X. (2000). "Structure of carbon and carbon artefacts," in *Sciences of Carbon Materials* H. Marsh and F. Rodriguez-Reinosso, eds, ch. 1, Univ. Alicantes Publisher.

Bourrat, X., Trouvat, B., Limousin, G., Vignoles, G. L., and Doux, F. (2000). J. Mater. Res., **15**, 92–101.

Bourrat, X., Lavenac, J., Langlais, F., and Naslain, R. (2001). "The role of pentagons in the structure of laminar pyrocarbons," Carbon, **39**, 2376–2380.

Bourrat, X., Fillion, A., Naslain, R., Chollon, G., and Brendle, H. (2002). "Regenerative laminar hydrocarbon," Carbon, **40**, 2931–2945.

Brown, A. R. G., Clark, D., and Eastabrock, J. N. (1959). *J. Less Common Metals*, **1**, 94.

Brown, H. R. G. and Watt, W. (1957). Conf. on Industrial Carbon and Graphite, London September 24–26, 1957, Soc. of Chemical Industry, publisher (1958), 86–100.

Bruneton, E., Narcy, B., and Oberlin, A. (1997). "Carbon–carbon composites prepared by rapid densification process II: structure and texture characterizations," Carbon, **35**, 1599–1611.

Buckley, J. D. (1993). "Carbon/carbon materials and composites using CVD and CVI processing (an overview)," Proceed. of 9th Inter. Conf. on Composite Mater., **3**, 675–682.

Coffin, J. R (1964). "Structure–properties relations for pyrolytic graphite," J. Am. Ceram. Soc., **47** (10), 473–478.

David, P., Narcy, B., Ravel, Fr., and Houdayer, M. (1995). "Manufacturing of ceramic composites by rapid densification," in Proc. 2nd French–US Meeting for Technical Interchange on Carbon/Carbon Composites and Related High Temperature Materials, La Jolla, CA, March 28–30, 1995.

Diefendorf, R. J. (1960). "The deposition of pyrolytic graphite," J. Chim. Phys., **57**, 815–821.

Diefendorf, R. J. (1970). "Deposition of pyrolytic carbons," in *Reactivity of Solids*, J. W. Mitchell, R. C. De Vries, R. W. Roberts, and P. Cannon, eds, Wiley Publisher, 461–475.

Doux, F. (1994). "La microscopie électronique en transmission au service des matériaux composites," Analusis Magazine, **22**, 1, 31–34.

Dupel, P., Pailler, R., Bourrat, X., and Naslain, R. (1994). "Pulse-chemical vapour deposition and infiltration of pyrocarbon in model pores with rectangular cross-sections: Part 2 – Study of the infiltration," J. Mater. Sci., **29**, 1056–1066.

Dupel, P., Bourrat, X., and Pailler, R. (1995). "Structure of pyrocarbon infiltrated by pulse CVI," Carbon, **33**(9), 1193–1204.

Féron, O. (1998). "CVD/CVI du pyrocarbon – Analyse *in-situ* de la phase gazeuse – Etude cinétique et structurale," Thèse No.1867, Université Bordeaux 1.

Féron, O., Langlais, F., Naslain, R., and Thébault, J. (1999). "On kinetics and microstructural transitions in the CVD of pyrocarbon from propane," Carbon, **37**, 1343–1353.

Fillion, A. (2000). "Matériaux céramiques et traitements de surface," Thèse No. 2168 Univ. Bordeaux 1 (France).

Ford, L. H. and Bilsby, C. F. (1976). "Porosity related to structure for low temperature propylene pyrocarbons," J. of Nuclear Materials, **60**, 79–88.

Fujimoto, H., Tokumitsu, K., Mabuchi, A., Kasuh, T., and Shiraishi, M. (1994). "New structural parameters for carbon: comprehensive crystallization index and cavity index," Carbon, **32** (7), 1249–1252.

Furuta, T., Sanada, Y., and Honda, H. (1969). "Core structure of phenol–formaldehyde resin carbons," Carbon, **7**, 510.

Golecki, I., Morris, R. C., Naraimhan, D., and Clements, N. (1995). "Rapid densification of carbon-carbon by thermal-gradient chemical vapor infiltration," in Proc. of 19th Annual Conf. on Composites, Advanced Ceramics, Materials and Structures-A (Cocoa Beach), 315–322, Am. Ceram. Soc. ed.

Goma, J. and Oberlin, A. (1985). "Microtexture and structure of high temperature massive pyrocarbons prepared on graphite substrates," Carbon, **23** (1), 85–90.

Goma, J. and Oberlin, A. (1986). "Characterization of low temperature pyrocarbons obtained by densification of porous substrates," Carbon, **24** (2), 135–142.

Granoff, B., Pierson, H. O., and Schuster, D. M. (1973). "The effect of chemical-vapor-deposition conditions of carbon on the properties of carbon–carbon composites," Carbon, **11**, 177–187.

Grisdale, R. O. (1953). "The formation of black carbon," J. of Appl. Phys., **24** (9), 1082–1091.

Guentert, O. J. (1962). J. Chem. Phys., 37, 844–891.

Hirai and Yajima (1967). "Structural Features of Pyrolytic Graphite," J. of Mat. Science, **2**, 18–27.

Jacques, S., Guette, A., Langlais, F., and Bourrat, X. (1997). J. of Mat. Science, **32**, 2969–2975.

Kaae, J. L., Gulden, T. D., and Liang, S. (1972). "Transmission electron microscopy of pyrolytic carbons deposited in a bed of fluidized particles," Carbon, **10**, 701–709.

Kaae, J. L. (1975). "Microstructures of isotropic pyrolytic carbons," Carbon, **13**, 52–62.

Kaae, J. L. (1985). "The mechanism of deposition of pyrolytic carbons," Carbon, **23**, 665–673.

Kotlensky, W. V., Bauer, D. W., Warren, J. W., Smith, W. H., Gray, E., and Campbell, J. (1971). In Tenth Biennial Conference on Carbon, 80.

Lamicq, P. J. (1984). "Propriétés et utilisation des composites carbone-carbone," J. Chim. Phys., 81, 11/12.

Lavenac, J. (2000). "CVD/CVI de pyrocarbones laminaires à partir du propane. Processus chimiques homogènes et hétérogènes, nanostructure," Thèse Université Bordeaux 1, No. 0: 2274.

Lavenac, J., Langlais, F., Féron, O., and Naslain, R. (2001). "Microstructure of the pyrocarbon matrix in carbon/carbon composites," Composite Science and Technology, **61**, 339–345.

Le Carbone Lorraine (1975). Fiche technique , PSP, **11** (2), F, Ed. 4–75.

Lieberman, M. L. and Pierson, H. O. (1974). "Effect of gas phase conditions on resultant matrix pyrocarbons," Carbon, **12**, 233–241.

Loll, P., Delhaès, P., Pacault, A., and Pierre, A. (1977). "Diagramme d'existence et propriétés de composites carbone-carbone," Carbon, **15**, 383–390.

Mar'yasin, I. L. and Tesner, P. A. (1961). *Doklady Akad. Nauk SSSR*, **140**, 5, 1121–24.

Pierson, H. O. and Lieberman, M. L. (1975). "The chemical vapor deposition of carbon on carbon fibers," Carbon, **13**, 159–166.

Oberlin, A. (1979). Carbon, **17**, 77.

Pappis, J. and Blum, S. L. (1961). "Properties of Pyrolytic Graphite," J. of Am. Ceram. Soc., **44**, 12, 592–597.

Parker, W. G. and Wolfhard, H. G. (1950). J. Chem. Soc., 2038.

Pelissier, J. and Lombard, L. (1975). "Transmission electron microscopy of isotropic pyrocarbon deposited on spherical particles for high temperature reactor," Carbon, **13**, 205–210.

Rovilain, D. (1999) "Procédé de densification rapide et caractérisation de composites carbone/carbone," Thèse Univ. Bordeaux 1, No. 0: 2067 (France).

Rouzaud, J. N., and Oberlin, A. (1983). "Carbon films: structure and microtexture (optical and electron microscopy, Raman spectroscopy)," Thin Solids Films 105, 75PR.

Stokes, C. A. (1951). J. Inst. Fuel, **24**, 90.

Sweitzer, C. N. and Heller, G. L. (1956). Rubber World, **134**, 855.

Tessner, P. A. (1984). “Kinetics of pyrolytic carbon formation,” in *Chemistry and Physics of Carbon*, P.A. Thrower ed., Marcel Dekker, New York, Vol. 19, 65–161.
Thomas, A. (1962). Combustible Flame, **6**, 46.
Tombrel, F. and Rappeneau, J. (1965). “Préparation et structure des pyrocarbones,” ch. XXV in *Les Carbones*, A. Pacault ed., Dunod editeur Paris, 783–836.
Warren, B. E. (1941). “X-ray diffraction in random layer lattices,” Phys. Rev., **59**, 693–699.

9

ROLE OF CHEMISTRY IN ADVANCED CARBON-BASED COMPOSITES

C. Vix-Guterl and P. Ehrburger

1 Introduction: principle of composite materials

Composites are heterogeneous materials and their properties will depend on several factors including the intrinsic characteristics of the fiber and the matrix, the interfacial bonding between both constituents, the relative amount of fibers and their mode of arrangement in the matrix (unidirectional or multidirectional reinforcement) (Fitzer, 1985). A conventional composite material is based on a matrix with rather low mechanical properties, for instance, organic resins, light metals or alloys, ceramics associated to filaments with high strength and stiffness (Hull, 1981). The strain to failure of matrix and fiber is also quite different. The fiber has a small deformation to ultimate failure and is brittle. The matrix is generally a ductile material, i.e. it undergoes a substantial deformation under load before failure. In some cases, the matrix of the composite may also be brittle (carbon or ceramic-based matrix) and the reinforcing effect in this type of composite will be discussed later on. The potential mechanical performance of a conventional composite relies mainly on stiffness and strength of the fibers. The role of the reinforcing filaments in the composite can however be fulfilled only if sufficient stress transfer from fiber to matrix and vice versa can take place by a proper bonding between the two constituents (Bunsell, 1988). This means that physical and to some extent chemical compatibility is required between fiber and matrix. Therefore, the structure and properties of the fiber–matrix interface play a major role in the mechanical and physical properties of composite materials.

1.1 Strength of composite

Consider an unidirectional composite in which all fibers are aligned in one direction and submitted to an uniaxial tension, the stress–strain curve of fiber and matrix, i.e. the load, σ, applied to the considered material as a function of its deformation, ε, will be quite different.

In the case of polymer-based composites, fibers display elastic deformation until failure whereas the polymer undergoes plastic deformation after a given strain (Fig. 9.1). Ultimate deformation of fiber determines generally the point of failure of the composite since deformation of polymer is generally larger than for fiber, $\varepsilon_m > \varepsilon_f$ (Fig. 9.1).

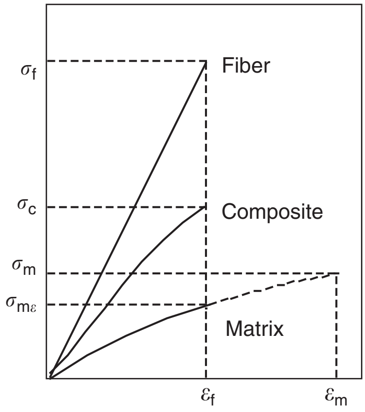

Figure 9.1 Stress–strain curve of fiber, matrix and composite subjected to a tensile load.

In this case, the tensile strength of an ideal composite, σ_c, can be calculated knowing the fiber strength, σ_f, the strength of the matrix at ultimate fiber deformation, $\sigma_{m\varepsilon}$, and the volumic fraction of fiber, V_f, by using the rule of mixture

$$\sigma_c = \sigma_f V_f + \sigma_{m\varepsilon}(1 - V_f) \tag{1}$$

For a sufficiently small amount of fibers in the composite, the load supported by them is lower than the one applied to the matrix. Hence, the fibers are then acting as defects in the continuous polymer phase and the above equation is no longer valid. The tensile strength of such a composite will in fact decrease linearly from the ultimate tensile strength of matrix, σ_m, with V_f according to the equation:

$$\sigma_c = \sigma_m(1 - V_f) \tag{2}$$

Hence, the tensile strength of a composite decreases at first with the introduction of a small fraction of fiber in the matrix and the reinforcing effect will only be observed above a given amount of fiber as schematically shown in Fig. 9.2. The value, V_{crit}, below which the fibers does not reinforce the matrix is generally quite small ($\leq 2\%$) in the case of organic resins and far below usual values of V_f in composites (~30–60%).

The behaviour of an ideal composite subjected to a tension applied parallel to the fiber axis may be well predicted. So far, end effects of fiber on stress and strain distribution in the composite has not been considered. They may however play an important role in the fracture of short fiber composite or to already damaged fibers in composite. The deformation of the matrix in the vicinity of a short fiber due to a load parallel to the fiber is illustrated in Fig. 9.3a. The difference in deformation of the fiber and the polymer induces a shear stress τ. The shear stress is the highest at the fiber end and decreases gradually over a length l (Fig. 9.3b). Fiber with length smaller than $2l$, the critical length, will not contribute to the polymer reinforcement. For fibers with length above the critical one the stress applied to the

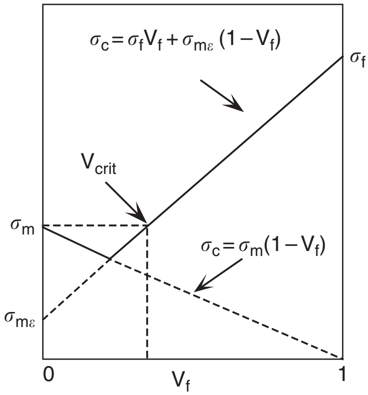

Figure 9.2 Variation in strength of a composite as a function of volumic fraction of fibers.

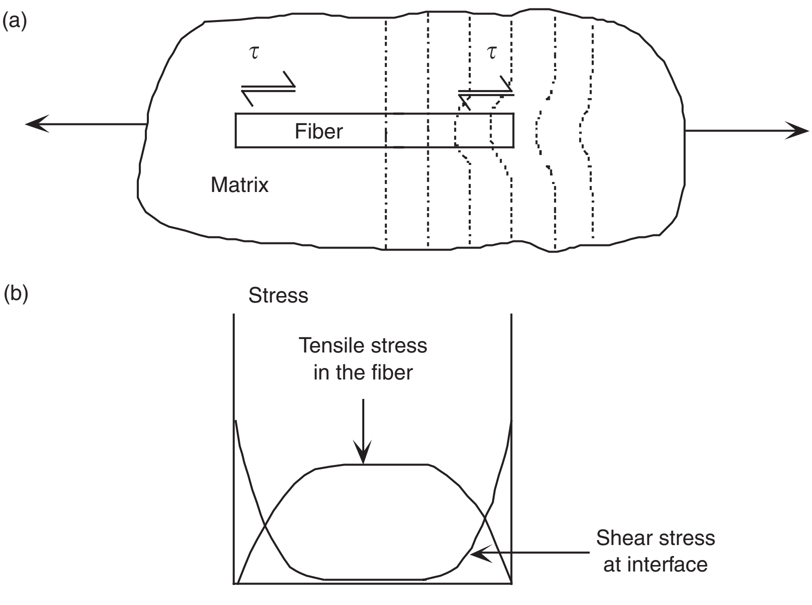

Figure 9.3 (a) Deformation in the vicinity of a fiber in a composite; (b) change of tensile stress in the fiber and of shear stress at the interface as a function of fiber length.

matrix will be transferred to the fiber which will then carry the load until its cohesive failure. In the case of a weak interfacial bonding the load transfer will be less efficient. Moreover, the large shear gradient at fiber ends contributes also to early failure of the composite by shear debonding at the interface. Hence the interfacial bond is a key factor in the achievement of advanced composites.

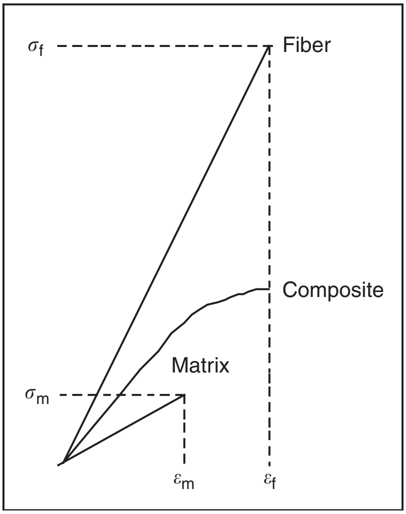

Figure 9.4 Stress–strain curve of composite with brittle matrix.

In the case of ceramic-based composites, a reverse situation is observed as shown in Fig. 9.4. The deformation to failure of the matrix is smaller than for the fiber $\varepsilon_f > \varepsilon_m$ and a reinforcing effect of the fibers is observed. The composite displays however a non-elastic behaviour at high strain due to progressive cracking of the matrix and gradual debonding at the fiber–matrix interface. Hence it is possible to improve a ‘brittle material’, for example a carbon matrix, with fibers since its stiffness and its deformation to failure are increased. The toughening effect of carbon fibers is also found for other types of ceramic matrix, namely refractory carbides and nitrides. There are several mechanisms involved in the improvement of the toughness of ceramics by fibers: matrix microcracking at sub-critical level, load transfer to the fiber, microcrack deflection by fiber and fiber pull-out (Cooper and Sillwood, 1972; Aveston and Kelly, 1973). A weak interfacial bonding is required for toughening a brittle matrix with fibers; it permits fiber–matrix debonding and sliding. A non-linear stress–strain curve results and final failure occurs by fiber pull-out. Toughness is achieved by a debond sliding mechanism.

1.2 Interface in composite

The mechanical properties of a composite subjected to flexural and/or shear stress are generally weaker than under tensile load. Two main reasons can be put forward for explaining this situation:

(i) in the direction perpendicular to the fiber axis the mechanical properties of the matrix control those of the composite;
(ii) the interfacial adhesion is too low.

Usually the value of intralaminar shear strength (ILSS) is considered to give an indication of the adhesion between fiber and matrix. The achieved degree of adhesion is measured by the intralaminar shear strength of the brittle material. There is no satisfactory method of measuring the strength of the bond between the fiber and the matrix but, nevertheless, it is very important to have some measure of the strength for the evaluation of composite properties and the development of well-designed interfaces. There are two main approaches for determining the bond strength in composites. The first one is based on single filament embedded in resin. These ‘single fiber composite’ samples are subjected to compressive or tensile load and the bond strength is determined using micromechanical models (Broutman, 1969). In the second approach unidirectional composites are tested in such a way that failure occurs in a shear mode parallel to the fibers or in a tensile mode perpendicular to the fibers. Both procedures which depend on fiber volume fraction have some severe theoretical limitations and do not provide a direct measurement of the bond strength. Among the technique that have been proposed and used to measure the intralaminar shear strength, the so-called ‘short beam test’ (three-point bending), ASTM D 2344 is by far the most popular because of the extreme simplicity in specimen preparation and testing. The load-deflection diagram corresponding to a short beam test provides qualitative indication on the mode of failure of the composite and in turn, on the interfacial adhesion. Two extreme situations can be found as shown in Fig. 9.5. The first one corresponds to a weak interfacial bond. In that case a pull-out of the fiber is generally observed when the composite is submitted to a shear stress. The charge transfer at the interface cannot take place and the composite delaminates at a very low level of shear stress (shear or progressive failure).

In the opposite situation, the interfacial bond is strong. The stress is then transferred from the matrix to the fiber until failure of the filaments. In that case, the composite breaks suddenly (tensile or catastrophic failure).

Intermediate situations between these two limiting cases can be observed, an adequate compromise being a high level of shear resistance associated to a non-catastrophic mode of failure. In that respect, the surface properties of the carbon fiber will play a determinant role for a given type of matrix.

Although the short beam test is not a pure shear test, it provides nevertheless an indication of the bond strength and it is therefore largely used for quality control of composites.

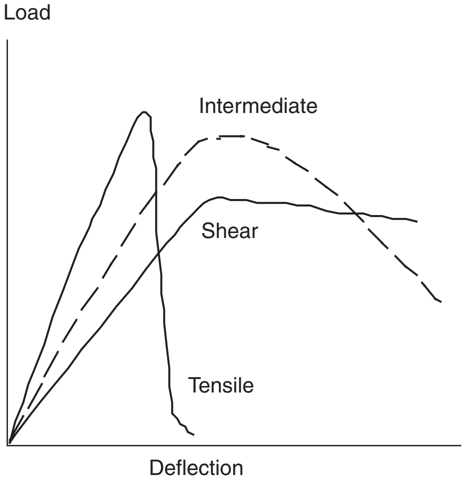

Figure 9.5 Different modes of failure of a composite.

An indirect measure of the strength of the interface bond can sometimes be obtained from the appearance of the fracture surface. In fact, observations by scanning electron micrographs of the composite after fracture may clearly illustrate the difference in mode of failure. Composites with untreated fibers undergo pull-out from the matrix before failure. In contrast, composites with extensively surface-treated fibers, i.e. with strong acidic surface groups, exhibit a smooth fracture which is characteristic of a brittle failure.

2 Surface properties of carbon fibers

Carbon fibers can be prepared from different precursors, polyacrylonitrile (PAN), pitch and rayonne. The highest temperature at which fibers have been subjected is an essential factor for their physical, mechanical and chemical properties. In particular, the surface properties of a carbon fiber will depend on its final heat treatment temperature and the description of their characteristics as a function of temperature would be a normal way to proceed. There are however two main disadvantages in such a presentation. The precise conditions of fiber preparation (temperature and time of heat treatment) are seldom indicated by the manufacturer and second, it is commonly accepted to distinguish between two main types of carbon fiber, high tensile strength and high modulus fiber. Generally speaking, high tensile strength (HT) fiber have not been heat-treated at a temperature higher than 1,200 °C. Ultimate tensile strength of these fibers is in the range of 3–7 GPa and their elastic modulus between 200 and 320 GPa. Their elongation to failure is about 1.3% or more. In contrast, the heat treatment temperature of high modulus (HM) fiber is generally above 2,000 °C. Their elastic modulus ranges from 350 to 900 GPa or more but their tensile strength is somewhat lower than for HT fiber. The elongation to failure of HM fiber is about 0.4–0.5%. Hence, in the following the distinction between HT and HM fiber will reflect difference in mechanical properties but primarily in heat treatment temperature of the fiber and consequently in surface properties.

2.1 Physical properties

Surface area of fiber is an important factor since it determines the extent of interfacial area in the composite. The geometric surface area, S_g, can be determined from the cross-section diameter according to the following relationship

$$S_g = 4\,\rho^{-1}\,D^{-1} \tag{3}$$

in which ρ is the fiber density and D the diameter of the cross section of the fibers considered as circular. The shape of the cross-section may however widely differ from a circular one depending on the spinning process of the precursor. Nevertheless, a fiber having a diameter equal to 10 μm and a mean density equal to 1.8 $\mathrm{g\,cm^{-3}}$, will have a geometric surface area equal to 0.2 $\mathrm{m^2\,g^{-1}}$, according to equation (3).

Measurements of specific surface area by krypton adsorption at 77 K lead to values ranging from a tenth to a few square meters per gram for untreated fibers. Hence, the rugosity factor of the carbon fibers, i.e. the ratio of the specific surface area to the geometric area lies between 1 and 50. The surface of untreated carbon fiber is generally considered as ‘smooth’. Upon heat treatment of carbon fibers at temperature over 2,000 °C, the surface tends to become very smooth due to the annealing of surface defects and closure of pores. In this case the rugosity factor is close to 1.

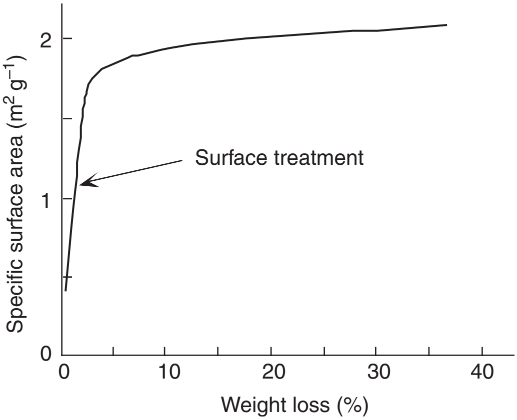

Figure 9.6 Change in specific surface area of HT carbon fiber during oxidation in air at 650 °C.

Like for other carbon materials, the surface area of carbon fibers increases when submitted to oxidative treatments. As an example the change in surface area of a HT fiber as a function of weight loss by oxidation in air at 650 °C is shown on Fig. 9.6 (Ehrburger, 1990). The sharp increase of specific surface area at the onset of oxidation is of interest in surface treatment of carbon fibers.

2.2 *Surface chemistry*

The reactivity of the surface is a major contributor to the strong bonding associated with carbon fibers. Carbon fibers like other types of carbon materials are essentially composed of elemental carbon associated with various elements mainly oxygen and hydrogen. In fact all types of carbon, particulate solids (cokes, chars or activated carbons, etc.), powders (carbon blacks), bulk materials (synthetic graphites, glassy carbons, pyrocarbons, etc.), fibers and filaments contain more than 90% by weight of the element carbon. Whatever their morphology and crystallinity, all these materials have in common the same basic lamellar structure which consists in polycondensed hexagonal rings. Their surface is also composed of aromatic lamellae of various sizes which constitute the basal planes. Different types of defects may be present on the surface: imperfect points like vacancies, dislocations, edges and steps in the outer basal planes. They form the so-called ‘prismatic planes’ or the ‘active surface area’ (ASA).

The surface chemistry of carbons has been extensively studied and two approaches have been considered. The first one is a ‘solid state chemistry’ approach developed on carbons with sufficient crystalline ordering. The second one emphasizes the organic character of the surface groups and applies more to the description of the surface properties of less ordered carbons.

Active surface area. In the ‘solid state chemistry’ approach the defects in the aromatic basal planes are considered as ‘active sites’ of the carbon surface. In fact the carbon atoms located at grain boundaries or edges of lamellae are more reactive than those in the basal planes. It leads to the concept of ASA and the procedure to determine it (Laine *et al.*, 1963). In its principle, the procedure consists to chemisorb oxygen on a clean carbon surface in such conditions that carbon gasification can be neglected (chemisorption temperature ~200–300 °C, oxygen partial pressure ~50–100 Pa). The amount of chemisorbed oxygen can be measured either directly or from the amount of CO and CO_2 which desorbs during a subsequent heating of the carbon in vacuum up to 950 °C. Knowing the area of an adsorption site ($0.083\,nm^2$) the area of the active sites is calculated (Hart *et al*., 1967). The values of ASA can be compared to the total surface area (TSA) of the carbon measured by physisorption of gases. Typical values of ASA and TSA are shown in Table 9.1.

For carbons annealed at high temperature, ASA is usually much smaller than TSA (Vulcan 3 graphitized at 2,800 °C, V3G). The value of ASA is less than 0.1% of TSA and reflects a very homogeneous surface essentially composed of basal planes. For less ordered materials like HT carbon fiber the ratio ASA/TSA is higher. It indicates that the surface has a larger amount of active sites and consequently is more heterogeneous. Annealing of surface defects takes place during the preparation of HM fiber and basal planes are more developed on its surface as compared to HT fiber. Chemical treatment like oxidation in air affects ASA and TSA. The density of active sites for HM and HT fibers increases after oxidation indicating a higher degree of surface defects and heterogeneity (Table 9.1). Therefore, ASA is related to the structural ordering of the carbon material which depends on the nature of the precursor and the thermal history of the carbon material.

Surface functional groups. The ‘organic surface groups’ approach deals with the nature and the functionality of the oxygen complexes chemisorbed on the edge carbon atoms (Boehm, 2000). As already mentioned edge carbon atoms chemisorb oxygen. Other gases like hydrogen, halogens or volatile sulphur compounds also interact with the edge carbon atoms. Study of the surface functionality of carbons consists mainly in the characterization of the chemical bond of the foreign elements with the carbon atoms, i.e. the nature of the surface groups or complexes. Oxygen is the most common foreign element present on carbon and emphasis will be given here to oxygen-containing functional groups. Depending on the nature of the precursor, nitrogen and sulphur may also be present in small amount in carbon fiber. For instance, PAN-based carbon fiber contains after carbonization a few percents of nitrogen which gives rise to pyridine-type or nitrile groups on the surface. These groups may contribute to some extent to the surface properties of carbon fiber by dipolar interactions.

Oxygen-containing surface groups. As early as 1863, Smith noticed that oxygen is chemically bound on a carbon heated in air (Smith, 1863). Since then, a great deal of attention has been given to the characterization of the chemical state of oxygen present on carbon surface. Carbons exposed to air at low temperature, typically below 400 °C, present

Table 9.1 Active surface area and total surface area of carbons

Carbon	*ASA* ($m^2\,g^{-1}$)	*TSA* ($m^2\,g^{-1}$)	*ASA/TSA* (%)
Heat-treated carbon black, V3G	<0.1	73	<0.15
V3G oxidized in air at 600 °C	4.2	97	4.3
HT fiber	0.05	0.45	11
HM fiber	0.02	0.50	4
HT fiber oxidized in air at 600 °C	0.43	1.95	22
HM fiber oxidized in air at 600 °C	0.34	1.50	13

an acidic character (L carbon in the older literature) whereas exposed to higher temperature and cooled in absence of oxygen, they adsorb acids after exposure to oxygen at room temperature so-called (H carbon). In 1957, Garten and Weiss proposed that oxygen is present on carbon surfaces as organic functional groups. The concept of 'organic surface groups' was further developed in the 1960s (Boehm *et al.*, 1964, 1966; Donnet, 1968). The existence of different types of functional groups was evidenced by means of organic chemical detection methods and titration techniques. More recently the study of surface groups has also been undertaken by spectroscopic methods, mainly Fourier Transform Infrared Spectroscopy (FTIR) (Zawadski, 1989) and X-ray photoelectron spectroscopy (XPS) (Kozlowski *et al.*, 1986). The various approaches used for the identification of the surface groups have been reviewed recently (Boehm, 1994). One distinguishes usually between two major types of surface oxides: the acidic and the basic surface groups.

Acidic surface groups. Several types of oxides having an acidic character have been clearly identified. The most important ones are the carboxyl and phenol groups. From these two structures, a few other groups may be build up at the carbon surface: anhydrides, lactones and lactols. Since the acidity constants of the various groups (carboxyls, phenols and lactones) differ by several order of magnitude, an estimate of their relative amount can be obtained by titration with bases of different strength (Boehm *et al.*, 1964).

Carbonyl groups are also present on the carbon surface as isolated or conjugated structures like quinones (Boehm, 1966; Donnet, 1968; Kinoshita and Bett, 1973; Raymond *et al.*, 1985). Ether-type functions which are stable even at high temperature are also currently postulated (Voll and Boehm, 1971; Hermann and Hüttinger, 1986).

Basic surface groups. Oxygenated functions with a basic character have been proposed in order to account for the adsorption of acids by carbons (Garten and Weiss, 1957; Voll and Boehm, 1971). When a carbon is heat-treated over 700 °C, it acquires a basic character after cooling in inert atmosphere and reexposure to oxygen at room temperature. In order to explain the uptake of acids, Garten and Weiss proposed a chromene structure, but γ-pyrone-like structures appear more plausible (Voll and Boehm, 1971). γ-pyrone consists in a quinone group conjugated with pyrane-type structure via aromatic carbon rings (Leon *et al.*, 1992).

Acidic and basic groups are simultaneously present on carbons. For instance, the amount of acidic and basic groups for an activated carbon is equal to 140 and 470 μeq g^{-1} respectively (Kuretzky and Boehm, 1992). Furthermore, it is generally observed that the amount of oxygen detected in functional groups is only a part – typically one third to two thirds – of the total oxygen content of carbon. This is probably due to the difficulty to determine accurately the respective amount of the various functional groups. Basic groups are more difficult to determine in particular for carbon fiber with low specific surface area but they contribute also to the interactions with polymer matrices.

Modification of surface functionality. There are two main processes for modifying the amount of acid and basic groups on carbons: (i) mild oxidation treatment; and (ii) thermal treatment.

Mild oxidation conditions of carbons can be obtained by treatment with oxidizing agents in aqueous medium and a very large variety of compounds can be used (nitric acid, sodium hypochlorite, permanganate, chromate or persulfate salts, hydrogen peroxide, ozone dissolved in water, etc.). Gas phase oxidation at temperature lower than 200 °C (ozone, nitric oxide, oxygen, for instance) gives similar results. Exposure of carbons for long periods of time to air at ambient temperature leads to a slow surface oxidation which may considerably alter their properties (ageing effect). It is generally observed that the number of acidic groups increases upon oxidation in liquid media (Ehrburger, 1990).

Thermal treatment of carbon in inert atmosphere followed by subsequent exposure to ambient air will lead to a decrease of the number and the strength of acidic groups as indicated by titration measurements (Dentzer, 1983). This is confirmed by the analysis by thermal programmed desorption (TPD) of the surface groups which are thermally unstable. For a TPD analysis, the sample is heated under vacuum at a constant linear heating rate and the evolved gases mainly CO_2 and CO are analyzed qualitatively and quantitatively by mass or infrared spectrometry. The evolution of CO_2 is generally attributed to the decomposition of carboxylic groups whereas the formation of CO would result from the break-down of carbonyl or phenol groups. A TPD diagram of a HM PAN-based carbon fiber oxidized in air is shown on Fig. 9.7. The desorption rate of CO_2 goes generally through a maximum at a temperature lower than the one of CO, reflecting a difference in thermal stability of various surface groups. It has been also shown that the oxidation in air leads to a significantly increase of the content in acidic groups whereas a slight decrease is found for the basic groups. When the oxidized sample is now heated for 1 h in N_2 at 500 °C, an increase in basic groups occurs with a concomitant decrease in acidic functions. This effect becomes even more pronounced in a reducing atmosphere. Hence the functionality of a carbon surface depends largely on the chemical and thermal treatment to which it was subjected. These effects are largely used for the surface treatment of carbon fibers.

Characterization of surface groups can also be carried out by XPS which is a well adapted technique for carbon fiber. The carbon peak, C1s, of a carbon surface includes several individual peaks of smaller intensity. These peaks correspond to various types of C—O or C—H bondings and are located at higher energy than the peak of graphite (284.4 eV), the energy shift lies between 1.6 eV (for hydroxyl groups) and 4.2 eV (for carboxyl groups). The analysis of an XPS signal is based on its careful decomposition into individual and well identified peaks. The decomposition of the oxygen peak, O1s, at 528–536 eV in individual peaks is generally less easier than for the C1s peak. XPS analysis of oxidized carbon fibers confirms that by moderate treatment mainly hydroxyl groups are formed and that after extensive oxidation carboxyls groups are also detected (Tagahaki and Ishitani, 1984).

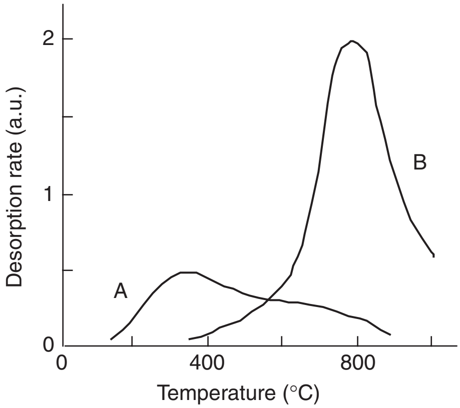

Figure 9.7 Gas evolution during TPD of an oxidized HM fiber: (A) CO_2, and (B) CO.

Table 9.2 XPS data of high tensile carbon fibers treated in various conditions (Tagahaki and Ishitani, 1984)

Fiber treatment	*O1s/C1s*
Control	0.16
Moderate oxidation	0.40
Extensive oxidation	0.66
Moderate oxidation and thermal treatment	0.15
Extensive oxidation and thermal treatment	0.16

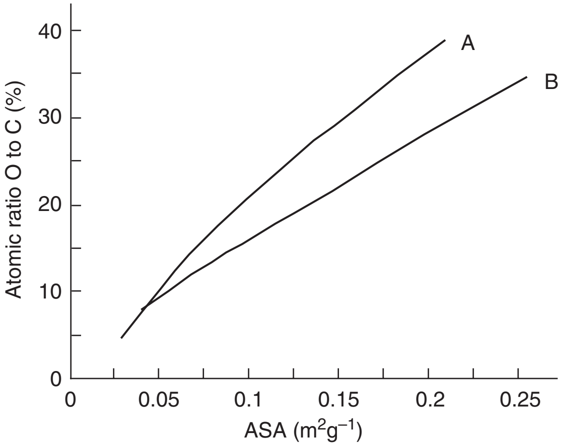

Figure 9.8 Change of oxygen content of a PAN-based carbon fiber as a function of its active surface area during anodic oxidation: (A) in alkaline electrolyte, and (B) in acidic electrolyte.

The amount of oxygenated groups present on carbon fibers may be estimated from the ratio of the intensity of the O1s to the C1s peak (Tagahaki and Ishitani, 1984). Depending on the extent of treatment, more or less oxygen is found on the carbon surface (Table 9.2). After heat treatment at 1,000 °C in vacuum, most of the surface groups formed during oxidation are removed. These few examples illustrate the manner by which oxidation and heat treatment in neutral atmosphere can modify the surface groups of carbon. Hence, a desired 'functionality' of carbon fiber can be achieved by combining both methods.

Chemical groups and active surface area. Since oxygenated groups are located on edge carbon atoms, a relationship between the amount of active sites and the number of surface groups may be expected in some cases. So far only a few attempts have been made in that sense. The chemisorption of oxygen at 100 °C gives essentially basic groups and this result is in agreement with the accepted formation mechanism of basic groups (Papirer *et al.*, 1991). There is however no direct relationship between the amount of acidic groups present on a carbon and the amount of oxygen which can be chemisorbed after cleaning the carbon surface. Correlation between the amount of oxygen present on a carbon surface and ASA has been found for carbon fibers anodically oxidized in acidic and alkaline medium respectively (Guilpain, 1988). ASA increases with the extent of surface treatment and so does the amount of oxygen on the surface as indicated by the atomic ratio O/C measured by XPS.

A different relationship is however found for each type of treatment (Fig. 9.8). Anodic oxidation in alkaline medium will generate acidic groups containing more oxygen than etching in acidic electrolyte (Guilpain, 1988). Hence ASA and surface groups are related but in a way which depends on the type of chemisorbed oxygen groups.

3 Surface treatment of carbon fibers

The presence of functional groups affects to a large extent the surface properties of carbon fibers and carbon materials in general. For instance, the hydrophilicity of a carbon black can be increased by the presence of acidic oxygen groups. Ionic exchange capacity, either cationic or anionic can be observed with carbons, depending on the prevailing surface functionality, acidic or basic. Surface charge and zeta potential of carbon particles in aqueous suspension is also conditioned by the nature of the surface groups.

The modification of the surface properties of carbon is generally based on chemical treatment, oxidation, reduction and pyrolysis. Systematic and comprehensive work has been undertaken for the surface treatment of carbon fibers in order to improve the intralaminar shear strength of their composites. There are two main techniques of carbon fiber treatment: (i) coating by means of chemical or physical vapour deposition; and (ii) modification of the surface properties of the fiber by chemical and physico-chemical methods.

Chemical deposition of pyrocarbon or silicon carbide (SiC) whiskers from the gas phase gives excellent results but the increase in intralaminar shear strength of the composite is mainly due to an enlargement of the fiber surface, i.e. the interfacial contact between fiber and matrix. These techniques are costly and difficult to handle and will not be considered further. The second type of treatment is based on oxidation or chemical etching of the carbon surface in order to increase its ‘affinity’ with the polymer. These methods are quite suitable for carbon fiber and are used industrially.

A comprehensive review of surface treatment, mainly oxidation, of carbon fiber was published as early as 1973 by McKee and Mimeault (1973). Electrochemical oxidation of carbon fiber and its effect on the interfacial bond has also been reviewed (Ehrburger and Donnet, 1985). Carbon fibers can be oxidized either by gases or by liquids and both types of process can be applied to them.

3.1 Gas phase oxidation

Essentially air or oxygen diluted in an inert gas is used. Since a prerequisite of fiber treatment is to maintain its mechanical strength, overoxidation of carbon filament must be carefully avoided and the oxidation time must be strictly controlled. This is particularly the case for HT fibers which are highly reactive toward oxygen. A threefold increase of ILSS of HM fiber reinforced-composite was reported upon prior oxidation of fiber in air (Clark *et al.*, 1974). The surface rugosity of the fiber is markedly enhanced as a result of oxidation. In that respect, metallic impurities present on the carbon fiber surface promote catalytic oxidation and may be used for enlargement of the surface rugosity. The catalytic activity must be however strictly controlled in order to avoid propagation of flaws in the inner part of the fiber.

3.2 Liquid phase oxidation

Almost all oxidation agents currently used for carbon and graphites have been applied to carbon fiber, especially nitric acid, sodium hypochlorite, potassium permanganate and potassium dichromate. The treatment of carbon filament by liquid reagents is interesting at a small scale. It is less attractive for pilot plant or industrial operations since it is a discontinuous process. Only two examples which are typical of the behaviour of HT and HM fiber will be considered.

Nitric acid treatment. HT and HM fibers react differently in boiling nitric acid due to their difference in thermal treatment. HT fibers are very sensitive to nitric acid; they undergo a considerable weight loss but the amount of formed oxygenated surface groups can be very high. In contrast, HM fibers are much less sensitive to chemical etching by nitric acid. As a consequence, a lower amount of surface groups is introduced by this technique on HM fiber as compared to HT fiber (about one tenth) (Fitzer *et al.*, 1979). Simultaneously to the increase of the number of surface groups, an enlargement of the surface area and of the rugosity is observed, this effect being however more pronounced for HT than for HM fiber. Mostly all of the above mentioned oxidation reagents act in a similar way and the following conclusions can be drawn: HT carbon fibers are very sensitive to oxidation in liquid phase whereas HM fibers are much less reactive.

Formation of a graphitic oxide layer. When the crystalline order of the graphitic layer is high enough, intercalation reactions may occur. In contrast to conventional oxidation reactions which take place essentially on edge sites or defects of the basal planes, intercalation reactions affect the whole lamellar structure. Generally speaking, the interlayer spacing of the graphitic layers increases in order to accomodate the species which are intercaled. A large variety of chemical compounds for instance metals and metallic compounds, halogens and ionic species can be intercalated. Graphitic oxide has an elemental composition which varies with its preparation conditions but the atomic ratio C/O generally lies between 2.7 and 2.8. A high proportion of oxygen is present in form of acidic groups. HM carbon fiber can be readily oxidized into graphitic oxide using potassium permanganate dissolved in concentrated sulphuric acid (Hummers reagent) (Donnet and Ehrburger, 1977). Since the lamellar oxide has only a weak mechanical strength, oxidation treatment must be strictly limited to the first external graphitic layers of the fiber. The effects of oxidation of HM fiber in nitric acid and in Hummers reagent are compared in Table 9.3. At first, a considerable difference in treatment time can be noticed for a similar carbon weight loss (~2%). Hummers reagent does not significantly modify the specific surface area but has a tremendous effect on the amount of acidic surface groups. In the same treatment conditions, HT fibers do not give lamellar oxide but undergo a slow oxidation similar to that observed in nitric acid.

3.3 Anodic etching

Anodic oxidation is well adapted for conductive materials like carbon filaments. It allows a continuous treatment process with great flexibility in the operating conditions (speed of

Table 9.3 Surface properties of oxidized HM fiber

Treatment	*Acidic groups* (μeq g^{-1})	*Specific surface area* (m^2 g^{-1})
None	3	0.38
Nitric acid (24 h)	21	1.40
Hummers reagent (10 min)	400	0.23

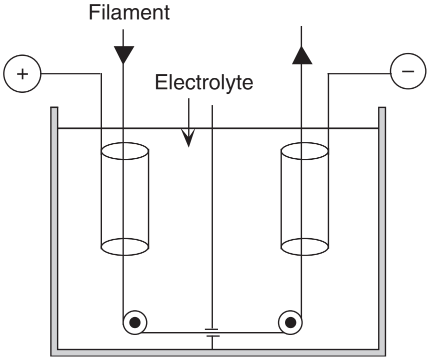

Figure 9.9 Anodic oxidation of carbon filament without electrical contact.

treatment, working potential, large selection of electrolyte, etc.). In fact, anodic oxidation is largely used for surface treatment of carbon filaments and yarns.

Two types of electrochemical process are described in the literature. In the first one, carbon filaments are put in electrical contact with anodes and then are immersed in an electrolyte (Courtaulds, 1971; Torey Industries Inc., 1972). Graphite cathodes are located in the vicinity of the immersed spools for the carbon filaments. Periodic inversion of electrical polarity during the process, i.e. successive oxidation and reduction cycles ensures a higher efficiency of the surface treatment as claimed in patents (Rhone Progil, 1975).

The second technique consists to etch the carbon filament without electrical contacts between the spools and the filaments (Maschinen Fabrikausburg-Nurnberg AG, 1977; Toray Industries Inc., 1979) (Fig. 9.9). The electrochemical reaction takes place in the solution and it is claimed that less surface flaws are introduced at the fiber surface during etching. Treatment time, electrical voltage and type of electrolyte are the key factors in anodic oxidation. The applied voltage is generally in the range of +1.0 to +2.5 V.

Treatment time is usually of the order of a few minutes or less and is considerably shorter than for chemical oxidation for which the time scale is the hour. It is however possible to detect a difference in the nature and the amount of surface groups with the type of electrolyte used. Strong acidic groups are mainly formed in alkaline electrolyte whereas both strong and weak acidic groups are formed in acidic one. These etching conditions maintain the original strength and surface area of the fiber. Commercially available carbon fibers are normally subjected to a surface treatment before coating with a sizing.

4 Carbon fiber reinforced polymers

4.1 Polymer matrix

Reinforcement of polymers is one of the most important application of carbon fibers. Two types of polymers are mainly used as matrix, thermosetting resins and thermoplastic polymers. Thermosets are made by mixing two components (a resin and a hardener) which react and harden, either at room temperature or on heating. Hence, processing of thermosetting resin-based composites include time and temperature of curing with respect to the glass transition temperature of the gelified resin. Shrinkage of the resin after curing will induce stresses in the matrix and at the fiber interface. This effect may be controlled by a post-curing treatment. The resulting polymer is usually heavily cross-linked, so thermosets are sometimes described as network polymers. Epoxy resins are the primary matrix material used in carbon-based composites. In this case, epoxy is harden when two components (a resin and a hardener) are heated together. Many composites are based on epoxies, though there is now a trend to using the cheaper unsaturated polyesters (Ashby and Jones, 1986).

The use of thermoplastic polymers (such as polyethylene) as matrix would facilitate the processing of composite as compared to thermosetting resins. In principle, the composite can be simply prepared by heating the thermoplastic polymer above its softening point. Two techniques can be used: the hybrid yarn method in which the polymer is assembled with the carbon preform in a textile structure, and the powder technique in which the thermoplastic matrix is added as a powder to the carbon fibers. Composites consisting of short carbon fibers in a polyamide (Nylon) matrix have been prepared in a way similar to glass fibers-based materials. For advanced composite, high softening point of thermoplastic polymer is desirable. Polyetheretherketone (PEEK) has a glass transition temperature equal to 143 °C and is a potential candidate.

4.2 Interfacial bond

A prerequisite condition for interfacial adhesion is the wetting of the carbon fiber by the molten thermoplastic polymer or the liquid precursor of thermosetting resin. The extent of interfacial contact depends on the wetting behaviour (contact angle and viscosity) of the fibrous preform by the matrix.

Wetting of carbon surface. The shape of a liquid droplet on a flat solid surface is determined by Young's equation:

$$\gamma_{sv} = \gamma_{sl} + \gamma_{lv} \cos \theta \tag{4}$$

where γ_{sv}, γ_{sl} and γ_{lv} are the surface tensions of the solid–vapour, solid–liquid and liquid–vapour interfaces respectively, and θ the contact angle. The lower the contact angle is, the better the liquid will wet the solid. Direct measurement of the surface energy of a solid is difficult to carry out and is generally obtained by determing the wetting behaviour of liquids of known surface energy, γ_{lv} (Schultz *et al.*, 1981). The surface energy of a solid, γ_s, can be decomposed into several components according to the equation

$$\gamma_s = \gamma_s^D + \gamma_s^P + \gamma_s^I + \cdots \tag{5}$$

where γ_s^D, γ_s^P, γ_s^I are the components of dispersive, polar and ionic interactions respectively. Metallic or covalent interactions may also be considered depending on the solid. In most cases however, the consideration of dispersive and polar interactions is sufficient for carbons and polymers. Values of γ_s^D and γ_s^P determined on highly oriented graphite (HOPG) after clivage are given in Table 9.4. Although their is some uncertainty in the experimental values, the following observations can be drawn. Basal planes display almost no polar component and dispersive interactions will determine their surface energy. In a similar way the contribution of dispersive interactions to the total surface energy is predominant for HM fiber. In contrast, the polar component represents almost one half of the dispersive one in the case of HT fiber. These results are consistent with the extent of active surface area of the

Table 9.4 Surface energy of pyrolytic graphite and carbon fibers (Donnet *et al*., 1986)

Carbon	γ_s^D (mJ m^{-2})	γ_s^P (mJ m^{-2})	γ_s (mJ m^{-2})
HOPG (basal plane)	60	0.15	60
Untreated HT fiber	26	12	38
Plasma-treated HT fiber	35	25	60
Untreated HM fiber	38	6	42
Plasma-treated HM fiber	13	32	45

considered carbons. The total surface energy, γ_s, is increased by oxidation of the carbon surface or by plasma etching (Donnet *et al*., 1986, 1987). It is noticed that the polar component increases and in some cases becomes the major factor contributing to the surface energy of the carbon fiber (Table 9.4). Similar results are found for industrial surface treatments of carbon fibers (Donnet *et al*., 1986).

Equation (4) indicates that epoxy resins ($\gamma_s \sim 40\,\mathrm{mJ\,m^{-2}}$) will wet carbon fibers after surface treatment since their surface energy is then much higher than for resin. Consequently physical bonding between fiber and matrix should be sufficient for achievement of high performance composite. This is however not always the case since the fiber surface may be contaminated by adsorbed species which will result in a lowering of the surface energy of the fiber. Another limiting effect results from the shrinkage of the liquid resin during polymerization which leads to interfacial defects. Nevertheless, wetting is an important factor for the achievement of an adequate impregnation of fiber tows and yarns by liquid resins.

Nature of the interfacial bond. After curing of the resin or solidification of the thermoplastic polymer an interfacial bond between matrix and carbon fiber will take place. There are basically two types of interfacial bonding, physical and chemical couplings. Physical coupling is based on Van der Waals forces which include mostly London dispersion forces, dipole–dipole interaction and hydrogen bonding. Their energy is usually in the range 8–16 kJ mole^{-1}. In the chemical coupling model, the formation of true chemical bonds (covalent and/or ionic) between fiber and matrix is assumed. In that case the strength of interfacial bonding is much higher than in the physical bonding (40–400 kJ mole^{-1}). The chemical bonding model is an extension of the physical coupling since the establishment of covalent bond requires first good wetting conditions. Although chemical coupling will lead to a strong interfacial adhesion, it is generally not recommended for composites since it will induce brittle failure under stress.

4.3 Effect of surface properties of carbon fibers on mechanical properties

The effect of surface properties of carbon fibers on the mechanical performance of composites will be discussed for intralaminar shear strength (ILSS) and for impact toughness (see also Section 1). Elastic modulus, *E*, of fibers and ILSS values of corresponding epoxy resin-based composites are compared in Table 9.5. Composites based on carbon fibers especially with HM have rather lower ILSS. After surface treatment of carbon fibers ILSS values of composites are then comparable to glass fiber-reinforced materials.

Table 9.5 Intralaminar shear strength of epoxy resin-based composites

Fiber	*E* (GPa)	*ILSS* (MPa)
HT carbon fiber	250	20
HM carbon fiber	500	10
E glass	73	100
Aramid	300	40
Surface-treated high tensile carbon fiber	250	70–130
Surface-treated HM carbon fiber	500	40–70

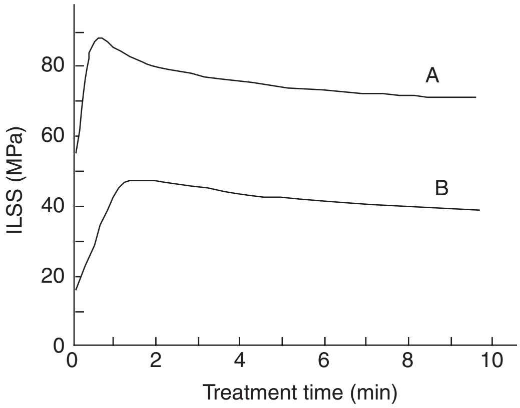

Figure 9.10 Effect of anodic etching time of (A) HT fibers; and (B) HM fibers on ILSS of composites.

As a general rule all oxidation treatment will give to some extent an increase in ILSS. Over treatment must however be avoided since it will decrease the fiber strength and in turn the bond strength. As an example, the change in ILSS as a function of anodic etching time of HT and HM fiber is shown in Fig. 9.10 (Ehrburger *et al.*, 1975). The composite material consists of an epoxy resin (Araldite LY 556) catalytically cured with a hardener (Ciba HT 973) with a volume fraction of carbon fibers equal to 75%. An increase in ILSS is attributed, in a first step, to a higher surface energy of the treated fiber and a better wetting of the resin during impregnation. After curing the resin is no longer liquid and the higher value of ILSS is also due to a stronger interfacial bond. In that respect ILSS should be correlated to the chemical properties of carbon fiber. Since the surface area of carbon fiber is not significantly modified by short periods of anodic etching, the increase of shear strength should be essentially due to the introduction of chemical groups on the carbon surface. Hence the nature and the amount of acidic groups appear to be key factors in the interfacial bond strength. This point has been verified with HT fiber-based epoxy composite. The nature and the amount of acidic groups of HT fiber has been modified by anodic etching in alkaline solution and subsequent pyrolysis at 900 °C in argon before incorporation in epoxy resin. The ILSS of the composite correlates approximatively with the amount of acidic groups present on the carbon surface as depicted in Fig. 9.11. Interestingly, the mode of failure of

Table 9.6 The nature of the acidic groups on the carbon fiber

Fiber treatment	*Acidic groups*		*ILSS* (MPa)	*Failure mode*
	Strong (μeq g^{-1})	*Weak* (μeq g^{-1})		
Untreated	7	3	55	Shear
Anodic oxidation	16	—	92	Tensile
Anodic oxidation and heat treatment	—	13	77	Intermediate

Note
— not measurable.

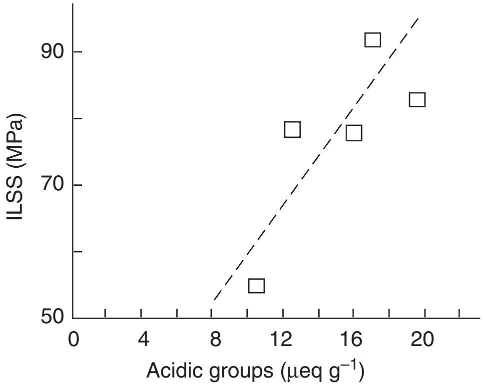

Figure 9.11 Relationship between the amount of fiber surface groups and ILSS of composites.

the composite depends on the nature of the acidic groups on the carbon fiber (Table 9.6) (Ehrburger *et al*., 1978). The composite containing untreated fibers displays a typical shear failure mode. After anodic etching, the composite has a higher ILSS value, but it undergoes now a tensile mode of failure.

After heat treatment of the etched fiber, the amount of acidic groups has slightly decreased and so has the ILSS of the composite (Table 9.6). Also the mode of failure of the composite becomes less catastrophic. Similar results are found by changing the type of electrolyte used for anodic oxidation, i.e. by changing the nature of the acidic surface groups. Hence the mode of failure is affected by the type of carbon surface groups. As a general trend, it is observed that strong acidic groups, in particular carboxyls and phenols, induce 'strong' interfacial adhesion (high ILSS value and brittle failure). Weak or neutral surface groups promote a less catastrophic mode of failure (high ILSS and less brittle failure). Hence, the functionality of the carbon surface (nature and amount of surface groups) has to be adjusted by a proper surface treatment of the carbon fibers.

The precise mechanism of interaction between carbon surface groups and resins is however not yet established. It is generally accepted that hydrogen bonds and Van der Waal's bonds are prevailing in the interfacial adhesion. In that respect, nitrogen groups present in HT PAN-based carbon will also contribute to the interfacial bond strength. Although a direct proof of the existence of covalent bonding between carbon fiber and epoxy matrix has yet not been established, there are however some experimental evidences for a 'chemical-like' interfacial coupling. Surface groups may also alter the polymerization mechanism of the resin in the vicinity of the fiber which in turn would affect the mechanical properties of the polymer in the interfacial region (Ehrburger and Donnet, 1980, 1985).

Resistance to fracture. Another important characteristic of composites is its notch sensitivity which is closely related to its resistance to fracture. The knowledge of the overall load which can be applied to a composite without catastrophic propagation of pre-existing flaws is an important characteristic of the material. The test generally used for this determination is the Charpy impact test in which the energy required for the propagation of flaw is determined. It consists in measuring the work done during the break of a notched bar test sample into two parts using a pendulum impact gauge.

Like intralaminar shear strength, fracture energy of the composite increases with prior surface treatment of high tensile fibers (Fitzer, 1983). The energy transmitted to the composite during the impact is dissipated by elastic deformation of the strained fibers. In the case of HM fibers, the fracture energy of composite decreases after surface treatment. This is attributed to an excessive interfacial bonding and to a low value of strain to failure of HM fiber, 0.4% as compared to 1.2% or more for HT fiber (Fitzer, 1983).

Fracture energy is also sensitive to the property of the matrix especially in the interfacial area. The introduction of a non-rigid layer at the interface is also a way to increase the fracture energy of composite. This can be achieved by coating the carbon fiber by a ‘flexible’ polymer layer compatible with the matrix. As previously discussed, the polymer layer must at least wet the fiber surface and preferably exert physical coupling with its surface groups. An oxidative surface treatment of the carbon fiber is therefore required. The indroduction of a flexible interlayer may significantly increase the fracture energy of the composite (Riess *et al*., 1974; Hancox and Wells, 1977).

4.4 Application of carbon-fiber reinforced polymers (CFRPs)

Carbon fiber-based composites are suitable materials for application in which strength, stiffness and low specific gravity are critical factors. They were designed and developed for the aeronautic industry during the sixties. In 1990, the total production of carbon fiber-based composites was of the order of 10,000 tons (Chuang-Hua, 1990). Nowadays, the aeronautic industry is still the largest market for these composites. They are used as primary structural parts of aircrafts like vertical stabilizer, wing components and flaps, i.e. for parts where stiffness is an essential property. In helicopters, carbon fiber-based composites are used for rotating blades, cockpit and tail structures. Another part of the market of these composites lies in the recreational area. A large variety of modern equipments for sports and leisure – sailing and rowing boats, gliders, tennis rackets, golf clubs, skis, racing and mountain bikes, fishing rods, etc. – is manufactured with carbon composites. A small part of the production is also used for industrial applications, for instance as fast moving parts in textile machinery, shafts and wheel connections for cars and trucks and specific parts for tools and automated systems. Some developments are also considered for weight saving in ground transportation systems.

5 Carbon–carbon composites

Carbon–carbon (C–C) composites or more precisely, carbon fiber reinforced carbon composites are materials based on carbon fibers embedded in a matrix also made of carbon.

They were developed for exhaust cones in rocket during the late sixties. C–C composites are remarkable materials since they combine toughness, low weight and refractory properties in inert atmosphere at high temperature up to 2,000 °C. In particular their resistance to impact and thermal shock is excellent due to high thermal conductivity and low thermal expansion behaviour. Therefore, C–C composites are high temperature materials par excellence. Described as the best of the refractory materials, carbon exhibits only one major disadvantage; that is, a sensitivity to high temperature.

They are manufactured using two routes: (i) densification of a carbon fiber preform by chemical vapour deposition–infiltration of pyrolytic carbon (CVD/CVI); (ii) impregnation of the fibrous preform by an organic liquid which will be carbonized. The CVD/CVI routes consist to deposit slowly layers of pyrolytic carbon by cracking of a hydrocarbon, methane for instance. The deposition rate must be very small in order to obtain uniform growth of the carbon matrix through the whole preform. The crystalline structure of the pyrolytic carbon is also depending on the deposition conditions. In the impregnation technique, the carbon matrix will be generated by an organic liquid which may be a coal tar pitch, a themosetting or thermoplastic resin. The impregnated carbon preform is then carbonized in an inert atmosphere at 800–1,100 °C (Granda *et al*., 1998). The weight loss and the volume shrinkage of the precursor will generate porosity in the composite. Multiple impregnation and carbonization cycles are usually required for obtaining C–C composite with high density. CVD technique can also be used for final densification of the composite made by the impregnation technique. For some applications C–C composites are heat-treated at 2,000 °C for graphitisation. High temperature treatment followed by cooling to room temperature will generate thermal stresses and induce microcracking especially at fiber–matrix interfaces. Hence these microcracks form an appropriate pathway for the oxidizing species and completely may favour the gasification of the carbon reinforcement.

5.1 Interfacial interaction in C–C composites

Like with polymer-based composites, the surface properties of carbon fibers exert an influence on the interfaces in C–C composites. This effect is particularly observed for samples prepared by the impregnation technique. The used liquid precursor should exibit a low viscosity, high wetting properties to the carbon substrate and rapid curability before carbonization in order to inhibit the loss of the liquid during further heating up. So far, as the liquid precursor for the matrix carbon is concerned, selection of a precursor material with high carbon yield should be made.

Interactions between the fiber surface and the liquid pitch or resin will take place during impregnation in a way similar to the preparation of polymer-based composites. The resin or the pitch matrix will then skrink during carbonization and the extent of shrinkage depends on (i) the amount of oxygen surface groups on the carbon fiber; and (ii) the devolatilization of the pitch or resin matrix. As an illustration, the extent of cross sectional skrinkage of the phenolic matrix in an unidirectional composite during pyrolysis at 1,000 °C is shown as a function of carbon yield in Fig. 9.12 (Huettner, 1989). HT and HM behave differently, the shrinkage being less pronounced for fibers heat-treated over 1,800 °C. After surface treatment, i.e. formation of oxygenated surface groups, the shrinkage becomes important for both types of fibers. This phenomenon is attributed to a more pronounced bonding of the organic matrix to the carbon fibers via the surface groups. Therefore, carbon fibers should be used, if possible without surface treatment.

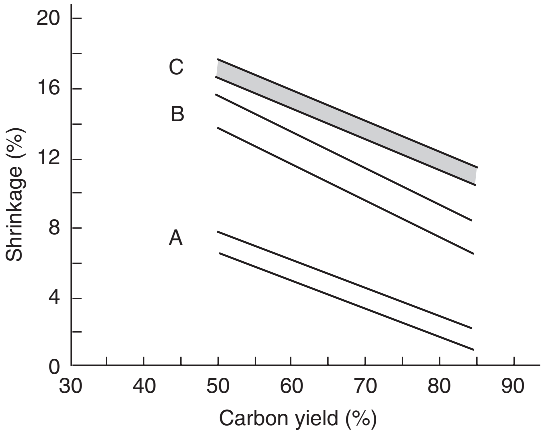

Figure 9.12 Cross-sectional shrinkage of phenolic resin during carbonization as a function carbon yield for different PAN-based carbon fibers (A) HM fiber, (B) HT fibers, and (C) HM and HT fibers after surface treatment (adapted from Huettner, 1989).

The quality of the fiber–matrice interface is also strongly influenced by the devolatilization of impregnated liquid during the first carbonization step. An important release of volatile compounds from the fluid but highly impervious binder pitch (Granda *et al.*, 1998, Ehrburger *et al.*, 1996) leads to the development of a porosity below 400 °C. The development of this porosity depends on the nature of the binder pitch. Further, the semi-coke is subjected to mechanical stress during the subsequent cooking which in turn may also induce microfissuration of the carbon matrix as well as fiber–matrix debonding. In a recent paper, the influence of the nature of the pitch – and in particular the influence of the pitch treatment – on the morphology (amount, size, shape of the pores) of the developed porosity in a pitch-based carbon composite has been described (Vix-Guterl *et al.*, 2001). The obtained results indicate that treatment in nitrogen or air of pitch used as matrix precursor strongly influences the pore size distribution of the intertow and intratow porosity which becomes narrower associated to a fraction of closed voids which significantly increases. Moreover, it has been shown that thermal treatment at 2,000 °C induces an extensive microfissuration of the matrix; phenomena more emphasized in the case of the pitch-based matrix treated in air.

Consequently, the fracture behaviour of C–C composite is also influenced by the surface properties of the carbon fibers and the quality of the impregnated pitch or resin. In the case of a phenolic resin-based C–C composite, the flexural strength is dramatically reduced by surface treatment of the carbon fibers (Fig. 9.13) (Huettner, 1989). It is assumed that too strong bonding of the resin with the fiber during impregnation and carbonisation induces excessive damage and promotes crack propagation through the matrix and the fibers. The quality of the impregnated liquid is also one of the more important control parameters of the behaviour of the C–C composites. Mechanical behaviour is affected, especially its fracture behaviour, and therefore fatigue and impact behaviour, as well.

In that respect the first impregnation cycle is crucial since it will determine, in a significant manner, the interfacial bonding between carbon fibers and carbon matrix and the subsequent mechanical properties.

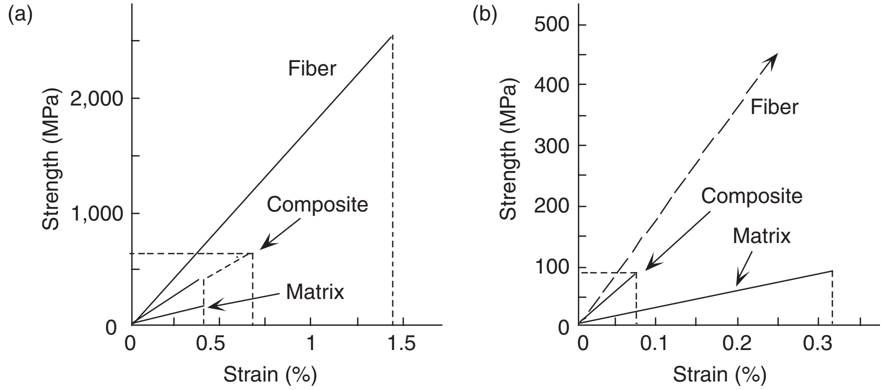

Figure 9.13 Flexural stress–strain diagram for unidirectional C–C composite (a) untreated HT fibers; and (b) surface-treated HT fibers (adapted from Huettner (1989)).

5.2 Protection against oxidation

A severe limitation in the use of C–C composites is due to the oxidation of carbon which starts at temperature lower than 500 °C. The interfaces are particularly sensitive to oxidation and very rapidly corrosion figures are formed indicating a great heterogeneity in carbon reactivity in the composite. Small amount of carbon gasification induces a rapid destruction of the material. It is generally accepted that 1% of carbon gasification will decrease the mechanical property by nearly 10%. Therefore, the behaviour of the composite will be extremely sensitive to its chemical environment. For instance the lifetime in air of a C–C composite under a static load corresponding to 75% of its load to failure decreases from 400 h at 360 °C to nearly zero at 500 °C (Fitzer, 1977). Furthermore, considering that the lifetime of the same composite in a non-oxidising environment is about the same at 2,500 °C than at 350 °C, one realizes the need of an efficient protection against oxidation for these composites (Fitzer, 1977). The reactivity of carbon with oxygen may be decreased by several additives acting as oxidation inhibitors.

Mechanism of inhibition. Carbon materials exhibit various types of texture and of structure on which the overall oxidation rate will largely depend. This is particularly important at moderate temperature (below 1,000 °C). At higher temperature the oxidation rate becomes so fast that the textural effects of the material can be neglected. As a consequence, the protection mechanism will be based on different concepts depending on the temperature. At moderate temperature, the lowering of the oxidation rate may be achieved by impregnation with inorganic salts, mostly boron oxide, phosphates and others. These compounds are attractive since they can be easily deposited on the carbon substrate using an impregnation technique. Deposition of phosphorus additives are made by this procedure starting with alkyl and aryl phosphorus precursors (McKee *et al.*, 1984). Aqueous solutions of orthoboric acid or ammonium borate and solution of organoborates in ethanol are also used (McKee *et al.*, 1984). The inhibitor is obtained by thermal decomposition of the precursor and it generally spreads over the entire carbon surface. Oxidation of the composite markedly decreases in the temperature range 500–1,000 °C in presence of inhibitor partly attributed to the blockage of the surfaces sites responsible for carbon gasification. The weight loss

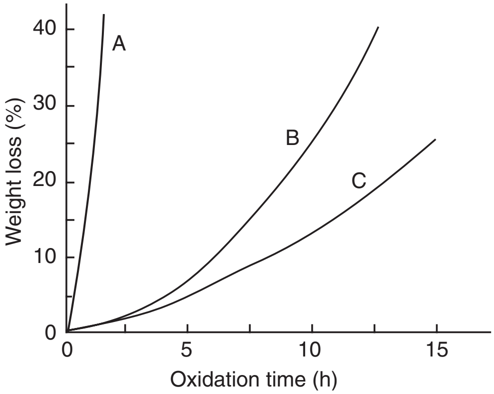

Figure 9.14 Weight loss of a C–C composite during oxidation in air: (A) untreated; (B) with 3 %; and (C) with 7 % boron oxide.

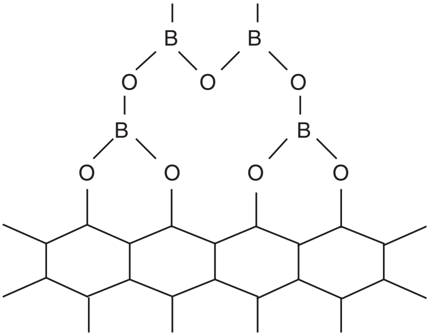

Figure 9.15 Interaction of boron oxide with carbon active sites (adapted from McKee *et al.*, 1994).

during oxidation at 710 °C of a C–C composite without inhibitor and with 3% and 7% by weight of boron oxide are compared in Fig. 9.14.

The inhibition effect is very pronounced at the beginning of oxidation (induction period). Thereafter a pseudo-linear oxidation regime is found as for the untreated composite (Isola *et al.*, 1998). The apparent activation energy of oxidation is not affected by the presence of the additive suggesting that the number of sites responsible for carbon oxidation has been decreased after addition of boron or phosphorus compounds. Hence the inhibitor strongly interacts with the sites of the carbon surface where oxidation normally takes place, resulting in a poisoning effect of the carbon–oxygen reaction (Fig. 9.15) (McKee *et al.*, 1984). By addition of small amounts of inhibitors, the oxidation rate of carbon can be decreased by a factor 10–20. A further lowering of the carbon oxidation requires a protective barrier against oxygen. In this case the overall gasification rate of carbon is limited by the diffusion rate of oxygen through the protective layer. This can be achieved by forming a glassy layer on the composite and the protective effect will increase with the thickness of the barrier. Mainly glasses containing boron, silica or phosphates are used since they combine inhibiting properties and ability to form a continuous coating (Ehrburger *et al.*, 1986; Ehrburger and Dallies-Labourdette, 1992; Isola *et al.*, 1998).

Hence, both inhibition and formation of a diffusion barrier contribute to the decrease of the carbon reactivity. The efficiency of a protective system, *Ef*, may be defined by the ratio of the oxidation rates of the carbon before and after protection determined in the same reaction conditions. The change in *Ef* with the amount of boron oxide deposited on a C–C composite oxidized at 710 °C is shown in Fig. 9.16. For small loadings, i.e. below 2% by weight, *Ef* increases strongly with boron oxide content due to a poisoning effect of the carbon–oxygen reaction. Thereafter *Ef* increases linearly with boron oxide content due to the formation of a protective layer. For the highest protective effect (*Ef* = 45), the mean thickness of the boron oxide layer on the composite would be equal to 20 μm. In the case of thicker coatings (0.2–0.5 mm in thickness) gasification of C–C composite can be almost suppressed for practical application at temperature below 1,000 °C in dry air (McKee, 1991). Boron-based coatings are also able to withstand thermal cycling due to the low viscosity of the liquid-like boron oxide layer and its good wettability of the carbon surface. At temperature higher than 1,000 °C, the vapour pressure of boron or phosphorus compounds becomes too important and continuous loss of coating will shorten the time of protection. In the presence of water vapour, volatile compounds are formed, for instance HBO_2 which will result in an even more rapid destruction of the protective coating (McKee, 1991).

For higher temperature ($T > 1{,}000$ °C) an efficient protection can only be obtained by oxidation resistant coatings (especially SiC coatings) which will act as diffusion barriers or getters of oxygen. The design of a refractory coating must take into account several physical and chemical requirements. First, the layer must act as a tight diffusion barrier for oxygen. Second, its reactivity with oxygen must lead to non-volatile compounds. Other requirements are chemical inertness with the carbon substrate and possibility of formation of a protective layer on complex composite structure.

Different types of compounds may be considered for designing protective layers. Refractory metals like iridium, carbides (SiC, TiC), silicides ($MoSi_2$, $TiSi_2$), nitrides (Si_3N_4) and combinations of these compounds can give efficient protection (Fitzer, 1977; Sheenan, 1989; Vix-Guterl *et al.*, 1993). Oxides react with carbon at elevated temperatures and therefore cannot be used directly. Nevertheless, ZrO_2 and HfO_2 are stable in presence of carbon at temperature up to 1,700 °C.

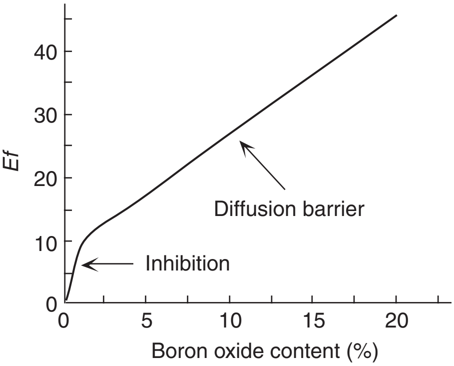

Figure 9.16 Efficiency of protection against oxidation of a C–C composite as a function of boron oxide content.

During the last decade, considerable work has been focused on SiC for the protection of C–C composite. The most common way to deposit SiC on carbon substrates is by chemical vapour infiltration of silanes at 1,100 °C, a process derived from the well-known chemical vapour deposition. The behaviour of SiC in dry and wet oxygen has been extensively studied in the last years (Fitzer and Ebi, 1973; Schiroky, 1987; Zheng *et al.*, 1990; Opila, 1995, 1999). Its oxidation becomes noticeable above 1,000 °C according to the reaction

$$2SiC + 3O_2 \rightarrow 2SiO_2 + 2CO \tag{6}$$

$$SiC + 3H_2O \rightarrow SiO_2 + 3H_2 + CO \tag{7}$$

Silicon nitride react with oxygen in a similar way

$$Si_3N_4 + 3O_2 \rightarrow 3SiO_2 + 2N_2 \tag{8}$$

and can also be used as a protective coating. However, the reaction rate is two- to three-order of magnitude lower than for SiC in the temperature range 1,100–1,400 °C

Silica has a larger specific volume than SiC and a self-healing effect is observed during oxidation (Vix-Guterl *et al.*, 1993). There is a general believe that the permeation of molecular oxygen through the growing oxide layer is the rate controlling step for oxidation below 1,720 K resulting in a parabolic law for the formation of silica. The reported activation energy value in this regime (around $120\,\mathrm{kJ\,mol^{-1}}$) agrees well with the energy required for molecular oxygen permeation in fused silica (Norton, 1961). In presence of impurities forming low melting glasses, alkaline metals for instance, the diffusion rate of oxygen can be greatly increased and will limit the protective effect. SiC also reacts with water vapour leading to the formation of SiO_2 layer. There is a general agreement within the literature that water vapour enhances the oxidation rate of SiC in the passive regime and that the oxidation kinetics of SiC follows a parabolic law over a long period of oxidation indicating that the reaction rate is controlled in a diffusion manner similar to the one in dry air (Maeda *et al.*, 1988; Opila, 1994; Vix-Guterl *et al.*, 2001). However, there is some discordance concerning the origin and the magnitude of this enhancement. Several explanations were proposed: (i) water vapour plays a strong influence on the crystallization of amorphous silica which is said to accelerate SiC oxidation by promoting devitrification; (ii) the high solubility of H_2O in amorphous silica leading to a less dense silica film which allows for faster diffusion of oxidizing species; and (iii) the oxidation rate of SiC is controlled by the diffusion of molecular H_2O and charged species, such as OH^-.

Moreover, the reactivity of SiC in water vapour will strongly depend on several other factors like: the purity of the SiC material, the nature of impurities in the SiC material and/or the oxidation environment (Opila, 1995; More, 2000). It is rather difficult to discriminate between the effects of water vapour and impurities.

The protective effect of ceramic coating may be also strongly reduced by the presence of microfissurations in the SiC layer at a temperature lower than the temperature of deposition, due to mismatch in the coefficients of thermal expansion of the carbon and the coating.

Hence, a glass-forming system acting as a sealant is needed at lower temperature. This is particularly important for uses of C–C composites requiring thermal cycling over a large interval of temperature. An efficient protection of C–C composite against oxidation includes therefore three main components each one acting in a specific range of temperature: (i) an inhibitor which can be deposited inside the porosity of the composite; (ii) a refractory coating on the composite; and (iii) a glass-sealant chemically compatible with the coating and its reaction products with oxygen (Fig. 9.17). The design of a protective system is thus based on a multilayer approach which takes in account the working conditions of the composite material, in particular, interval of temperature cycling and exposure time to oxidation. However, in the case of glass-sealant, the application will be limited to temperature lower than 1,470K. Therefore, the concept of the multi-layer coating has been extensively extended to other ceramic materials in the last years (Westwood *et al.*, 1996). The main advantage in the development of a multi-layer coating is the possibility of associating complementary specific properties and gaining the advantages of each layer while limiting their drawbacks. As an example, Bentson *et al.* (1989) have patented a complex four layer protection system for C–C composites which comprises inner and outer glass sealant layers covered with inner and outer ceramic layers (Bentson *et al.*, 1989). An idealized four-layer coating for protecting C–C composites at temperatures in excess of 1,800 °C has been proposed by Strife and Sheehan (1988).

Limiting chemical reactions in protection. There is generally a limiting temperature in the physical or chemical stability of refractory coatings. Above 1,900 °C, the oxidation of SiC gives gaseous SiO according to the equation

$$SiC + O_2 \rightarrow SiO_{(g)} + CO \tag{9}$$

In that case, the SiC layer will be rapidly consumed by formation of volatile products, SiO and CO. The reaction is called ‘active oxidation’ in contrast to the formation of silica (equation (9)) which corresponds to a ‘passive oxidation’ mechanism. The transition between passive and active oxidation regimes depends on the partial pressure of oxygen (Gubransen and Jansson, 1972; Nickel, 1992).

It has been suggested that the passive/active transition is controlled by the following reaction between SiC and SiO_2:

$$SiC_{(s)} + 2SiO_{2(s)} \rightarrow 3SiO_{(g)} + CO_{(g)} \tag{10}$$

For instance the transition from passive to active oxidation occurs at 1,700 °C for an oxygen pressure equal to 60 mbar and it takes place at 1,100 °C when the pressure of oxygen is reduced to 6×10^{-4} mbar (Gulbransen and Jansson, 1972). However, several authors suggest that the transition is also sensible to other parameters like the total pressure, the presence of an inert gas, the nature of SiC … (Rosner and Allendorf, 1970; Hinze *et al.*, 1976;

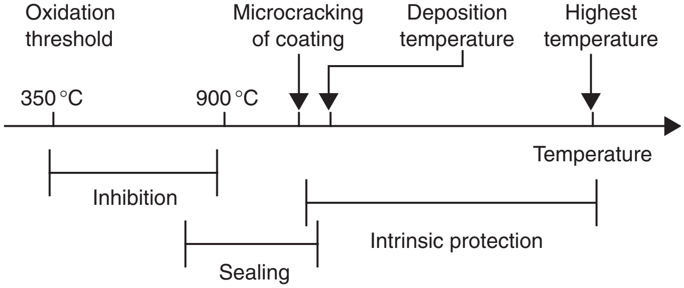

Figure 9.17 Principle of protection of a C–C composite against oxidation (adapted from Strife and Sheehan (1988)).

Vaughn and Maahs, 1990). Therefore, reaction between the carbide and the oxide induces considerable damage in the refractory layer and the transition from the passive to the active oxidation regime determines the limit of the protective effect. The thermal stability of $SiC–SiO_2$ interface is noticeably decreased at low partial pressure of oxygen and the use of such protection in reduced atmosphere is limited.

Another refractory coating which has been considered is silicon nitride. It undergoes however at high temperature a decomposition reaction into silicon and gaseous nitrogen which limits its use as a protective coating. Once the protective coating undergoes a physical or a chemical decomposition, decohesion of its interface with the carbon substrate will accelerate its destruction and the composite will rapidly fail. It is then necessary to design multilayer coatings, each component having its specific function. Physical and chemical compatibility must be sufficient in order to avoid or minimize interfacial reactions which may accelerate degradation of the multilayer protection. Hence, thermodynamical and kinetical considerations are the key factors in the design of appropriate protection systems of C–C composites against oxidation.

5.3 Applications of C–C composites

The main application of these materials is in the field of space and aeronautic industry where refractory properties and extreme resistance to thermal shocks are required. Other potential applications are furnace equipments like walls or heat shields. C–C composites are also used as brakes for aircrafts due to their excellent tribological properties at high temperature. They are also used as prostheses like hip joint stem and implants due to their biocompatibility associated with strength and resistance to wear. Future development of C–C composites are expected in the field of specialized mechanical engineering where specific mechanical constraints are associated with severe environmental conditions. The production cost of these composites remains however today the major factor which limits their use. More detailed informations about potential applications on this type of composite can be found in Chapter 5.

6 Carbon-based composites with other matrices

The reinforcement of light metals, aluminium, magnesium and light alloys has been considered at the early stages of carbon composites development. Carbon fibers are however hardly wet by liquid metals which renders the processing of composites more complicated (need of vacuum and/or pressure during infiltration). Furthermore, at higher temperature carbon reacts with metals by giving carbides which in turn will decrease the mechanical properties of the composite. Various solutions has been proposed for improving the wetting of carbon by liquid metals like deposition of alkaline metal in small quantity, coating by noble or transition metals or ceramics (Rocher *et al.*, 1986). The formation of a boron carbide layer by reaction of boron trichloride with the carbon fiber does not affect its mechanical properties but limits its reactivity with metal matrices (Vincent *et al.*, 1992). The processing of economical carbon fiber-reinforced metals is still hindered by these factors. Light metals reinforced with carbon fibers may be used in a very large area ranging from parts of car engines to structural application in aeronautics.

Glass and ceramic matrices has also been reinforced by carbon fibers. Glass–carbon fiber composites are characterized by high strength, stiffness and toughness. They also have low friction and high wear resistance. The chemical characteristics of the glass–carbon interface will determine the mechanical properties of the reinforced glasses, in a way similar to polymer-based composites (Tredway *et al.*, 1989). Their maximal temperature of use will depend on the nature of the glass and may be as high as 1,200 °C in absence of oxygen. Carbon fibers are also used in ceramic matrices, like SiC or nitride and their mechanical properties are those of brittle matrix reinforced by brittle fibers. The most common way to obtain the SiC matrix is by chemical vapour infiltration starting from silanes as precursors as already described in the previous paragraph. The obtained material is then denominated as 'C/SiC composite'. The knowledge of the reactivity of such composite is of prime importance for their potential applications. As commonly described in the literature, the reactivity of C/SiC composite may be quantitatively determined by using thermogravimetry analysis. The main drawback of this technique is the measurement of an overall weight variation which makes it difficult to assess the extent of carbon gasification from SiC oxidation. In this way, the reactivity of a given type of C/SiC composites in O_2 and in particular in presence of water vapour has been recently studied using a method which combines mass spectrometry and thermogravimetry (Vix-Guterl *et al.*, 2001). It was then possible to determine the respective part of the carbon gasification and SiC oxidation during the oxidation of the C/SiC composite in various oxidizing environment at 1,200 °C as illustrated in Fig. 9.18.

As seen in this figure, the gasification of the carbon remains the predominant reaction during the oxidation of the studied composite although a significant fraction of SiC is oxidized into SiO_2. A similar trend was observed in O_2 but, in this case the reactivity of SiC is lower. This effect is partly attributed to the fact that SiC does not uniformly cover the carbon prepreg and to the presence of microfissurations resulting from different thermal expansion coefficient of the composite during the infiltration process. However, the reactivity of the carbon material in the C/SiC composite is reduced by a factor close to 60 as compared to the corresponding carbon composite without SiC.

Generally speaking, ceramic–carbon composites have in principle a higher resistance to oxidation than C–C composites. However, it appears that in some cases the role of protection of SiC is limited in dry and wet air at high temperature. The development of additional coatings for long term applications has then been required. Like for C–C composite, various multi-layer protection has been proposed which mainly consists of a ceramic bond layer, an inner sealant, an outer erosion layer of ceramic (Franc and Macret, 1990; Goujard *et al.*,

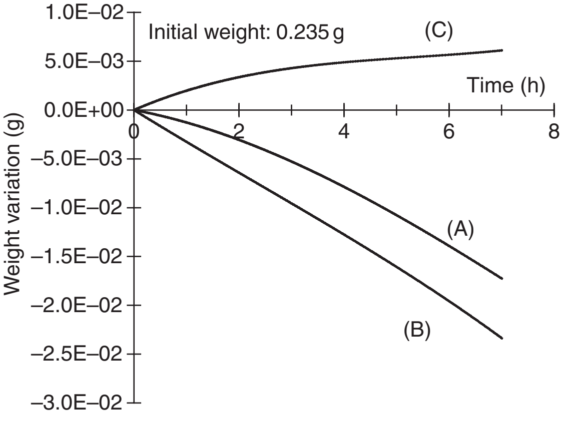

Figure 9.18 Oxidation of C/SiC composite by water vapour at 1,470 K; (A) overall weight variation; (B) weight loss due to carbon gasification; (C) weight gain due to SiC oxidation.

1994). The potential use of ceramic–carbon composites is in gas turbine engine components and structural components in aeronautics. The potential application of C/SiC composite has been envisaged. To extent there application to other industrial fields (like furnace industry, domestic industry …), new protection methods have to be developed. In fact, the use of the CVD technology to prepare the ceramic coating is not adapt and too expensive in the frame of such applications. Recently a new way of preparing such coating has been proposed based on carbothermal reaction and sol-gel process (Vix-Guterl *et al*., 1997, 1999). It has been shown that the properties of the formed SiC coatings are strongly influenced by the surface properties of the carbon fibers (Alix *et al*., 1998; Vix-Guterl *et al*., 1999).

Another application of carbon fibers is the reinforcement of cements and concretes (Briggs *et al*., 1974; Ohama, 1989). In this case, carbon fibers with low mechanical properties, i.e. the so-called ‘general purpose’ fibers made by melt spinning of isotropic pitch can be used. A dramatic reinforcement effect is observed even for volumic fraction of carbon fibers not exceeding a few percents (Ohama, 1989). Due to the chemical inertness of carbon with cement, no corrosion effect is observed when the reinforced concrete is exposed to an humid environment like with metal or glass fibers. The strength of these composites can be improved after surface treatment of the carbon fibers (Kojima *et al*., 1989). Cement–carbon composites are developed mainly in Japan for application requiring weight saving for building and road constructions (Inagaki, 1991). The electrical resistivity of cement is markedly decreased after inclusion of carbon fibers and these materials can be used for new applications such as heating elements, electrical shielding and anti-static flooring in buildings.

7 Conclusion

The performance of carbon composites based on polymer, carbon or ceramic matrices are now well established and their field of applications is well recognized. The properties of such composites, in particular their mechanical properties, are strongly influenced by the quality of the fiber–matrix interface. The quality is mainly determined by the surface chemical properties of the carbon fibers and the nature of the matrix. In most cases, a surface treatment of carbon fibers is required in order to optimize the interfacial bonding. Therefore, the role of chemistry in advanced carbon-based composites is of prime importance and should be taken in consideration for assessing the behaviour of such materials. New developments of these materials can be expected from a larger use in industries by lowering materials and processing costs. The design of advanced carbon composites responding to specific characteristics is another route for new applications and development.

References

Alix, I., Vix-Guterl, C. and Ehrburger, P. (1998), in Proc. Eurocarbon’98, France, Strasbourg 457–458.

Asby, M. F. and Jones, D. R. H. (1986), in *Engineering Materials 2*, International Series on Materials Science and Technology, **39**, Pergamon Press.

Aveston, J. and Kelly, A. (1973), *J. Mat. Sci.* **8**, 352.

Bentson, L. D., Price, R. J., Purdy, M. J. and Stover, E. R. (1989), E.R. US Pat 5298 311.

Boehm, H. P. (1966), in *Adv. in Catalysis*, D. D. Eley, ed., Academic Press, New York, Vol. 16, 179–274.

Boehm, H. P. (1994), *Carbon*, **32**, 759.

Boehm, H. P. (2000), in *World of Carbon*, P. Delhaès, ed., Vol. 1, chapter 7, Graphite and precursors, Gordon and Breach Publ.

Boehm, H. P., Diehl, E. and Heck, W. (1966), *Proc. 2nd Int London Carbon & Graphite Conf.*, Soc. Chem. Ind. London, 369.

Boehm, H. P., Diehl, E., Heck, W. and Sappock, R. (1964), *Angew. Chem. Int. Ed.* **3**, 69.

Briggs, A., Bowen, D. H. and Kollek, J. (1974), *Proc. 2nd Carbon Fibers Conference*, The Plastics Institute, London, 114.

Broutman, L. J. (1969), Interfaces in Composites, ASTM Special Technical Publication, American Society for Testing and Materials, 452.

Bunsell, A. (1988), *Fiber Reinforcement for Composite Materials*, Composite Materials Series, Vol. 2, Elsevier, Amsterdam.

Chuang-Hua, L. (1990), *Proc. Int. Symp. on Carbon*, Tsukuba (Japan), 666.

Clark, D., Wadsworth, N. J. and Watt, W. (1974), *Proc. 2nd Carbon Fiber Conference*, The Plastics Institute, London, 44.

Cooper, G. A. and Sillwood, J. M. (1972), *J. Mat. Sci.* **7**, 325.

Courtaulds Limited (15 Jan. 1971), French Patent 70.09.686.

Dentzer, J., (1983), Thesis Mulhouse (France).

Donnet, J. B. (1968), *Carbon*, **6**, 161.

Donnet, J. B. and Ehrburger, P. (1977), *Carbon* **15**, 143.

Donnet, J. B., Brendle, M., Dhami, T. L. and Bahl, O. P. (1986), *Carbon*, **24**, 757.

Donnet, J. B., Dhami, T. L., Dong, S. and Brendlé, M. (1987), *J. Phys. D., Appl. Phys.*, **20**, 269.

Ehrburger, P., Sanseigne, E., Tahon, B., (1996), *Carbon*, **34** (12), 1493–1499.

Ehrburger, P. (1990), in *Carbon Fibers and Filaments*, J. L. Figueiredo *et al*., ed., NATO ASI SERIES E: Applied Sciences – Kluwer Academic Publishers, **177**, 147–161.

Ehrburger, P. and Donnet, J. B. (1980), *Phil. Trans. R. Soc.,* London, **A294**, 495.

Ehrburger, P. and Donnet, J. B. (1985), in *Strong Fibers*, W. Watt and B. V. Perov eds, North-Holland, Amsterdam, 577–603.

Ehrburger, P. and Dallies-Labourdette, E. (1992), *TANSO*, **155**, 359.

Ehrburger, P., Baranne, P. and Lahaye, J. (1986),*Carbon*, **24**, 495.

Ehrburger, P., Herqué, J. J. and Donnet, J. B. (1975), in *Petroleum Derived Carbons*, ACS Symposium Series, **21**, 324–334, M. Deviney and T. O'Grady eds, The American Chemical Society.

Ehrburger, P., Herqué, J. J., and Donnet, J. B. (1978), *Proc. of the Fifth London International Carbon and Graphite Conference*, **1**, 303, The Society of Chemical Industry, London.

Fitzer, E. (1985), *Carbon Fibers and their Composites*, Springer-Verlag, Berlin.

Fitzer, E. (1977), *Carbon*, **16**, 3.

Fitzer, E. and Ebi, R. (1973), in *Silicon Carbide*, C. R. C. Marshall, J. W. Faust, and C. E. Ryan eds, 320–328, University of South Carolina Press, Columbia SC.

Fitzer, E. and Weiss, R. (1983), *Proc. 16th Biennial Conf. on Carbon*, The American Carbon Society, Univ. of San Diego, 473.

Fitzer, E., Geigl, K. H., Hüttner, W. and Weiss, R. (1979), *Carbon*, **18**, 389.

Franc, O. and Macret, J. L. (1990), in 'Proceedings of ESA Symposium, ESTEC,' Noordwijk, 21–23 March.

Garten, V. A. and Weiss, D. E. (1957), *Aust. J. Chem.* **10**, 309.

Garten, V. A. and Weiss, D. E. (1957), *Rev. Pure Appl. Chem. Aust.* **7**, 69.

Goujard, S., Vandenbulke, L. and Tawil, H. (1994), *J. Mater. Science*, **29**, 6212.

Granda, M., Patrick, J. W., Walker, A., Casal, E., Bermejo, J. and Menendez, R. (1998), *Carbon*, **36**, 7–8, 943.

Guilpain, G., PhD Thesis (1988), Ehede du traitement superficiel de fibres de carbone par voie électrolytique, Mulhouse (France).

Gulbransen, E. A. and Jansson, S. A. (1972), *Oxidation of Metals*, **4**, 181.

Hancox, N. L. and Wells, H. (1977), *Fiber Science Technol.*, **10**, 9.

Hart, P. J., Vastola, F. J. and Walker, P. L Jr. (1967), *Carbon*, **5**, 363.

Herman, G. and Hüttinger, K. J. (1986), *Carbon*, **24** (6), 705–713.

Hinze, J. W. and Graham, H. C. (1976), *J. Electrochem. Soc.*, **123**, 7, 1066.

Huettner, W. (1989), in *Carbon Fibers and Filaments Composites*, Figueiredo, J. L., Bernardo, C. A., Baker, R. T. K., and Hüttinger, K. J., eds, 275–300, Kluwer Academic Publishers, Dordrecht.

Hull, D. (1981), *An Introduction to Composite Materials*, Cambridge Solid State Science Series, Cambridge University Press.

Inagaki, M. (1991), *Carbon*, **29**, 287.

Isola, C., Appendino, P., Bosco, F., Ferraris, M. and Salvo, M. (1998), *Carbon*, **36**, 7–8, 1213.

Kinoshita, K. and Bett, J. A. S. (1973), *Carbon*, **11**, 403.

Kojima, A., Otani, S., Nakamura, K., Furukawa, S., Ohta, T. and Kurihara, H. (1989), *Tanso*, **136**, 9.

Kozlowski, C. and Sherwood, P. M. A. (1986), *Carbon*, **3**, 357.

Kuretzky, T. and Boehm, H. P. (1992), *Proc. Carbon'92*, Essen, Germany, 260.

Laine, N. R., Vastola, F. J. and Walker, P. L. Jr (1963), *J. Phys. Chem.*, **67**, 2030.

Leon Y Leon, C. A., Solar, J. M., Calemma, V. and Radovic, L. R. (1992), *Carbon*, **30**, 797.

Maeda, M., Nakamura, K. and Ohkubo, T. (1988), *J. Mat. Science*, **23**, 3933–3938.

Maschinen Fabrik Augsburg-Nürnberg AG (27 Sept., 1977), US Patent, 4050997.

McKee, D. W. (1991), in *Fundamentals Issues in Control of Carbon Gasification Reactivity* Lahaye, J. and Ehrburger, P., eds, 483–510, Kluwer Academic Publishers Dordrecht.

McKee, D. W. and Mimeault, V. J. (1973), in *Chemistry and Physics of Carbon*, P. L. Walker and P. A. Thrower, eds, **8**, 151–180, Marcel Dekker, New York.

McKee, D. W., Spiro, C. L., and Lamby, E. J. (1984a), *Carbon*, **22**, 285, 507.

More, K. L. (2000), J. Am. Ceram. Soc., **83**, 1, 211–213.

Nickel, K. G. (1992), *J. Europ. Ceram. Soc.*, **9**, 3–8.

Norton, F. J. (1961), *Nature*, **191**, 701.

Ohama, Y. (1989), *Carbon*, **27**, 729.

Opila, E. J. (1995), *J. Am. Ceram. Soc.*, **78**, 4, 1107–1110.

Opila, E. J. (1999), *J. Am. Ceram. Soc.*, **82**, 3, 625–636.

Papirer, E., Dentzer, J., Sheng, L. and Donnet, J. B. (1991), *Carbon*, **29**, 69.

Raymond, J. A., Yu, L. T., Boettner, J. C., Petit, J. C. and Ehrburger, P. (1985), *Bull. Soc. Chim. France*, **6**, 1147.

Rhône Progil (11 Feb. 1975), United States Patent, 3865 705.

Riess, G., Bourdeaux, M. Brie, M. and Jouquet, G. (1974), *Proc. 2nd Carbon Fibers Conference*, The Plastics Institute, London, 52.

Rocher, J. P., Girot, F., Quenisset, J. M., Pailler, R. and Naslain, R. (1986), *Revue de Métallurgie*, 69.

Rosner D. E. and Allendorf, H. D. (1970), *J. Phys. Chem.*, **74**, 1829.

Schiroky, G. H. (1987), *Advanced Ceramic Materials*, **2**, 2, 137–141.

Schultz J., Cazeneuve, C., Shanahan, M. E. R. and Donnet, J. B. (1981), *J. Adhesion*, **12**, 221.

Sheenan, J. E. (1989), *Carbon*, **27**, 709.

Smith, A. (1863), *Proc. Roy. Soc.*, **A12**, 424.

Strife, J. S. and Sheenan, J. E. (1988), *Ceramic Bulletin*, **67**, 369.

Tagahaki, T. and Ishitani, A. (1984), *Carbon*, **22**, 43.

Toray Industries Inc. (19 July 1972), Japanese Patent 47/26999.

Toray Industries Inc. (24 Oct. 1979), United Kingdom Patent Application 2018827 A.

Tredway, W. K., Prewo, K. M. and Pantano, C. G. (1989), *Carbon*, **27**, 717.

Vaughn, W. L. and Maahs, H. G. (1990), *J. Am. Ceram. Soc.*, **73**, 1540.

Vincent, H., Vincent, C., Sharff, J. P., Mourichoux, H. and Bouix, J. (1992), *Carbon*, **30**, 495.

Vix-Guterl, C., Lahaye, J. and Ehrburger, P. (1993), *Carbon*, **31**, 4, 629.

Vix-Guterl, C., Alix, I. and Ehrburger, P. (1999), in Proc. 'ECerS 1999' à Brighton (GB), Vol. I, 337–338.

Vix-Guterl, C., McEnaney, B. and Ehrburger, P. (1999), *J. European Ceramic Society*, **19**, no. 4, 427–432.

Vix-Guterl, C., Grotzinger, C., Dentzer, J., Bacos, M.-P. and Ehrburger, P. (2001), *J. European Ceramic Society*, **21**, 3, 315–323.

Voll, M. and Boehm, H. P. (1971), *Carbon*, **9**, 481.

Westwood, M. E., Webster, J. D., Day, R. J., Hayes, F. H. and Taylor, R., (1996), *J. Mat. Science*, **31**, 1389–1397.

Zawadski, J. (1989), in *Chemistry and Physics of Carbon*, P. A. Thrower ed., Vol. 21, 147–380, Marcel Dekker, New York.

Zheng, Z., Tressler, R. E. and Spear, K. E. (1990), *J. Electrochem. Soc.*, **137**, 3, 854–858.

10

CARBON–CEMENT COMPOSITES

D. D. L. Chung

1 Introduction

Carbon–cement composites refer to cement–matrix composites that contain carbon (e.g. carbon fibers). Carbon in a discontinuous form is usually used, because this form can be added to the cement mix in the mixer (i.e. it can be used as an admixture). In contrast, carbon in a continuous form cannot be used as an admixture. Mixing is the most convenient way of incorporating any ingredient in a cement-based material. Not only is mixing inexpensive, it can be done in the field. Another disadvantage of using continuous carbon fibers is the high cost of continuous fibers compared to discontinuous fibers. Low cost is essential for a concrete to be practical. Although there are many forms of discontinuous carbon, short carbon fibers are the only form that has been shown to be useful for improving the properties of cement-based materials. Therefore, this chapter is focused on cement–matrix composites containing short carbon fibers.

Carbon fiber cement–matrix composites are structural materials that are gaining in importance quite rapidly due to the decrease in carbon fiber cost (Newman, 1987) and the increasing demand of superior structural and functional properties. These composites contain short carbon fibers, typically 5 mm in length. However, due to the weak bond between carbon fiber and the cement matrix, continuous fibers (Furukawa *et al.*, 1987; Saito *et al.*, 1989; Wen and Chung, 1999a) are much more effective than short fibers in reinforcing concrete. Surface treatment of carbon fiber (e.g. by heating (Sugama *et al.*, 1989) or by using ozone (Fu *et al.*, 1996, 1998a), silane (Xu and Chung, 1999a, 2000), SiO_2 particles (Yamada *et al.*, 1991) or hot NaOH solution (Sugama *et al.*, 1988)) is useful for improving the bond between fiber and matrix, thereby improving the properties of the composite. In the case of surface treatment by ozone or silane, the improved bond is due to the enhanced wettability by water. Admixtures such as latex (Fu *et al.*, 1996; Larson *et al.*, 1990), methylcellulose (Fu *et al.*, 1996) and silica fume (Katz *et al.*, 1995) also help the bond.

The effect of carbon fiber addition on the properties of concrete increases with fiber volume fraction (Park and Lee, 1993), unless the fiber volume fraction is so high that the air void content becomes excessively high (Chen *et al.*, 1997). (The air void content increases with fiber content and air voids tend to have a negative effect on many properties, such as the compressive strength.) In addition, the workability of the mix decreases with fiber content (Park and Lee, 1993). Moreover, the cost increases with fiber content. Therefore, a rather low volume fraction of fibers is desirable. A fiber content as low as 0.2 vol% is effective (Chen and Chung, 1993a), although fiber contents exceeding 1 vol% are more common (Akihama *et al.*, 1984; Brandt and Kucharska, 1996). The required fiber content increases with the particle size of the aggregate, as the flexural strength decreases with increasing particle size (Kamakura *et al*., 1983).

Effective use of the carbon fibers in concrete requires dispersion of the fibers in the mix. The dispersion is enhanced by using silica fume (a fine particulate) as an admixture (Ohama and Amano, 1983; Ohama *et al*., 1985; Katz and Bentur, 1994; Chen *et al*., 1997). A typical silica fume content is 15% by weight of cement (Chen *et al*., 1997). The silica fume is typically used along with a small amount (0.4% by weight of cement) of methylcellulose for helping the dispersion of the fibers and the workability of the mix (Chen *et al*., 1997). Latex (typically 15–20% by weight of cement) is much less effective than silica fume for helping the fiber dispersion, but it enhances the workability, flexural strength, flexural toughness, impact resistance, frost resistance and acid resistance (Soroushian *et al*., 1991; Zayat and Bayasi, 1996; Chen *et al*., 1997). The ease of dispersion increases with decreasing fiber length (Ohama *et al*., 1985).

The improved structural properties rendered by carbon fiber addition pertain to the increased tensile and flexible strengths, the increased tensile ductility and flexural toughness, the enhanced impact resistance, the reduced drying shrinkage and the improved freeze-thaw durability (Kamakura *et al*., 1983; Ohama and Amano, 1983; Akihama *et al*., 1984; Ohama *et al*., 1985; Lal, 1990; Park and Lee, 1990; Soroushian, 1990; Park *et al*., 1991; Soroushian *et al*., 1992a,b; Park and Lee, 1993; Toutanji *et al*., 1993; Chen and Chung, 1993a; Katz and Bentur, 1994; Banthia *et al*., 1994a,b, 1998; Banthia and Sheng, 1996; Pigeon *et al*., 1996; Zayat and Bayasi, 1996; Chen *et al*., 1997). The tensile and flexural strengths decrease with increasing specimen size, such that the size effect becomes larger as the fiber length increases (Urano *et al*., 1996). The low drying shrinkage is valuable for large structures and for use in repair (Chen *et al*., 1995; Ali and Ambalavanan, 1998) and in joining bricks in a brick structure (Zhu and Chung, 1997; Zhu *et al*., 1997).

The functional properties rendered by carbon fiber addition pertain to the strain sensing ability (Chen and Chung, 1993b, 1995a, 1996a,b; Chung, 1995; Zhao *et al*., 1995; Fu and Chung, 1996, 1997a; Mao *et al*., 1996a,b; Fu *et al*., 1997, 1998a,b; Sun *et al*., 1998, 2000; Shi and Chung, 1999; Wen and Chung, 2000a, 2001a,b, 2002a,b) (for smart structures), the temperature sensing ability (Sun *et al*., 1998a,b; Wen and Chung, 1999b, 2000b–d), the damage sensing ability (Chen and Chung, 1993b, 1996b; Lee and Batson, 1996; Bontea *et al*., 2001; Wen and Chung, 20001f), the thermoelectric behavior (Chen and Chung, 1993b, 1996b; Sun *et al*., 1998a,b; Wen and Chung, 1999c, 2000b–d), the thermal insulation ability (Shinozaki, 1990; Fu and Chung, 1999; Xu and Chung, 1999b) (to save energy for buildings), the electrical conduction ability (Clemena, 1988; Banthia *et al*., 1992; Chen and Chung, 1993c, 1995b; Fu and Chung, 1995; Shui *et al*., 1995; Xie *et al*., 1996; Brousseau and Pye, 1997; Hou and Chung, 1997; Wang *et al*., 1998; Wen and Chung, 2001c–f) (to facilitate cathodic protection of embedded steel and to provide electrical grounding or connection), and the radio wave reflection/absorption ability (Shimizu *et al*., 1986; Fujiwara and Ujie, 1987; Fu and Chung, 1997b, 1998a,b) (for electromagnetic interference or EMI shielding, for lateral guidance in automatic highways, and for television image transmission).

In relation to the structural properties, carbon fibers compete with glass, polymer, and steel fibers (Lal, 1990; Mobasher and Li, 1994, 1996; Banthia *et al*., 1994a,b, 1998; Banthia and Sheng, 1996; Pigeon *et al*., 1996; Chen and Chung, 1996c). Carbon fibers (isotropic pitch based) (Chen and Chung, 1996c; Newman, 1987) are advantageous in their superior ability to increase the tensile strength of concrete, even though the tensile strength, modulus and ductility of the isotropic pitch based carbon fibers are low compared to most other fibers. Carbon fibers are also advantageous in the relative chemical inertness (Uomoto and Katsuki, 1994–5). PAN-based carbon fibers are also used (Ohama and Amano, 1983; Katz and Bentur, 1994; Toutanji *et al.*, 1993, 1994), although they are more commonly used as continuous fibers than short fibers. Carbon-coated glass fibers (Huang *et al.*, 1996, 1997) and submicron diameter carbon filaments (Shui *et al.*, 1995; Xie *et al.*, 1996; Fu and Chung, 1998a,b) are even less commonly used, although the former is attractive for the low cost of glass fibers and the latter is attractive for its high radio wave reflectivity (which results from the skin effect). C-shaped carbon fibers are more effective for strengthening than round carbon fibers (Kim and Park, 1998), but their relatively large diameter makes them less attractive. Carbon fibers can be used in concrete together with steel fibers, as the addition of short carbon fibers to steel fiber reinforced mortar increases the fracture toughness of the interfacial zone between steel fiber and the cement matrix (Igarashi and Kawamura, 1994). Carbon fibers can also be used in concrete together with steel bars (Bayasi and Zeng, 1997; Campione *et al.*, 1999), or together with carbon fiber reinforced polymer rods (Yamada *et al.*, 1995).

In relation to most functional properties, carbon fibers are exceptional compared to the other fiber types. Carbon fibers are electrically conducting, in contrast to glass and polymer fibers, which are not conducting. Steel fibers are conducting, but their typical diameter ($\geq 60\,\mu m$) is much larger than the diameter of a typical carbon fiber ($15\,\mu m$). The combination of electrical conductivity and small diameter makes carbon fibers superior to the other fiber types in the area of strain sensing and electrical conduction. However, carbon fibers are inferior to steel fibers for providing thermoelectric composites, due to the high electron concentration in steel and the low hole concentration in carbon.

Although carbon fibers are thermally conducting, addition of carbon fibers to concrete lowers the thermal conductivity (Fu and Chung, 1999), thus allowing applications related to thermal insulation. This effect of carbon fiber addition is due to the increase in air void content. The electrical conductivity of carbon fibers is higher than that of the cement matrix by about eight orders of magnitude, whereas the thermal conductivity of carbon fibers is higher than that of the cement matrix by only one or two orders of magnitude. As a result, the electrical conductivity is increased upon carbon fiber addition in spite of the increase in air void content, but the thermal conductivity is decreased upon fiber addition.

The use of pressure after casting (Delvasto *et al.*, 1986), and extrusion (Shao *et al.*, 1995; Park, 1998) can result in composites with superior microstructure and properties. Moreover, extrusion improves the shapability (Shao *et al.*, 1995).

This chapter is focused on short carbon fiber reinforced cement–matrix composites, including concrete (with fine and coarse aggregates), mortar (with fine aggregate and no coarse aggregate) and cement paste. Previous reviews are noted (Ohama, 1989; Inagaki,

Table 10.1 Properties of isotropic-pitch-based carbon fibers

Filament diameter	$15 \pm 3\,\mu m$
Tensile strength	690 MPa
Tensile modulus	48 GPa
Elongation at break	1.4%
Electrical resistivity	$3.0 \times 10^{-3}\,\Omega\,cm$
Specific gravity	$1.6\,g\,cm^{-3}$
Carbon content	98 wt%

1991; Lin, 1994; Zheng and Feldman, 1995; Banthia, 1996; Kucharska and Brandt, 1997; Chung, 1999, 2000).

Table 10.1 shows the properties of the isotropic-pitch-based carbon fibers (15 μm in diameter, nominally 5 mm long) used by the author in the cement–matrix composites described below for the purpose of illustration.

2 Structural behavior

The properties relevant to the structural behavior of cement–matrix composites containing short carbon fibers are given in this section.

Tables 10.2 and 10.3 show the tensile strength and modulus respectively of twelve types of cement pastes (Xu and Chung, 1999a, 2000). The strength is slightly increased by the addition of methylcellulose and defoamer, but the modulus is slightly decreased by the addition of methylcellulose and defoamer. However, both strength and modulus are increased by the addition of fibers. The effectiveness of the fibers in increasing strength and modulus increases in the following order: as-received fibers, O_3-treated fibers, dichromate-treated

Table 10.2 Tensile strength (MPa) of cement pastes with and without fibers

Formulation	*As-received silica fume*	*Silane-treated silica fume*
A	1.53 ± 0.06	2.04 ± 0.06
A^+	1.66 ± 0.07	2.25 ± 0.09
A^+F	2.00 ± 0.09	2.50 ± 0.11
A^+O	2.25 ± 0.07	2.67 ± 0.09
A^+K	2.32 ± 0.08	2.85 ± 0.11
A^+S	2.47 ± 0.11	3.12 ± 0.12

Notes
A: cement + water + water reducing agent + silica fume
A^+: A + methylcellulose + defoamer.
A^+F: A^+ + as-received fibers.
A^+O: A^+ + O_3-treated fibers.
A^+K: A^+ + dichromate-treated fibers.
A^+S: A^+ + silane-treated fibers.

Table 10.3 Tensile modulus (GPa) of cement pastes with and without fibers. Refer to Note in Table 10.2

Formulation	*As-received silica fume*	*Silane-treated silica fume*
A	10.2 ± 0.7	11.5 ± 0.6
A^+	9.3 ± 0.5	10.7 ± 0.4
A^+F	10.9 ± 0.3	12.9 ± 0.7
A^+O	11.9 ± 0.3	13.1 ± 0.6
A^+K	12.7 ± 0.4	14.3 ± 0.4
A^+S	13.3 ± 0.5	15.2 ± 0.8

Table 10.4 Tensile ductility (%) of cement pastes with and without fibers. Refer to Note in Table 10.2

Formulation	*As-received silica fume*	*Silane-treated silica fume*
A	0.020 ± 0.0004	0.020 ± 0.0004
A^+	0.023 ± 0.0004	0.021 ± 0.0004
A^+F	0.025 ± 0.0003	0.024 ± 0.0004
A^+O	0.026 ± 0.0003	0.027 ± 0.0004
A^+K	0.028 ± 0.0003	0.030 ± 0.0004
A^+S	0.031 ± 0.0004	0.034 ± 0.0004

Table 10.5 Air void content (%, ± 0.12) of cement pastes with and without fibers. Refer to Note in Table 10.2

Formulation	*As-received silica fume*	*Silane-treated silica fume*
A	3.73	3.26
A^+	3.42	3.01
A^+F	5.32	4.89
A^+O	5.07	4.65
A^+K	5.01	4.49
A^+S	4.85	4.16

fibers, and silane-treated fibers. This trend applies whether the silica fume is as-received or silane-treated. For any of the formulations, silane-treated silica fume gives substantially higher strength and modulus than as-received silica fume. The highest tensile strength and modulus are exhibited by cement paste with silane-treated silica fume and silane-treated fibers. Silane treatments of silica fume and of fibers are about equally valuable in providing strengthening.

Table 10.4 shows the tensile ductility. It is slightly increased by the addition of methylcellulose and defoamer, and is further increased by the further addition of fibers. The effectiveness of the fibers in increasing the ductility also increases in the above order. This trend applies whether the silica fume is as-received or silane-treated. For any of the formulations involving surface treated fibers, silane-treated silica fume gives higher ductility than as-received silica fume. The highest ductility is exhibited by cement paste with silane-treated silica fume and silane-treated fibers.

Table 10.5 shows the air void content. It is decreased by the addition of methylcellulose and defoamer, but is increased by the further addition of fibers, whether the fibers have been surface treated or not. Among the formulations with fibers, the air void content decreases in the following order: as-received fibers, O_3-treated fibers, dichromate-treated fibers and silane-treated fibers. This trend applies whether the silica fume is as-received or silane-treated. For any of the formulations (including those without fibers), silane-treated silica fume gives lower air void content than as-received silica fume.

Tables 10.6 and 10.7 give the dynamic flexural properties of twelve types of cement pastes. Six of the types have as-received silica fume; the other six have silane-treated silica fume. The loss tangent (Table 10.6) is increased slightly by the addition of methylcellulose.

Table 10.6 Loss tangent (tan δ, ± 0.002) of cement pastes. Refer to Note in Table 10.2

Formulation	*With as-received silica fume* (Hz)			*With silane-treated silica fume* (Hz)		
	0.2	*1.0*	*2.0*	*0.2*	*1.0*	*2.0*
A	0.082	0.030	$<10^{-4}$	0.087	0.032	$<10^{-4}$
A^+	0.102	0.045	$<10^{-4}$	0.093	0.040	$<10^{-4}$
A^+F	0.089	0.033	$<10^{-4}$	0.084	0.034	$<10^{-4}$
A^+O	0.085	0.043	$<10^{-4}$	0.084	0.032	$<10^{-4}$
A^+K	0.079	0.039	$<10^{-4}$	0.086	0.035	$<10^{-4}$
A^+S	0.076	0.036	$<10^{-4}$	0.083	0.033	$<10^{-4}$

Table 10.7 Storage modulus (GPa, ± 0.03) of cement pastes. Refer to Note in Table 10.2

Formulation	*With as-received silica fume* (Hz)			*With silane-treated silica fume* (Hz)		
	0.2	*1.0*	*2.0z*	*0.2*	*1.0*	*2.0*
A	12.71	12.14	11.93	16.75	16.21	15.95
A^+	11.52	10.61	10.27	15.11	14.73	14.24
A^+F	13.26	13.75	13.83	17.44	17.92	18.23
A^+O	14.14	14.46	14.72	18.92	19.36	19.57
A^+K	15.42	16.15	16.53	19.33	19.85	20.23
A^+S	17.24	17.67	15.95	21.34	21.65	21.97

Table 10.8 Drying shrinkage strain (10^{-4}, ± 0.015) different curing ages

Formulation	*With as-received silica fume* (days)				*With silane-treated silica fume* (days)			
	1	*4*	*8*	*19*	*1*	*4*	*8*	*19*
B	1.128	3.021	3.722	4.365	1.013	2.879	3.623	4.146
BF	0.832	2.417	3.045	3.412	0.775	2.246	2.810	3.113
BO	0.825	2.355	3.022	3.373	0.764	2.235	2.793	3.014
BK	0.819	2.321	3.019	3.372	0.763	2.232	2.790	3.010
BS	0.812	2.316	2.976	3.220	0.752	2.118	2.724	2.954

Notes
B: cement + water + water reducing agent + silica fume + methylcellulose + defoamer.
BF: B + as-received fibers.
BO: B + O_3-treated fibers.
BK: B + dichromate-treated fibers.
BS: B + silane-treated fibers.

Further addition of carbon fibers decreases the loss tangent. The loss tangent decreases in the following order: as-received fibers, ozone-treated fibers, dichromate-treated fibers and silane-treated fibers, at least for the case of as-received silica fume at 0.2 Hz. The storage modulus (Table 10.7) is decreased by the addition of methylcellulose. Further addition of carbon fibers increases the storage modulus, such that the modulus increases in the order: as-received fibers, ozone-treated fibers, dichromate-treated fibers and silane-treated fibers.

Table 10.8 gives the drying shrinkage strain of ten types of cement paste as a function of curing age. The drying shrinkage is decreased by the addition of carbon fibers, such that it decreases in the following order: as-received fibers, ozone-treated fibers, dichromate-treated fibers, and silane-treated fibers. The drying shrinkage is decreased by the use of silane-treated silica fume in place of as-received silica fume, whether fibers are present or not.

3 Thermal behavior

Table 10.9 shows the specific heat of cement pastes (Xu and Chung, 1999b, 2000). The specific heat is significantly increased by the addition of silica fume. It is further increased by the further addition of methylcellulose and defoamer. It is still further increased by the still further addition of carbon fibers. The effectiveness of the fibers in increasing the specific heat increases in the following order: as-received fibers, O_3-treated fibers, dichromate-treated fibers and silane-treated fibers. For any of the formulations, silane-treated silica fume gives higher specific heat than as-received silica fume. The highest specific heat is exhibited by the cement paste with silane-treated silica fume and silane-treated fibers. Silane treatment of fibers is more valuable than that of silica fume for increasing the specific heat.

Table 10.10 shows the thermal conductivity. It is significantly decreased by the addition of silica fume. The further addition of methylcellulose and defoamer or the still further

Table 10.9 Specific heat ($Jg^{-1}K^{-1}$, ± 0.001) of cement pastes. The value for plain cement paste (with cement and water only) is $0.736\,J\,g^{-1}K^{-1}$. Refer to Note in Table 10.2

Formulation	*As-received silica fume*	*Silane-treated silica fume*
A	0.782	0.788
A^+	0.793	0.803
A^+F	0.804	0.807
A^+O	0.809	0.813
A^+K	0.812	0.816
A^+S	0.819	0.823

Table 10.10 Thermal conductivity ($Wm^{-1}K^{-1}$, ± 0.03) of cement pastes. The value for plain cement paste (with cement and water only) is 0.53 $Wm^{-1}K^{-1}$. Refer to Note in Table 10.2

Formulation	*As-received silica fume*	*Silane-treated silica-fume*
A	0.35	0.33
A^+	0.34	0.30
A^+F	0.35	0.34
A^+O	0.38	0.36
A^+K	0.39	0.37
A^+S	0.34	0.32

addition of fibers has little effect on the density. Surface treatment of the fibers by ozone or dichromate slightly increases the thermal conductivity, whereas surface treatment of the fibers by silane has negligible effect. For any of the formulations, silane-treated silica fume gives slightly lower (or essentially the same) thermal conductivity as as-received silica fume. Silane treatments of silica fume and of fibers contribute comparably to reducing the thermal conductivity.

4 Electrical behavior

Figure 10.1 gives the volume electrical resistivity of composites at seven days of curing. The resistivity decreases much with increasing fiber volume fraction, whether a second filler (silica fume or sand) is present or not (Chen and Chung, 1995b). When sand is absent, the addition of silica fume decreases the resistivity at all fiber volume fractions except the highest volume fraction of 4.24%; the decrease is most significant at the lowest fiber volume fraction of 0.53%. When sand is present, the addition of silica fume similarly decreases the resistivity, such that the decrease is most significant at fiber volume fractions below 1%. When silica fume is absent, the addition of sand decreases the resistivity only when the fiber volume fraction is below about 0.5%; at high fiber volume fractions, the addition of sand even increases the resistivity due to the porosity induced by the sand. Thus, the addition of a second filler (silica fume or sand) that is essentially non-conducting decreases the resistivity of the composite only at low volume fractions of the carbon fibers and the maximum fiber volume fraction for the resistivity to decrease is larger when the particle size of the filler is smaller. The resistivity decrease is attributed to the improved fiber dispersion due to

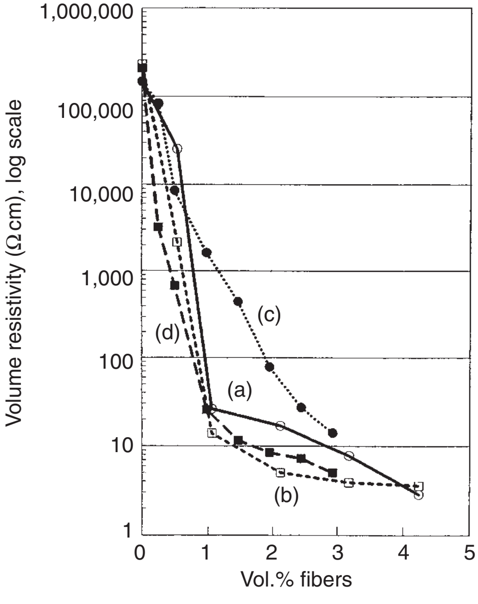

Figure 10.1 Variation of the volume electrical resistivity with carbon fiber volume fraction (Chen and Chung, 1995b). (a) Without sand, with methylcellulose, without silica fume; (b) Without sand, with methylcellulose, with silica fume; (c) With sand, with methylcellulose, without silica fume; (d) With sand, with methylcellulose, with silica fume.

the presence of the second filler. Consistent with the improved fiber dispersion is the increased flexural toughness and strength due to the presence of the second filler.

The use of both silica fume and sand results in an electrical resistivity of $3.19 \times 10^3\ \Omega\,\text{cm}$ at a carbon fiber volume fraction of just 0.24 vol. %. This is an outstandingly low resistivity value compared to those of polymer-matrix composites with discontinuous conducting fillers at similar volume fractions.

Electrical conduction in cement reinforced by short carbon fibers below the percolation threshold is governed by carrier hopping across the fiber-matrix interface. The activation energy is decreased by increasing the fiber crystallinity, but is increased by using intercalated fibers. The carbon fibers contribute to hole conduction, which is further enhanced by intercalation, thereby decreasing the absolute thermoelectric power and the resistivity (Wen and Chung, 2001e).

Electric polarization induces an increase of the measured electrical resistivity of carbon fiber reinforced cement paste during resistivity measurement. The effect is diminished by increasing the conductivity of the cement paste through the use of carbon fibers that are more crystalline, the increase of the fiber content, or the use of silica fume instead of latex as an admixture. Intercalation of crystalline fibers further increases the conductivity of the composite, but it increases the extent of polarization. Voltage polarity switching effects are dominated by the polarization of the sample itself when the four-probe method is used, but are dominated by the polarization at the contact-sample interface when the two-probe method is used. Polarization reversal is faster and more complete for the latter (Wen and Chung, 2001d).

5 Radio wave reflectivity

Due to the electrical conductivity of carbon fibers, the addition of carbon fibers to cement significantly increases the ability of the composite to reflect radio waves, thus allowing EMI shielding and lateral guidance in automatic highways. However, due to the skin effect (the phenomenon in which electromagnetic radiation at a high frequency, such as 1 GHz, penetrates only the near surface region of a conductor), discontinuous carbon filaments of 0.1 μm diameter, as made from carbonaceous gases by catalytic growth, are much more effective for radio wave reflection than conventional pitch-based carbon fibers of diameter 15 μm (Fu and Chung, 1997b, 1998a,b). However, the 0.1 μm diameter filaments are less effective than the 15 μm diameter fibers as a reinforcement.

The cement–matrix composites are more effective than corresponding polymer–matrix composites for radio wave reflection, due to the slight conductivity of the cement matrix and the insulating nature of the polymer matrix. The conductivity of the cement matrix allows some electrical connectivity of the filler units, even when the filler concentration is below the percolation threshold (Fu and Chung, 1998b).

6 Cathodic protection of steel reinforcement in concrete

Cathodic protection is one of the most common and effective methods for corrosion control of steel reinforced concrete. This method involves the application of a voltage so as to force electrons to go to the steel reinforcing bar (rebar), thereby making the steel a cathode. As the steel rebar is embedded in concrete, the electrons need to go through the concrete in order to reach the rebar. However, concrete is not electrically very conductive. The use of carbon fiber reinforced concrete for embedding the rebar to be cathodically protected facilitates cathodic protection, as the short carbon fibers enhance the conductivity of the concrete. Although the increase in conductivity is not desirable for the corrosion resistance of the embedded rebar, the presence of either silica fume or latex along with the fibers compensates for this negative effect, because the silica fume or latex reduces the water absorptivity (Hou and Chung, 2000).

For directing electrons to the steel reinforced concrete to be cathodically protected, an electrical contact is needed on the concrete. The electrical contact is electrically connected to the voltage supply. One of the choices of an electrical contact material is zinc, which is a coating deposited on the concrete by thermal spraying. It has a very low volume resistivity (thus requiring no metal mesh embedment), but it suffers from poor wear and corrosion resistance, the tendency to oxidize, high thermal expansion coefficient, and high material and processing costs. Another choice is a conductor filled polymer (Pangrazzi *et al.*, 1994), which can be applied as a coating without heating, but it suffers from poor wear resistance, high thermal expansion coefficient and high material cost. Yet another choice is a metal (e.g. titanium) strip or wire embedded at one end in cement mortar, which is in the form of a coating on the steel reinforced concrete. The use of carbon fiber reinforced mortar for this coating facilitates cathodic protection, as it is advantageous to enhance the conductivity of this coating.

Due to the decrease in volume electrical resistivity associated with carbon fiber addition (0.35 vol%) to concrete (embedding steel rebar), concrete containing carbon fibers and silica fume reduces by 18% the driving voltage required for cathodic protection compared to plain concrete, and by 28% compared to concrete with silica fume. Due to the decrease in resistivity associated with carbon fiber addition (1.1 vol%) to mortar, overlay (embedding titanium wires for electrical contacts to steel reinforced concrete) in the form of mortar containing carbon fibers and latex reduces by 10% the driving voltage required for cathodic protection, compared to plain mortar overlay. In spite of the low resistivity of mortar overlay with carbon fibers, cathodic protection requires multiple metal electrical contacts embedded in the mortar at a spacing of 11 cm or less.

7 Strain sensing

Cement reinforced with short carbon fibers is capable of sensing its own strain due to the effect of strain on the volume electrical resistivity (a phenomenon known as piezoresistivity) (Chen and Chung, 1993b, 1995a, 1996a,b; Chung, 1995; Zhao *et al.*, 1995; Fu and Chung, 1996, 1997a; Fu *et al.*, 1996, 1997, 1998b; Mao *et al.*, 1996a,b; Sun *et al.*, 1998; Shi and Chung, 1999; Wen and Chung, 2000a, 2001a) and due to the effect of strain on the relative dielectric constant (a phenomenon known as direct piezoelectricity) (Wen and Chung, 2002a,b).

7.1 Piezoresistivity

Uniaxial tension of carbon fiber reinforced cement in the elastic regime causes reversible increases in the volume electrical resistivity in both longitudinal and transverse directions, such that the gage factor (fractional change in resistance per unit strain) is comparable in magnitude in the two directions (Wen and Chung, 2000a). In contrast, uniaxial compression causes reversible decreases in the resistivity in both directions (Wen and Chung, 2001a).

Table 10.11 Gage factor of carbon-fiber cement pastes under uniaxial compression and under uniaxial tension (Wen and Chung, 2000a, 2001a)

	Carbon-fiber silica-fume cement paste	*Carbon-fiber latex cement paste*
Compression		
Longitudinal	+350	+210
Transverse	−390	−80
Tension		
Longitudinal	+89	+51
Transverse	−59	−36

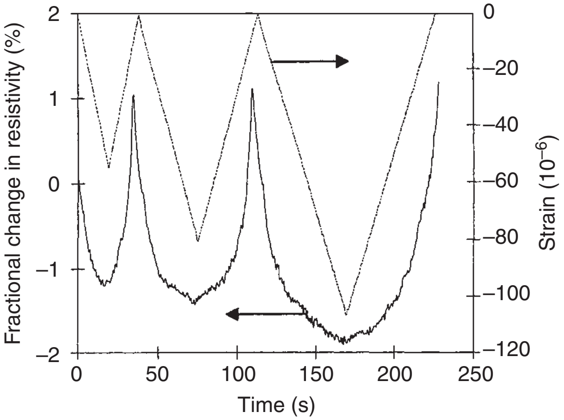

Figure 10.2 Variation of the fractional change in volume electrical resistivity with time and of the strain (negative for compressive strain) with time during dynamic compressive loading at increasing stress amplitudes within the elastic regime for carbon-fiber latex cement paste at 28 days of curing (Wen and Chung, 2001a).

Without the fibers, the resistivity changes are much smaller and less reversible. The resistivity increase is attributed to defect generation or aggravation under tension and defect healing under compression. The fractional change in resistance per unit strain (i.e. the gage factor) is higher in magnitude for carbon-fiber silica-fume cement paste than carbon-fiber latex cement paste, as shown in Table 10.11.

Figure 10.2 shows the fractional change in resistivity along the stress axis as well as the strain during repeated compressive loading at an increasing stress amplitude for carbon-fiber latex cement paste at 28 days of curing. The strain varies linearly with the stress up to the highest stress amplitude. The strain returns to zero at the end of each cycle of loading. The resistivity decreases upon loading in every cycle (due to fiber push-in) and increases upon unloading in every cycle (due to fiber pull-out). The resistivity has a net increase after the first cycle, due to very minor damage. Little further damage occurs in subsequent cycles, as shown by the resistivity after unloading not increasing much after the first cycle. The greater the strain amplitude, the more is the resistivity decrease during loading, although the

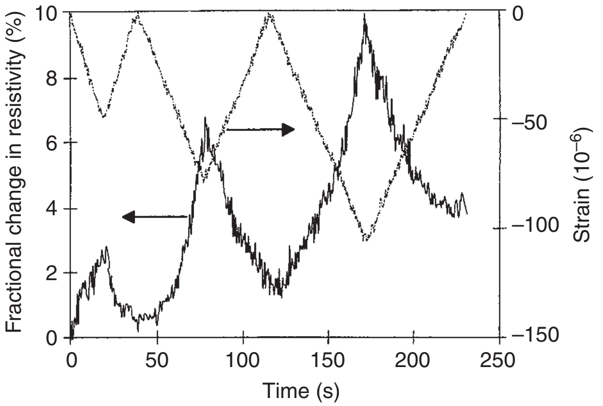

Figure 10.3 Variation of the fractional change in volume electrical resistivity with time and of the strain (negative for compressive strain) with time during dynamic compressive loading at increasing stress amplitudes within the elastic regime for carbon-fiber latex cement paste at 7 days of curing (Wen and Chung, 2001a).

resistivity and strain are not linearly related. The effects of Fig. 10.2 were similarly observed in carbon-fiber silica-fume cement paste at 28 days of curing.

Figure 10.3 gives the corresponding plots for carbon-fiber latex cement paste at 7 days of curing. Comparison of Figs 10.2 and 10.3 shows that (i) the resistivity increases upon loading at 7 days (Figs 10.3), but decreases upon loading at 28 days (Fig. 10.2); (ii) the resistivity increase upon loading at 7 days is not totally reversible, whereas the resistivity decrease upon loading at 28 days is totally reversible; and (iii) the fractional increase in resistivity upon loading is up to 10% at 7 days, but the fractional decrease in resistivity upon loading is only up to 2% at 28 days, though R_0 is similar at 7 and 28 days. The effects in Fig. 10.3 were similarly observed in carbon-fiber silica-fume cement paste at 7 days. The changeover from the 7-day behavior to the 28-day behavior occurs between 7 and 14 days.

Although the fractional change in resistivity upon loading is larger at 7 days (Fig. 10.3) than at 28 days (Fig. 10.2) for carbon-fiber latex cement paste, the greater reversibility upon unloading and the less noise in the resistivity variation at 28 days makes the behavior at 28 days more attractive than that at 7 days for use in resistance-based strain sensing. In practice, concrete is used in a fully cured state (exceeding 28 days of curing). Therefore, the behavior at 28 days is practically more important than that at 7 days. Nevertheless, the behavior at 7 days is of fundamental interest.

Comparison of Figs 10.4 and 10.3 (both at 7 days) shows that the effects are qualitatively similar with fibers (Fig. 10.3) and without fibers (Fig. 10.4), though (i) the fractional change in resistivity is larger in the presence of fibers; and (ii) the resistivity increase upon loading is more reversible in the presence of fibers. Thus, the origins of the effects in Figs 10.4 and 10.3 are basically similar, though the presence of fibers, which are electrically conductive, in Fig. 10.3 adds to the types of defects that are generated upon loading and the fiber-related defects make the resistivity changes more pronounced and more reversible.

Comparison of Figs 10.5 and 10.2 (both at 28 days) shows that the effects are qualitatively and quantitatively different between latex cement paste (Fig. 10.5) and carbon-fiber latex

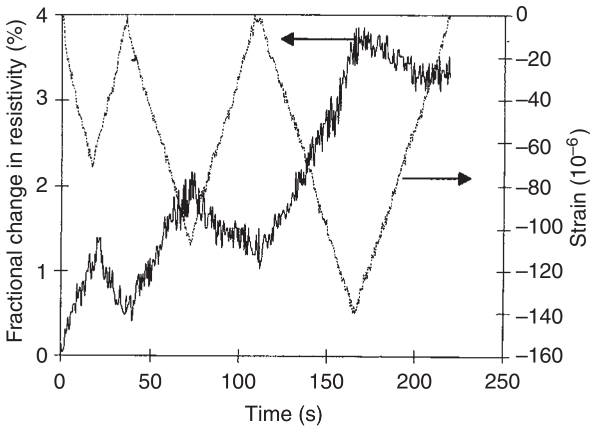

Figure 10.4 Variation of the fractional change in volume electrical resistivity with time and of the strain (negative for compressive strain) with time during dynamic compressive loading at increasing stress amplitudes within the elastic regime for latex cement paste at 7 days of curing (Wen and Chung, 2001a).

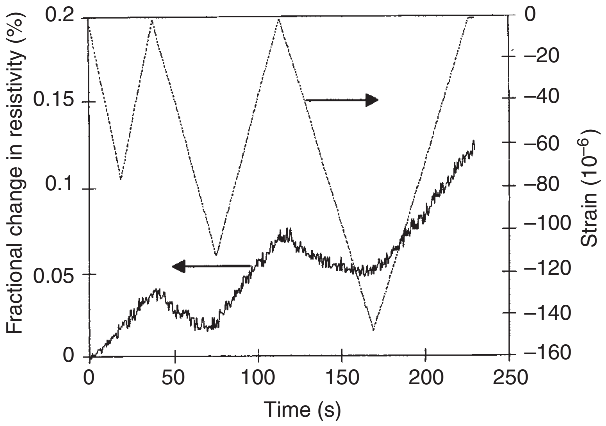

Figure 10.5 Variation of the fractional change in volume electrical resistivity with time and of the strain (negative for compressive strain) with time during dynamic compressive loading at increasing stress amplitudes within the elastic regime for latex cement paste at 28 days of curing (Wen and Chung, 2001a).

cement paste (Fig. 10.2). In the presence of carbon fibers, the resistivity decreases reversibly upon loading; in the absence of fibers, the resistivity mainly increases upon unloading.

Figures 10.2–10.5 show that the effect of carbon fibers on the variation of the resistivity with strain is more drastic at 28 days than at 7 days.

7.2 Direct piezoelectricity

The direct piezoelectric effect was observed in cement pastes by voltage measurement (Sun *et al.*, 2000) and by measurement of the relative dielectric constant (10 kHz) (Wen and

Chung, 2001b) in the stress direction during repeated compressive loading (Wen and Chung, 2002a,b). The effect is particularly large when the cement paste contains short steel fibers (8 μm diameter, 0.18 vol. %) and polyvinyl alcohol (0.16 vol. %). In this case, the longitudinal piezoelectric coupling coefficient is $2.5 \times 10^{-11}\,\mathrm{mV}^{-1}$ and the piezoelectric voltage coefficient is $1.1 \times 10^{-3}\,\mathrm{m}^2\,\mathrm{C}^{-1}$ (10 kHz) (Wen and Chung, 2002a).

8 Damage sensing

Figure 10.6 (Bontea *et al.*, 2000) shows the fractional change in longitudinal resistance, strain and stress during repeated compressive loading at increasing and decreasing stress amplitudes for carbon fiber concrete at 28 days of curing. The highest stress amplitude is 60% of the compressive strength. A group of cycles in which the stress amplitude increases cycle by cycle and then decreases cycle by cycle back to the initial low stress amplitude is hereby referred to as a group. Figure 10.6 shows the results for three groups. The strain returns to zero at the end of each cycle for any of the stress amplitudes, indicating elastic behavior. The resistance decreases upon loading in each cycle, as in Fig. 10.2. An extra peak at the maximum stress of a cycle grows as the stress amplitude increases, resulting in two peaks per cycle. The original peak (strain induced) occurs at zero stress, while the extra peak (damage induced) occurs at the maximum stress. Hence, during loading from zero stress within a cycle, the resistance drops and then increases sharply, reaching the maximum resistance of the extra peak at the maximum stress of the cycle. Upon subsequent unloading, the resistance decreases and then increases as unloading continues, reaching the maximum resistance of the original peak at zero stress. In the part of this group where the stress

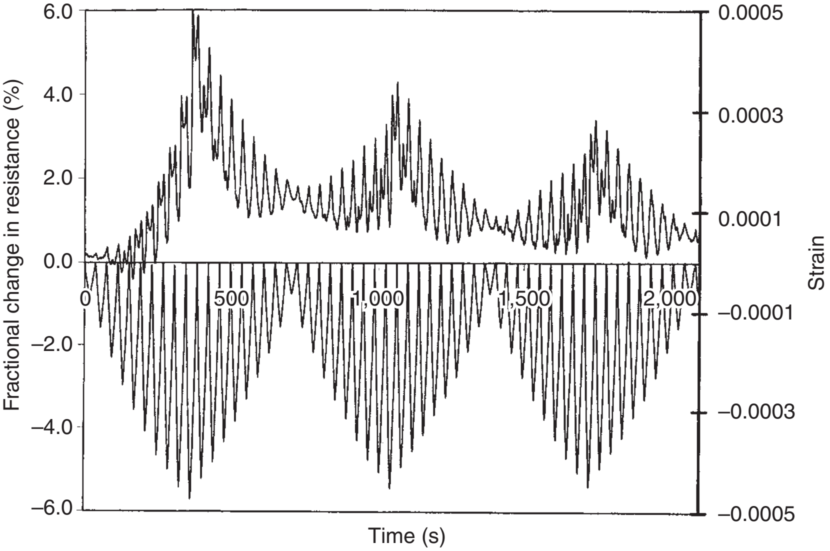

Figure 10.6 Fractional change in resistance and strain during repeated compressive loading at increasing and decreasing stress amplitudes, the highest of which was 60% of the compressive strength, for carbon fiber concrete at 28 days of curing (Bontea *et al.*, 2000).

amplitude decreases cycle by cycle, the extra peak diminishes and disappears, leaving the original peak as the sole peak. In the part of the second group where the stress amplitude increases cycle by cycle, the original peak (peak at zero stress) is the sole peak, except that the extra peak (peak at the maximum stress) returns in a minor way (more minor than in the first group) as the stress amplitude increases. The extra peak grows as the stress amplitude increases, but, in the part of the second group in which the stress amplitude decreases cycle by cycle, it quickly diminishes and vanishes, as in the first group. Within each group, the amplitude of resistance variation increases as the stress amplitude increases and decreases as the stress amplitude subsequently decreases.

The greater the stress amplitude, the larger and the less reversible is the damage-induced resistance increase (the extra peak). If the stress amplitude has been experienced before, the damage-induced resistance increase (the extra peak) is small, as shown by comparing the result of the second group with that of the first group (Fig. 10.6), unless the extent of damage is large (Fig. 10.7 for a highest stress amplitude of > 90% the compressive strength). When the damage is extensive (as shown by a modulus decrease), damage-induced resistance increase occurs in every cycle, even at a decreasing stress amplitude, and it can overshadow the strain-induced resistance decrease (Fig. 10.7). Hence, the damage-induced resistance increase occurs mainly during loading (even within the elastic regime), particularly at a stress above that in prior cycles, unless the stress amplitude is high and/or damage is extensive.

At a high stress amplitude, the damage-induced resistance increase cycle by cycle as the stress amplitude increases causes the baseline resistance to increase irreversibly (Fig. 10.7). The baseline resistance in the regime of major damage (with a decrease in modulus)

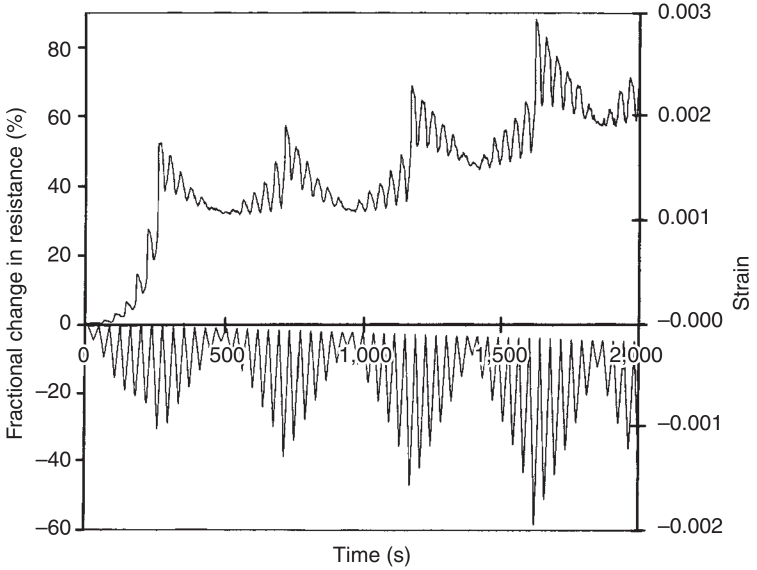

Figure 10.7 Fractional change in resistance and strain during repeated compressive loading at increasing and decreasing stress amplitudes, the highest of which was > 90% of the compressive strength, for carbon fiber concrete at 28 days of curing (Bontea *et al.*, 2000).

provides a measure of the extent of damage (i.e. condition monitoring). This measure works in the loaded or unloaded state. In contrast, the measure using the damage-induced resistance increase (Fig. 10.6) works only during stress increase and indicates the occurrence of damage (whether minor or major) as well as the extent of damage.

The damage causing the partially reversible damage-induced resistance increase is probably mainly associated with partially reversible degradation of the fiber-matrix interface. The reversibility rules out fiber fracture as the main type of damage, especially at a low stress amplitude. At a high stress amplitude, the extent of reversibility diminishes and fiber fracture may contribute to causing the damage. Fiber fracture can occur during the opening of a crack that is bridged by a fiber. The fiber-matrix interface degradation may be associated with slight fiber pull-out upon slight crack opening for cracks that are bridged by fibers. The severity of the damage-induced resistance increase supports the involvement of the fibers in the damage mechanism.

9 Temperature sensing through the thermistor effect

A thermistor is a thermometric device consisting of a material (typically a simiconductor, but in this case a cement paste) whose electrical resistivity decreases with rise in temperature.

Figure 10.8 (Wen and Chung, 1999b) shows the current–voltage characteristic of carbon-fiber (0.5% by weight of cement) silica-fume (15% by weight of cement) cement paste at 38 °C during stepped heating. The characteristic is linear below 5 V and deviates positively from linearity beyond 5 V. The resistivity is obtained from the slope of the linear portion. The voltage at which the characteristic starts to deviate from linearity is referred to as the critical voltage.

Figure 10.9 shows a plot of the resistivity versus temperature during heating and cooling for carbon-fiber silica-fume cement paste. The resistivity decreases upon heating and the effect is quite reversible upon cooling. That the resistivity is slightly increased after a heating-cooling cycle is probably due to thermal degradation of the material. From the Arrhenius plot of log conductivity (conductivity = 1/resistivity) versus reciprocal absolute temperature, the activation energy was found to be 0.390 ± 0.014 and 0.412 ± 0.017 eV during heating and cooling, respectively.

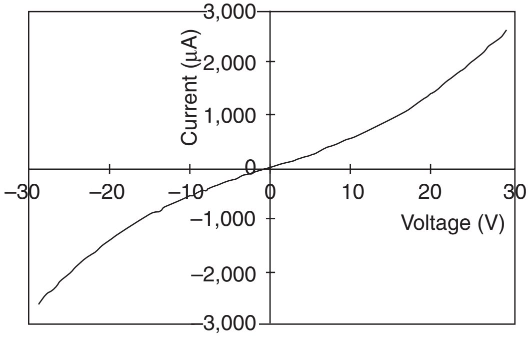

Figure 10.8 Current–voltage characteristic of carbon-fiber silica-fume cement paste at 38 °C during stepped heating (Wen and Chung, 1999b).

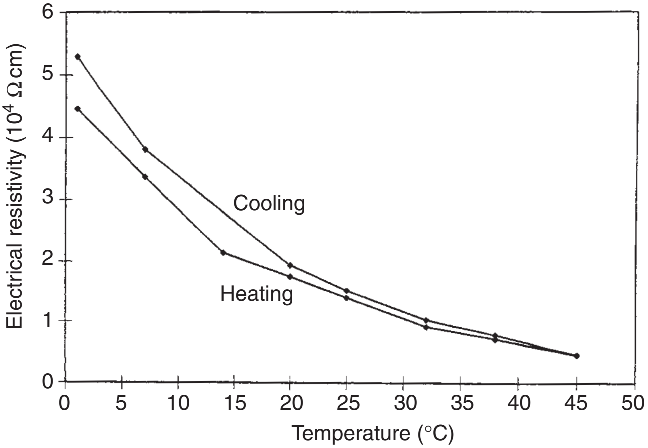

Figure 10.9 Plot of volume electrical resistivity versus temperature during heating and cooling for carbon-fiber silica-fume cement paste (Wen and Chung, 1999b).

Table 10.12 Resistivity, critical voltage and activation energy of five types of cement paste (Wen and Chung, 1999b)

Formulation	*Resistivity at 20°C* (Ω cm)	*Critical voltage at 20°C* (V)	*Activation energy* (eV)	
			Heating	*Cooling*
Plain	$(4.87 \pm 0.37) \times 10^5$	10.80 ± 0.45	0.040 ± 0.006	0.122 ± 0.006
Silica fume	$(6.12 \pm 0.15) \times 10^5$	11.60 ± 0.37	0.035 ± 0.003	0.084 ± 0.004
Carbon fibers + silica fume	$(1.73 \pm 0.08) \times 10^4$	8.15 ± 0.34	0.390 ± 0.014	0.412 ± 0.017
Latex	$(6.99 \pm 0.12) \times 10^5$	11.80 ± 0.31	0.017 ± 0.001	0.025 ± 0.002
Carbon fibers + latex	$(9.64 \pm 0.08) \times 10^4$	8.76 ± 0.35	0.018 ± 0.001	0.027 ± 0.002

Results similar to those of carbon-fiber silica-fume cement paste were obtained with carbon-fiber (0.5% by weight of cement) latex (20% by weight of cement) cement paste, silica-fume cement paste, latex cement paste, and plain cement paste. However, for all these four types of cement paste, (i) the resistivity is higher by about an order of magnitude; and (ii) the activation energy is lower by about an order of magnitude, as shown in Table 10.12. The critical voltage is higher when fibers are absent (Table 10.12).

10 Thermoelectric behavior

The Seebeck effect is a thermoelectric effect which is the basis for thermocouples for temperature measurement. This effect involves charge carriers moving from a hot point to a cold point within a material, thereby resulting in a voltage difference between the two points. The Seebeck coefficient is the voltage difference (hot minus cold) per unit temperature difference (hot minus cold) between the two points. Negative carriers (electrons) make it more negative and positive carriers (holes) make it more positive.

Eight types of cement paste were studied comparitively, namely (i) plain cement paste (consisting of just cement and water); (ii) silica-fume cement paste (consisting of cement, water, and silica fume); (iii) carbon-fiber silica-fume cement paste (consisting of cement, water, silica fume, methylcellulose, defoamer, and carbon fibers in the amount of 0.5% by weight of cement); (iv) carbon-fiber silica-fume cement paste (same as (iii) except for having carbon fibers in the amount of 1.0% by weight of cement); (v) carbon-fiber silica-fume cement paste (same as (iii) except for having carbon fibers in the amount of 1.5% by weight of cement); (vi) latex cement paste (consisting of cement, water, latex, and antifoam); (vii) carbon-fiber latex cement paste (consisting of cement, water, latex, antifoam, and carbon fibers in the amount of 0.5% by weight of cement; and (viii) carbon-fiber latex cement paste (same as (vii) except for having carbon fibers in the amount of 1.0% by weight of cement).

Table 10.13 (Wen and Chung, 1999c, 2000b–d) shows the Seebeck coefficient (with copper as the reference) and the absolute thermoelectric power. A positive value of the absolute thermoelectric power indicates p-type (hole) behavior; a negative value indicates n-type (electron) behavior. All types of cement paste studied are n-type except pastes (iv) and (v), which were p-type. The higher the fiber content, the less n-type (the more p-type) is the paste, whether silica fume or latex is present. Without fibers, the absolute thermoelectric power is − 2 μV/ °C, whether silica fume and latex are present or not. This is consistent with the similar values of the electrical conductivity for cement pastes with silica fume and with latex, but without fibers. Thus, silica fume or latex addition does not have much influence on the thermoelectric power when fibers are absent, but carbon fiber addition does by enhancing the hole conduction.

As shown in Table 10.13, the thermopower results obtained during heating and cooling are very close. Figure 10.10 shows the variation of the Seebeck voltage versus the temperature difference during heating and cooling for paste (iii). With fibers present, the variation is linear and essentially identical during heating and cooling. Without fibers, the variation is non-linear and hysteretic (i.e. not totally reversible upon cooling subsequent to heating). Thus, although the fiber addition does not increase the magnitude of the absolute

Table 10.13 Seebeck coefficient (μV/°C) and absolute thermoelectric power (μV/°C) of eight types of cement paste (Wen and Chung, 1999c, 2000b,c,d)

Cement paste	*Heating*		*Cooling*	
	*Seebeck coefficient**	*Absolute thermoelectric power*	*Seebeck coefficient**	*Absolute thermoelectric power*
(i) Plain	0.35 ± 0.03	−1.99 ± 0.03	0.38 ± 0.05	−1.96 ± 0.05
(ii) Silica fume	0.31 ± 0.02	−2.03 ± 0.02	0.36 ± 0.03	−1.98 ± 0.03
(iii) 0.5% fibers + silica fume	1.45 ± 0.09	−0.89 ± 0.09	1.45 ± 0.09	−0.89 ± 0.09
(iv) 1.0% fibers + silica fume	2.82 ± 0.11	+0.48 ± 0.11	2.82 ± 0.11	+0.48 ± 0.11
(v) 1.5% fibers + silica fume	3.10 ± 0.14	+0.76 ± 0.14	3.10 ± 0.14	+0.76 ± 0.14
(vi) Latex	0.28 ± 0.02	−2.06 ± 0.02	0.30 ± 0.02	−2.04 ± 0.02
(vii) 0.5% fibers + latex	1.20 ± 0.05	−1.14 ± 0.05	1.20 ± 0.05	−1.14 ± 0.05
(viii) 1.0% fibers + latex	2.10 ± 0.08	−0.24 ± 0.08	2.10 ± 0.08	−0.24 ± 0.08

Note
* With copper as the reference.

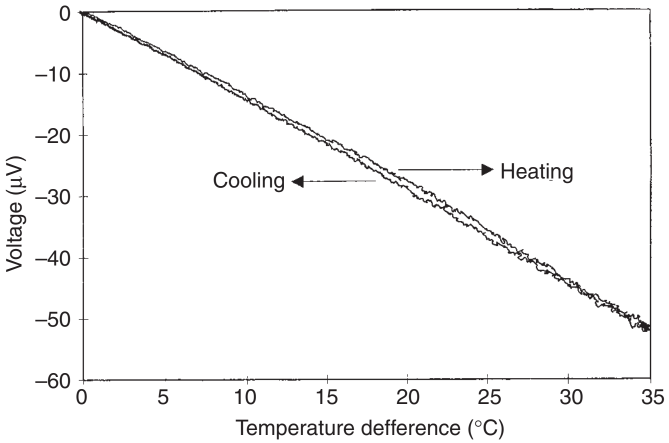

Figure 10.10 Variation of the Seebeck voltage (with copper as the reference) versus the temperature difference during heating and cooling for carbon-fiber silica-fume cement paste (Wen and Chung, 1999c).

thermoelectric power, it enhances the linearity and reversibility of the Seebeck effect. This enhancement is attributed to the increase in the contribution of holes to the electrical conduction and the association of hole conduction to conduction through the fibers.

The absolute thermoelectric power monotonically becomes less negative (more positive) as the fiber content increases through the percolation threshold, which is at a fiber content between 0.5% and 1.0% by weight of cement. The change of the absolute thermoelectric power from negative to positive values occurs at a fiber content between 0.5% and 1.0% by weight of cement when silica fume is present. This means that at this fiber content, which happens to be the percolation threshold, compensation takes place between the electron contribution from the cement matrix and the hole contribution from the fibers. It should be noted that, at any fiber content, electrons and holes contribute additively to the electrical conductivity, but subtractively to the thermopower. The correlation between the percolation threshold and change in sign of the absolute thermoelectric power is reasonable since the fibers dominate the conduction by means of holes above the percolation threshold and the cement matrix dominates the conduction by means of electrons below the percolation threshold. In the presence of latex instead of silica fume, the highest fiber content investigated was 1.0% by weight of cement and a change in sign of the absolute thermoelectric power was not observed, even though the percolation threshold is also between fiber contents of 0.5% and 1.0% by weight of cement for the case of latex. Although a change in sign of the absolute thermoelectric power was not observed for the case of latex, the absolute thermoelectric power is a negative value of a very small magnitude at a fiber content of 1.0% by weight of cement and the magnitude of the absolute thermoelectric power decreases monotonically with increasing fiber content. Based on this trend, it is highly probable that a change in sign would occur just above 1.0% by weight of cement for the case of latex. That a change in sign of the absolute thermoelectric power does not occur at the percolation threshold (but probably just above the threshold) is attributed to the low conductivity of carbon-fiber latex cement paste compared to carbon-fiber silica-fume cement paste at the same fiber content and the associated weaker hole conduction in the latex case. This is consistent with the observation that, at the same fiber content (whether 0.5% or 1.0% by weight of cement), the absolute thermoelectric power is more positive for the latex case than the silica fume case (Table 10.13).

The use of steel fibers instead of carbon fibers results in highly negative (as negative $-68\,\mu V/^\circ C$) values of the absolute thermoelectric power, as steel fibers involve electron conduction whereas carbon fibers involve hole conduction (Wen and Chung, 2000a–d). The highly negative values mean that the use of steel fibers gives a superior thermoelectric material then the use of carbon fibers.

A cement-based thermocouple in the form of a junction between dissimilar cement pastes exhibits thermocouple sensitivity $70 \pm 7\,\mu V/^\circ C$ (Wen and Chung, 2001g). The dissimilar cement pastes are steel fiber cement paste (n-type) and carbon-fiber silica-fume cement paste (p-type). The junction is made by pouring the cement pastes side by side. In addition to serving as a thermocouple junction, the junction provides electric current rectification (Wen and Chung, 2001f).

11 Corrosion resistance

Carbon fibers decrease the corrosion resistance of steel rebar in concrete, mainly due to the decrease in the volume electrical resistivity of concrete. However, the negative effect can be compensated by adding either silica fume or latex. Silica fume is more effective than latex for improving the corrosion resistance of carbon fiber concrete. This is mainly because silica fume reduces the water absorptivity. The small increases in electrical resistivity of carbon fiber concrete after adding either silica fume or latex contribute only slightly to the effect on corrosion. Corrosion of rebar in concrete with silica fume and carbon fibers is inactive in $Ca(OH)_2$ solution, but active in NaCl solution. However, the corrosion resistance in NaCl is better than rebar in plain concrete and similar to that of rebar in latex concrete without fibers (Hou and Chung, 2000).

12 Conclusion

Short carbon fiber cement–matrix composites exhibit attractive tensile and flexural properties, low drying shrinkage, high specific heat, low thermal conductivity, high electrical conductivity, high corrosion resistance, and weak thermoelectric behavior. Moreover, they facilitate the cathodic protection of steel reinforcement in concrete, and have the ability to sense their own strain, damage, and temperature. The strain sensing is associated with piezoresistivity and piezoelectricity.

Acknowledgment

This work was supported in part by the National Science Foundation of USA.

References

Akihama, S., Suenaga, T., and Banno, T. (1984). *Int. J. Cem. Composites & Lightweight Concrete*, **6** (3), 159.

Ali, A. and Ambalavanan, R. (1998). *Indian Concrete J.*, **72** (12), 669.

Banthia, N. (1996). *Indian Concrete J.*, **70** (10), 533.

Banthia, N., Djeridane, S., and Pigeon, M. (1992). *Cem. Concr. Res.*, **22** (5), 804.

Banthia, N., Moncef, A., Chokri, K., and Sheng, J. (1994a). *Can. J. Civil Eng.*, **21** (6), 999.

Banthia, N., Chokri, K., Ohama, Y., and Mindess, S. (1994b). *Adv. Cem. Based Mater.*, **1** (3), 131.

Banthia, N. and Sheng, J. (1996). *Cem. Concr. Composites*, **18** (4), 251.

Banthia, N., Yan, C., and Sakai, K. (1998). *Com. Concr. Composites*, **20** (5), 393.

Bayasi, M. Z. and Zeng, J. (1997). *ACI Structural J.*, **94** (4), 442.

Bontea, D., Chung, D. D. L., and Lee, G. C. (2000). *Cem. Concr. Res.*, **30** (4), 651.

Brandt, A. M. and Kucharska, L. (1996). *Materials for the New Millennium*, Proc. Mater. Eng. Conf., Vol. 1, ASCE, New York, 271–280.

Brousseau, R. J. and Pye, G. B. (1997). *ACI Mater. J.*, **94** (4), 306.

Campione, G., Mindess, S., and Zingone, G. (1999). *ACI Mater. J.*, **96** (1), 27.

Chen, P. and Chung, D. D. L. (1993a). *Composites*, **24** (1), 33.

Chen, P. and Chung, D. D. L. (1993b). *Smart Mater. Struct.*, **2**, 22.

Chen, P. and Chung, D. D. L. (1993c). *Smart Mater. Struct.*, **2**, 181.

Chen, P. and Chung, D. D. L. (1995a). *J. Am. Ceram. Soc.*, **78** (3), 816.

Chen, P. and Chung, D. D. L. (1995b). *J. Electron. Mater.*, **24** (1), 47.

Chen, P. and Chung, D. D. L. (1996a). *Composites*, Part B, **27B**, 11.

Chen, P. and Chung, D. D. L. (1996b). *ACI Mater. J.*, **93** (4), 341.

Chen, P. and Chung, D. D. L. (1996c). *ACI Mater. J.*, **93** (2), 129.

Chen, P. Fu, X., and Chung, D. D. L. (1995). *Cem. Concr. Res.*, **25** (3), 491.

Chen, P. Fu, X., and Chung, D. D. L. (1997). *ACI Mater. J.*, **94** (2), 147.

Chung, D. D. L. (1995). *Smart Mater. Struct.*, **4**, 59.

Chung, D. D. L. (1999). *TANSO* (190), 300.

Chung, D. D. L. (2000). *Smart Mater. Struct.*, **9** (4), 389.

Clemena, G. G. (1988). *Materials Performance*, **27** (3), 19.

Delvasto, S., Naaman, A. E., and Throne, J. L. (1986). *Int. J. Cem. Composites & Lightweight Concrete*, **8** (3), 181.

Fu, X. and Chung, D. D. L. (1995). *Cem. Concr. Res.*, **25** (4), 689.

Fu, X. and Chung, D. D. L. (1996). *Cem. Concr. Res.*, **26** (1), 15.

Fu, X. and Chung, D. D. L. (1996). *Cem. Concr. Res.*, **26** (10), 1467.

Fu, X. and Chung, D. D. L. (1997a). *Cem. Concr. Res.*, **27** (9), 1313.

Fu, X. and Chung, D. D. L. (1997b). *Cem. Concr. Res.*, **27** (2), 314.

Fu, X. and Chung, D. D. L. (1998a). *Cem. Concr. Res.*, **28** (6), 795.

Fu, X. and Chung, D. D. L. (1998b). *Carbon*, **36** (4), 459.

Fu, X. and Chung, D. D. L. (1999). *ACI Mater. J.*, **96** (4), 455.

Fu, X. Lu, W., and Chung, D. D. L. (1996). *Cem. Concr. Res.*, **26** (7), 1007.

Fu, X. Ma, E., Chung, D. D. L., and Anderson, W. A. (1997). *Cem. Concr. Res.*, **27** (6), 845.

Fu, X. Lu, W. and Chung, D. D. L. (1998a). *Carbon*, **36** (9), 1337.

Fu, X. Lu, W. and Chung, D. D. L. (1998b). *Cem. Concr. Res.*, **28** (2), 183.

Fujiwara, T. and Ujie, H. (1987). *Tohoku Kogyo Daigaku Kiyo, 1: Rikogakuhen* (7), 179.

Furukawa, S., Tsuji, Y., and Otani, S. (1987). *Proc. 30th Japan Congress on Materials Research*, Soc. Mater. Sci., Kyoto, Japan, 149–152.

Huang, C. M., Zhu, D., Dong, C. X., Kriven, W. M., Loh, R., and Huang, J. (1996). *Ceramic Eng. Sci. Proc.*, **17** (4), 258.

Huang, C. M., Zhu, D., Cong, X., Kriven, W. M., Loh, R. R., and Huang, J. (1997). *J. Am. Ceramic Soc.*, **80** (9), 2326.

Hou, J. and Chung, D. D. L. (1997). *Cem. Concr. Res.*, **27** (5), 649.

Hou, J. and Chung, D. D. L. (2000). *Corrosion Sci.*, **42** (9), 1489.

Igarashi, S., and Kawamura, M. (1994). *Doboku Gakkai Rombun-Hokokushu/Proc. Japan Soc. Civil Eng.*, (502), pt 5–25, 83.

Inagaki, M. (1991). *Carbon*, **29** (3), 287.

Kamakura, M., Shirakawa, K., Nakagawa, K., Ohta, K., and Kashihara, S. (1983). *Sumitomo Metals*.

Katz, A. and Bentur, A. (1994). *Cem. Concr. Res.*, **24** (2), 214.

Katz, A., Li, V. C., and Kazmer, A. (1995). *J. Materials Civil Eng.*, **7** (2), 125.

Kim, T.-J., and Park, C.-K. (1998). *Cem. Concr. Res.*, **28** (7), 955.

Kucharska, L. and Brandt, A. M. (1997). *Archives of Civil Engineering*, **43** (2), 165.

Lal, A. K. (1990), *Batiment Int./Building Research & Practice*, **18** (3), 153.

Larson, B. K., Drzal, L. T., and Sorousian, P. (1990). *Composites*, **21** (3), 205.

Lee, J., and Batson, G. (1996). *Materials for the New Millennium*, Proc. 4th Mater. Eng. Conf., Vol. 2, ASCE, New York, 887–896.

Lin, S.-S. (1994). *SAMPE J.*, **30** (5), 39.

Mao, Q., Zhao, B., Shen, D., and Li, Z. (1996a). *J. Wuhan U. Tech.*, Mater. Sci. Ed., **11** (3), 41.

Mao, Q., Zhao, B., Shen, D., and Li, Z. (1996b). *Fuhe Cailiao Xuebao/Acta Materiae Compositae Sinica*, **13** (4), 8.

Mobasher, B. and Li, C. Y. (1994). *Infrastructure: New Materials and Methods of Repair*, Proc. Mater. Eng. Conf. (804), ASCE, New York, 551–558.

Mobasher, B. and Li, C. Y. (1996). *ACI Mater. J.*, **93** (3), 284.

Newman, J. W. (1987). *Int. SAMPE Symp. Exhib.*, **32**, SAMPE, Covina, CA, 938–944.

Ohama, Y. and Amano, M. (1983). *Proc. 27th Japan Congress on Materials Research*, Soc. Mater. Sci., Kyoto, Japan, 187–191.

Ohama, Y., Amano, M., and Endo, M. (1985). *Concrete Int.: Design & Construction*, **7** (3), 58.

Ohama, Y. (1989). *Carbon*, **27** (5), 729.

Pangrazzi, R., Hartt, W. H., and Kessler, R. (1994). *Corrosion* (Houston), **50** (3), 186.

Park, C. (1998). Nippon Seramikkusu Kyokai *Gakujutsu Ronbunshi – J. Ceramic Soc. Japan*, **106** (1231), 268.

Park, S. B. and Lee, B. I. (1990). *High Temperatures – High Pressures*, **22** (6), 663.

Park, S. B. and Lee, B. I. (1993). *Cem. Concr. Composites*, **15** (3), 153.

Park, S. B, Lee, B. I., and Lim, Y. S. (1991). *Cem. Concr. Res.*, **21** (4), 589.

Pigeon, M., Azzabi, M., and Pleau, R. (1996). *Cem. Concr. Res.*, **26** (8), 1163.

Saito, K., Kawamura, N., and Kogo, Y. (1989). *Advanced Materials: The Big Payoff*, National SAMPE Technical Conf., **21**, Covina, CA, 796–802.

Shao, Y., Marikunte, S., and Shah, S. P. (1995). *Concrete Int.*, **17** (4), 48.

Shui, Z., Li, J., Huang, F., and Yang, D. (1995). *J. Wuhan Univ. Tech.*, Mater. Sci. Ed., **10** (4), 37.

Shi, Z. and Chung, D. D. L. (1999). *Cem. Concr. Res.*, **29** (3), 435.

Shimizu, Y., Nishikata, A., Maruyama, N., and Sugiyama, A. (1986). *Terebijon Gakkaishi/J. Inst. Television Engineers of Japan*, **40** (8), 780.

Shinozaki, Y. (1990). *Adv. Mater.: Looking Ahead to the 21st Century*, Proc. 22nd National SAMPE Technical, Conf. **22**, SAMPE, Covina, CA, 986–997.

Soroushian, P. (1990). *Construction Specifier*, **43** (12), 102.

Soroushian, P., Aouadi, F., and Nagi, M. (1991). *ACI Mater. J.*, **88** (1), 11.

Soroushian, P., Nagi, M., and Hsu, J. (1992a). *ACI Mater. J.*, **89** (3), 267.

Soroushian, P., Nagi, M., and Okwuegbu, A. (1992b). *ACI Mater. J.*, **89** (5), 491.

Sugama, T., Kukacka, L. E., Carciello, N., and Galen, B. (1988). *Cem. Concr. Res.*, **18** (2), 290.

Sugama, T., Kukacka, L. E., Carciello, N., and Stathopoulos, D. (1989). *Cem. Concr. Res.*, **19** (3), 355.

Sun, M., Li, Z., Mao, Q., and Shen, D. (1998a). *Cem. Concr. Res*., **28** (4), 549.

Sun, M., Li, Z., Mao, Q., and Shen, D. (1998b). *Cem. Concr. Res*., **28** (12), 1707.

Sun, M., Mao, Q., and Li, Z. (1998). *J. Wuhan U. Tech.*, Mater. Sci. Ed., **13** (4), 58.

Sun, M., Liu, Q., Li, Z., and Hu, Y. (2000). *Cem. Concr. Res.,* **30** (10), 1593.

Toutanji, H. A., El-Korchi, T., Katz, R. N., and Leatherman, G. L. (1993). *Cem. Concr. Res.*, **23** (3), 618.

Toutanji, H. A., El-Korchi, T., and Katz, R. N. (1994). *Com. Con. Composites*, **16** (1), 15.

Uomoto, T. and Katsuki, F. (1994–5). *Doboku Gakkai Rombun-Hokokushu/Proc. Japan Soc. Civil Engineers* (490), pt 5–23, 167.

Urano, T., Murakami, K., Mitsui, Y., and Sakai, H. (1996). *Composites – Part A: Applied Science & Manufacturing*, **27** (3), 183.

Wang, X., Wang, Y., and Jin, Z. (1998). *Fuhe Cailiao Xuebao/Acta Materiae Compositae Sinica*, **15** (3), 75.

Wen, S. and Chung, D. D. L. (1999a). *Cem. Concr. Res.*, **29** (3), 445.

Wen, S. and Chung, D. D. L. (1999b). *Cem. Concr. Res.*, **29** (6), 961.

Wen, S. and Chung, D. D. L. (1999c). *Cem. Concr. Res.*, **29** (12), 1989.

Wen, S. and Chung, D. D. L. (2000a). *Cem. Concr. Res.*, **30** (8), 1289.

Wen, S. and Chung, D. D. L. (2000b). *Cem. Concr. Res.*, **30** (4), 661.

Wen, S. and Chung, D. D. L. (2000c). *Cem. Concr. Res.*, **30** (8), 1295.

Wen, S. and Chung, D. D. L. (2000d). *J. Mater. Res.,* **15** (12), 2844.

Wen, S. and Chung, D. D. L. (2001a). *Cem. Concr. Res.,* **31** (2), 297.

Wen, S. and Chung, D. D. L. (2001b). *Cem. Concr. Res.,* **31** (4), 665.

Wen, S. and Chung, D. D. L. (2001c). *J. Electron. Mater.,* **30** (11), 1448.

Wen, S. and Chung, D. D. L. (2001d). *Cem. Concr. Res.,* **31** (2), 141.

Wen, S. and Chung, D. D. L. (2001e). *Carbon*, **39**, 369.

Wen, S. and Chung, D. D. L. (2001f). *Cem. Concr. Res.,* **31** (2), 129.

Wen, S. and Chung, D. D. L. (2001g). *Cem. Concr. Res.,* **31** (3), 507.

Wen, S. and Chung, D. D. L. (2001h). *Cem. Concr. Res*., **31** (4), 673.

Wen, S. and Chung, D. D. L. (2002a). *Cem. Concr. Res*., **32** (3), 335.

Wen, S. and Chung, D. D. L. (2002b). *Cem. Concr. Res*., **32** (9), 1429.

Xie, P., Gu, P., and Beaudoin, J. J. (1996). *J. Mater. Sci.*, **31** (15), 4093.

Xu, Y. and Chung, D. D. L. (1999a). *Cem. Concr. Res.*, **29** (5), 773.

Xu, Y. and Chung, D. D. L. (1999b). *Cem. Concr. Res.*, **29** (7), 1117.

Xu, Y. and Chung, D. D. L. (2000). *ACI Mater. J.*, **97** (3), 333.

Yamada, T., Yamada, K., Hayashi, R., and Herai, T. (1991). *Int. SAMPE Symp. Exhib.*, **36**, SAMPE, Covina, CA, pt 1, 362–371.

Yamada, T., Yamada, K., and Kubomura, K. (1995). *J. Composite Mater.*, **29** (2), 179.

Zayat, K. and Bayasi, Z. (1996). *ACI Mater. J.*, **93** (2), 178.

Zhao, B., Li, Z., and Wu, D. (1995). *J. Wuhan Univ. Tech.*, Mater. Sci. Ed., **10** (4), 52.

Zheng, Z. and Feldman, D. (1995). *Progress in Polymer Science*, **20** (2), 185.

Zhu, M. and Chung, D. D. L. (1997). *Cem. Concr. Res.*, **27** (12), 1829.

Zhu, M., Wetherhold, R. C., and Chung, D. D. L. (1997). *Cem. Concr. Res.*, **27** (3), 437.

INDEX